Small Conjugated Push-Pull Molecular Donors for Organic Photovoltaics : characterization and Devices Optimization

Amirhossein Habibi

UNIVERSITE MATIERE BRETAGNE MOLECULES LOIRE ET MATERIAUX

université angers

THÈSE DE DOCTORAT

DE L'UNIVERSITÉ D'ANGERS
COMUE UNIVERSITÉ BRETAGNE LOIRE

ÉCOLE DOCTORALE N° 596
Matière, Molécules, Matériaux (3M)
Spécialité : Sciences des matériaux, Photovoltaïque, Physico-chimie

Amirhossein HABIBI

Small Conjugated Push-Pull Molecular Donors for Organic Photovoltaics: Characterization and Devices Optimization

Thèse présentée et soutenue à Angers, le 7 février 2020

Unité de recherche : **Laboratoire MOLTECH-Anjou – CNRS UMR 6200**

Thèse N° : 181239

Composition du Jury

Rapporteurs :

Christine LARTIGAU-DAGRON	Maître de Conférences, Université de Pau et des Pays de l'Adour
Johann BOUCLÉ	Maître de Conférences, Université de Limoges

Examinateurs :

Laurence VIGNAU	Professeur, Université de Bordeaux
Jean-Manuel RAIMUNDO	Professeur, Université d'Aix-Marseille

Invité :

Clément CABANETOS	Chargé de Recherche au CNRS, Université d'Angers

Directeur de Thèse :

Philippe BLANCHARD	Directeur de Recherche au CNRS, Université d'Angers

Co- encadrant :

Olivier SEGUT	Maître de Conférences, Université d'Angers

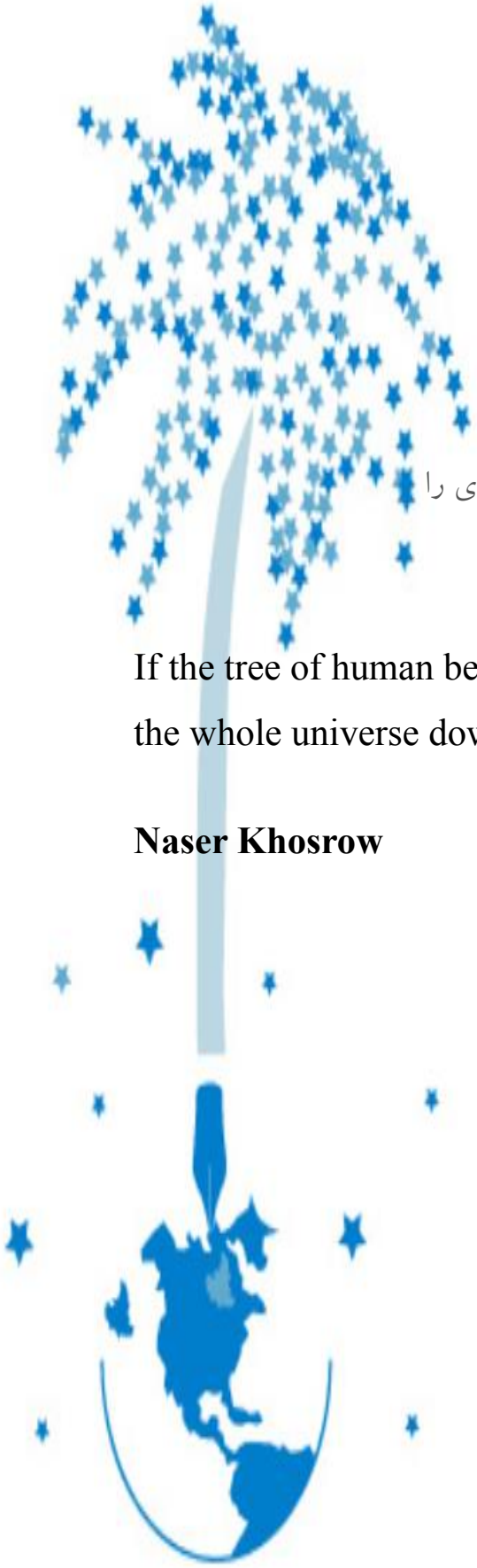

درخت تو گر بار دانش بگیرد به زیر آوری چرخ نیلوفری را

ناصر خسرو

If the tree of human being gets the fruit of knowledge, you can bring the whole universe down.

Naser Khosrow

For my family

Acknowledgements

The topic of my Ph.D. thesis made me proud to research about organic solar cells optimization for three years and I hope this research will help to conserve nonrenewable resources and the environment. This thesis becomes a reality with the kind support and help of many individuals and I would like to use this page to thank all those who made this period so enjoyable and fruitful for me.

I would like to thank *Prof. Marc SALLÉ*, director of MOLTECH-Anjou laboratory for his welcome and the excellent atmosphere that reigns there.

I would like to thank *Dr. Christine LARTIGAU-DAGRON* and *Dr. Johann BOUCLÉ* for agreeing to be reviewers for this work. I also thank *Prof. Laurence VIGNAU* and *Prof. Jean-Manuel RAIMUNDO* for their participation on this thesis jury as examiners.

I give my sincerest thanks to my excellent supervisor *Prof. Dr. Philippe BLANCHARD* for his great mentorship and guidance over the years. While he was an extremely busy professor holding about many students in his research group and a lot of domestic and international travels for seminars and conferences, he never hesitated to discuss with me when I knocked on his office's door. Our discussion often went over one hour in his tight schedule, but he did not stop until we reached clear conclusions and decided what to do next, thank you again for supervising me and providing the inspiration and efforts in assisting me with this work.

I would like to express my sincere gratitude to my *co-supervisors Dr. Olivier SEGUT* and *Dr. Clément CABANETOS* for the continuous support of my Ph.D. studies and suggestions as I worked to develop and complete my thesis, for their patience, motivation, and immense knowledge.

I am thoroughly grateful to *Prof. Sébastien CLÉMEN*T, from University of Montpellier in France, who has provide us cathode interlayer materials and *Prof. Sabine LUDWIGS,* from University of Stuttgart in Germany, to provide us spectroelectrochemical data.

Thanks to all the permanent members at the MOLTECH-Anjou staff who contributed to this work: my office mate *Martin BLAIS,* he is symbol of patience, ethics and kindness and let's say in one word "firefighter" and I will never forget we have suffered a lot to find suitable thickness by Profilometer. Thanks to SFR MATRIX group providing me solar cells

equipments, *Dr. Eric LEVILLAIN*, *Dr. Olivier ALÉVÊQUE* and also thanks to *Dr. Sylvie DABOS-SEIGNON* for AFM. I thank and acknowledge the help and assistance of the wonderful staff, in particular *Dr. Ingrid FREUZE* and *Sonia JERJIR* for mass spectrometry, *Benjamin SIEGLER* for the NMR, *Magali ALLAIN* for the resolution of the crystal structures, *Valérie BONNIN*, *Cécile MÉZIÈRE* and *Stéphane CHESNÉ*. In general, the entire staff of the MOLTECH-Anjou laboratory is thanked for the pleasant atmosphere that reigns there.

My labmates have played a key role in successful completion of my research work. A huge thanks to *Dr. Pierre JOSSE (PhD)*, *Dr. Antoine LABRUNIE (PhD)*, *Illia LENKO (Master)* and *Dr. Jérémie GROLLEAU (PhD)* have synthesized some of the donor push-pull molecules of my Ph.D. thesis. I am also thankful to *Dr. Youssef AIDIBI (PhD)*, *Pablo SIMON MARQUES*, *José MARÍA ANDRÉS CASTAN* and *Dr. Clément DALINOT* and all members of SCL group, for being a good companion in the lab.

I thank people of Angers who made me feel less homesick, *Francoise PLACE* and her family, *Béatrice ERVAIS-MARC* and *Monique HENRI*.

I would like to dedicate this thesis to my sincere and generous ***father***, my loving ***mother*** and ***sister*** who encouraged and helped me at every stage of my life and longed to see this achievement come true. I am indebted to my parents for their moral support throughout my Ph.D. tenure and without their understanding and support, it would be impossible for me to do this work.

Summary

Chapter 1: Fundamentals of organic photovoltaic devices

1.1. Introduction

Nowadays the energy and environment issues have become one of the global concern. Presently, the world uses energy sources at a rate of approximately 4.1×10^{20} joules/year, which is equivalent to 13 terawatts (TW), while energy from the sunlight that strikes the Earth in one hour, is estimated to 4.3×10^{20} joules/h (a watt (W) is a unit of power in the International System of Units (SI), which corresponds to 1 joule per second). In addition, Sun is the main natural power source and the best source of clean and abundant energy. The generated energy from the Sun by using solar cell to convert sunlight into electricity would be the best solution to save our environment from the pollution of fossil fuel and keep the non-renewable energy for the future. Therefore, sunlight represents a highly interesting source of energy that can generate electricity.[1-3] The solar spectrum irradiance is shown in Figure 1.1, the unit of irradiance is joules per second per m^2 of surface that is illuminated per μm of wavelength (W m^{-2} μm^{-1}).[4]

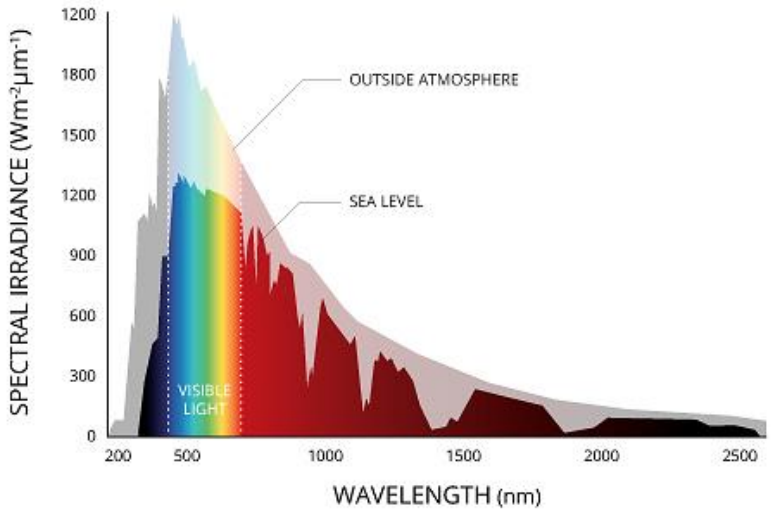

Figure 1.1. Spectrum of solar radiations received on earth. Data are obtained from ASTM.[4]

Figure 1.1 shows that the visible light corresponds only to a small part of the solar spectrum with wavelengths extending from 400 to 700 nm. In fact, the visible light corresponds to 42% of all the solar spectrum. Semiconducting materials with bandgaps between *ca*. 1.77 eV and 3.10 eV can thus absorb the wavelengths from the visible spectrum.

The term of air mass (AM) is very often used for the measurement of the amount of atmosphere the Sun's rays have to pass through. The amount of electricity produced by photovoltaic solar panels is significantly affected by the loss of photons absorbed by ozone, water or carbon dioxide and scattered by particles in the atmosphere. The solar spectrum outside the atmosphere is referred to as AM 0 (zero atmosphere) and corresponds to an integrated spectral radiance of 1366.1 W m^{-2}.[5] AM 1 (one atmosphere) corresponds to the incident power of light received on earth when the sun reaches the zenith

(θ = 0°). For a specific θ angle that the Sun makes with the vertical line (the zenith angle) perpendicular to the horizontal plane (Figure 1.2), AM X is defined as follows:

$$\text{AM X} = \text{AM}\left(\frac{1}{Cos\theta}\right)$$

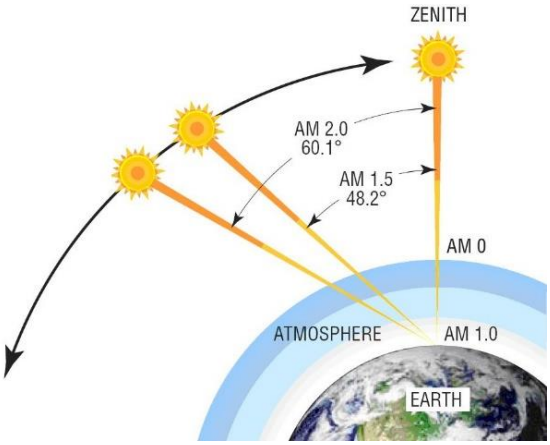

Figure 1.2. Illustration of AM 0, AM 1, AM 1.5 and AM 2.

For the Northern hemisphere like Canada, the United States, and Europe countries the sun's rays cross the atmosphere over a greater distance to reach the surface of the Earth, and the air mass determined for these regions is AM 1.5, which corresponds to the angle of Sun relative to the equator of 48.2° associated to an incident light power of 1000 W m^{-2}. In an artificial environment such as in the lab (MOLTECH-Anjou), a solar simulator is used to mimic the Sun and is tuned to deliver light in the AM 1.5 conditions with an incident light power of 100 mW cm^{-2} to measure the power conversion efficiency (PCE) of organic solar cells in standard conditions.

Solar cells can be produced from different types of semiconducting inorganic, organic or hybrid materials. The solar cells performance evolution with time is regularly updated by the National Renewable Energy Laboratory (NREL) which shows a graph representing the 'Best Research-Cell Efficiencies' for research cells for a wide range of photovoltaic technologies (Figure 1.3).[6]

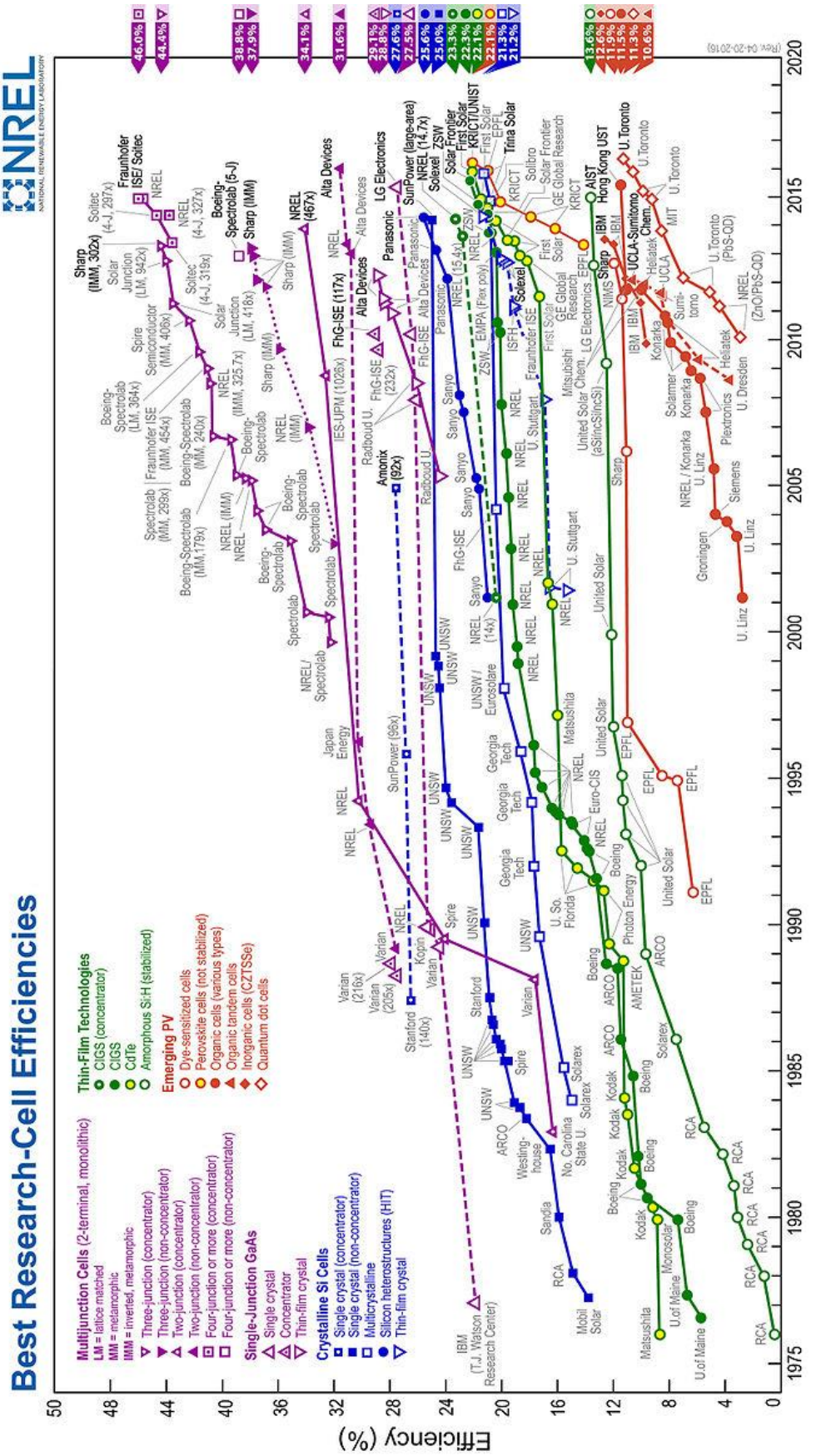

Figure 1.3. Evolution of power conversion efficiencies versus time for different types of solar cells.[6]

Photovoltaic devices can be classified into first, second and third generations (Figure 1.4). The first generation (1G) is based on silicon wafers which include mono-crystalline and polycrystalline silicon. Today 90% of the photovoltaic market is dominated by crystalline silicon (mono and multi-crystalline)[7] which can reach PCEs up to 26.7% for mono-crystalline and 22.3% for polycrystalline silicon in commercial modules.[8] The silicon-based solar cells have many advantages however their competitiveness is reduced due to their relative high production cost and environmental impact, heavy weight, lack of flexibility and difficulties for recycling.

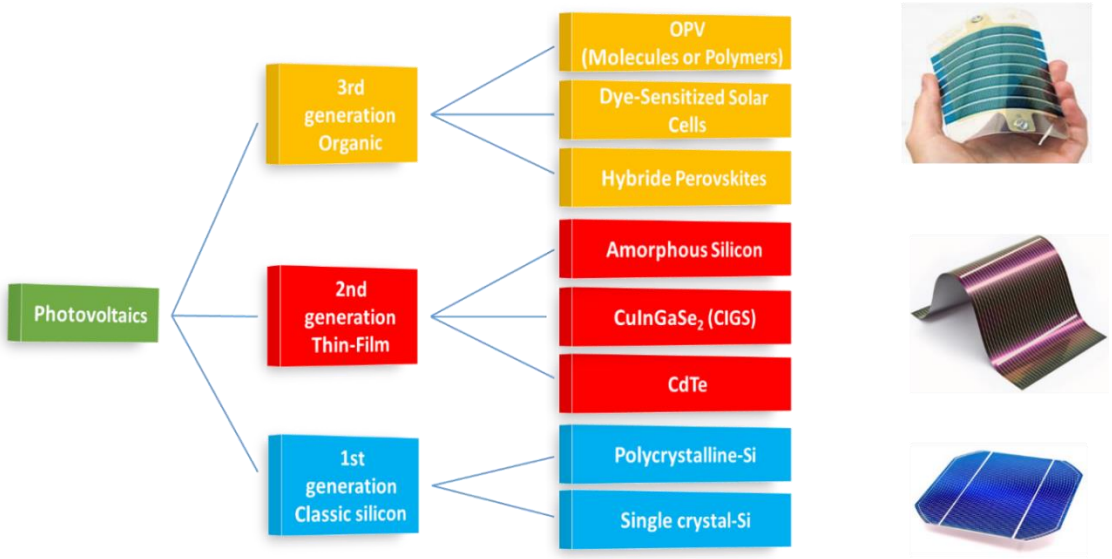

Figure 1.4. Classification of the different generations of solar cells.[8]

Second generation (2G) of photovoltaic cells is based on thin films of amorphous silicon, CdTe and CIGS ($CuInGaSe_2$). This technology reduces the amount of active layer material allowing for good flexibility. On the other hand, 2G thin film solar cells may contain highly toxic elements (Cd) which represent an issue in terms of ecological impact.

The third generation (3G) is also based on thin films using different emerging technologies and materials. All these 3G photovoltaic devices include, more or less, organic materials. They can be divided in: i) organic solar cells (OSCs) with photoactive layers derived from conjugated molecules or polymers, ii) dye-sensitized solar cells (DSSCs)[9-11] based on wide bandgap inorganic semiconductors sensitized with organic dyes and iii) hybrid organic-inorganic perovskite solar cells (PSCs).[12-14] Organic materials present the advantage to be processable in solution hence potentially reducing the costs of fabrication. These devices can be flexible, transparent and light and show better indoor efficiency compared to silicon. Although their record efficiencies are now nearly competing with amorphous or even multicrystalline silicon (*ca*. 16% for single-junction OSCs,[15] *ca*. 14% for DSSC [16-18] and *ca*. 23% for single junction PSCs),[12] they still suffer from shorter lifetimes than the 1G and 2G photovoltaic

devices. In addition, in the case of PSCs, the presence of toxic lead (Pb) atoms remains a problematic issue for potential industrialization. Research in these directions is underway however some companies, such as Armor in France or Heliatek in Germany, have already started, albeit on a small scale, to commercialize photovoltaic panels based on the OSC technology.

Organic photovoltaics (OPV) is a fascinating and promising technology, which can be developed in parallel to the silicon technology. For instance, some of their inherent properties such as flexibility, lightness, transparency and indoor efficiency can become an advantage for some applications for wearable devices or building integration. From 1986, when C. W. Tang developed the first bi-layer heterojunction with nearly 1% efficiency (see below), organic solar cells (OSCs) have been the subject of considerable efforts recently leading to a certified record PCE of 17.3% for an all-organic tandem solar cell.[19]

These significant progresses will be briefly summarized in the following paragraphs. This chapter also introduces the key concepts of OSCs. Section 1.2 will focus on the development of OPV since the beginning highlighting some important breakthroughs. Section 1.3 will present how OSCs are characterized and Section 1.4 will introduce the operating principle of OSCs. Different classes of organic materials used in OSCs will be described in Section 1.5. Finally, the end of this chapter will be specifically devoted to small π-conjugated push-pull molecules as electron-donor materials for OPV. The main goal of this PhD thesis deals with the characterization of new push-pull molecular systems and the optimization of corresponding OSCs using different fabrication conditions and new device architectures.

1.2. Development of OPV

On April 25, 1954, the first silicon solar cell was invented in the Bell Laboratories at New Jersey by D. Chapin, G. Pearson and C. Fuller, who announced that the world finally had an efficient way to turn sunlight into electricity. The power conversion efficiency of this first practical silicon solar cell was around 4%.[20] Still nowadays, silicon is the most commonly used inorganic semiconducting material in photovoltaics. On the other hand, whereas organic materials have been considered as isolating materials for a long time, the second part of the 20th century has triggered a considerable interest on some specific classes of organic materials which could exhibit fascinating and original properties such as strong absorption, electroluminescence, electrical conductivity and finally semiconductivity which led to the development of the field of Organic Electronics. As described in the following paragraph, this field is related to π-conjugated systems.

1.2.1. Organic Semiconductors

The discovery of conducting polymers by A. J. Heeger, A. G. MacDiarmid and H. Shirakawa in the 1970s is considered as a key step in the history of electronic organics. As shown in Figure 1.5, they succeeded in synthesizing high quality flexible copper-coloured films of the *cis*-isomer (1) and silvery films of the *trans*-isomer (2) of polyacetylene in the presence of a Ziegler catalyst, those polymers exhibiting high conductivity in their oxidized state (*p*-doped state).[21] Few years later, this major result has triggered the development of organic semiconductors based on neutral π-conjugated systems and their application in organic light-emitting diodes (OLEDs), organic field-effect transistors (OFETs) and organic solar cells (OSCs). This earned A. J. Heeger, A. G. MacDiarmid and H. Shirakawa the Nobel Prize of Chemistry in 2000.[22-24]

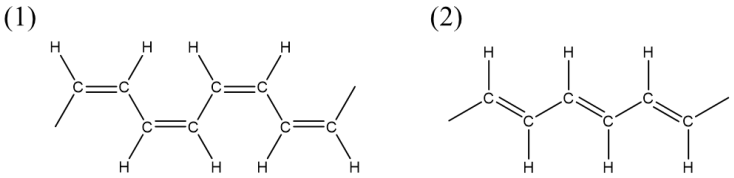

Figure 1.5. *Cis*-isomer (1) and *trans*-isomer (2) of polyacetylene.[21]

Organic semiconductors are based on molecular or polymeric π-conjugated systems constituted by an alternance of σ and π bonds. As described in Figure 1.6, the construction of the energetic diagram of polyacetylene starts from the simplest Ethylene fragment which contains two sp^2 hybridized carbon atoms linked together by one σ bond and one π bond originating respectively from the overlap of two sp^2 and two lateral p_z orbitals of each carbon. Combination of atomic orbitals of carbon and hydrogen atoms leads to several molecular orbitals, with a bonding or antibonding character, filled with or free of electrons, respectively. More specifically the two molecular frontier orbitals, namely the Highest Occupied Molecular Orbital (HOMO) and the Lowest Unoccupied Molecular Orbital (LUMO) play a crucial role. Then, further extension of the π-conjugated systems by combining increasing number of Ethylene segments leads to longer π-conjugated oligomers by overlapping p_z orbitals of the carbon atoms hence increasing the number of molecular orbitals. Most importantly, the concomitant destabilization of the HOMO level and stabilization of the LUMO level result in a progressive reduction of the HOMO-LUMO energy difference from 6.7 eV for Ethylene to 3.1 eV for Octatetraene.

Due to the monodimensional (linear) character of polyacetylene, a Peierls transition arises leading to the localization of σ and π bonds within the π-conjugated chain producing different lengths of carbon-carbon bonds, hence opening of a bandgap of energy E_g close to 1.5 eV.[25] Consequently polyacetylene is a semiconducting material in its neutral state with, by analogy with inorganic materials, a valence-like band and its upper "HOMO" level, and a conduction-like band with its lower "LUMO" level.[26, 27]

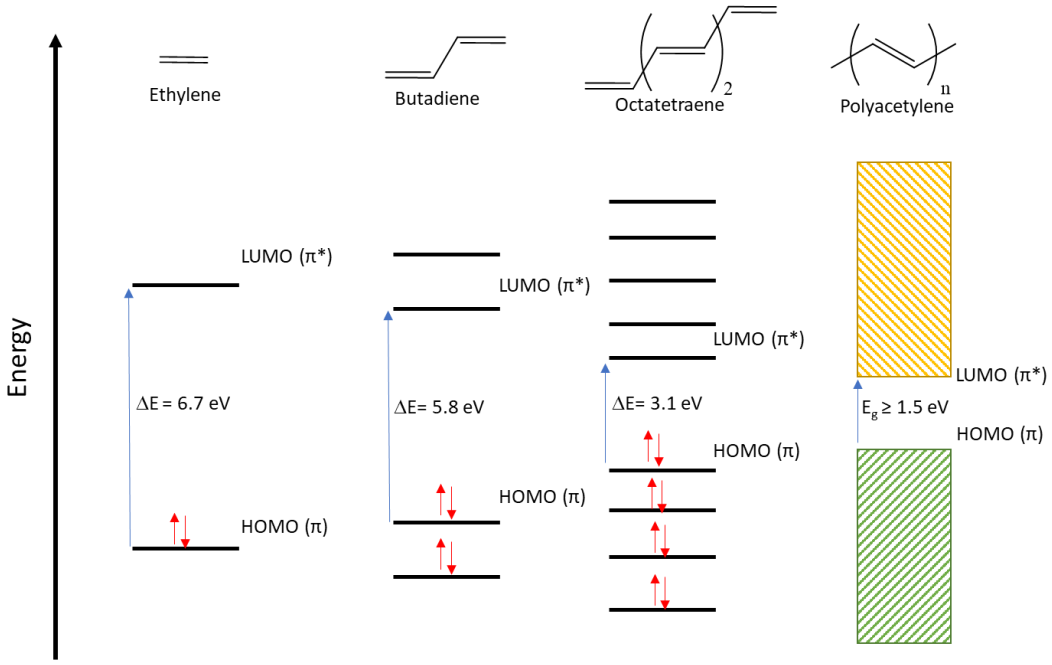

Figure 1.6. Energy levels of alkene oligomers: from Ethylene to Polyacetylene.

Depending on the structure of the conjugated polymers, organic semiconductors with different bandgaps E_g ranging from 1.5 to *ca*. 3 eV, can be designed. For example, compared to polyacetylene (**PA**), more stable aromatic π-conjugated polymers have led to organic semiconductors with various E_g values [28, 29] such as poly*para*phenylene (**PPP**, E_g = 3.0 eV),[30] poly*para*phenylenevinylene (**PPV**, E_g = 2.4 eV),[31] polypyrrole (**PPy**, E_g = 2.8 eV),[32] polythiophene (**PT**, E_g = 2.0-2.2 eV) [33-35] or poly(3,4-ethylenedioxythiophene) (**PEDOT**, E_g = 1.6-1.7 eV).[36]

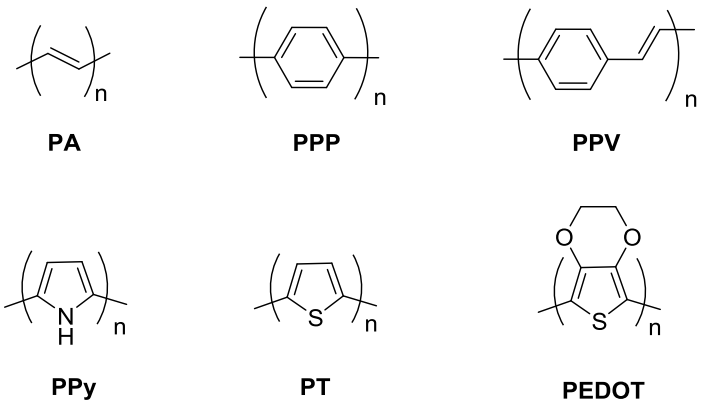

Figure 1.7. Examples of π-conjugated polymers.

The bandgap energy of π-conjugated systems (typically: 1.5 eV < E_g < 3 eV) corresponds to the energy range of the wavelengths of the visible spectrum. Thus the later will be absorbed by π-conjugated systems hence promoting electronic transitions from the levels of the "valence band" to the free levels

of the "conduction band". On the other hand, electronic excited states will be de-activated *via* radiative transitions to the ground state possibly leading to emission in the visble spectrum. As a result, π-conjugated systems have found applications in OLEDs and OSCs. In addition, these types of devices consist of multilayers of organic π-conjugated systems that present the advantage to be processed either in solution (dip-coating, spin-coating and doctor blade techniques …) or by thermal evaporation.

Basically, OSCs are based on a photoactive organic semiconducting layer sandwiched between a cathode and an anode electrodes. Usually, aluminum or silver are used as opaque cathode while an indium tin oxide (ITO) transparent electrode is used as anode allowing the absorption of the light by the photoactive layer. Over time, various architectures of OSCs have appeared, some of them will be briefly presented and discussed in the following sections.

1.2.2. Single-layer OSCs

The first concept of OSCs was developed in 1958 by D. Kearns and M. Calvin from the University of California. In their article entitled *''Photovoltaic Effect and Photoconductivity in Laminated Organic Systems''*, they prepared single-layer OSCs by deposition of **magnesium phthalocyanine** (**MgPc**) as active material between two electrodes of air-oxidized tetramethyl *p*-phenylenediamine (TMPPD) thin film.[37] A single layer OSC consists of only one organic semiconductor photoactive layer material sandwiched between two electrodes with different work functions and is often referred as a Schottky type device or Schottky diode. In this architecture, photons of the visble light are partly absorbed by the organic material which reaches its excited state, generating excitons (electron/hole pairs) that can diffuse within the material and dissociate in positive and negative charges at the interfaces with the electrodes thus generating a photocurrent (Figure 1.8).

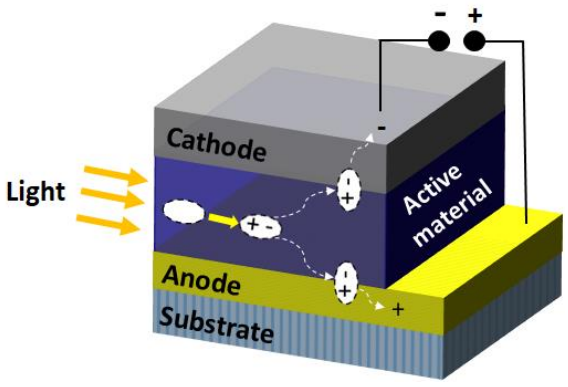

Figure 1.8. Architecture of a single layer organic solar cell (Schottky device).

In 1975, C. W. Tang *et al*. worked on the natural **Chlorophylle-a** as photoactive material which was sandwiched between chromium and mercury as the electrodes (Cr/Chlorophylle-a/Hg) (Figure 1.9).[38] OSCs based on **hydroxyl squarylium** as photoactive layer were fabricated by V. Y. Merritt and

H. J. Hovel in 1976 with this structure: Ga/hydroxyl squarylium/In_2O_3.[39] In 1984, the first polymer based on thiophene **poly(3-methylthiophene)** has been used for OPV.[40, 41]

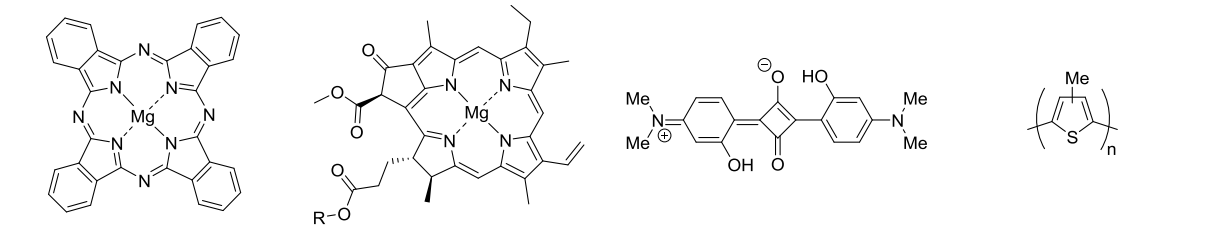

Magnesium Phthalocyanine
0.01% (670 nm)

Chlorophylle A
0.01% (745 nm)

Hydroxy squaraine
0.2% (850 nm)
0.06% (21 mW.cm^{-2})

Poly(methylthiophene)
4% (470 nm)
0.007% (1 mW.cm^{-2})

Figure 1.9. Examples of molecules or polymers used in single layer solar cells and their PV performance.

The architecture of single layer OSCs is simple however they present severe limitations in terms of photovoltaic (PV) efficiency due to several reasons. Excitons can be quenched close the metal electrodes. The photoactive layer is usually thin, limiting absorption, and dissociated charges have to pass through the same region to reach the electrodes resulting in high charge recombination. In addition, by using a single type of molecule, the absorption of the visible spectrum is limited to a narrow range of wavelengths.[42] As a consequence, the maximum power conversion efficiency reported with these device architectures is very low, less than 0.1% under white light illumination.[43]

1.2.3. Planar bi-layer heterojunction OSCs

Ching W. Tang

In 1986, C. W. Tang *et al*. achieved a significant breaktrough by introducing the concept of donor-acceptor heterojunction solar cells. They prepared planar bi-layer OSCs by using a vacuum deposited layer of copper phthalocyanine (**CuPc**) as electron-donor material, and a vacuum-deposited layer of an electron-deficient perylene derivative (3,4,9,10-perylenetetracarboxylic-bisbenzimidazole (**PTCBI**)). Under simulated AM 2 (75 mW/cm^2) illumination, they reported an efficiency close to 1 % (Figure 1.10).[44] Interestingly, considering the actual race for the development of non-fullerene acceptors, both **CuPC** and **PTCBI** were already shown to participate to the photocurrent. Then PV efficiencies of bi-layer OSCs based on **CuPc** have been improved up to 4.4% in heterojunction devices[45] and 5.7% for a tandem cell under standard sun simulator AM 1.5 (100 mW/cm^2), as reported by Forrest *et al*.[46] Since the discovery of C. W. Tang, many new donor and acceptor materials have been investigated.

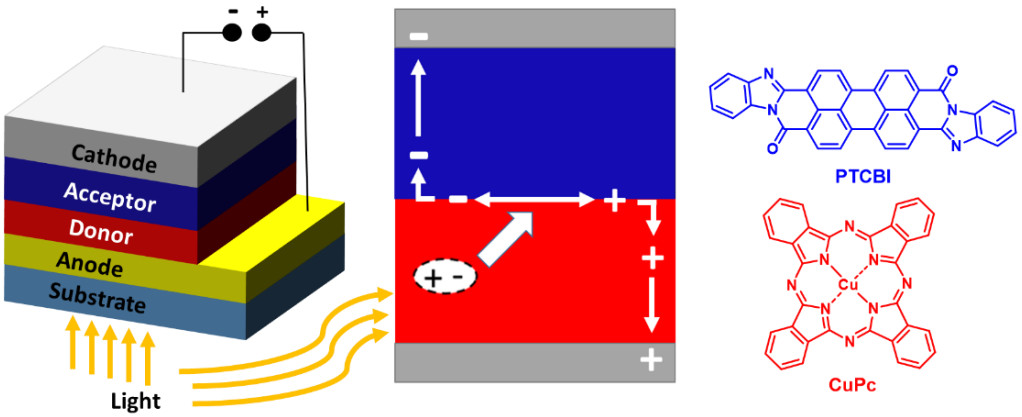

Figure 1.10. Architecture and operating principle of a bi-layer organic solar cell including a donor (red) and acceptor (blue) materials.[44]

Bi-layer heterojunction OSCs involve two organic materials with different energy levels. After absorption of the light by the donor and the acceptor layers, excitons are created and can diffuse to the donor/acceptor interface where an internal electric field allows for charge separation resulting in holes and electrons that can be transported through the donor or the acceptor layer, respectively, to the electrodes hence generating a photocurrent (Figure 1.10).

Although these solar cells showed better performance than single layer devices, they present some inherent limitations. Due to their small diffusion length (typically below 20 nm), excitons can recombine through non-radiative or radiative pathway, far away from the donor/acceptor interface if the donor or acceptor layer is too thick. Secondly, after charge separation, hole and electron mobilities must be sufficiently high to favor an efficient charge transport through the donor and acceptor layers in order to be collected to the electrodes. However, organic semiconductors exhibit much lower charge mobilities than silicon, for example. Thus, very thin layers are required for bi-layer OSCs to maximize charge generation from excitons and charge transport leading, on the other hand, to weak absorption. As a result, although they are very useful to investigate the PV potential of new materials, the PV performance of bi-layer OSCs are necessarily limited.

1.2.4. Bulk heterojunction OSCs

In 1992, A. J. Heeger and his colleagues, discovered the existence of an ultrafast (< ps) photoinduced electron transfer from **MEH-PPV**, after light excitation, to the fullerene C_{60}, as described in Figure 1.11.[47] Then N. S. Sariciftci and A. J. Heeger proposed to mix these two materials. To do so, the famous soluble fullerene derivative ($PC_{61}BM$) reported by F. Wudl was used in

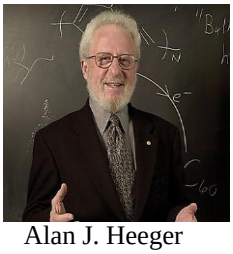
Alan J. Heeger

combinations with different soluble π-conjugated polymers as donors. A so-called "bulk heterojunction" (BHJ), with interpenetrating networks of donor and acceptor, was created.[48]

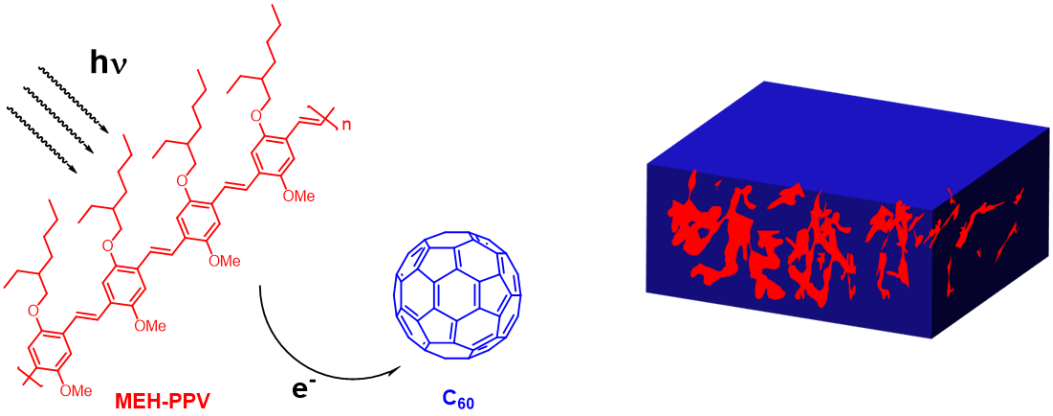

Figure 1.11. Ultrafast photoinduced electron transfer between **MEH-PPV** and C_{60} and schematic representation of a bulk heterojunction showing interpenetrating networks of a donor and an acceptor.[48]

In the mid-1990s, bulk heterojunction organic solar cells (BHJ OSCs) were developed by A. J. Heeger.[49] In general, BHJ OSCs consist of a photoactive layer obtained by blending one electron donor and one electron acceptor. This photoactive layer is generally deposited by solution or thermal co-evaporation process (Figure 1.12). These BHJ OSCs show considerably better performance because the donor/acceptor interface area is much increased hence favoring the exciton dissociation. In addition, the donor-acceptor phase separation that occurs in optimized blend leads to separated networks of donor and acceptor with nano-domain sizes (< 20 nm) maximizing also the exciton dissociation and charge percolation for charge transport to the electrodes. In BHJ OSCs, additional layers such as electron or hole blocking layers are also introduced close to the electrodes improving selective charge collection.[50-59]

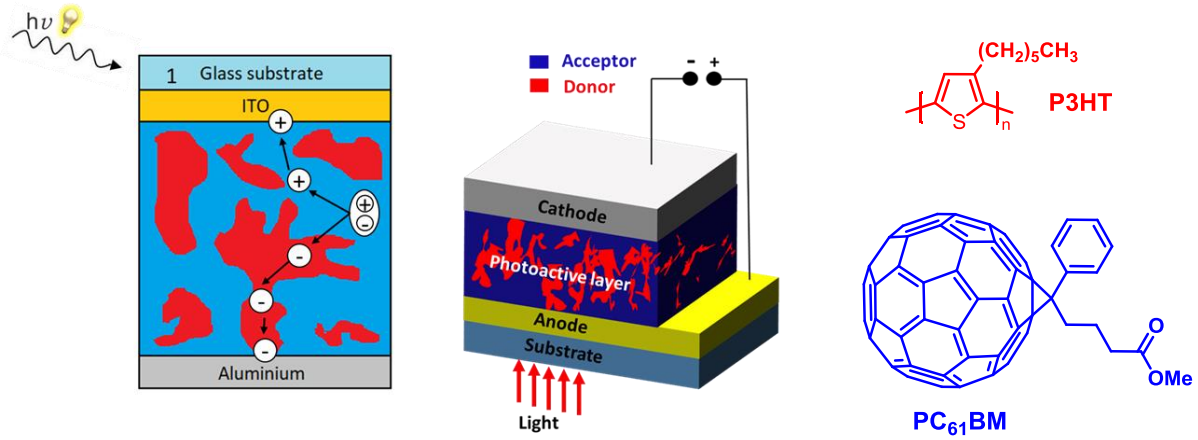

Figure 1.12. Representation of bulk heterojunction organic solar cells, operating principle and structure of the well-known P3HT/PC_{61}BM couple.

As expected, the efficiency of BHJ OSCs is strongly dependent on the thickness and the morphology of the photoactive layer which must be optimized *e.g.* by selecting the good solvent or a combination of solvents for deposition, thermal or solvent annealing, using additives and modifying molecule structures with different functional groups.[60,61,62] The P3HT:$PC_{61}BM$ couple, where **P3HT** stands for regioregular poly(3-hexylthiophene), has been largely investigated and optimized for BHJ OSCs.[63] For example, thermal annealing of P3HT:$PC_{61}BM$ was found to improve carrier mobility due to crystallization of **P3HT** in the BHJ.[64] Of crucial importance, the high regioregularity of **P3HT** led to improved absorption properties and better stacking of **P3HT** chains hence leading to more efficient BHJ OSCs.[65] Also optimization of the P3HT:$PC_{61}BM$ ratio [66] and using additives [67] can increase the performance as well.

It is worth noting that many works have been recently devoted to very efficient ternary blends BHJ OSCs.[68-72] This approach using three compounds instead of two allows for an optimal absorption of the visible spectrum by using optically complementary materials, better exciton dissociation and energy transfer through cascade processes and, sometimes, to better morphology.

Compared to the aforementioned single-junction BHJ OSCs, an elegant alternative to absorb complementarily the visible spectrum is to distribute a higher number organic materials in multi-junction OSCs such as tandem OSCs.

1.2.5. Tandem OSCs

Tandem or multi-junction OSCs consist of two or a higher number of sub-cells connected in series, each made of organic materials with complementary absorption, leading to improved power conversion efficiency.[73] Assembling the solar cells in series can produce a large overall V_{oc} corresponding to the sum of the open-circuit voltage V_{oc} of each sub-cell while active layers with different absorption regions can allow the cell to absorb the light in a broader wavelength range. For example (Figure 1.13), conventional tandem OSCs based on two BHJ photoactive layers of P3HT:$PC_{61}BM$ (V_{oc} = 0.55 V, PCE = 2.6%) and ZnPc:C_{60} (V_{oc} = 0.47 V, PCE = 2.2%) and a 1 nm thick Au intermediate recombination layer showed an improved V_{oc} of 1.02 V and enhanced spectral coverage. However in this case, the resulting short-circuit current J_{sc} was reduced leading to a PCE of 2.3% due to a lack of optimization of the respective thicknesses of the subcells.[74]

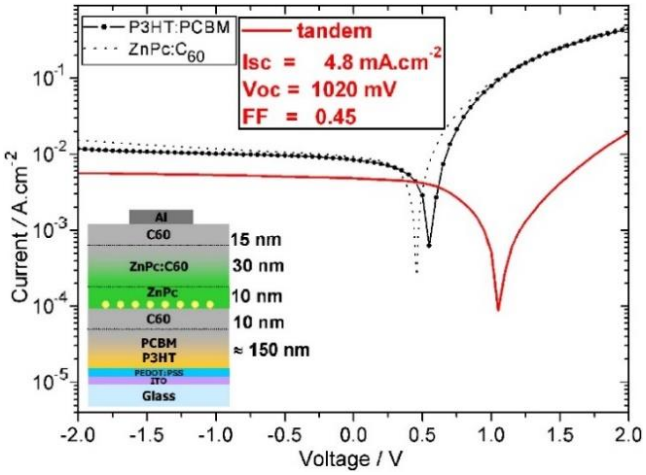

Figure 1.13. Current density *vs* voltage of the ZnPc⁄ZnPc:C_{60}⁄C_{60} individual cell, the P3HT:$PC_{61}BM$ diffused bilayer individual cell, and the tandem cell (red lie). The inset describes the structure of the tandem cell.[74]

The later tandem devices were prepared by combining two different deposition techniques, the second sub-cell being easier deposited by vacuum-evaporation avoiding any perturbation of the previously deposited layer. Thus the elaboration of tandem OSCs is rather difficult from a technological point of view since the top layer should not diffuse into the bottom layer. However, it has been possible to elaborate tandem OSCs by a full solution process using TiO_2/PEDOT:PSS [75] or ZnO/PEDOT:PSS[76] as interlayer (recombination layer) between sub-cells. On the contrary, to avoid any solution process, the group of K. Leo in Germany described the all vacuum-process preparation of triple junction OSCs exhibiting 24 layers based on evaporable π-conjugated molecules leading to PCE beyond 10%.[77]

1.2.6. Conventional *vs* inverted OSCs

Two types of geometry are encountered for OSCs, namely conventional (or standard) and inverted OSCs. They differ from each others by the opposite direction of the hole and electron flows as represented in Figure 1.14. In conventional OSCs, the top electrode with a relatively low working function, *e.g.* in aluminium (W_f = - 4.3 eV), is used as a cathode for the extraction of electrons while the transparent ITO electrode, with a higher work function (W_f = - 4.7 eV) is used as anode for the collection of holes. In the case of inverted OSCs, the ITO electrode is modified usually by depositing an electron transporting layer such as zinc oxide (ZnO) with a conduction band edge of *ca.* - 4.4 eV which allows for the selective extraction of electrons whereas the introduction of a hole-transporting material such as molybdenium oxide (MoO_3) is required before the deposition of the top electrode generally in silver or aluminium.

One advantage of inverted OSCs is, in general, their better stability owing to the possibility to use silver as top electrode contrary to aluminum or calcium which are not stable under atmospheric

conditions.[78] In addition, it avoids also the use of the weakly stable PEDOT-PSS as hole extracting layer in conventional OSCs (see next paragraphs and Chapter 2).

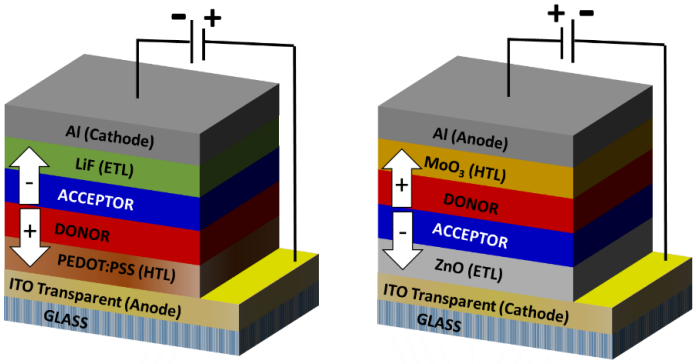

Figure 1.14. Conventional (left) and inverted (right) organic solar cells.

Thus inverted OSCs are widely used. For instance, the certified highest OPV efficiency ever reported of 17.3% by Y. Chen *et al*. in 2018, is based on tandem OSCs with an inverted architecture (Figure 1.15). The photoactive front sub-cell involves a binary blend of a conjugated polymer **PBDB-T** as donor associated with a molecular non-fullerene acceptor **F-M** while the rear sub-cell is derived from a ternary mixture of one conjugated donor polymer **PTB7-Th** and two acceptors, namely the fullerene derivative **$PC_{71}BM$** and a molecular non fullerene compound **O6T-4F**.[19]

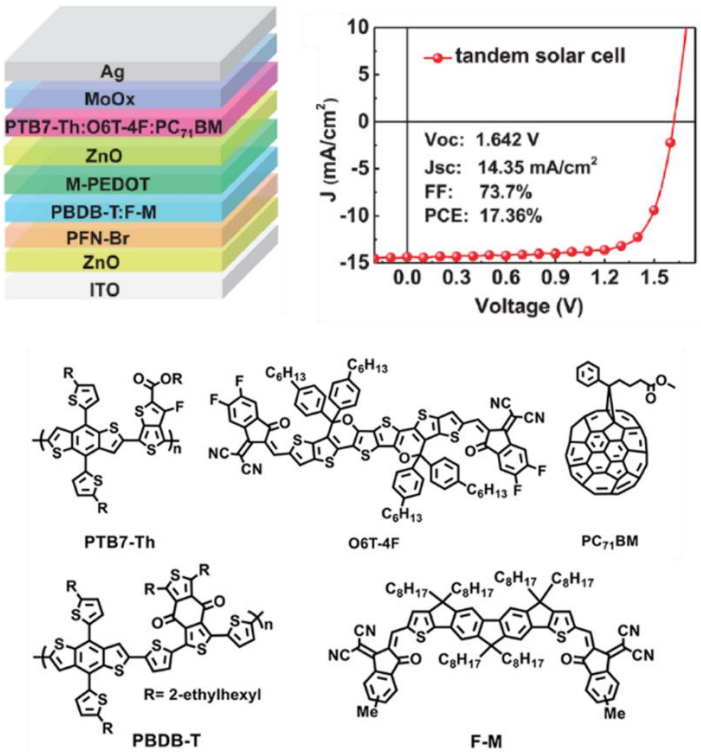

Figure 1.15. Architecture of the highest efficient OSCs ever reported with a tandem configuration operating in an inverted mode.[19]

1.3. Photovoltaic characterization

The most common way to characterize a photovoltaic cell is the measurement of their current density-voltage (J-V) characteristics which provide information about the behavior of the cell how it's working and photovoltaic parameters allowing us to calculate the power conversion efficiency (PCE) of the photovoltaic cells.

1.3.1. J-V characteristic

The J-V characteristic is represented as a curve, and standard parameters used to characterize the solar cell performance are described in this section. This J-V curve is measured in the dark or under illumination as shown in Figure 1.16. The J-V curve recorded in the dark exhibits the typical behavior of a diode characterized by a zero current from negative potentials to a positive threshold potential after which the current increases rapidly.

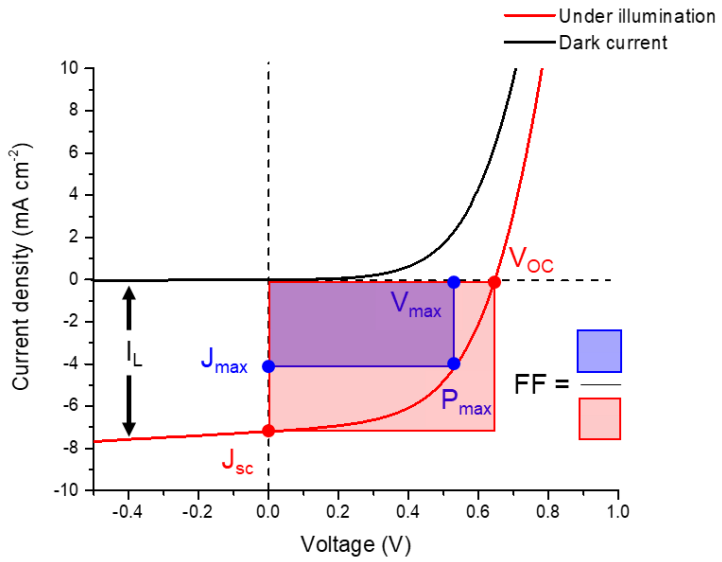

Figure 1.16. J-V characteristics of a photovoltaic cell recorded in the dark and under white light illumination.

The J-V curve under illumination gives the short-current density (J_{sc}) corresponding to the number of charge carriers that has been generated and collected at the electrodes at short circuit conditions (V = 0 V). The value of the J_{sc} parameter is generally increased by using organic materials exhibiting a small bandgap, high absorption coefficient and high charge mobility.

The open-circuit voltage (V_{oc}) corresponds to the voltage of the device at open circuit conditions (J = 0 mA cm^{-2}). The V_{oc} depends on i) the work function of the two different electrodes, ii) the energy difference between the HOMO level of the donor and the LUMO level of the acceptor and iii) the binding energy of the excitons which will be decribed in section 1.4.4 (Figure 1.17).

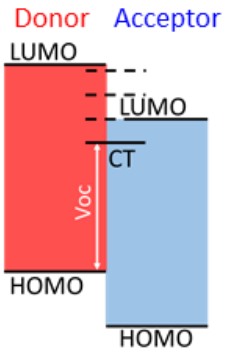

Figure 1.17. Representation of V_{oc}.

The Fill Factor (*FF*) defines the shape of the J-V curve compared to an ideal solar cell. *FF* is related to the maximum power output (P_{max}), where P_{max} is the maximum product of current (J_{max}) and voltage (V_{max}) respectively. *FF* corresponds to the ratio of the area of the blue rectangle with respect the red rectangle shown in Figure 1.16.

$$P_{max} = J_{max} \times V_{max}$$

$$FF = \frac{J_{max}V_{max}}{J_{sc}V_{oc}} = \frac{P_{max}}{J_{sc}V_{oc}}$$

The power conversion efficiency (*PCE*) corresponds to the maximum power delivered by the solar cell (P_{max}) as compared with the power of the incident light P_{in}:

$$PCE = \frac{P_{max}}{P_{in}} = \frac{J_{max}V_{max}}{P_{in}} = FF\frac{J_{sc}V_{oc}}{P_{in}}$$

Typically OSCs are characterized under a white light with an incident power density P_{in} of 100 mW cm^{-2} in the AM 1.5 conditions. To achieve maximum PCE, V_{oc}, J_{sc} and *FF*, need to be optimized.

The equivalent electric circuit of an organic solar cell is shown in Figure 1.18.[79] This circuit: 1) includes a diode with ideality factor $\boldsymbol{n}$ and saturation current $\boldsymbol{I_0}$ in the dark at the reverse bias, 2) shows a photocurrent $\boldsymbol{I_L}$ generated during illumination, 3) includes a series resistance $\boldsymbol{R_s}$ related to the conductivity of the organic semiconductors and electrodes at the interface between each layer, 4) includes a shunt resistance $\boldsymbol{R_{sh}}$ associated to the connectivity of the two different electrodes. Poor values of $\boldsymbol{R_{sh}}$ are typically due to manufacturing defects in the thin films. In order to get performant OPV devices, $\boldsymbol{R_s}$ needs to be low and $\boldsymbol{R_{sh}}$ must be high.

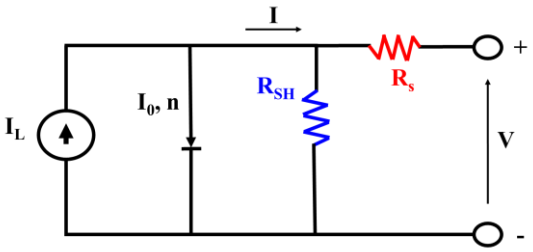

Figure 1.18. Equivalent electric circuit of an OPV device.

The R_{sh} is related to recombination of charge carriers close to the donor and acceptor interface. R_s also includes recombination further away from the donor and acceptor interface near the electrode. R_{sh} can be determined by taking the inverse slope of the tangent of the curve at around 0 V. The R_s considers conductivity for example mobility of the specific charge carrier in the respective transport medium. R_s is also increased with a longer traveling distance of the charges for example in thicker layers. R_s can be estimated from the inverse slope of the tangent of the curve at a positive voltage > V_{oc} where the J-V curve become linear. Note that the J-V characteristic of an ideal diode would be obtained if R_s = 0 Ω and R_{sh} = ∞ Ω.

1.3.2. Quantum efficiency

The other important characterization of solar cells is the measurement of the External Quantum Efficiency (EQE) or also called incident-photon-to-current efficiency. The EQE is defined as the ratio between the number of photoinduced charges extracted out of the solar cell (extracted electron-hole pair) and the number of incident photons for a given wavelength.

$$EQE = \frac{Nb\ of\ electrons\ of\ external\ circuit}{Nb\ of\ incident\ photons}$$

An EQE spectrum is thus recorded, in principle, over all the visible spectrum to determine an EQE value for each wavelength. The short-circuit current density J_{sc} can be estimated from the EQE spectrum and the spectral irradiance of the light source by integrating the product of the EQE and the photon flux density.

$$J_{sc} = \int_0^{\infty} qEQE\ (\lambda)\ \frac{\lambda}{hc} E_{\lambda}^{AM\ 1.5} d\lambda$$

where $\frac{hc}{\lambda}$ represents the energy of a photon of wavelength λ, h being the Plank's constant, c the speed of light and q the elementary charge and $E_{\lambda}^{AM\ 1.5}$ the spectral irradiance of the AM 1.5 spectrum.

1.4. Operating principle of organic solar cells

The operating principle of an organic solar cell under sunlight can be briefly described by the following four steps (Figure 1.19): 1) generation of excitons (electron-hole pairs) after absorption of photons by the donor material (Channel 1), for example; 2) exciton diffusion to the donor/acceptor interface; 3) exciton dissociation into free charges at the donor/acceptor interface resulting from an electron transfer from the LUMO of the donor to the lower LUMO of the acceptor and 4) charge transport and finally charge collection at the two different electrodes to generate a photocurrent. It is worth noting that the acceptor can also absorb light (Channel 2) generating excitons and hence a single electron transfer can take place spontaneously from the HOMO of the donor to the partially occupied HOMO of the acceptor, this different route leading to the same final situation as for the formation of excitons from the donor material (Figure 1.20).[80]

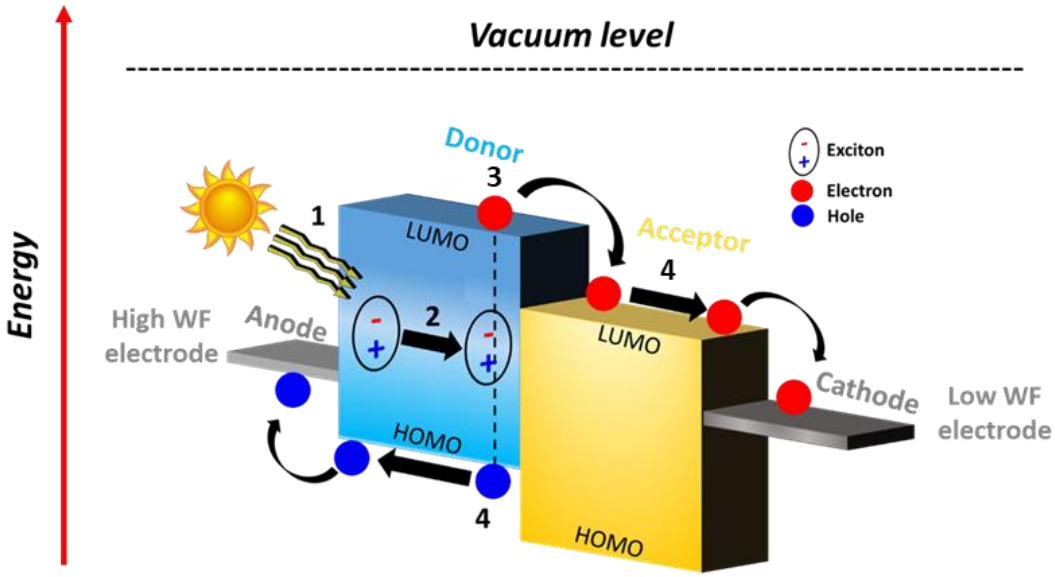

Figure 1.19. PV conversion mechanisms in OSCs: 1) exciton generation upon light absorption; 2) exciton diffusion; 3) exciton dissociation at the donor/acceptor interface and 4) charge transport and collection at the electrodes.

Each step of this mechanism presents some limitation and must be optimized for efficient power generation as explained below.

1.4.1. Light absorption and exciton generation

The first step in the PV process consists in the absorption of the photon by one material or both donor and acceptor. Although C. W. Tang already demonstrated that both materials can absorb light and contribute to the photocurrent,[44] the donor material, typically a π-conjugated polymer, has long been considered to be the main absorbing material as compared to fullerene derivatives used as acceptor

counterpart for a long time. Indeed, π-conjugated oligomers and polymers exhibit a relatively low bandgap ($1.5 < E_g <$ *ca*. 3 eV) and high absorption coefficients allowing their efficient absorption of the visible spectrum. Thus materials with high absorption coefficients on a wide range of wavelengths in the visible spectrum are of high interest for OPV. This is particularly true due to the fact that the thickness of photoactive layer is generally low, *ca*. 20-30 nm for each layer for a bi-layer OSCs, thus limiting the percentage of the absorption of light. In the case of BHJ OCS, the thickness of the photoactive layer can be increased up to 200 nm giving rise to a better absorption process. However, the thickness must remain enough small to favor an efficient charge transport and charge collection after exciton dissociation.

1.4.2. Exciton diffusion

For singlet excitons, diffusion occurs *via* different energy transfer processes between neighbouring molecules or conjugated chains constituting the material. In general, organic semiconductors exhibit an exciton diffusion length (L_D) smaller than 10-20 nm. This length corresponds to the distance that an exciton can travel within a given material before recombination (decay of the excited state to the ground state) through a non-radiative pathway or eventually by emission. The small values of L_D explains why each layer of a bi-layer OSC must be very thin (20-30 nm) to ensure that most of the generate excitons can reach the donor/acceptor interface.

The exciton diffusion length (L_D) is described by the following equation[81]:

$$L_D = \sqrt{D \times \tau}$$

D: diffusion coefficient
τ: exciton life time

1.4.3. Exciton dissociation

Contrary to silicon, photoexcitation of organic semiconductors does not lead to instantaneous free carrier generation. Owing to the low dielectric constants of organic semiconductors, there is a strong Coulomb binding E_B of the order of 0.3 eV within the hole-electron pair (exciton)[80] which is greater than k_BT at room temperature. To overcome this exciton binding, heterojunctions have been introduced by C. W. Tang [44] by using two differents organic semiconductors, a donor and acceptor with different energy levels providing a driving force for the successful dissociation of excitons.

In the case of channel 1 (Figure 1.20), after exciton generation in the donor material, the photoinduced electron transfer (PET) from the "LUMO" level (associated to the electron affinity of the donor EA_D) to the "LUMO" level of the acceptor (associated to the electron affinity of the acceptor EA_A) requires a difference EA_D-EA_A higher than the binding energy of the donor exciton E_B^D. On the

other hand, for channel 2, a photoinduced hole transfer (PHT) will take place from the acceptor to the donor if the difference of the respective ionization potential IP_A-IP_D becomes higher than E_B^A:

$$EA_D\text{-}EA_A > E_B^D \text{ (Channel 1)}$$

$$IP_A\text{-}IP_D > E_B^A \text{ (Channel 2)}$$

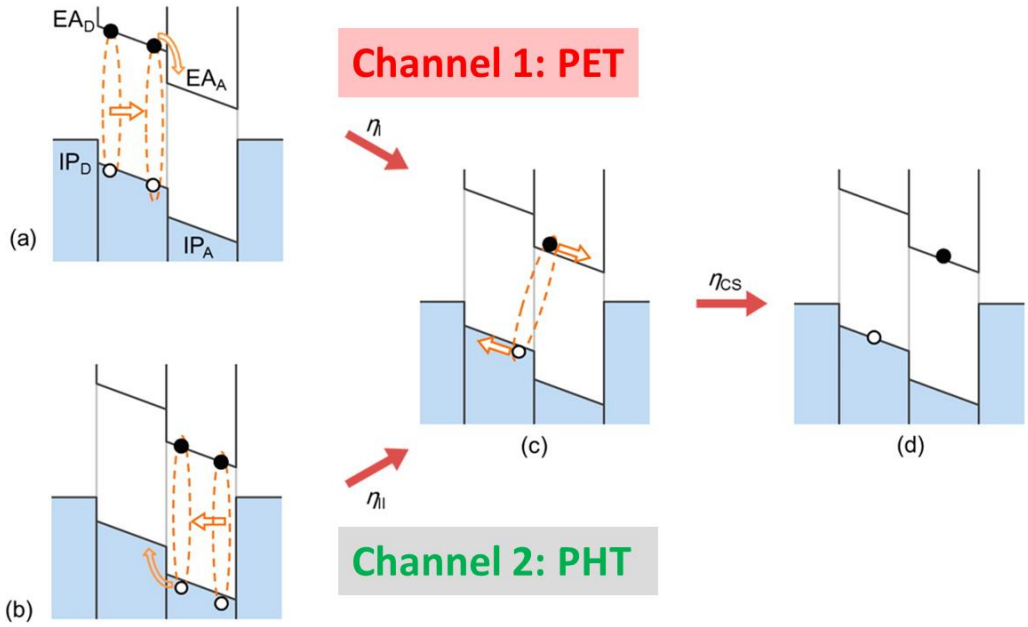

Figure 1.20. Photoinduced electron transfer (PET) for channe1 and photoinduced hole transfer (PHT) for channel 2. Adapted from.[80]

The charge transfer between the donor and acceptor is commonly very fast typically within a time range < 100 fs.[82] However, if the driving force is lower than *ca*. 0.2-0.3 eV, the exciton will decay without contributing to the photocurrent.[83]

1.4.4. Charge transfer state

After dissociation of the exciton, an electron is transferred to the "LUMO" level of the acceptor following Channel 1. Subsequently an intermediate charge transfer (CT) state occurs for which the hole and the electron are still close from each other at the donor/acceptor interface and thus still subjected to Coulombic attraction (Figure 1.21).[84, 85] The binding energy of the CT exciton state (E_B^{CT}) was reported in this range of 0.1-0.5 eV.[86, 87] At this stage, geminate recombination of hole and electron can arise hence decreasing the photocurrent generation.

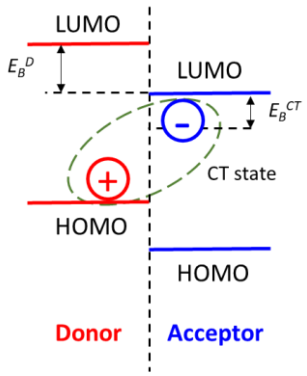

Figure 1.21. Generation of a charge-transfer state.

1.4.5. Charge transport in the donor and acceptor

Under the electric field stemming from the difference of work function of the two electrodes of the device, hole and electron from the CT exciton state are fully separated and transported in the donor and the acceptor materials, respectively, to the electrodes. The driving force is chiefly dependent on the gradient of electrons and holes. However bimolecular non-geminate recombination between electrons and holes during the transport process can arise at the donor/acceptor interface especially in BHJ OSCs for which multiple interfaces are distributing within all the photoactive layer.

The charge transport occurs by a hopping mechanism.[88] The efficiency of the charge carrier transport depends on the hole mobility (μ_h) for the donor material and the electron mobility (μ_e) for the acceptor material and are determined by the electrical conductivity and impedance of organic materials.[3, 86, 89]

1.4.6. Charge extraction at the electrodes

Electrons and holes must be extracted at the cathode and the anode, respectively. The use of an anode with a high work function close to the "HOMO" of the donor material will facilitate the extraction of holes by decreasing the energetic barrier and favoring Ohmic contacts. ITO is an anode of choice with its work function of -4.7 eV quite close to the HOMO of many π-extended conjugated systems. On the other side, the work function of the cathode is generally low, matching with the "LUMO" of acceptors.[90] If the energy barrier is too high, the extraction rate of charge carriers will be limited potentially producing accumulation or recombination of charges resulting in lower fill factors (FF) and PV performance. This behaviour can lead also to the existence of J-V curves showing a S-shape.[91]

Collection of charges at the wrong electrodes can also arise. To overcome this issue, electron and hole transporting layers (ETL and HTL), hole- and electron-blocking layers (HBL and EBL) or buffer layers, can be deposited between the active layer and one electrode to select one charge species and improve the collection of charges.[92-94]

1.4.7. Charge transporting and buffer interlayers

As introduced just above, anode and cathode interlayers can significantly improve the OSCs performance by facilitating charges extraction. Electron transporting layer (ETL) and hole transporting layer (HTL) could be adapted to the cathode and the anode, respectively. Inorganic interlayer engineering with metal oxides, such as ZnO,[95, 96] TiO_X, [97] MoO_3, [98] LiF, [99] or Ca [98] are extremely studied and applied in OSCs fabrication. Organic interlayer materials were investigated and gave good results, such as bathocuproine (or 2,9-dimethyl-4,7-diphenyl-1,10-phenanthroline) (BCP), [100] perylene derivatives or the poly [(9,9-bis(3'-(*N*,*N*-dimethylamino)propyl)-2,7-fluorene)-alt-2,7-(9,9–dioctylfluorene)] (PFN) [101] that improved interfacial contacts. BCP is used close to the cathode as hole-blocking layer and electron transporting layer leading to improved performance, however it presents also some drawbacks such as thermal instability and easy crystallization in the presence of moisture and at high temperature.[102, 103] The composite conducting polymer poly(3,4-ethylenedioxythiophene):polystyrenesulfonate (PEDOT:PSS) is also widely used as anode interlayer at the ITO electrode because its lower work function of – 5.1 eV compared to that of ITO, favors hole extraction.

Alkali earth metals, for example, Ca, Ba, Mg and and alkali metal compounds like Cs_2CO_3 and LiF can be used as cathode interlayer to favor electron extraction while these interlayers can prevent aluminum or silver electrode to diffuse into the organic photoactive layer during the thermal evaporation process.[104-107] To select the suitable metal oxide, ETL and HTL materials, the energy levels of their conduction band or valence band must be considered. HTL materials, for example V_2O_5, [108-111] MoO_3, [98] WO_3, [112-114] and NiO [115-120] can replace PEDOT:PSS. [109] TiO_x and ZnO are ETLs which have been used for both conventional and inverted OSCs.[104]

Charge transporting layers and buffer interlayers used in this PhD work will be described more in details in the following chapter.

1.5. Donor and acceptor materials for OSCs

The design of new donor and acceptor materials for OPV has significantly contributed to the progress of PV efficiency. Absorption properties and frontier orbital energy levels of π-conjugated systems can be controlled by molecular engineering.[121] It is possible by design and synthesis, in principle, to optimize PV parameters such as J_{sc} and V_{oc}, the former being related to optical absorption and the later depends on the difference of energy HOMO (D) – LUMO (A).[79] It is also crucial to control intermolecular π-interactions in the solid state to get high charge mobility which can in turn affect J_{sc} and FF as well.

In the following paragraphs, some strategies to optimize donor materials based on π-conjugated polymers and small oligomers, will be briefly described. The most known fullerene derivatives used as acceptors in OPV will be depicted and their properties will be compared to the most promising classes of non-fullerene acceptors (NFAs).

1.5.1. Polymeric donor materials for OSCs

A considerable number of low bandgap conjugated polymers has been developed for OPV applications.[122] However wide bandgap conjugated polymers ($E_g^{opt} > 1.8$ eV) such as **P3HT** (poly(3-hexythiophene)) have also significantly contributed to the development of OPV. **P3HT** is a soluble conjugated polymer which shows a *p*-type semiconducting behavior in the solid state. Thus, **P3HT** has long been used as a reference donor material in combination with the fullerene derivative $PC_{61}BM$ (phenyl-C_{61}-butyric acid methyl ester) for solution-processed BHJ OSCs leading to PV efficiencies between 3.5-5% (Figure 1.12).[63]

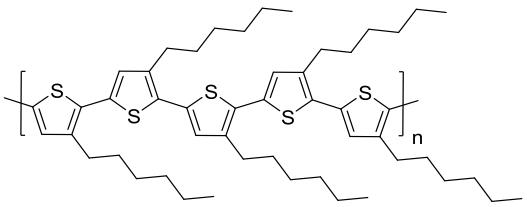

Figure 1.22. Regioregular **P3HT**.

The OPV performance of **P3HT** depends on its regioregularity and its molecular weight as well.[123] High molecular weight leads to better PV performance while high regioregularity induces absorption at higher wavelengths due to a longer conjugated pathway, and improves hole transport in the solid state owing to more ordered intermolecular packing (Figure 1.22).[124] Thermal annealing of the P3HT/$PC_{61}BM$ as deposited layer is generaly required to favor phase separation and hence good PV properties. However this process should be controlled to avoid the formation of too big domains or excessive crystallization or phase aggregation of each constituent which could be detrimental for OPV. To avoid these issues, the use of less regioregular **P3HT** (*e.g.* 86% regioregular) has been recommended.[125]

The optical bandgap of regioregular **P3HT** is around 1.9 eV with an onset of absorption at 650 nm (Figure 1.23). Considering that the emission solar spectrum has a maximum at *ca*. 1.8 eV (700 nm), **P3HT** is capable to harvest up to 22.4% of the photons from Sun.[126-128] In addition, due to its soccer-ball symmetry which forbiddens lowest energy transitions, $PC_{61}BM$ is relatively inert optically and does

not collect much photons from the visible spectrum.[129] As a consequence, thin-films of P3HT/$PC_{61}BM$ absorb less than *ca*. 30% of the solar spectrum.

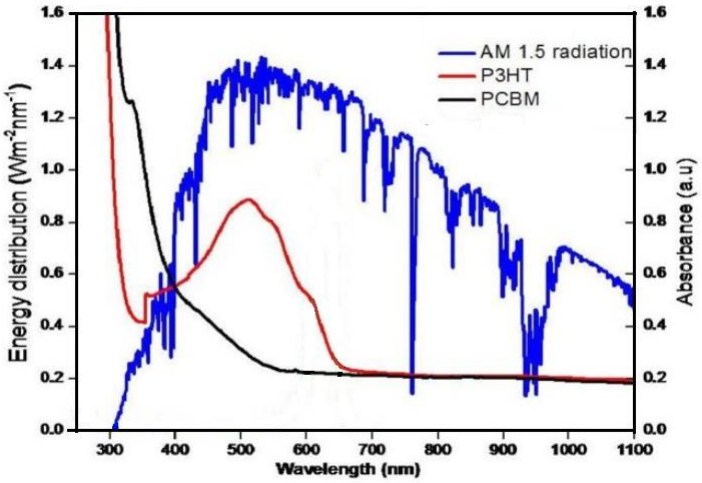

Figure 1.23. Absorption spectra of thin-films of **P3HT** or $PC_{61}BM$ and standard AM 1.5 solar spectrum.[130]

This result shows that optimization of the bandgap of π-conjugated polymers or molecules is needed to collect a higher number of photons from the solar spectrum. Various molecular engineering strategies have been shown to affect the bandgap of π-conjugated systems such as chemical rigidification, non-covalent intramolecular interactions, the control of the aromatic character, the introduction of substituents with inductive/mesomeric effects, the regioregularity-induced interchain coupling and the formation of an intramolecular charge transfer (ICT) by alternating electron-donating (eD) and electron-accepting (eA) building blocks leading to $(eD–eA)_n$ type conjugated systems.[35, 131, 132]

The later approach has been proven to be particularly successful leading to $(eD–eA)_n$ based conjugated polymers with low bandgaps (E_g < 1.8 eV), resulting from a stabilization of the LUMO level thanks to the eA units and the destabilization of the HOMO level due to eD units. For instance, the thiophene-based polymers including electron-rich platforms such as benzo[1,2-b:4,5-b']dithiophene and electron-deficient moieties such as 3-fluorothieno[3,4-b]thiophene, 5,6-difluorobenzo[c][1,2,5]thiadiazole or benzo[1,2-c:4,5-c']dithiophene-4,8-dione described in Figure 1.24, have been used as donor materials in combination with different acceptor materials for the fabrication of highly performant BHJ OSCs with power conversion efficiencies beyond 10% and up to 13%.[133-140]

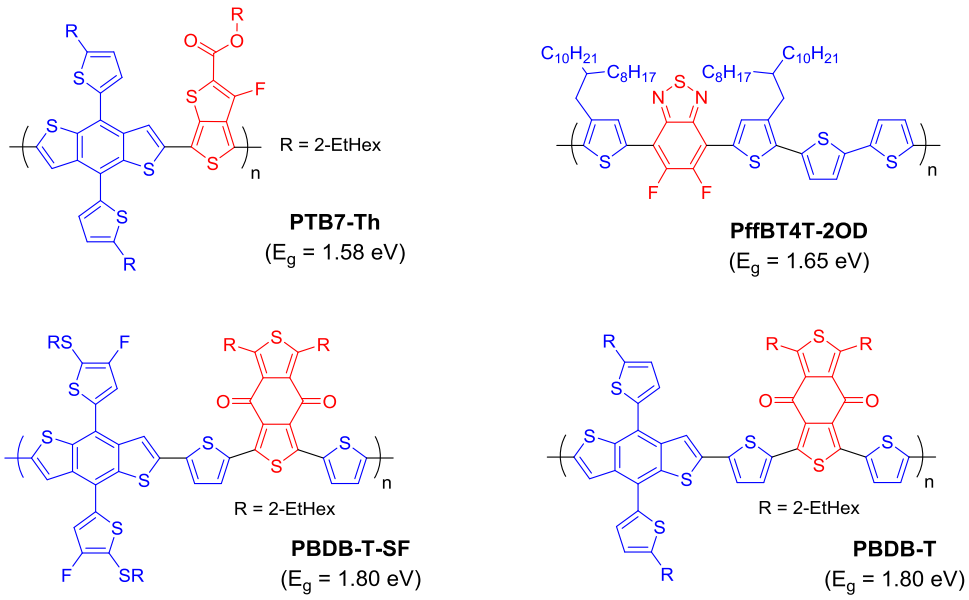

Figure 1.24. Low bandgap π-conjugated polymers as donors for BHJ OSCs.

1.5.2. Molecular donor materials for OSCs

Efficient and discrete molecular donors have been also widely investigated for OPV.[141-147] Compared to polymers, they exibit a well-defined structure allowing for more accurate structure-property relationships and they are easier to purify. In addition, they can be processed in solution or by vacuum evaporation depending on their molecular weight.

Among the most performant conjugated molecules for OPV, oligothiophene derivatives functionalized by eA groups in α,ω-terminal positions or inserted in the conjugated spacer, have given rise to highly efficient OSCs.[147] For example (Figure 1.25), the introduction of two terminal electron-withdrawing dicyanovinyl (DCV) groups in oligothiophene derivatives **DCVnT** (n = 2-4) significantly reduced their HOMO-LUMO gap, hence improving their absorption in the visible spectrum. This class of molecular donors presents the advantage to be vacuum-deposited. P. Bäuerle, K. Leo and co-workers demonstrated their great interest for performant single junction planar or BHJ OSCs with PCEs beyond 5%,[148-151] while their use in tandem or multiple-junction OSCs gave even higher efficiencies beyond 10%.[77] Following this strategy, longer and soluble oligomers such as **DRCN5T**, **BTID-2F** or **BDTSTNTTR** with other electron-withdrawing groups led to solution-processed BHJ OSCs with remarkable efficiences beyond 10% [152] or 11%,[153, 154] respectively.

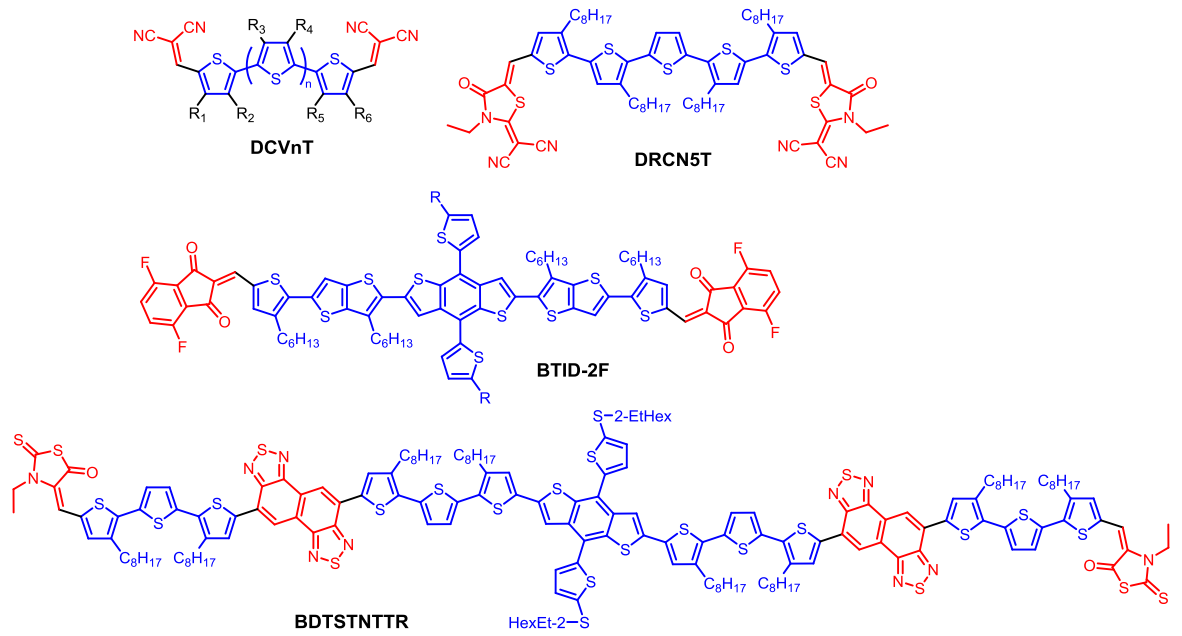

Figure 1.25. Low bandgap oligothiophene derivatives as efficient donors for BHJ OSCs.

The choice of the acceptor counterpart is of course of importance to achieve highly performant OSCs. As discussed below, while fullerene derivatives have long been considered as essential and still represent key acceptors, non fullerene acceptors (NFAs) have emerged few years ago boosting the PV efficiency.

1.5.3. Fullerene and molecular non-fullerene acceptors for OSCs

Commercially avalaible fullerene derivatives such as **C_{60}**, **C_{70}** and their soluble analogues **$PC_{61}BM$** and **$PC_{71}BM$** represent reference acceptors for OPV (Figure 1.26).[155] These compounds exhibit relatively good electron-transport properties with electron mobilities μ_e of 1 $cm^2.V^{-1}.s^{-1}$ for **C_{60}** (measured by OFETs),[156-160] 3.4 x 10^{-3} cm^2 V^{-1} s^{-1} for **C_{70}** (OFETs),[161] 0.21 (OFET) and 2 × 10^{-3} $cm^2.V^{-1}.s^{-1}$ (by SCLC: Space Charge Limited Current method) for **$PC_{61}BM$** and 0.1 $cm^2.V^{-1}.s^{-1}$ (OFET) and 6.8 × 10^{-4} $cm^2.V^{-1}.s^{-1}$ (SCLC) for **$PC_{71}BM$**.[156, 158-160, 162, 163]

In agreement with their LUMO levels lower than *ca.* -3.9 eV, these fullerene derivatives have been used as acceptor materials. The monofunctionalization of C_{60} and C_{70} induces an increase of LUMO level associated with a decrease of electron affinity. In this context, the double functionalization of C_{60} was also developed leading for example to **$IC_{60}BA$**, which showed a even higher LUMO level hence affording a higher V_{oc} and better PV performance, in particular when associated with **P3HT** (PCE = 6.5%).[163] Due to their lower symmetry, the **C_{70}** analogues show better absorption properties in the visible spectrum than for **C_{60}** derivatives (see Chapter 2).[161, 164] Thus, although they are much expensive, C_{70} derivatives often lead to better PV efficiencies.

However, fullerene derivatives present some drawbacks such as relative low absorption in the visible, a limited structural tunability of their energy levels, dimerization upon illumination and the tendency to lead to a too pronounced phase segregation in the photoactive layer resulting in lower PV performance.

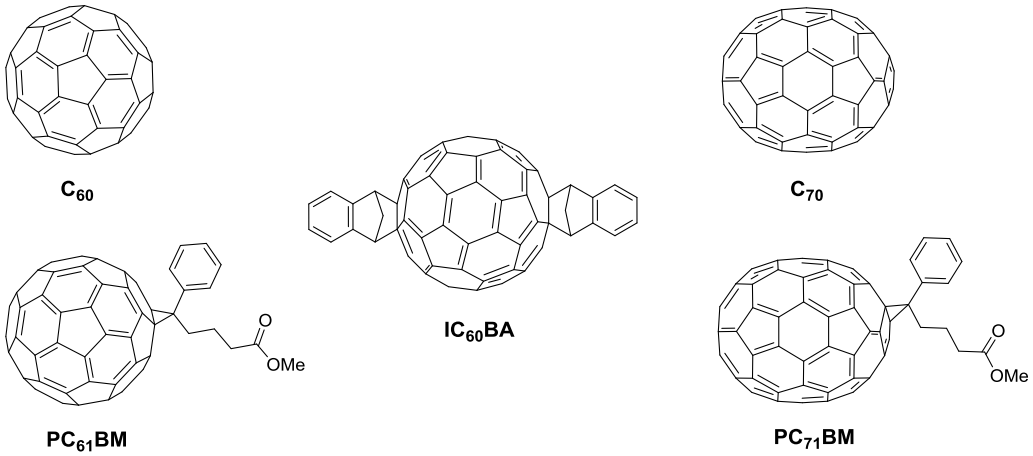

Figure 1.26. Chemical structures of fullerene acceptor derivatives commonly used in OPV.

Recently non-fullerene acceptors (NFAs) have attracted much considerable attention due to their better absorption properties and easier tunable energy levels.[165] Compared to fullerene, they boosted the PCE of OSCs beyond 11% up to 16-17%. Figure 1.27 describes some relevant examples of NFAs. Multimers of perylenebisdiimide (PBI) such as the dimer **SdiPBI-S** combined with the PBDTS-Se polymer led to BHJ OSCs exhibiting a PCE of 8.4%.[166] The use of multimers avoids the tendency of mono PBI to aggregate and form too high crystalline domain size.

Another class of NFAs is based on a central extended π-conjugated core, containing fused aromatic rings, functionalized by two terminal eA groups. This is the case of **IT-4F** which combined with the polymer PBDB-T-2F led to single junction BHJ OSCs with a PCE of 14%.[140] More recently, the fused molecular structure **Y6** was discovered yielding an exceptionally high PCE of 15.7%,[15] triggering futher rapid improvements by side chain engineering (**N3**, PCE = 16.4%)[167] or replacing the initial fluorine atoms by chlorine ones (**BTP-4Cl**, PCE = 16.7%) (Figure 1.27).[168]

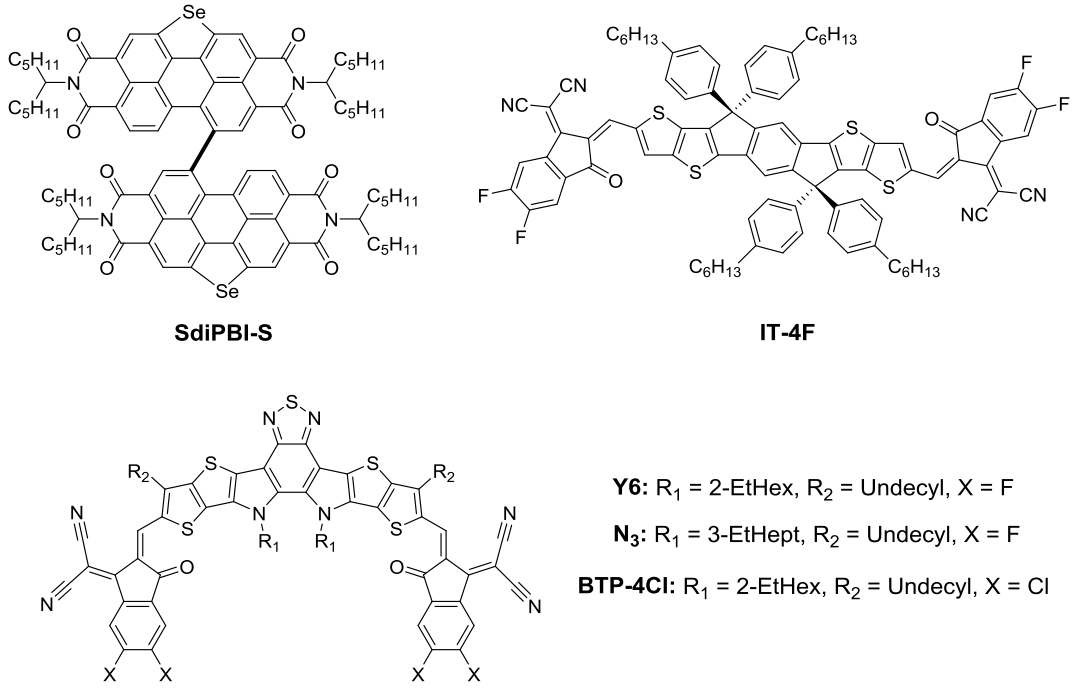

Figure 1.27. Chemical structure of efficient non-fullerene acceptors for OPV.

The interest of NFAs relies on the possible tuning of: i) their complementary absorption relative to that of the donor material allowing a better coverage of the visible spectrum, ii) their energy levels to match those of the donor material in order to reach high V_{oc} and iii) their morphology by using the concept of multimers or introduction of side-chains.[169]

This non exhaustive overview of the literature has highlighted some of the best donors and acceptors used in OPV. Molecular systems which are smaller than polymers present some advantages in terms of purification and reproducibility. However, the more efficient molecular donors and NFAs still exhibit relatively complex structures whose synthesis in multiple steps represents a challenging task. In the context of potential industrialization of the OPV technology, one must take into account the accessibility and simplicity of molecules. Small push-pull conjugated molecules are accessible and simple while exhibiting easily tunable absorption properties in the visible spectrum. These features are a prerequisite for OPV applications.

1.5.4. Small push-pull molecules as donor materials

A lot of push–pull conjugated molecules have been developed in the field of non linear optics.[170, 171] This class of D-π-A conjugated compounds are based on an electron-donating group (eD or D for simplicity) linked to an electron-accepting group (eA or A for simplicity) through a π-conjugated spacer (π). Different geometries can be envisaged from linear (D-π-A), quadrupole (D-π-A-D-π or A-π-D-π-A) to octupolar/tripodal ((D–π)$_3$A or (A–π)$_3$D) systems. In general, D are based on groups with a *+M*

mesomeric effect such as such as NR_2, OR, NH_2 and OH, heterocyclic moieties such as thiophene[172] and proaromatic pyran-4-ylidines[173, 174] and also some metallocenes.[175, 176] Electron-accepting units A with $-M$ effect correspond, for instance, to CHO, CN, NO_2 and electron deficient heterocyclic compounds such as (di)azines,[177] benzothiazole[178] and imidazole.[179]

As shown in Figure 1.28, the UV-vis spectrum of the simple D-π-A system based on *para*-nitroaniline shows an intense intramolecular charge-transfer (ICT) band due to electronic intramolecular interaction between D (-NH_2) and A (-NO_2) through the benzene π-spacer associated with a perturbation of both HOMO and LUMO levels.[180] The excitation of the electrons between the new molecular orbitals can be achieved using visible light, and hence push–pull molecules are commonly colored and referred to as charge-transfer chromophores.[181-184] The ICT is also responsible for the polarization of the push–pull chromophore and generation of a strong molecular dipole in the quinoid form of the push-pull system.[180]

Figure 1.28 reveals also that this bathochromically shifted ICT band completely disappears for mono functionalized benzene while *meta*-nitroaniline exhibits a weak ICT band as a result of a much less conjugating pathway between the amino and nitro groups, as expected.

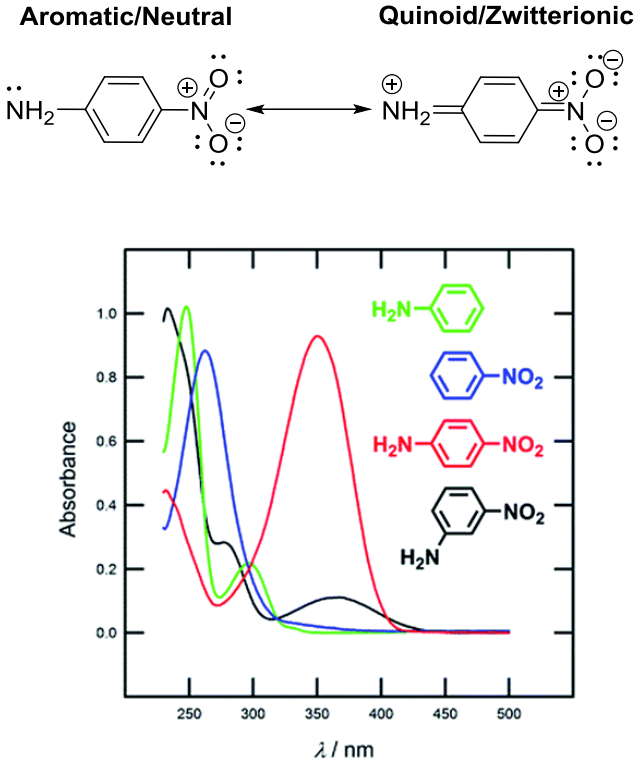

Figure 1.28. Limit resonance forms and UV-Vis spectra of simple D-π-A systems based on nitroaniline.[180]

Taking advantage of this class of coloured compounds, a first D-π-A push-pull molecule for OPV, namely **TPA(-T-DCV)$_3$**, was synthesized in our group by J. Roncali and co-workers in 2006

(Figure 1.29). Triphenylamine (TPA) was used as central electron-donating block D and functionalized with three thiophene (T)-dicyanovinyl (DCV) branches.[185, 186] An efficient ICT takes place between the electron donating TPA and the electron accepting DCV groups leading to a broad absorption band in the visble spectrum. The star-shaped molecule **TPA(-T-DCV)$_3$** was tested as donor material in bi-layer OSCs with C_{60} as electron acceptor leading to PCE of 1.85% (at 80 mW under AM 1.5 simulated solar irradiation).

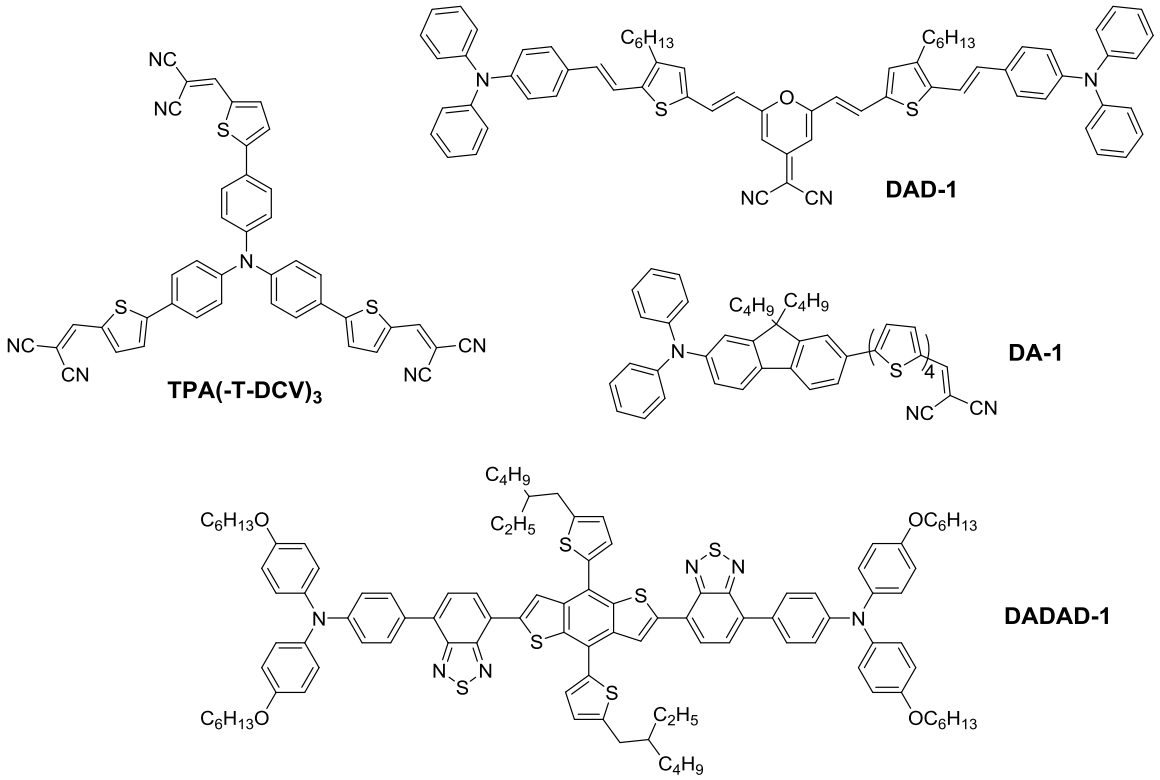

Figure 1.29. Push-pull molecules based on TPA for OPV.

Many push-pull molecules of different geometries and D-A combination have been designed for OPV.[132, 187]

For example, when **DAD-1** and **DADAD-1** push-pull molecules are combined with $PC_{71}BM$, BHJ OSCs with PCEs of 2.10% [187] and 6.13% [187, 188] were obtained, respectively. The improvement of PCE for **DADAD-1** is due to the π-extension of the conjugated bridge between the two TPA units and the insertion of electron-deficient benzothiadiazole blocks.[188] The linear push-pull molecule **DA-1** showing good charge transport properties in the solid state, was associated to C_{60} to give bi-layer OSCs with a PCE of 2.67%.[189]

In parallel to these OSCs prepared by solution process, push-push molecules have been also deposited by vacuum process (Figure 1.30). Small molecules are requested for vacuum evaporation. The small merocyanine **DA-2** was co-evaporated with C_{60} to give the following ITO/MoO_3/**DA-2**:C_{60}

(9:11)/BCP/Ag BHJ OSCs leading to a very high PCE of 6.1%, considering the size of the molecule.[190] Similarly, by surrounding a co-evaporated **DTDCPB**:C_{70} layer by thin-layers of **DTDCPB** and C_{70}, the resulting complexified ITO/MoO_3/**DTDCPB**/**DTDCPB**:C_{70} (1:1.6)/C_{70}/BCP/Ag device afforded a PCE of 6.8%.[191]

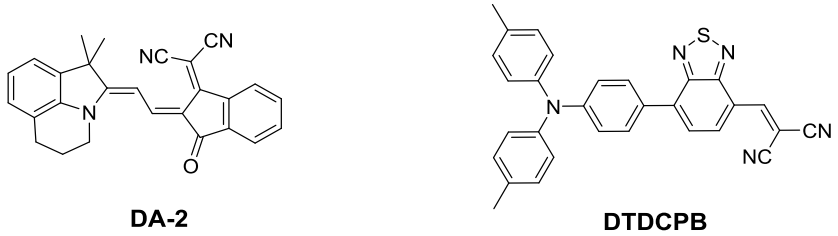

Figure 1.30. Vacuum-processed push-pull molecules for OPV.

Since the development of **TPA(-T-DCV)$_3$** for OPV, our group has developed a large number of small linear DA push-pull molecules.[192] In particular the reference compound **TPA-T-DCV** was deposited from solution to fabricate a bi-layer device ITO/PEDOT-PSS/**TPA-T-DCV**/C_{60}/Al showing a PCE of 2.53%, higher than the one measured for the more complex star-shaped molecule **TPA(-T-DCV)$_3$**.[193, 194] In addition, **TPA-T-DCV** could be produced in only few steps on the gram scale and further optimization by preparing BHJ OSCs by co-evaporation with C_{60} led to a promising PCE of 4.0%.[195]

Interestingly the replacement of one terminal phenyl ring of **TPA-T-DCV** by a methyl group, giving rise to **DPMA-T-DCV** (Figure 1.31), strongly affected the molecular organization in the solid state undergoing a 50 time increase of hole mobility μ_h up to 5.0×10^{-4} cm^2 V^{-1} s^{-1}, as compared to that of **TPA-T-DCV**. Moreover, preliminary results showed that improved C_{60}-based bi-layer OSCs, fabricated by depositing **DPMA-T-DCV** by spin-casting or evaporation, were obtained affording PCEs of 2.92% and 3.03%, respectively.[196]

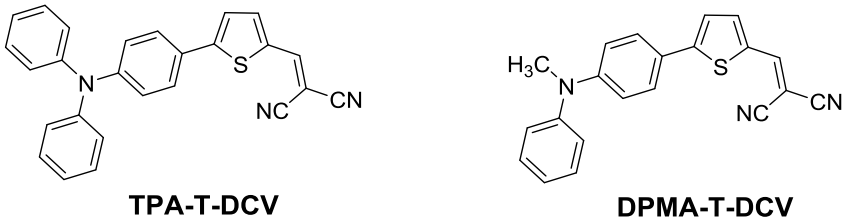

Figure 1.31 Structure of **TPA-T-DCV** and **DPMA-T-DCV**, DPMA stands for **D**i**P**henyl**M**ethyl**A**mine.

1.6. Objectives of the PhD thesis

In this chapter, the fundamental of OSCs has been briefly described. An overview of organic semiconductors and the history of the development of organic photovoltaics have been provided as well as the operating principle of OSCs. Different OSC architectures and their characterization were described. Some important photoactive organic donor and acceptor materials for OPV have been described. Among them, push-pull molecules can be considered as relatively simple, accessible and efficient molecules as donors for OPV.

In this context, preliminary results have shown that the molecular donor **DPMA-T-DCV** combines good transport properties and promising PV efficiency. One of the objectives of this PhD thesis will deal with further exploration of the PV potential of this molecule by optimizing the architecture of OSCs (Chapter 2). Chapter 3 will then investigate the properties and the PV performance of a new π-extended **DPMA-T-DCV** analogue. A series of carbazole and selenophene analogues of **DPMA-T-DCV** will be also characterize and tested (Chapter 4) while the last chapter will be devoted to new push-pull multimers for OPV.

References:

1. N. S. Lewis and G. Crabtree, *Journal*, 2005.
2. V. Andersson, K. Tvingstedt and O. Inganas, *Journal of Applied Physics*, 2008, **103**, 094520.
3. H. Bässler and A. Köhler, in *Unimolecular and supramolecular electronics I*, Springer, 2011, pp. 1-65.
4. https://www.nrel.gov/grid/solar-integration-data.html, *National Renewable Energy Laboratory*.
5. https://www.astm.org/Standards/E490.htm, *ASTM INTERNATIONAL*, 2014.
6. https://www.nrel.gov/pv/cell-efficiency.html, *National Renewable Energy Laboratory, Date accessed:*, May, 2019.
7. O. Edenhofer, R. Pichs-Madruga, Y. Sokona, K. Seyboth, S. Kadner, T. Zwickel, P. Eickemeier, G. Hansen, S. Schlömer and C. von Stechow, *Renewable energy sources and climate change mitigation: Special report of the intergovernmental panel on climate change*, Cambridge University Press, 2011.
8. M. A. Green, Y. Hishikawa, E. D. Dunlop, D. H. Levi, J. Hohl-Ebinger, M. Yoshita and A. W. Y. Ho-Baillie, *Progress in Photovoltaics: Research and Applications*, 2019, **27**, 3-12.
9. B. O'regan and M. Grätzel, *nature*, 1991, **353**, 737.
10. A. Hagfeldt, G. Boschloo, L. Sun, L. Kloo and H. Pettersson, *Chem Rev*, 2010, **110**, 6595-6663.
11. I. Benesperi, H. Michaels and M. Freitag, *Journal of Materials Chemistry C*, 2018, **6**, 11903-11942.
12. S. I. Seok, M. Gratzel and N. G. Park, *Small*, 2018, **14**, e1704177.
13. N. N. Lal, Y. Dkhissi, W. Li, Q. C. Hou, Y. B. Cheng and U. Bach, *Advanced Energy Materials*, 2017, **7**, 1602761.
14. S. D. Yang, W. F. Fu, Z. Q. Zhang, H. Z. Chen and C. Z. Li, *Journal of Materials Chemistry A*, 2017, **5**, 11462-11482.
15. J. Yuan, Y. Q. Zhang, L. Y. Zhou, G. C. Zhang, H. L. Yip, T. K. Lau, X. H. Lu, C. Zhu, H. J. Peng, P. A. Johnson, M. Leclerc, Y. Cao, J. Ulanski, Y. F. Li and Y. P. Zou, *Joule*, 2019, **3**, 1140-1151.
16. M. Freitag and G. Boschloo, *Current Opinion in Electrochemistry*, 2017, **2**, 111-119.
17. K. Kakiage, Y. Aoyama, T. Yano, K. Oya, J. Fujisawa and M. Hanaya, *Chem Commun (Camb)*, 2015, **51**, 15894-15897.
18. S. Mathew, A. Yella, P. Gao, R. Humphry-Baker, B. F. E. Curchod, N. Ashari-Astani, I. Tavernelli, U. Rothlisberger, M. K. Nazeeruddin and M. Gratzel, *Nature Chemistry*, 2014, **6**, 242-247.
19. L. Meng, Y. Zhang, X. Wan, C. Li, X. Zhang, Y. Wang, X. Ke, Z. Xiao, L. Ding, R. Xia, H. L. Yip, Y. Cao and Y. Chen, *Science*, 2018, **361**, 1094-1098.
20. A. Chodos, *American Physical Society*, 2009, **18**, 2.
21. H. Shirakawa, E. J. Louis, A. G. MacDiarmid, C. K. Chiang and A. J. Heeger, *Journal of the Chemical Society, Chemical Communications*, 1977, 578-580.
22. Y.-S. Gal and S.-H. Jin, *Bulletin of the Korean Chemical Society*, 2004, **25**, 777-778.
23. H. S. Kolla, S. P. Surwade, X. Zhang, A. G. Macdiarmid and S. K. Manohar, *J Am Chem Soc*, 2005, **127**, 16770-16771.
24. A. J. Heeger, *Angew Chem Int Ed*, 2001, **40**, 2591.
25. R. E. Peierls, *Quantum theory of solids*, Clarendon Press, 1996.
26. J. L. Bredas, J. P. Calbert, D. A. da Silva Filho and J. Cornil, *Proc Natl Acad Sci U S A*, 2002, **99**, 5804-5809.
27. I. Kymissis, *Organic field effect transistors: theory, fabrication and characterization*, Springer Science & Business Media, 2008.
28. A. P. Monkman, H. D. Burrows, L. J. Hartwell, L. E. Horsburgh, I. Hamblett and S. Navaratnam, *Phys Rev Lett*, 2001, **86**, 1358-1361.
29. N. C. Greenham and R. H. Friend, in *Solid state physics*, Elsevier, 1996, vol. 49, pp. 1-149.
30. C. H. Lee, G. W. Kang, J. W. Jeon, W. J. Song, S. Y. Kim and C. Seoul, *Synthetic Metals*, 2001, **117**, 75-79.
31. A. Kraft, A. C. Grimsdale and A. B. Holmes, *Angewandte Chemie International Edition*, 1998, **37**, 402-428.

32. G. Zotti, S. Martina, G. Wegner and A. D. Schlüter, *Advanced Materials*, 1992, **4**, 798-801.
33. T.-C. Chung, J. Kaufman, A. Heeger and F. Wudl, *Physical Review B*, 1984, **30**, 702.
34. J. Roncali, *Chemical Reviews*, 1992, **92**, 711-738.
35. J. Roncali, *Chem Rev*, 1997, **97**, 173-206.
36. L. Groenendaal, F. Jonas, D. Freitag, H. Pielartzik and J. R. Reynolds, *Advanced materials*, 2000, **12**, 481-494.
37. D. Kearns and M. Calvin, *The Journal of chemical physics*, 1958, **29**, 950-951.
38. C. Tang and A. Albrecht, *Nature*, 1975, **254**, 507.
39. V. Merritt and H. Hovel, *Applied Physics Letters*, 1976, **29**, 414-415.
40. S. Glenis, G. Horowitz, G. Tourillon and F. Garnier, *Thin Solid Films*, 1984, **111**, 93-103.
41. S. Glenis, G. Tourillon and F. Garnier, *Thin Solid Films*, 1984, **122**, 9-17.
42. K. Vivek and G. Agrawal, *Energy Technology & Ecological Concerns: A Contemporary Approach*, 87.
43. F. J. Kampas and M. Gouterman, *The Journal of Physical Chemistry*, 1977, **81**, 690-695.
44. C. W. Tang, *Applied physics letters*, 1986, **48**, 183-185.
45. F. Yang, K. Sun and S. R. Forrest, *Advanced Materials*, 2007, **19**, 4166-4171.
46. J. G. Xue, S. Uchida, B. P. Rand and S. R. Forrest, *Applied Physics Letters*, 2004, **85**, 5757-5759.
47. N. S. Sariciftci, L. Smilowitz, A. J. Heeger and F. Wudl, *Science*, 1992, **258**, 1474-1476.
48. A. J. Heeger, *Adv Mater*, 2014, **26**, 10-27.
49. G. Yu, J. Gao, J. C. Hummelen, F. Wudl and A. J. Heeger, *Science*, 1995, **270**, 1789-1791.
50. M. C. Scharber and N. S. Sariciftci, *Prog Polym Sci*, 2013, **38**, 1929-1940.
51. R. Pandey and R. J. Holmes, *IEEE Journal of Selected Topics in Quantum Electronics*, 2010, **16**, 1537-1543.
52. R. Pandey and R. J. Holmes, *Adv Mater*, 2010, **22**, 5301-5305.
53. A. Hadipour, B. de Boer and P. W. M. Blom, *Journal of Applied Physics*, 2007, **102**, 074506.
54. M. Niggemann, M. Riede, A. Gombert and K. Leo, *Phys Status Solidi A*, 2008, **205**, 2862-2874.
55. D. Duché, J. Simon, L. Escoubas, P. Torchio, J. Le Rouzo, W. Vervisch and F. Flory, 2009.
56. W. Van Sark, 2012.
57. Y. Liu, C. C. Chen, Z. Hong, J. Gao, Y. M. Yang, H. Zhou, L. Dou, G. Li and Y. Yang, *Sci Rep*, 2013, **3**, 3356.
58. G. Hodes, *Science*, 2013, **342**, 317-318.
59. J. B. You, L. T. Dou, Z. R. Hong, G. Li and Y. Yang, *Progress in Polymer Science*, 2013, **38**, 1909-1928.
60. T. J. Savenije, J. E. Kroeze, X. Yang and J. Loos, *Advanced Functional Materials*, 2005, **15**, 1260-1266.
61. G. Li, Y. Yao, H. Yang, V. Shrotriya, G. Yang and Y. Yang, *Advanced Functional Materials*, 2007, **17**, 1636-1644.
62. H. Y. Chen, J. H. Hou, S. Q. Zhang, Y. Y. Liang, G. W. Yang, Y. Yang, L. P. Yu, Y. Wu and G. Li, *Nature Photonics*, 2009, **3**, 649-653.
63. M. T. Dang, L. Hirsch and G. Wantz, *Adv Mater*, 2011, **23**, 3597-3602.
64. P. Vanlaeke, A. Swinnen, I. Haeldermans, G. Vanhoyland, T. Aernouts, D. Cheyns, C. Deibel, J. D'Haen, P. Heremans, J. Poortmans and J. V. Manca, *Solar Energy Materials and Solar Cells*, 2006, **90**, 2150-2158.
65. Y. Kim, S. Cook, S. M. Tuladhar, S. A. Choulis, J. Nelson, J. R. Durrant, D. D. Bradley, M. Giles, I. McCulloch and C.-S. Ha, in *Materials For Sustainable Energy: A Collection of Peer-Reviewed Research and Review Articles from Nature Publishing Group*, World Scientific, 2011, pp. 63-69.
66. H. Hoppe and N. S. Sariciftci, *Journal of Materials Chemistry*, 2006, **16**, 45-61.
67. Y. Yao, J. H. Hou, Z. Xu, G. Li and Y. Yang, *Advanced Functional Materials*, 2008, **18**, 1783-1789.
68. T. Ameri, P. Khoram, J. Min and C. J. Brabec, *Adv Mater*, 2013, **25**, 4245-4266.
69. P. Cheng and X. W. Zhan, *Materials Horizons*, 2015, **2**, 462-485.
70. H. Huang, L. Yang and B. Sharma, *Journal of Materials Chemistry A*, 2017, **5**, 11501-11517.
71. R. N. Yu, H. F. Yao and J. H. Hou, *Advanced Energy Materials*, 2018, **8**, 1702814.
72. P. Q. Bi and X. T. Hao, *Solar Rrl*, 2019, **3**, 1800263.

73. T. Ameri, N. Li and C. J. Brabec, *Energy & Environmental Science*, 2013, **6**, 2390-2413.
74. G. Dennler, H. J. Prall, R. Koeppe, M. Egginger, R. Autengruber and N. S. Sariciftci, *Applied Physics Letters*, 2006, **89**, 073502.
75. J. Y. Kim, K. Lee, N. E. Coates, D. Moses, T. Q. Nguyen, M. Dante and A. J. Heeger, *Science*, 2007, **317**, 222-225.
76. J. Gilot, M. M. Wienk and R. A. J. Janssen, *Applied Physics Letters*, 2007, **90**, 143512.
77. R. Meerheim, C. Korner, B. Oesen and K. Leo, *Applied Physics Letters*, 2016, **108**, 103302.
78. C. H. Peters, I. T. Sachs-Quintana, J. P. Kastrop, S. Beaupre, M. Leclerc and M. D. McGehee, *Advanced Energy Materials*, 2011, **1**, 491-494.
79. H. Hoppe and N. S. Sariciftci, *Journal of Materials Research*, 2004, **19**, 1924-1945.
80. D. M. Stoltzfus, J. E. Donaghey, A. Armin, P. E. Shaw, P. L. Burn and P. Meredith, *Chem Rev*, 2016, **116**, 12920-12955.
81. J. L. Bredas, J. E. Norton, J. Cornil and V. Coropceanu, *Accounts of Chemical Research*, 2009, **42**, 1691-1699.
82. R. R. Lunt, N. C. Giebink, A. A. Belak, J. B. Benziger and S. R. Forrest, *Journal of Applied Physics*, 2009, **105**, 053711.
83. J.-M. Nunzi, *Comptes Rendus Physique*, 2002, **3**, 523-542.
84. A. Petersen, A. Ojala, T. Kirchartz, T. A. Wagner, F. Wurthner and U. Rau, *Physical Review B*, 2012, **85**, 245208.
85. B. A. Gregg and J. van de Lagemaat, *Nature Photonics*, 2012, **6**, 278-280.
86. X. Y. Zhu, Q. Yang and M. Muntwiler, *Accounts of Chemical Research*, 2009, **42**, 1779-1787.
87. T. Drori, C. X. Sheng, A. Ndobe, S. Singh, J. Holt and Z. V. Vardeny, *Phys Rev Lett*, 2008, **101**, 037401.
88. H. Bassler, *Phys Status Solidi B*, 1993, **175**, 15-56.
89. R. C. Chiechi, R. W. A. Havenith, J. C. Hummelen, L. J. A. Koster and M. A. Loi, *Materials Today*, 2013, **16**, 281-289.
90. C. J. Brabec, A. Cravino, D. Meissner, N. S. Sariciftci, T. Fromherz, M. T. Rispens, L. Sanchez and J. C. Hummelen, *Advanced Functional Materials*, 2001, **11**, 374-380.
91. A. Wagenpfahl, D. Rauh, M. Binder, C. Deibel and V. Dyakonov, *Physical Review B*, 2010, **82**, 115306.
92. R. Po, C. Carbonera, A. Bernardi and N. Camaioni, *Energy & Environmental Science*, 2011, **4**, 285-310.
93. S. Lattante, *Electronics*, 2014, **3**, 132-164.
94. G. J. A. H. Wetzelaer and P. W. M. Blom, *Npg Asia Materials*, 2014, **6**, e110.
95. J. Wei, G. Ji, C. Zhang, L. Yan, Q. Luo, C. Wang, Q. Chen, J. Yang, L. Chen and C. Q. Ma, *ACS Nano*, 2018, **12**, 5518-5529.
96. C. J. Zhang, Q. Luo, H. Wu, H. Y. Li, J. Q. Lai, G. Q. Ji, L. P. Yan, X. F. Wang, D. Zhang, J. Lin, L. W. Chen, J. L. Yang and C. Q. Ma, *Organic Electronics*, 2017, **45**, 190-197.
97. J. H. Lee, S. Cho, A. Roy, H. T. Jung and A. J. Heeger, *Applied Physics Letters*, 2010, **96**, 83.
98. D. Zhao, P. Liu, X. Sun, S. Tan, L. Ke and A. Kyaw, *Applied Physics Letters*, 2009, **95**, 275.
99. C. J. Brabec, S. E. Shaheen, C. Winder, N. S. Sariciftci and P. Denk, *Applied Physics Letters*, 2002, **80**, 1288-1290.
100. I. Lee, J. Noh, J. Y. Lee and T. S. Kim, *ACS Appl Mater Interfaces*, 2017, **9**, 37395-37401.
101. L. Nian, W. Q. Zhang, S. P. Wu, L. Q. Qin, L. L. Liu, Z. Q. Xie, H. B. Wu and Y. G. Ma, *Acs Applied Materials & Interfaces*, 2015, **7**, 25821-25827.
102. H. W. Lin, C. W. Lu, L. Y. Lin, Y. H. Chen, W. C. Lin, K. T. Wong and F. Lin, *Journal of Materials Chemistry A*, 2013, **1**, 1770-1777.
103. P. Peumans, A. Yakimov and S. R. Forrest, *Journal of Applied Physics*, 2003, **93**, 3693-3723.
104. T. H. Lai, S. W. Tsang, J. R. Manders, S. Chen and F. So, *Materials Today*, 2013, **16**, 424-432.
105. M. O. Reese, M. S. White, G. Rumbles, D. S. Ginley and S. E. Shaheen, *Applied Physics Letters*, 2008, **92**, 35.
106. G. Li, C. W. Chu, V. Shrotriya, J. Huang and Y. Yang, *Applied Physics Letters*, 2006, **88**, 253503.
107. J. Huang, Z. Xu and Y. Yang, *Advanced Functional Materials*, 2007, **17**, 1966-1973.
108. H.-H. Liao, L.-M. Chen, Z. Xu, G. Li and Y. Yang, *Applied physics letters*, 2008, **92**, 156.
109. V. Shrotriya, G. Li, Y. Yao, C. W. Chu and Y. Yang, *Applied Physics Letters*, 2006, **88**, 073508.

110. K. Takanezawa, K. Tajima and K. Hashimoto, *Applied Physics Letters*, 2008, **93**, 297.
111. J. S. Huang, C. Y. Chou, M. Y. Liu, K. H. Tsai, W. H. Lin and C. F. Lin, *Organic Electronics*, 2009, **10**, 1060-1065.
112. M. Y. Chan, C. S. Lee, S. L. Lai, M. K. Fung, F. L. Wong, H. Y. Sun, K. M. Lau and S. T. Lee, *Journal of Applied Physics*, 2006, **100**, 094506.
113. S. Han, W. S. Shin, M. Seo, D. Gupta, S. J. Moon and S. Yoo, *Organic Electronics*, 2009, **10**, 791-797.
114. C. Tao, S. P. Ruan, G. H. Xie, X. Z. Kong, L. Shen, F. X. Meng, C. X. Liu, X. D. Zhang, W. Dong and W. Y. Chen, *Applied Physics Letters*, 2009, **94**, 29.
115. M. D. Irwin, B. Buchholz, A. W. Hains, R. P. H. Chang and T. J. Marks, *P Natl Acad Sci USA*, 2008, **105**, 2783-2787.
116. M. T. Greiner, M. G. Helander, Z. B. Wang, W. M. Tang and Z. H. Lu, *J Phys Chem C*, 2010, **114**, 19777-19781.
117. E. L. Ratcliff, J. Meyer, K. X. Steirer, N. R. Armstrong, D. Olson and A. Kahn, *Organic Electronics*, 2012, **13**, 744-749.
118. E. L. Ratcliff, J. Meyer, K. X. Steirer, A. Garcia, J. J. Berry, D. S. Ginley, D. C. Olson, A. Kahn and N. R. Armstrong, *Chemistry of Materials*, 2011, **23**, 4988-5000.
119. K. X. Steirer, J. P. Chesin, N. E. Widjonarko, J. J. Berry, A. Miedaner, D. S. Ginley and D. C. Olson, *Organic Electronics*, 2010, **11**, 1414-1418.
120. J. R. Manders, S. W. Tsang, M. J. Hartel, T. H. Lai, S. Chen, C. M. Amb, J. R. Reynolds and F. So, *Advanced Functional Materials*, 2013, **23**, 2993-3001.
121. D. Wu.
122. Y. Cai, L. Huo and Y. Sun, *Adv Mater*, 2017, **29**, 1605437.
123. C. J. Brabec, S. Gowrisanker, J. J. Halls, D. Laird, S. Jia and S. P. Williams, *Advanced Materials*, 2010, **22**, 3839-3856.
124. I. Osaka and R. D. McCullough, *Acc Chem Res*, 2008, **41**, 1202-1214.
125. C. H. Woo, B. C. Thompson, B. J. Kim, M. F. Toney and J. M. Frechet, *J Am Chem Soc*, 2008, **130**, 16324-16329.
126. E. Bundgaard and F. C. Krebs, *Solar Energy Materials and Solar Cells*, 2007, **91**, 954-985.
127. R. Kroon, M. Lenes, J. C. Hummelen, P. W. M. Blom and B. De Boer, *Polymer Reviews*, 2008, **48**, 531-582.
128. G. P. Smestad, F. C. Krebs, C. M. Lampert, C. G. Granqvist, K. Chopra, X. Mathew and H. Takakura, *Journal*, 2008.
129. P. R. Berger and M. Kim, *Journal of Renewable and Sustainable Energy*, 2018, **10**, 013508.
130. M. Tembo, M. Munyati, S. Hatwaambo and M. Maaza, *African Journal of Pure and Applied Chemistry*, 2015, **9**, 50-57.
131. Y. J. Cheng, S. H. Yang and C. S. Hsu, *Chem Rev*, 2009, **109**, 5868-5923.
132. V. Malytskyi, J.-J. Simon, L. Patrone and J.-M. Raimundo, *RSC Advances*, 2015, **5**, 354-397.
133. S. H. Liao, H. J. Jhuo, Y. S. Cheng and S. A. Chen, *Advanced materials*, 2013, **25**, 4766-4771.
134. J. D. Chen, C. Cui, Y. Q. Li, L. Zhou, Q. D. Ou, C. Li, Y. Li and J. X. Tang, *Adv Mater*, 2015, **27**, 1035-1041.
135. Y. Liu, J. Zhao, Z. Li, C. Mu, W. Ma, H. Hu, K. Jiang, H. Lin, H. Ade and H. Yan, *Nat Commun*, 2014, **5**, 5293.
136. D. P. Qian, L. Ye, M. J. Zhang, Y. R. Liang, L. J. Li, Y. Huang, X. Guo, S. Q. Zhang, Z. A. Tan and J. H. Hou, *Macromolecules*, 2012, **45**, 9611-9617.
137. S. Li, L. Ye, W. Zhao, S. Zhang, S. Mukherjee, H. Ade and J. Hou, *Adv Mater*, 2016, **28**, 9423-9429.
138. W. Zhao, S. Li, H. Yao, S. Zhang, Y. Zhang, B. Yang and J. Hou, *J Am Chem Soc*, 2017, **139**, 7148-7151.
139. J. Hou, O. Inganas, R. H. Friend and F. Gao, *Nat Mater*, 2018, **17**, 119-128.
140. S. Zhang, Y. Qin, J. Zhu and J. Hou, *Adv Mater*, 2018, **30**, e1800868.
141. J. Roncali, P. Frère, P. Blanchard, R. de Bettignies, M. Turbiez, S. Roquet, P. Leriche and Y. Nicolas, *Thin solid films*, 2006, **511**, 567-575.
142. J. Roncali, *Acc Chem Res*, 2009, **42**, 1719-1730.
143. A. Mishra and P. Bauerle, *Angew Chem Int Ed Engl*, 2012, **51**, 2020-2067.
144. J. Roncali, P. Leriche and P. Blanchard, *Advanced Materials*, 2014, **26**, 3821-3838.

145. J. Du, M. C. Biewer and M. C. Stefan, *Journal of Materials Chemistry A*, 2016, **4**, 15771-15787.
146. A. Tang, C. Zhan, J. Yao and E. Zhou, *Adv Mater*, 2017, **29**, 1600013.
147. A. Mishra, C. Q. Ma and P. Bauerle, *Chemical Reviews*, 2009, **109**, 1141-1276.
148. K. Schulze, C. Uhrich, R. Schüppel, K. Leo, M. Pfeiffer, E. Brier, E. Reinold and P. Bäuerle, *Advanced Materials*, 2006, **18**, 2872-2875.
149. R. Fitzner, E. Reinold, A. Mishra, E. Mena- Osteritz, H. Ziehlke, C. Körner, K. Leo, M. Riede, M. Weil and O. Tsaryova, *Advanced Functional Materials*, 2011, **21**, 897-910.
150. R. Fitzner, C. Elschner, M. Weil, C. Uhrich, C. Körner, M. Riede, K. Leo, M. Pfeiffer, E. Reinold and E. Mena- Osteritz, *Advanced Materials*, 2012, **24**, 675-680.
151. F. Baert, C. Cabanetos, A. Leliege, E. Kirchner, O. Segut, O. Alévêque, M. Allain, G. Seo, S. Jung and D. Tondelier, *Journal of Materials Chemistry C*, 2015, **3**, 390-398.
152. B. Kan, M. Li, Q. Zhang, F. Liu, X. Wan, Y. Wang, W. Ni, G. Long, X. Yang, H. Feng, Y. Zuo, M. Zhang, F. Huang, Y. Cao, T. P. Russell and Y. Chen, *J Am Chem Soc*, 2015, **137**, 3886-3893.
153. D. Deng, Y. Zhang, J. Zhang, Z. Wang, L. Zhu, J. Fang, B. Xia, Z. Wang, K. Lu, W. Ma and Z. Wei, *Nat Commun*, 2016, **7**, 13740.
154. J. H. Wan, X. P. Xu, G. J. Zhang, Y. Li, K. Feng and Q. Peng, *Energy & Environmental Science*, 2017, **10**, 1739-1745.
155. C. H. Cui, Y. W. Li and Y. F. Li, *Advanced Energy Materials*, 2017, **7**, 1601251.
156. S. Y. Nam, E. Y. Park, T. D. Kim, S. Cho, J. G. Park and K. S. Lee, *Current Applied Physics*, 2011, **11**, E44-E48.
157. L. M. Andersson, *Organic Electronics*, 2011, **12**, 300-305.
158. E. von Hauff, V. Dyakonov and J. Parisi, *Synthetic Met*, 2008, **158**, 468-472.
159. P. H. Wöbkenberg, D. D. Bradley, D. Kronholm, J. C. Hummelen, D. M. de Leeuw, M. Cölle and T. D. Anthopoulos, *Synthetic Metals*, 2008, **158**, 468-472.
160. J. E. Anthony, A. Facchetti, M. Heeney, S. R. Marder and X. Zhan, *Adv Mater*, 2010, **22**, 3876-3892.
161. S. Pfuetzner, J. Meiss, A. Petrich, M. Riede and K. Leo, *Applied Physics Letters*, 2009, **94**, 145.
162. V. D. Mihailetchi, J. K. J. van Duren, P. W. M. Blom, J. C. Hummelen, R. A. J. Janssen, J. M. Kroon, M. T. Rispens, W. J. H. Verhees and M. M. Wienk, *Advanced Functional Materials*, 2003, **13**, 43-46.
163. F. J. Zhang, Z. L. Zhuo, J. Zhang, X. Wang, X. W. Xu, Z. X. Wang, Y. S. Xin, J. Wang, J. Wang, W. H. Tang, Z. Xu and Y. S. Wang, *Solar Energy Materials and Solar Cells*, 2012, **97**, 71-77.
164. Y. He and Y. Li, *Phys Chem Chem Phys*, 2011, **13**, 1970-1983.
165. Z. Zhang, J. Yuan, Q. Wei and Y. Zou, *Front Chem*, 2018, **6**, 414.
166. D. Meng, D. Sun, C. Zhong, T. Liu, B. Fan, L. Huo, Y. Li, W. Jiang, H. Choi, T. Kim, J. Y. Kim, Y. Sun, Z. Wang and A. J. Heeger, *J Am Chem Soc*, 2016, **138**, 375-380.
167. K. Jiang, Q. Y. Wei, J. Y. L. Lai, Z. X. Peng, H. Kim, J. Yuan, L. Ye, H. Ade, Y. P. Zou and H. Yan, *Joule*, 2019, **3**, 3020-3033.
168. Y. Cui, H. Yao, J. Zhang, T. Zhang, Y. Wang, L. Hong, K. Xian, B. Xu, S. Zhang, J. Peng, Z. Wei, F. Gao and J. Hou, *Nat Commun*, 2019, **10**, 2515.
169. Z. Z. Zhang, J. Yuan, Q. Y. Wei and Y. P. Zou, *Frontiers in Chemistry*, 2018, **6**, 414.
170. L. R. Dalton, A. W. Harper, R. Ghosn, W. H. Steier, M. Ziari, H. Fetterman, Y. Shi, R. Mustacich, A.-Y. Jen and K. J. Shea, *Chemistry of materials*, 1995, **7**, 1060-1081.
171. T. J. Marks and M. A. Ratner, *Angewandte Chemie International Edition in English*, 1995, **34**, 155-173.
172. I. F. Perepichka and D. F. Perepichka, *Handbook of Thiophene-Based Materials: Applications in Organic Electronics and Photonics, 2 Volume Set*, John Wiley & Sons, 2009.
173. R. Andreu, L. Carrasquer, S. Franco, J. Garín, J. Orduna, N. Martinez de Baroja, R. Alicante, B. Villacampa and M. Allain, *The Journal of organic chemistry*, 2009, **74**, 6647-6657.
174. R. Andreu, E. Galán, J. Garín, V. Herrero, E. Lacarra, J. Orduna, R. Alicante and B. Villacampa, *The Journal of organic chemistry*, 2010, **75**, 1684-1692.
175. N. J. Long, *Angewandte Chemie International Edition in English*, 1995, **34**, 21-38.
176. H. S. Nalwa, *Applied Organometallic Chemistry*, 1991, **5**, 349-377.
177. S. Achelle, C. Baudequin and N. Ple, *Dyes and Pigments*, 2013, **98**, 575-600.

178. P. Hrobarik, V. Hrobarikova, I. Sigmundova, P. Zahradnik, M. Fakis, I. Polyzos and P. Persephonis, *J Org Chem*, 2011, **76**, 8726-8736.
179. J. Kulhánek and F. Bureš, *Beilstein journal of organic chemistry*, 2012, **8**, 25-49.
180. F. Bureš, *RSC Advances*, 2014, **4**, 58826-58851.
181. M. Kivala and F. Diederich, *Accounts of chemical research*, 2008, **42**, 235-248.
182. S.-i. Kato and F. Diederich, *Chemical Communications*, 2010, **46**, 1994-2006.
183. H. Meier, *Angewandte Chemie International Edition*, 2005, **44**, 2482-2506.
184. M. Kivala and F. Diedericht, *Pure and Applied Chemistry*, 2008, **80**, 411-427.
185. S. Roquet, A. Cravino, P. Leriche, O. Alévêque, P. Frere and J. Roncali, *Journal of the American Chemical Society*, 2006, **128**, 3459-3466.
186. A. Cravino, P. Leriche, O. Alévêque, S. Roquet and J. Roncali, *Advanced Materials*, 2006, **18**, 3033-3037.
187. P. Blanchard, C. Malacrida, C. Cabanetos, J. Roncali and S. Ludwigs, *Polymer International*, 2019, **68**, 589-606.
188. C. V. Kumar, L. Cabau, E. N. Koukaras, G. D. Sharma and E. Palomares, *Organic Electronics*, 2015, **26**, 36-47.
189. P. F. Xia, X. J. Feng, J. Lu, S. W. Tsang, R. Movileanu, Y. Tao and M. S. Wong, *Advanced Materials*, 2008, **20**, 4810-4815.
190. V. Steinmann, N. M. Kronenberg, M. R. Lenze, S. M. Graf, D. Hertel, K. Meerholz, H. Bürckstümmer, E. V. Tulyakova and F. Würthner, *Advanced Energy Materials*, 2011, **1**, 888-893.
191. Y.-H. Chen, L.-Y. Lin, C.-W. Lu, F. Lin, Z.-Y. Huang, H.-W. Lin, P.-H. Wang, Y.-H. Liu, K.-T. Wong and J. Wen, *Journal of the American Chemical Society*, 2012, **134**, 13616-13623.
192. C. Cabanetos, P. Blanchard and J. Roncali, *The Chemical Record*, 2019, **19**, 1123-1130.
193. A. Leliège, C.-H. Le Régent, M. Allain, P. Blanchard and J. Roncali, *Chemical Communications*, 2012, **48**, 8907-8909.
194. A. Leliège, J. Grolleau, M. Allain, P. Blanchard, D. Demeter, T. Rousseau and J. Roncali, *Chemistry–A European Journal*, 2013, **19**, 9948-9960.
195. J. W. Choi, C.-H. Kim, J. Pison, A. Oyedele, D. Tondelier, A. Leliege, E. Kirchner, P. Blanchard, J. Roncali and B. Geffroy, *Rsc Advances*, 2014, **4**, 5236-5242.
196. Y. Jiang, C. Cabanetos, M. Allain, P. Liu and J. Roncali, *Journal of Materials Chemistry C*, 2015, **3**, 5145-5151.

Chapter 2: Organic solar cells based on DPMA-T-DCV

2.1. Introduction

Small π-conjugated D-π-A push-pull molecules have received a great attention over the last decade as molecular donors for photovoltaic applications.[1-3] These compounds present the advantage to be processed in solution or by vacuum evaporation. A. Mishra, P. Bäuerle and G. D. Sharma and co-workers have recently described a soluble heteropentacene **TPA-SN5-DCV** end-capped by an electron-donating triphenylamine (TPA) unit on one side and a dicyanovinyl (DCV) electron-withdrawing group on the other side (Chart 2.1). When this compound was mixed with $PC_{71}BM$ as acceptor, one of the best efficiencies for solution-processed BHJ OSCs was reported (PCE = 7.26 %).[4] On the other hand, the group of K. T. Wong and, more recently, the one of M. Pshenichnikov have developed smaller systems for the fabrication of vacuum-processed BHJ OSCs such as **DTDCPB**, **DTDCTB** [5, 6] and **TPA-T-DCV-Ph**[7] leading to PCEs beyond 5%. Then K. T. Wong and co-workers described efficient vacuum-deposited ternary OSCs reaching a PCE of 8.02%, after optimization of the composition and the thickness of the photoactive layer prepared by co-evaporation of C_{70}, **DTDCTB** and **DTTz**.[8]

In parallel, S. R. Forrest and colleagues thoroughly investigated the PV potential of molecules described by K. T. Wong, namely **DTDCPB** and **DTDCTB**. After preparing a single junction OSC based on co-evaporation of **DTDCTB** and C_{60} (PCE = 5.3%), further improvement was achieved using the photoactive layer **DTDCTB**:C_{60} as the front subcell of a tandem cell (PCE = 10.0%) and as the middle subcell of a triple junction OSC (PCE = 11.1%).[9] Very recently, the same group has reported one of the highest PCE for an OSC, namely 15.0% for an organic tandem OSC of 2 mm^2 active area, combining a vacuum-processed subcell built by co-evaporation of **DTDCPB** and C_{70}, and a solution-processed subcell combining the PTB7-Th polymer and a non-fullerene acceptor.[10]

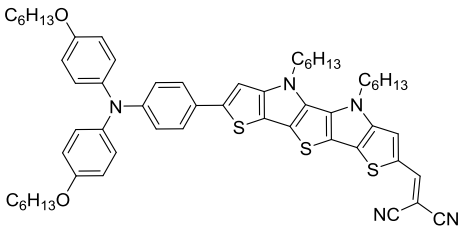

TPA-SN5-DCV (7.26 %, $PC_{71}BM$)

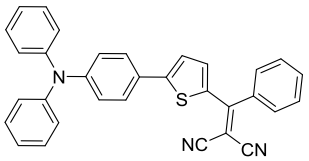

TPA-T-DCV-Ph (5.11 %, C_{70})

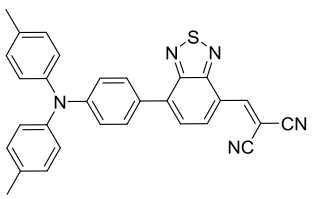

DTDCPB (6.8 %, C_{70})

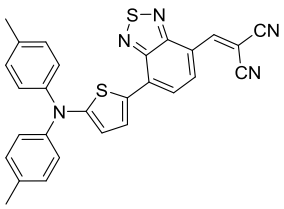

DTDCTB (5.81 and 6.52 %, C_{70})

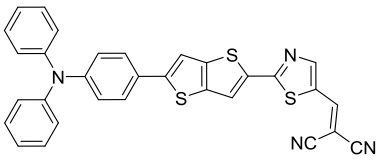

DTTz (6.52 %, C_{70})

Chart 2.1. Push–pull molecules used as donors in solution or vacuum-processed single junction OSCs.

All these literature data show the high interest of push-pull molecules for OPV. Our group has been involved at the very beginning of the development of push-pull molecules for OPV.[3, 11] The first example **TPA(-T-DCV)$_3$** reported in 2006 consisted in a central TPA functionalized with three thienyl (T)-DCV branches (Chart 2.2).[12] Bi-layer OSCs with C_{60} led to a PCE of 1.85% with an exceptional high V_{oc} of 1.15 V. It was shown that push-pull molecules can efficiently absorb the visible light and the introduction of electron-withdrawing groups such as DCV increased the oxidation potential of the resulting molecule, and hence the V_{oc} of related OSCs. Few years later, the structure of **TPA(-T-DCV)$_3$** has been simplified affording a more accessible molecule, namely **TPA-T-DCV** which has been initially used in bi-layer OSCs with C_{60} leading to a higher PCE of 2.5%.[13, 14] Subsequent improvements were achieved by fabricating solution-processed BHJ OSCs with $PC_{61}BM$ (PCE = 3.0 %)[15] and vacuum-processed BHJ OSCs with C_{60} (PCE = 4.0%).[16] However this compound suffered from a low hole mobility as measured by the Space Charge Limited Current (SCLC) method ($\mu_h = 1 \times 10^{-5}$ cm^2 V^{-1} s^{-1}).

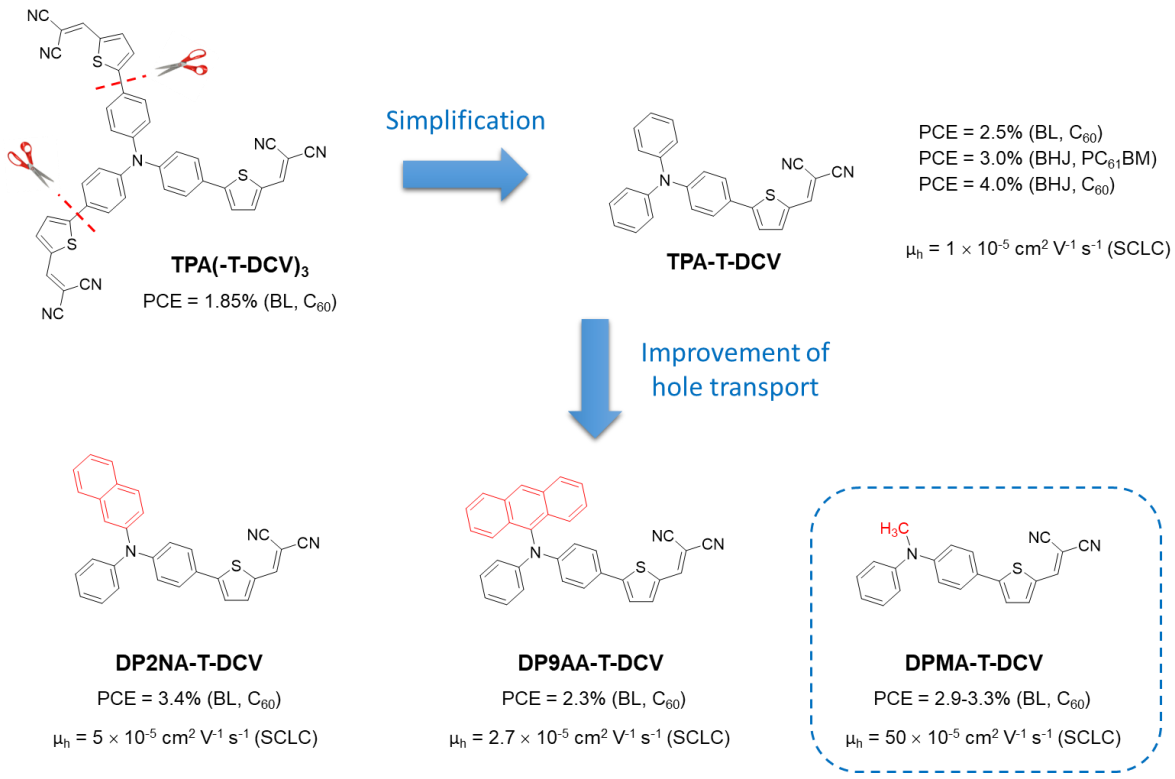

Chart 2.2. Molecular engineering combining structure simplification and improvement of charge hole properties giving rise to **DPMA-T-DCV** as push-pull donor for OPV.

Several strategies were investigated to improve hole transport properties of **TPA-T-DCV**. One of the external phenyl ring of TPA was replaced by a 2-naphthyl or a 9-anthryl moiety giving rise to **DP2NA-T-DCV**[17] or **DP9AA-T-DCV**[18] which were successfully used as donors in bi-layer OSCs exhibiting maximum PCEs of 3.4 and 2.3%, respectively. More importantly, introduction of such extended π-platforms was shown to increase the hole mobility of **DP2NA-T-DCV** and **DP9AA-T-DCV**

compared to **TPA-T-DCV**. Following the same approach, introduction of a methyl group in **DPMA-T-DCV** produced a hole mobility of 5×10^{-4} cm^2 V^{-1} s^{-1}, a 50 time higher value than the one of **TPA-T-DCV**. As a result, more performant bi-layer OSCs with C_{60} were reached using thin-films of **DPMA-T-DCV** prepared either by spin-coating from chloroform solutions (PCE = 2.9%) or vacuum evaporation (PCE = 3.3%).[19]

Following these preliminary and promising results, this chapter will explore further the potential of **DPMA-T-DCV** as donor material for OPV by combining other fullerene derivatives, optimizing the conditions of device fabrication and developing new solar cell architectures.

2.2. Synthesis and characterization of DPMA-T-DCV

As described in scheme 2.1, push-pull molecule **DPMA-T-DCV** has been synthesized using a slightly different procedure described in the literature by J. Roncali and C. Cabanetos.[19]

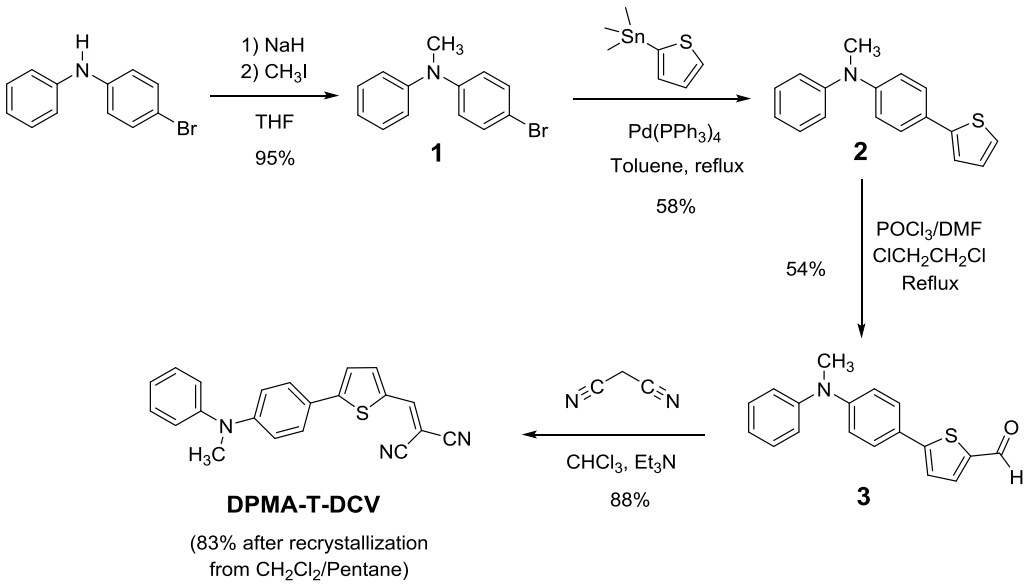

Scheme 2.1. Synthesis of **DPMA-T-DCV**.

As a first step, 4-bromo-*N*-phenylaniline was reacted with iodomethane in the presence of sodium hydride in anhydrous tetrahydrofuran giving compound **1** in 95% yield, a more straightforward reaction with a much higher yield than the one involving *N*-methylaniline and 1-bromo-4-iodobenzene in the presence of *t*-butoxide and tris(dibenzylidedeeacetone)-dipalladium(0).[19] The Stille coupling of **1** with trimethyl(thiophen-2-yl)stannane in toluene with tetrakis(triphenylphosphine) palladium as the catalyst, gave compound **2** in 58% yield. Subsequent Vilsmeier formylation led to carboxaldehyde **3** in 54% yield. A Knoevenagel condensation between malononitrile and the later carbaldehyde led to the target product **DPMA-T-DCV** in 83% yield after recrystallization. Thus, the push-pull molecule was obtained in only four steps synthesis in relatively large scale (*ca*. 500 mg).

2.2.1. Optical properties

The optical properties of **DPMA-T-DCV** were investigated by absorption and emission spectroscopy in diluted dichloromethane solutions, *ca*. 10^{-5} and 10^{-6} M, respectively (Figure 2.1a). Thin films prepared by spin-casting a solution of **DPMA-T-DCV** in chloroform (5 mg/mL) on clean glass substrate were also investigated (Figure 2.1b). The optical properties data are summarized in Table 2.1.

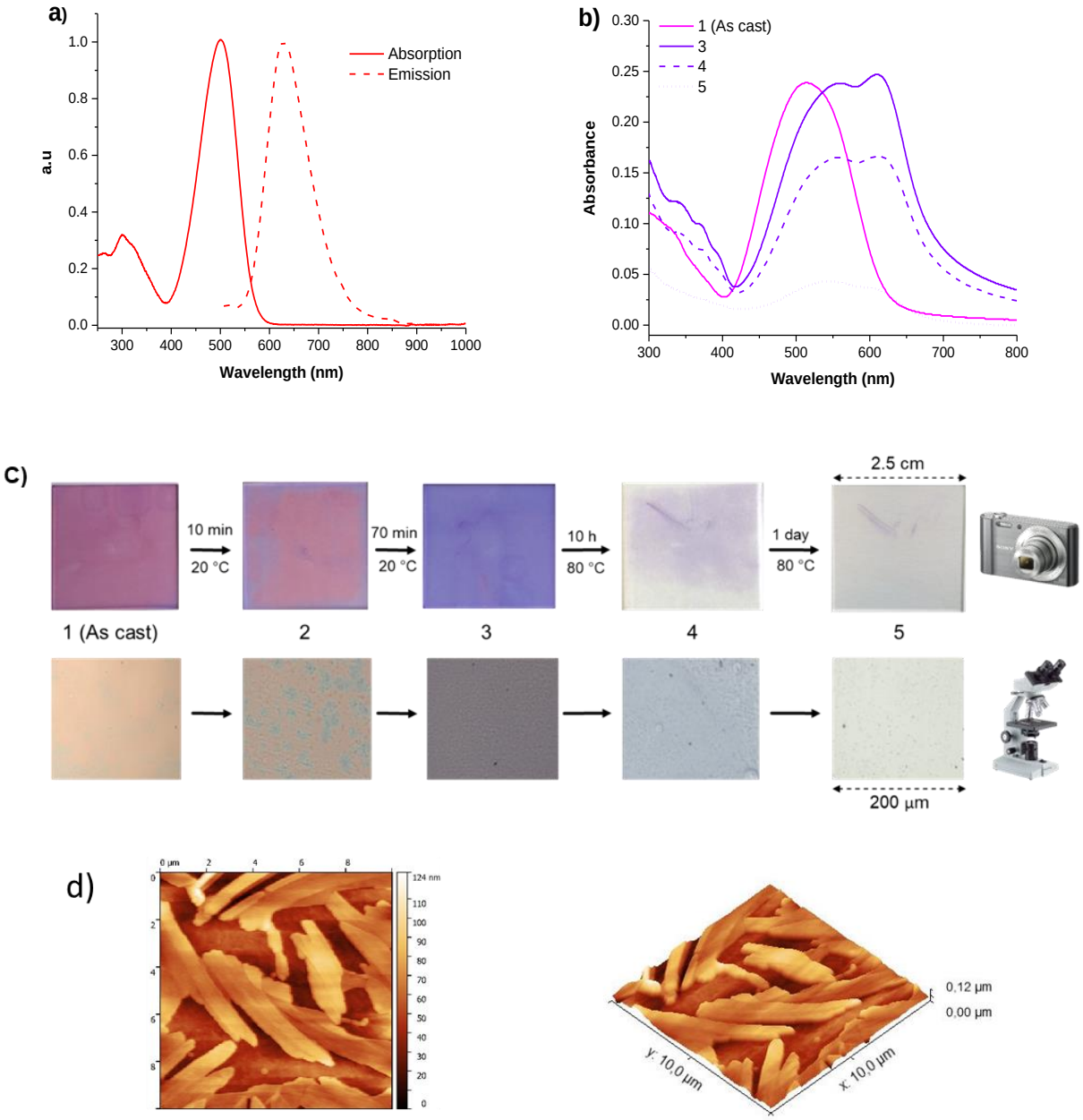

Figure 2.1. a) Absorption and emission spectra of **DPMA-T-DCV** in dichloromethane solution. b) Absorption spectra of a thin film of **DPMA-T-DCV** on glass as cast (pink solid line, stage 1) and at stages 3, 4 and 5 as described in c). c) Evolution of the surface of a thin-film of **DPMA-T-DCV** studied with a camera or an optical microscope. d) AFM pictures of a violet thin film of **DPMA-T-DCV** deposited on a ITO/PEDOT:PSS substrate.

The UV-Vis spectrum of the titled D-π-A molecule in solution shows a broad absorption band in the visible spectrum between 400 and 600 nm with a maximum at 498 nm and a high extinction coefficient (ε) of *ca.* 44100 M^{-1} cm^{-1}. This broad and intense band is related to an internal charge transfer (ICT) taking place from the electron-rich D unit to the electron-withdrawing A unit. **DPMA-T-DCV** exhibits emission properties in solution with a single emission band with a maximum at 628 nm associated to a quantum fluorescence emission yield (Φ_f) of 7 %, as measured using Rhodamine B as reference.

Table 2.1. Optical data for **DPMA-T-DCV** in solution and as thin film and thermal properties.

			solution				thin film	
	T_d (°C)[a]	T_m (°C)[b]	λ_{abs} (nm)	ε_{max} (L mol^{-1} cm^{-1})	λ_{em} (nm)[c]	ΔE^{opt} (eV)[d]	λ_{abs} (nm)	E_g^{opt} (eV)
DPMA-T-DCV	299	207	498	44100	628	2.20	515 (pink)	1.98
							610 (violet)	1.77

[a] *Decomposition temperature corresponding to a 5% weight loss under N_2 determined by TGA.* [b] *Melting temperature determined from DSC.* [c] *λ_{exc} = 500 nm, Standard: Rhodamine B in Ethanol (Φ_f = 0.50).* [d] *Optical HOMO-LUMO gap estimated from the intercept of the absorption and emission spectra.*

As already reported,[19] the optical properties of an as-cast thin-film of **DPMA-T-DCV** evolves with time (Figures 2.1b and 2.1c) at room temperature or upon thermal annealing at 80 °C. Interestingly the initial UV-Vis spectrum showing a broad band at λ_{max} = 515 nm, is subjected to a progressive bathochromic shift together with the appearance of a vibrational structure with new bands at 553 and 610 nm. This evolution leads to a change of colour from pink to violet and stops after 80 min at room temperature. As shown by the AFM pictures of Figure 2.1d, this change is associated to a structural reorganization of the material leading to the formation of a violet crystalline thin-film.

Figure 2.2 shows information on the determination of the optical bandgap of thin-films of **DPMA-T-DCV** in their initial and final state (stage 3, Figure 2.1c) leading to values of E_g^{opt} of 1.98 eV (pink curve) and 1.77 eV (violet curve), respectively, corresponding to onsets of absorption at *ca.* 626 and 700 nm estimated from the cross point of absorption onset line and corrected baseline.

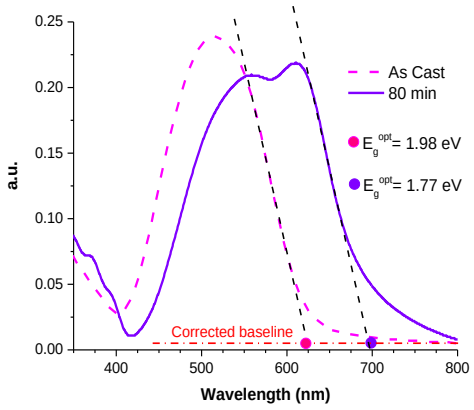

Figure 2.2. Determination of optical band gap of thin films of **DPMA-T-DCV**.

Interestingly, the same change of colour from pink to violet can be obtained faster upon thermal annealing at 80 °C for few minutes, however after a prolonged treatment at this temperature, a dewetting process occurs leading to a contraction of the material on the glass surface and hence a progressive decrease of the intensity of the absorbance of the thin-film (see also Chapter 4).

2.2.2. Thermal properties

Prior to fabrication of vacuum-processed OSCs, the thermal stability of **DPMA-T-DCV** was investigated by thermogravimetric analysis (TGA) and differential scanning calorimetry (DSC) under an inert atmosphere of nitrogen (Figure 2.3). The decomposition temperature (T_d, ~5% weight loss) occurs at 299 °C as observed by TGA. The good thermal stability of this push pull molecule suggests the possibility of preparing thin-films by thermal evaporation.

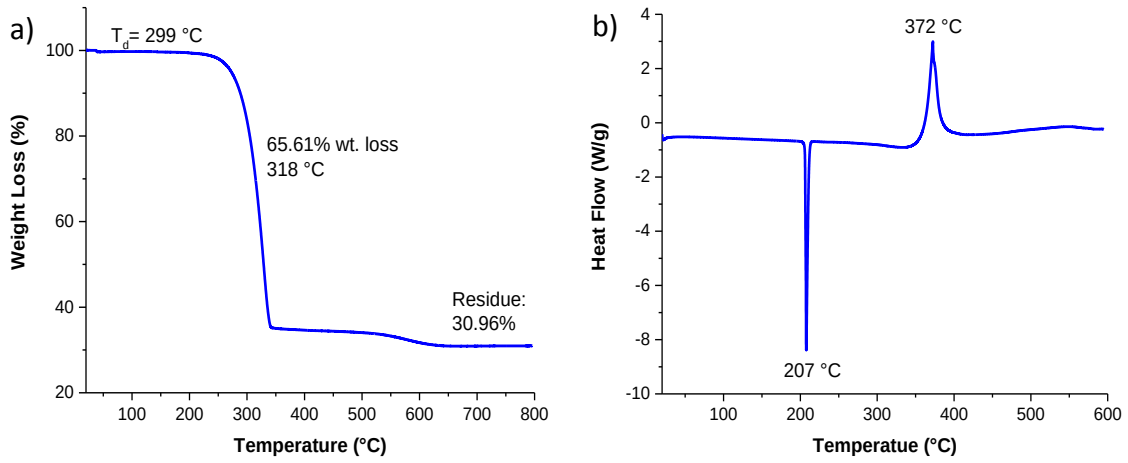

Figure 2.3. a) TGA thermogram and b) DSC curve of **DPMA-T-DCV** measured under N_2 at a heating rate of 10 °C/min.

The DSC curve shows one sharp endothermic peak at 207 °C corresponding to the melting temperature (T_m) after which the compound starts to decompose at much higher temperature above *ca*. 350 °C, which is illustrated by the broad exothermic peak at 372° C in the DSC curve. In the following paragraphs, vacuum-processed OSCs have been successfully fabricated by evaporation of **DPMA-T-DCV** at *ca*.119 °C under a pressure of 10^{-7} mbar, with a deposition rate of *ca*. 0.5 Å/S

2.2.3. Electrochemical properties

The electrochemical properties of the **DPMA-T-DCV** have been analyzed by cyclic voltammetry using dichloromethane in the presence of 0.10 M tetrabutylammonium

hexafluorophosphate (Bu_4NPF_6) as the supporting electrolyte and Pt was used as a working electrode (Figure 2.4).

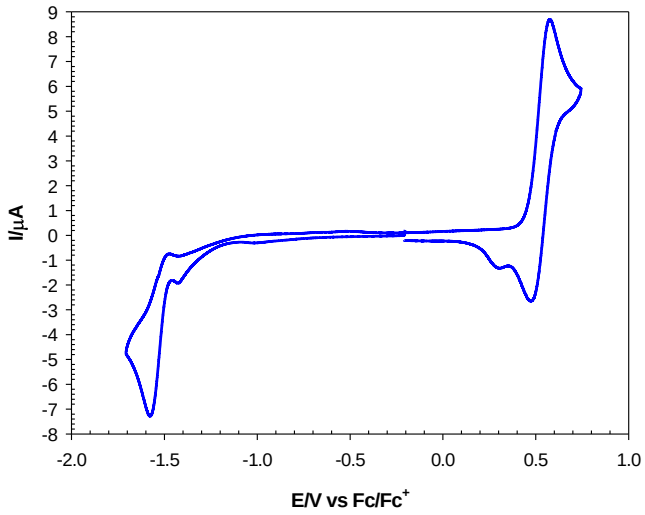

Figure 2.4. Cyclic voltammogram of **DPMA-T-DCV** 1 mM in 0.10 M Bu_4NPF_6/CH_2Cl_2, scan rate 100 mV s^{-1}, Pt working electrode

The cyclic voltammogram (CV) of **DPMA-T-DCV** showed one quasi-reversible oxidation wave peaking at E_{pa} = 0.59 V *vs*. the ferrocene/ferrocenium redox couple (Fc/Fc^+), associated with the formation of a radical cation species. In the negative potentials region, an irreversible reduction wave at E_{pc} = -1.57 V was observed, which could be assigned to the reduction of the DCV electron-withdrawing group.[20] HOMO and LUMO energy levels were calculated from the onset of the first oxidation and reduction peaks and data are reported in Table 2.2.

Table 2.2. Cyclic voltammetric data of **DPMA-T-DCV** with respect to ferrocene/ferrocenium (Fc/Fc^+).

Compd	E_{pc} [V]	E_{pa} [V]	$E_{ox,onset}$ [V]	$E_{red,onset}$ [V]	E_{HOMO}[a] [eV]	E_{LUMO}[b] [eV]	ΔE^{elec} [eV]
DPMA-T-DCV	-1.57	0.59	0.46	-1.46	-5.56	-3.64	1.92

[a] E_{HOMO} *(eV)* = - *(*$E_{ox,onset}$ *vs Fc/Fc*$^+$ + 5.1), [b] E_{LUMO} *(eV)* = - *(*$E_{red,onset}$ *vs Fc/Fc*$^+$ + 5.1).[21]

The HOMO and LUMO energies levels were estimated to -5.56 eV and -3.64 eV respectively while the electrochemical HOMO-LUMO gap (ΔE^{elec}) of 1.92 eV was in a relatively good agreement with the optical HOMO-LUMO gap of 2.20 eV. In the following paragraph, the ionization potential of **DPMA-T-DCV** has been measured and combined with its optical band gap to draw the energetic diagram in the solid state.

2.2.4. Energetic Diagram from PYSA and E_g^{opt}

The ionization potential (IP) of thin films of **DPMA-T-DCV** spun-casted from chloroform solutions (*ca*. 5 mg/mL) on ITO (indium tin oxide) substrates were determined by photoemission yield spectroscopy in air (PYSA). The UV excitation energy range extends from 4 to 6.2 eV (Figure 2.5). The ionization potential, assimilated to the "HOMO" level, was determined using the intercept between the base line and the tangent of the curve at high energy.

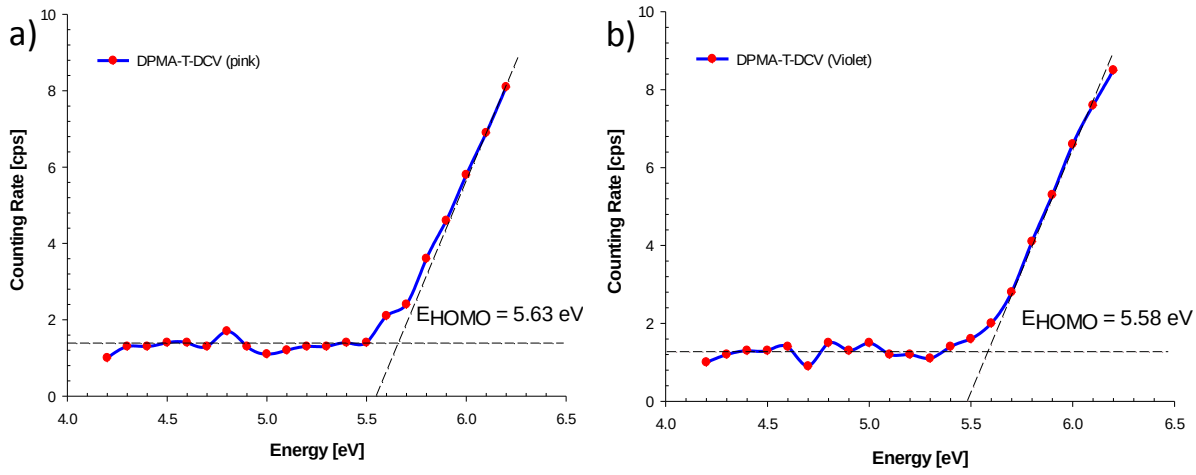

Figure 2.5. PYSA spectra of films of **DPMA-T-DCV** on ITO a) as cast (pink film, left) and b) after reorganization with time (violet film, right) .

The HOMO energy level of **DPMA-T-DCV** was found to be -5.63 eV while after thermal annealing at 80 °C for 5 minutes or 80 min at room temperature in air, an increase of +0.05 eV of the HOMO energy level is observed giving a HOMO value of -5.58 eV. These two values are quite comparable suggesting that the difference in optical properties of the pink and violet thin-films is more related to a change in the LUMO level. The LUMO energy levels were determined by adding the optical band gap of the thin films (Figure 2.2) to their HOMO levels. Thus, the pink film exhibits a LUMO level at -3.65 eV whereas the violet one is significantly stabilized down to -3.81 eV. This result highlights the effect of the structural organization of thin-films on their electronic properties.

The HOMO and LUMO levels of the pink and violet films and those of C_{60}, C_{70}, $PC_{61}BM$ and $PC_{71}BM$ that will be used as acceptors in organic solar cells, are represented in the energetic diagram of Figure 2.6. In fact, different values have been reported in the literature for the fullerene derivatives either determined in solution (from cyclic voltammetry) or in the solid state. One article of J. L. Brédas and co-workers gathers experimental ionization potentials IPs and electron affinities EAs of C_{60}, C_{70}, $PC_{61}BM$ and $PC_{71}BM$ in the solid state, measured under high vacuum by UPS (Ultraviolet Photoelectron Spectroscopy) and IEPS (Inverse PhotoEmission Spectroscopy), respectively.[22] These values have been used for HOMO and LUMO levels as represented in Figure 2.6. It is important to note that for our

molecular donors, the IP (HOMO) was measured using PYSA which is a similar technique as UPS but operating in air. In addition, we have estimated their LUMO levels by taking into account their optical bandgap E_g^{opt}. Therefore, it must be kept in mind that the levels of the donors are not strictly comparable to those of the fullerene derivatives.

The LUMO levels of **DPMA-T-DCV** in its different forms (pink or violet), are relatively higher than most of LUMO levels of the different fullerene derivatives making possible a photoinduced electron transfer from the former to the acceptors, and their HOMO levels are relatively closer to the PEDOT-PSS level indicative of possible hole extraction.

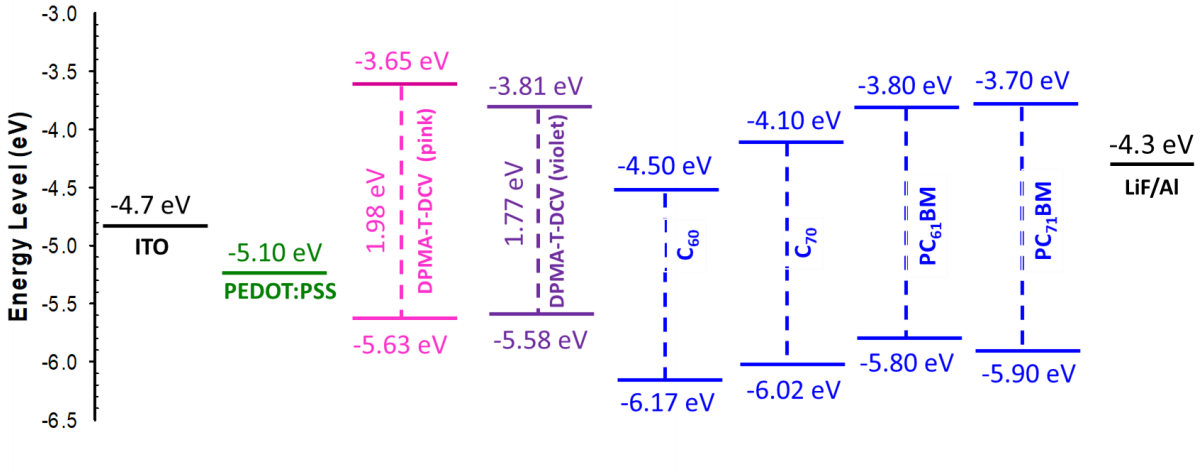

Figure 2.6. Energy level diagrams of **DPMA-T-DCV**, C_{60}, C_{70}, $PC_{61}BM$, $PC_{71}BM$ and electrodes used in OPV devices.

2.3. Charge transporting and buffer layers

Interfacial engineering represents an efficient approach to achieve OSCs with high PCEs.[23-26] Inorganic or organic interlayers can i) adjust the energy barriers between the photoactive layer and the electrodes, ii) select one type of charge carriers and reduce the charge recombination, iii) introduce dipoles close to the electrodes favoring charge extraction and iv) prevent oxygen or moisture penetration into the BHJ composite/electrode interface. Buffer layers (interlayers) can be used as hole transporting layer (HTL), electron transporting layer (ETL), hole blocking layer (HBL) and electron blocking layer (EBL). Metal oxides, ionic and electrolytic molecular or polymeric materials, graphene oxide and plasmonic materials represent the most important classes of interfacial materials.

a) Anode Interlayer Materials

Two types of interfacial layer at the anode have been used in this work. The first one, namely poly(3,4-ethylenedioxythiophene):poly(styrenesulfonate) (PEDOT:PSS), consists of a composite material based on a positively-doped conducting polymer PEDOT blended with a non-conjugated anionic water soluble PSS polymer.[27] PEDOT:PSS can be replaced by molybdenum trioxide (MoO_3) which structure is described also in Figure 2.7.

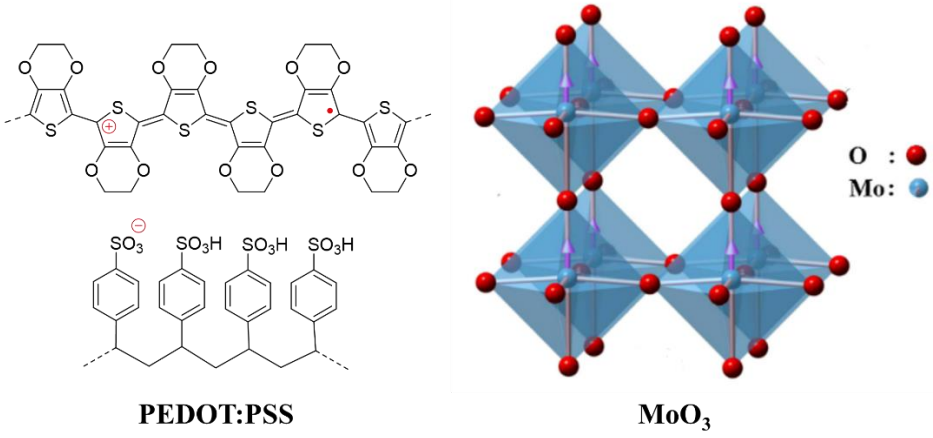

Figure 2.7. Structure of PEDOT:PSS and MoO_3 lattice (orthorhombic phase).

PEDOT:PSS is often applied for conventional OSCs and deposited by solution process between the transparent ITO electrode and the photoactive layer. This interlayer plays the role of hole transporting layer, can smooth the ITO surface to improve the conductivity, can prevent the ITO electrode from diffusing into the active layer, and exhibits a higher work function (-5.0/-5.1 eV) than ITO (-4.7 eV), hence reducing the energy barriers between ITO and organic materials.[28] On the other hand, thin films of MoO_3 are grown by vacuum process and have been used as hole transporting layer in conventional and inverted OSCs. The work function of MoO_3 is *ca*. -6.86 eV, however *p*-doping occurs at the metal oxide/organic interface interfacial leading to apparent work functions often between -5.3 and -5.8 eV.[24] Note also that the work function of MoO_3 can vary from -5.35 eV to -4.24 eV upon cesium intercalation showing that MoO_3 can become an ETL.[25] The OSCs performance depend on the thickness of the MoO_3 layer, many reports suggesting to use a thickness below 20 nm since higher values lead to a decrease of J_{sc}.[29] The substitution of PEDOT:PSS by MoO_3 can be beneficial in OSCs, due to the fact that the PEDOT:PSS layer can absorb moisture from air during the spin coating process and that PEDOT-PSS becomes more acidic at elevated temperature. In addition MoO_3 is cheaper.

b) Cathode Interlayer Materials

Different types of cathode interlayer materials have been used in this thesis. LiF (typically *ca*. 1 nm of thickness) was deposited by vacuum process onto the photoactive BHJ layer. LiF generates permanent dipole moments at the interface facilitating electron extraction.

ZnO is a very common *n*-type metal oxide, with a wide band gap of 3.3 eV and a conduction band edge of *ca*. - 4.4 eV, which has been used for ITO modification in OPV. ZnO layer can improved the performance of OSCs due to its high electron mobility (200-300 cm^2/Vs) [30] minimizing Ohmic loss in devices and its hole blocking ability preventing carrier recombination at the interface with the photoactive layer.[31] ETLs based on ZnO are synthesized by sol-gel method using a zinc acetate precursor that can be deposited on ITO by solution processes followed by a thermal treatment for the fabrication of inverted OSCs structures.

Alcohol/water-soluble polyelectrolytes composed of a π-conjugated backbone and surfactant-like side groups have already been reported as buffer layers between the BHJ layer and the top cathode electrode,[23-26] showing excellent electron-injection ability and leading to improved PCEs as in the case of poly[(9,9-dioctyl-2,7-fluorene)-alt-(9,9-bis(3′-(N,N-dimethylamino)propyl)-2,7-fluorene)] (PFN).[32-34] Typically, the thickness of these cathode interlayers is very thin from 1 to 5 nm. As another example, the phosphonium-functionalized poly(3-hexylthiophene) P3HTPMe$_3$,TFSI has been introduced as cathode interlayer improving the efficiency of PBDTTPD:PC_{71}BM solar cells by 20% as compared to calcium.[35] TFSI stands for bis(trifluoromethane)sulfonamide anion. P3HTPMe$_3$,TFSI together with the new molecular polyelectrolyte derived from a zinc tetraphenylporphyrin complex, namely ZnTPPIm,TFSI, have been provided by Prof. Sébastien Clément (University of Montpellier) and tested in this PhD work, as cathode interlayer in OSCs fabricated from D-π-A push-pull molecules (Figure 2.8).

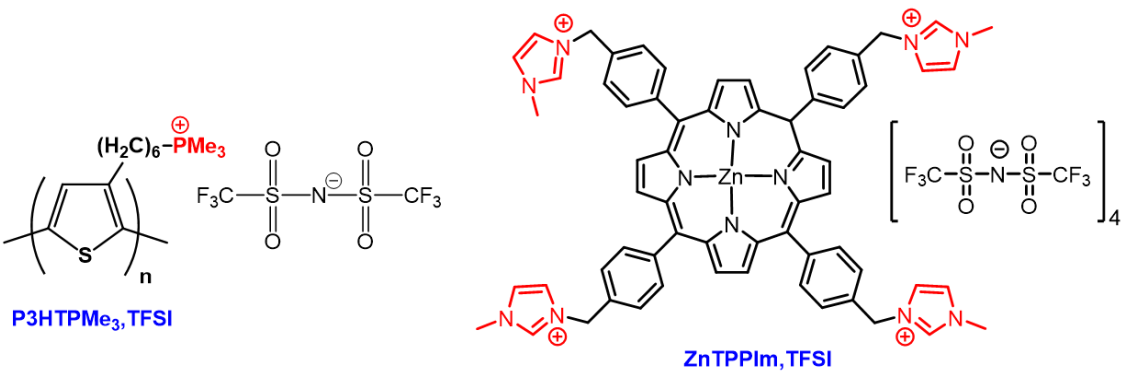

Figure 2.8. Structures of P3HTPMe$_3$,TFSI and ZnTPPIm,TFSI as cathode interlayers.

The optical properties of P3HTPMe$_3$,TFSI and ZnTPPIm,TFSI in diluted methanol solutions (*ca*. 10^{-5}) and as thin films prepared by spin-casting corresponding solutions (0.5 mg/mL of methanol)

on clean glass substrates, were analyzed by UV-Vis spectroscopy (Figure 2.9). Related optical data are gathered in Table 2.3.

The absorption band observed for P3HTPMe$_3$,TFSI in methanol at λ_{max} = 444 nm associated to the conjugated polymer, is broaden and significantly red-shifted to 485 nm in the solid state. Using the conditions of deposition of P3HTPMe$_3$,TFSI for the fabrication of OSCs (0.5 mg/mL of P3HTPMe$_3$,TFSI in methanol and a speed rate of 5000 rpm for spin-casting),[35] the resulting thin film afforded a very low optical density maximum of 0.004. The progressive decrease of speed rate down to 500 rpm, led to an increase of optical density up to 0.014 however, the corresponding thickness was not sufficient to be measured by profilometry suggesting a very small thickness, probably below 5 nm, in agreement with the typical thicknesses (1-5 nm) of cathode interlayers reported in the literature.[32-34, 36]

As expected in the case of ZnTPPIm,TFSI in methanol, the conjugated porphyrin macrocycle exhibits an intense feature at 422 nm characteristic of the "Soret" band, followed by two weaker absorptions (Q bands) at higher wavelengths at 556 and 596 nm. Again the passage to the solid state led to a slight red-shift of the absorption spectrum. The optical bandgaps of P3HTPMe$_3$,TFSI and ZnTPPIm,TFSI determined at the onset of absorption at low energy gave values of 2.10 and 2.00 eV which combined with the HOMO levels, -5.50 and -5.72 eV as measured by PYSA, afforded their LUMO levels at -3.40 and -3.72 eV, respectively.

Table 2.3. Optical data for P3HTPMe$_3$,TFSI and ZnTPPIm,TFSI in solution and as thin films.

Compd	solution		thin film			
	λ_{abs} (nm)	ΔE^{opt} (eV)	λ_{abs} (nm)	E_g^{opt} (eV)	E_{HOMO} [eV][a]	E_{LUMO} [eV][b]
P3HTPMe$_3$,TFSI	444	2.34	485	2.10	-5.50	-3.40
ZnTPPIm,TFSI	596	2.02	603	2.00	-5.72	-3.72

[a] HOMO energy levels were determined by PYSA of thin films.[b] $E_{LUMO} = E_{HOMO} + E_g^{opt}$.

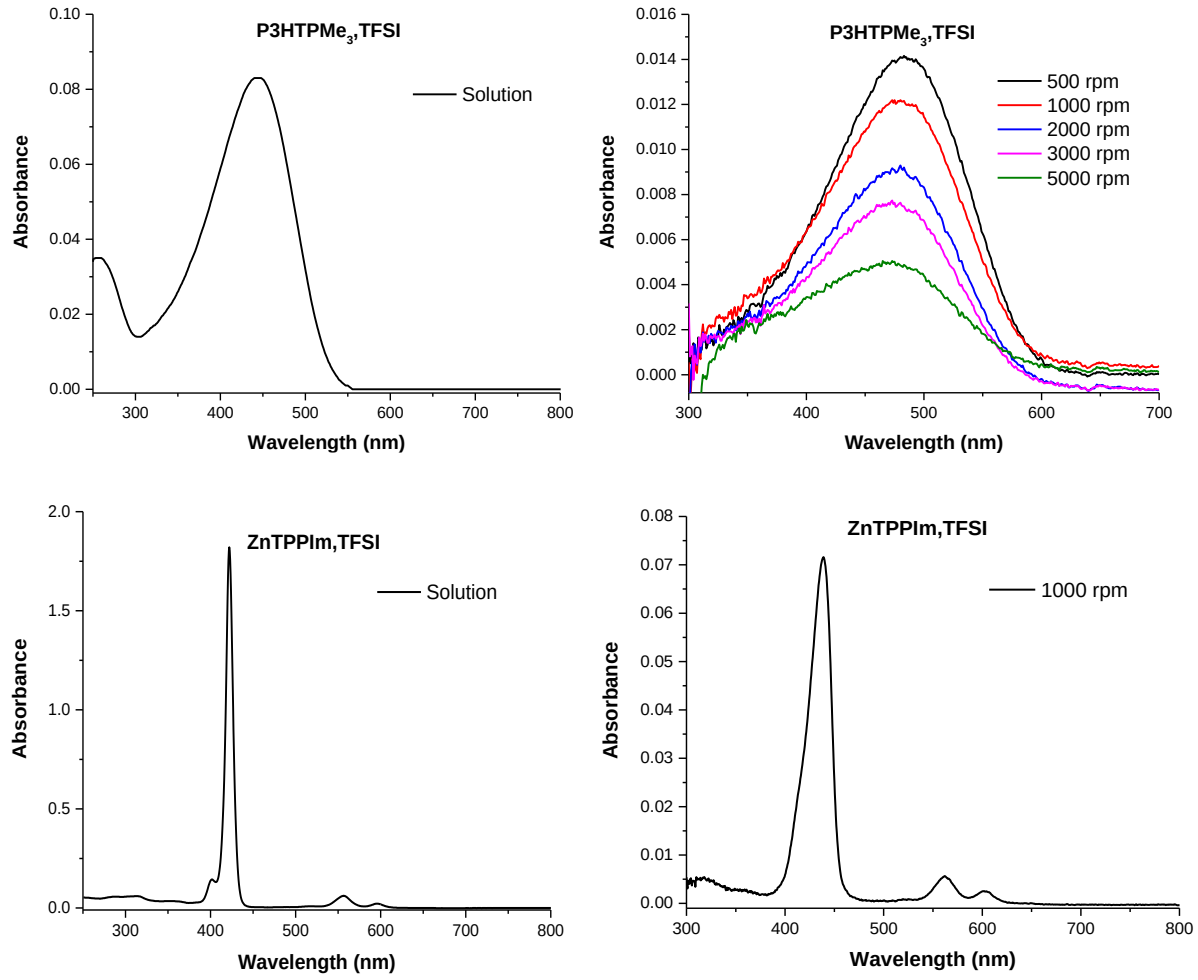

Figure 2.9. UV-Vis spectrum of P3HTPMe$_3$,TFSI and ZnTPPIm,TFSI in methanol solution and as thin films on glass prepared by spin-casting solutions of 0.5 mg/mL in methanol using different speed rates.

Finally, bathocuproine (BCP) is a wide band gap material (HOMO = - 6.7 eV and LUMO = - 3.2 eV) (Figure 2.10).[37] BCP has been used in this work as HBL or exciton blocking layer when inserted between the metal electrode (Al) and the organic photoactive layer of conventional OSCs, the related results will be described in section 2.6.

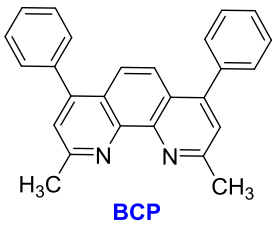

Figure 2.10. Structure of bathocuproine (BCP).

2.4. Bi-layer organic solar cells

DPMA-T-DCV was used as electron-donor material in conventional or inverted bi-layer solar cells with fullerene derivatives C_{60} and C_{70} (99.5% and 99% purity from Solenne b.v, respectively) as electron acceptors. The performance of OSCs have been optimized by modification of the solar cells architecture and the thickness of the organic layers, by thermal annealing of the completed device, and by introducing buffer layers.

2.4.1. Conventional solution-processed bi-layer OSCs

A first layer of PEDOT:PSS was deposited by spin-coating on cleaned commercially available ITO substrates. The general conditions of PEDOT:PSS thin film preparation are described in the experimental procedure. Then, the donor layer was deposited under atmospheric conditions by spin-coating a solution of **DPMA-T-DCV** in chloroform (10 mg/mL) using different speed rates for thickness optimization. The samples were transferred inside a glove box under N_2, equipped with a mask defining a disk of 0.28 cm^2 surface and put in a vacuum chamber. Under a vacuum between 10^{-6} and 10^{-7} mbar, C_{60} or C_{70} (30 nm of thickness) was deposited by vacuum evaporation with an evaporation rate of ~1.5 Å/s and next, an Al electrode of 100 nm thickness was thermally deposited (Figure 2.11). For all OSCs of this PhD work, unless otherwise stated, the shape of the devices is displayed in Figure 2.11 and the surface of the photoactive disk area is 0.28 cm^2. The current density–voltage (J–V) characteristics were recorded under AM 1.5 illumination (100 mW cm^{-2}) under a N_2 atmosphere within the glove box.

Figure 2.11. General device architecture of bi-layer organic solar cells and picture of the mask used for the one-step fabrication of 18 devices on 9 ITO substrates.

Bi-layer OSCs of the following architecture ITO/PEDOT:PSS/**DPMA-T-DCV**/C_{60} (30 nm)/Al (100 nm) were first prepared and optimized by controlling the thickness of the donor thin-film using different speed-rates (2000, 3000 and 4000 rpm) for the deposition by spin-coating. All thicknesses were measured by profilometry. Table 2.4 shows the J-V parameters of the best bi-layer OSCs before and after thermal treatment of the completed devices at 80 °C.

Table 2.4. J-V parameters of ITO/PEDOT:PSS/**DPMA-T-DCV** (*solution-processed*)/C_{60}/Al devices.

Speed rate (rpm)	Thickness (nm)	Conditions	J_{sc} (mA cm^{-2})	V_{oc} (V)	FF (%)	PCE_{max} (%)
2000	31±2	As cast @ 20 °C	4.96	0.29	27	0.29
3000	24±2		5.82	0.47	32	0.87
4000	-		4.09	0.32	28	0.37
2000	-	20 min @ 80 °C	11.50	0.56	33	2.17
3000	-	40 min @ 80 °C	13.40	0.59	35	2.78
4000	-	50 min @ 80 °C	11.43	0.52	32	1.91

The initial power conversion efficiencies of the OSCs (0.3 < PCE < 0.9%) were significantly improved after a thermal treatment at 80 °C leading, for instance, to a maximum of PCE of 2.78% for bi-layer OSCs prepared with a speed rate of 3000 rpm associated to a thickness of 24 nm, corresponding to the best trade-off between absorption, exciton diffusion length and hole transport properties of **DPMA-T-DCV**. The better PV performance obtained upon thermal treatment may result from an inter-diffusion of the donor and acceptor layers hence increasing their interface and the dissociation of excitons, however further experiments would be required to confirm this hypothesis.

Although the PCE of 2.78% seems in agreement with previously reported results for the same OSC architecture fabricated in the same conditions (PCE = 2.92%),[19] the higher value of J_{sc} (13.40 mA cm^{-2}) and the lower value of FF (35%) observed in this work are different from the reported ones (J_{sc} = 6.34 mA cm^{-2} and FF = 46%). In fact, as exemplified in the case of bi-layer OSCs with a 24 nm thickness of **DPMA-T-DCV** (Figure 2.12), all devices, whatever the thickness of the donor layer, did not give the expected diode-like behavior in the dark. The Ohmic behaviour of the J-V curves in the dark suggests the existence of short circuit or leakage current arising from a lack of homogeneity of the donor layer which can be subjected to crystallization with time or dewetting with thermal treatment, as described above. Of course, other factors can be involved such as the insertion of aluminium within the organic D/A thin layer (< 50 nm) during the vacuum deposition of the top electrode.

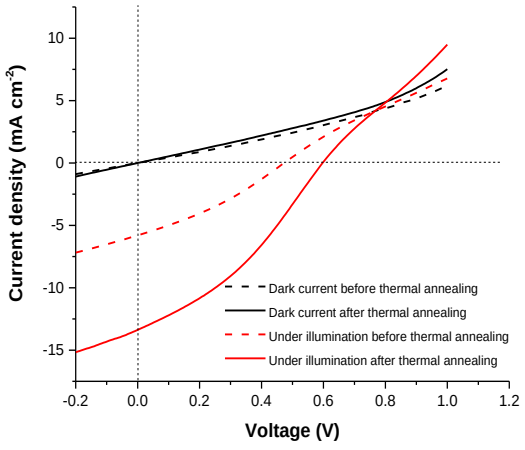

Figure 2.12. J-V curves of ITO/PEDOT:PSS/**DPMA-T-DCV** (*solution-processed at 3000 rpm*)/C_{60}/Al devices recorded in the dark and under simulated solar illumination (100 mW cm^{-2}) before (dashed lines) and after (solid line) treatment at 80 °C for 40 min.

As a next step, C_{60} has been replaced by C_{70} leading to bi-layer OSCs with the following structure: ITO/PEDOT:PSS/**DPMA-T-DCV**/C_{70} (30 nm)/Al (100 nm). Indeed, C_{70} derivatives are known to exhibit better absorption properties in the visible spectrum possibly leading to improved PV performance. Figure 2.13 shows the absorption properties of thin-films of C_{60} and C_{70} (20 nm of thickness) deposited by thermal evaporation, in full agreement with literature results,[38] and those of thin-films on glass prepared by spin-coating solutions of $PC_{61}BM$ or $PC_{71}BM$ in chloroform.

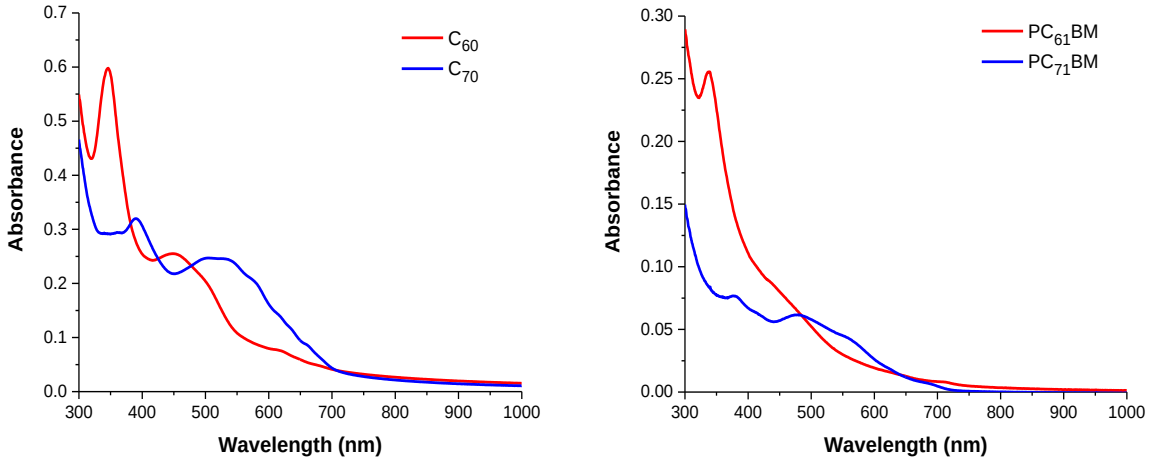

Figure 2.13. UV-Vis spectra of thin films of fullerene derivatives deposited on glass.

Again the thickness of **DPMA-T-DCV** layer was varied (500, 1000, 2000 and 3000 rpm). Table 2.5 summarizes the J-V characteristics before and after thermal annealing at 80 °C for an optimized time. Figure 2.14 shows an example of evolution of PV performance with time upon thermal treatment.

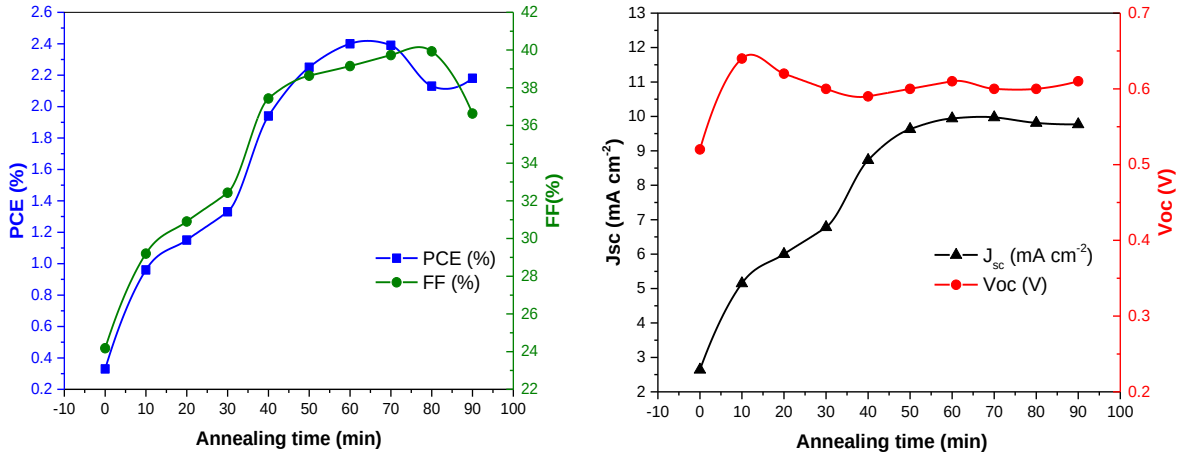

Figure 2.14. Evolution of J-V parameters *vs*. thermal annealing time at 80 °C for the best C_{70}-based solution-processed bi-layer OSCs using a speed-rate of 1000 rpm.

Table 2.5. J-V parameters of ITO/PEDOT:PSS/**DPMA-T-DCV** (*solution-processed*)/C_{70}/Al devices.

Speed rate (rpm)	Thickness (nm)	J_{sc} (mA cm^{-2})	V_{oc} (V)	FF (%)	PCE_{max} (%)	Thermal treatment
500	55±3	2.31	0.41	26	0.24	As cast (25 °C)
1000	33±2	2.64	0.52	24	0.33	
2000	31±2	3.36	0.41	29	0.39	
3000	24±2	3.96	0.58	29	0.66	
500	-	9.71	0.60	38	2.26	50 min@80 °C
1000	-	9.94	0.61	39	2.40	60 min@80 °C
2000	-	9.81	0.59	39	2.33	60 min@80 °C
3000	-	9.20	0.58	39	2.07	60 min@80 °C

Surprisingly, as exemplified in Figure 2.15a, all C_{70}-based bi-layer OSCs exhibit a much better diode-like behavior in the dark whatever the donor thickness in strong contrast with C_{60}-based OSCs. In addition, thermal annealing significantly contributes to improve PCE values and the PV performance are homogeneous for all speed rate values (2.07 % < PCE < 2.40%). The best one has been obtained by using a speed rate of 1000 rpm corresponding to a 33 nm thick layer of donor leading to a PCE of 2.40% with a V_{oc} of 0.61 V, a J_{sc} of 9.94 mA cm^{-2} and a FF of 39% after 60 minutes of thermal treatment of the device at 80 °C (Figure 2.15). Compared to the already reported C_{60}-based bilayer OSCs (V_{oc} = 0.88 V, J_{sc} = 6.34 mA cm^{-2}, FF = 46% and PCE = 2.92%),[19] a higher J_{sc} value was obtained with C_{70} in agreement with its better absorption in the visible spectrum.

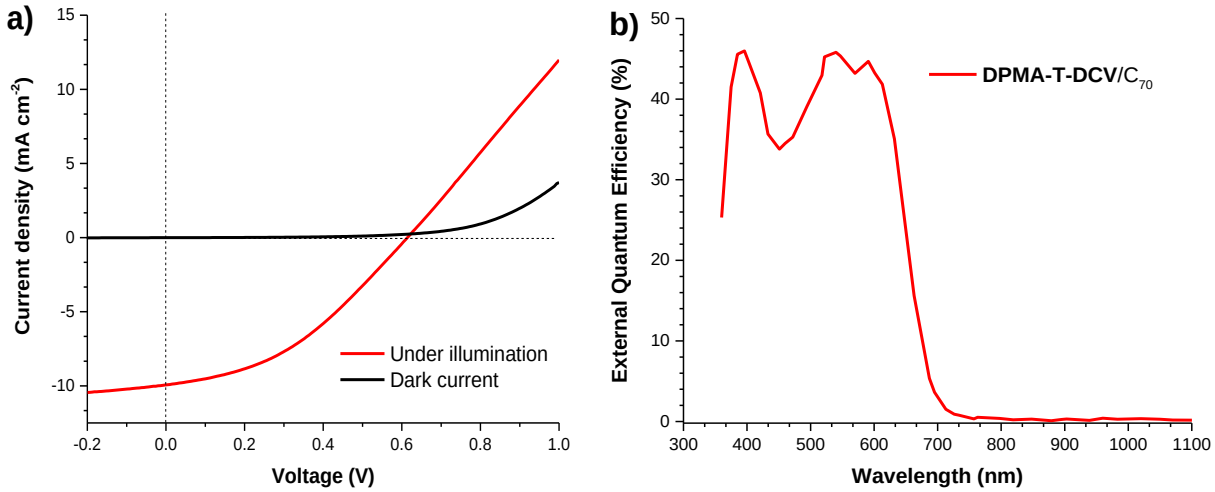

Figure 2.15. a) J-V curves of the best bi-layer OSCs using **DMPA-T-DCV**/C_{70} as photoactive layer under illumination and in the dark and b) corresponding external quantum efficiency spectrum.

The external quantum efficiency (EQE) spectrum of the best C_{70}-based bi-layer OSC shows two broad bands centered at *ca*. 540 nm and 589 nm with maxima of EQE of 46% and 44% corresponding to the contribution to the photocurrent of the push pull molecule in its π-extended violet form in the

solid state (Figure 2.15b). A sharp peak is also observed at 392 nm which may be assigned to the contribution of C_{70} in agreement with its absorption spectrum in the solid state (Figure 2.13).

Our results showed that it was easier to get bi-layer OSCs with a diode-like behaviour in the dark by using C_{70} instead of C_{60}. The origin of this phenomenon is not clear. In the following paragraph, thin-films of **DPMA-T-DCV** were prepared by vacuum process.

2.4.2. Conventional vacuum-processed bi-layer OSCs

In order to assess the impact of the processing conditions of the donor layer, bi-layer OSCs with the following architecture ITO/PEDOT:PSS/**DPMA-T-DCV**/C_{60} or C_{70}/Al (100 nm) have been fabricated by thermal vacuum evaporation of **DPMA-T-DCV**.

Thin-films of **DPMA-T-DCV** with different controlled thicknesses (15, 20 and 25 nm) were prepared with a deposition rate of ~ 0.5 Å/s under a pressure of 10^{-7} mbar at *ca*. 119 °C. Next, a layer of 30 nm of C_{60} was deposited by vacuum evaporation. As before, the time of thermal annealing at 80 °C of the completed devices has been optimized for each donor thickness and the PV performance are summarized in Table 2.6. Figure 2.16 shows the best J-V curves in the dark and under illumination for each donor thickness. Importantly, the J-V curve in the dark evidences an Ohmic behavior for the smallest thickness of 15 nm while increasing progressively this value leads to the appearance of a diode-like behaviour. When a thickness of 25 nm was reached, the OSCs showed a diode behaviour in the dark and a PCE of 2.41% was measured after 50 min of thermal annealing at 80 °C, associated to a J_{sc} of 9.88 mA cm^{-2}, a V_{oc} of 0.60 V and a FF of 40% (Table 2.6). However the corresponding J-V curve exhibits a S shape under illumination similarly to analogue bi-layer OSCs prepared by solution process (Figure 2.12).

Although its origin is not always clear, this S-shaped "kink" can be observed under illumination of certain types of organic solar cells and may arise from poor charge transport materials, charge accumulation at interfaces, misaligned metal work functions and selective blocking contacts producing injection barriers, and insulating interfacial layers between the metal and the active layers producing extraction barriers. In planar heterojunctions, as in our case, S-kinks can be caused by a strong imbalance of charge carrier mobilities (larger than 100).[39] This explanation maybe plausible here for **DPMA-T-DCV** (μ_h = 5 x 10^{-4} cm^2 V^{-1} s^{-1}) and C_{60} (μ_e = 1 cm^2 V^{-1} s^{-1}).[19, 40] In the case of bulk heterojunction OSCs, some reports incriminate the role of hole selective layer with low mobility[41] or the poor extraction of electrons at the cathode.[42]

Table 2.6. J-V parameters of ITO/PEDOT:PSS/**DPMA-T-DCV** (*vacuum-processed*)/C_{60}/Al devices.

Thickness (nm)	J_{sc} (mA cm^{-2})	V_{oc} (V)	FF (%)	PCE_{max} (%)	Thermal annealing time (80 °C)
15	*10.50*	*0.48*	*31*	*1.56*	40 min
20	9.63	0.64	44	2.72	30 min
25	9.88	0.60	40	2.41	50 min

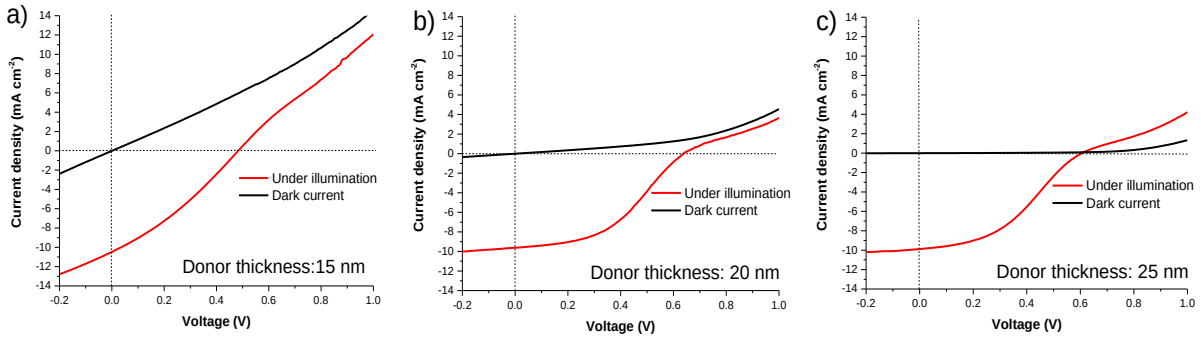

Figure 2.16. Evolution of J–V curves for ITO/PEDOT:PSS/**DPMA-T-DCV** (vacuum deposited)/C_{60}/Al under illumination and in the dark with increasing donor thickness: a) 15 nm, b) 20 nm and c) 25 nm.

The same study was achieved by evaporating C_{70} instead of C_{60}. Based on the results obtained with C_{60}, we choose to use slightly higher thicknesses of donor. Thus vacuum-processed ITO/PEDOT:PSS/**DPMA-T-DCV** (vacuum-deposited)/C_{70} (30 nm)/Al (100 nm) devices were fabricated with thicknesses of 20, 25 and 30 nm.

Table 2.7. J-V parameters of ITO/PEDOT:PSS/**DPMA-T-DCV** (*vacuum-processed*)/C_{70}/Al devices.

Thickness (nm)	J_{sc} (mA cm^{-2})	V_{oc} (V)	FF (%)	PCE_{max} (%)	Thermal annealing time (80 °C)
20	10.73	0.63	35	2.36	60 min
25	11.99	0.60	36	2.62	80 min
30	9.41	0.60	43	2.44	80 min

Again the higher thickness of donor (30 nm), probably limiting short-circuit, provided a better J-V curve in the dark. In addition the S shaped curve under illumination is suppressed leading to a PCE of 2.44% (Table 2.7 and Figure 2.17). The absence of S kink may be related to the lower electron mobility of C_{70} (μ_e = 3.4 x 10^{-3} cm^2 V^{-1} s^{-1}) [38] as compared to C_{60} which can lead to a more balanced charge carrier transport with **DPMA-T-DCV**.

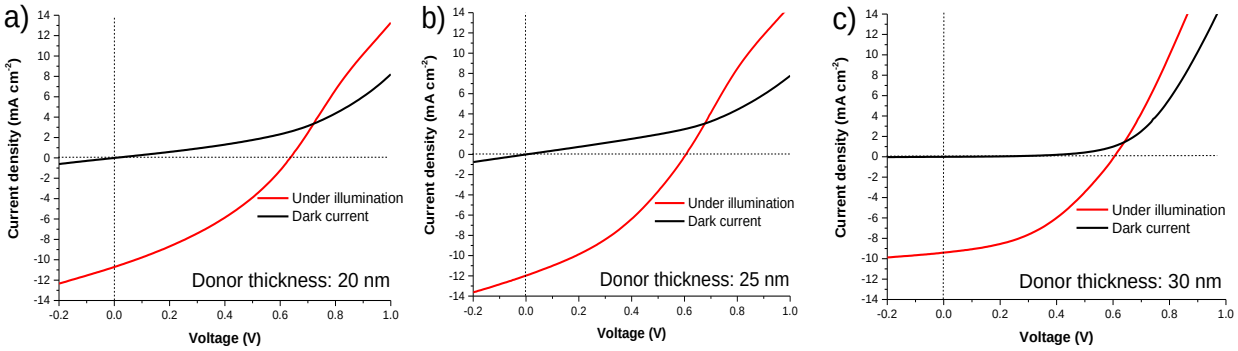

Figure 2.17. Evolution of J–V curves for ITO/PEDOT:PSS/**DPMA-T-DCV** (vacuum-deposited)/C_{70}/Al devices in the dark and under illumination with increasing donor thickness: a) 20 nm, b) 25 nm and c) 30 nm.

To summarize, the preparation of conventional bi-layer OSCs by vacuum deposition of **DPMA-T-DCV** requires a minimum of 25-30 nm of donor thickness to provide a correct J-V curve in the dark while the use of C_{60} or C_{70} (30 nm) has a weak impact on the PV performance since a comparable PCE of 2.4% was obtained for each. However, the use of C_{70} instead of C_{60} led to the suppression of the S kink observed under illumination.

As a further attempt to improve the PV performance, inverted bi-layer OSCs have been also investigated by vacuum deposition of the donor layer avoiding any modification of the first deposited acceptor layer.

2.4.3. Inverted vacuum-processed bi-layer OSCs

Three different structures of inverted bi-layer solar cells have been investigated as shown in Figure 2.18 with the following architecture using C_{70} as acceptor:

1) ITO/C_{70}/**DPMA-T-DCV**/MoO_3/Ag,
2) ITO/ZnO/C_{70}/**DPMA-T-DCV**/MoO_3/Ag,
3) ITO/ZnO/ZnTPPIm,TFSI/C_{70}/**DPMA-T-DCV**/MoO_3/Ag.

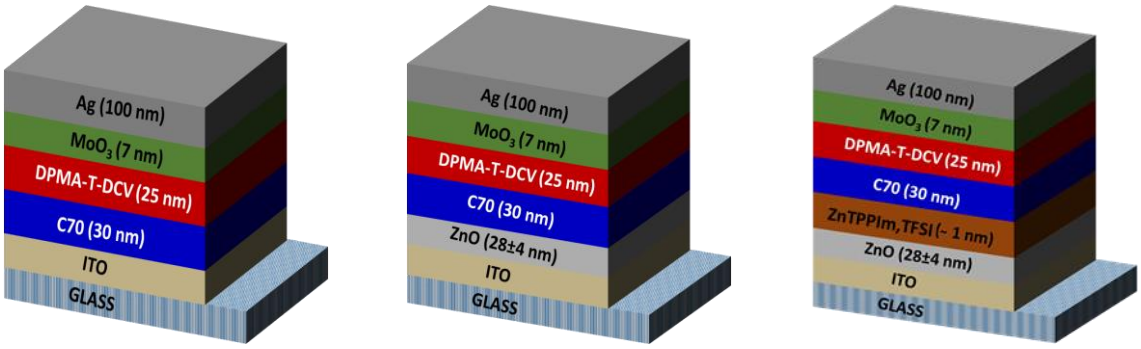

Figure 2.18. Illustration of the inverted OSCs devices.

In the first case, C_{70} was directly deposited on ITO and was expected to play the role of both acceptor and ETL as already reported for C_{60} or C_{70} [38, 43-45] while ZnO was used as well-known transparent ETL for inverted OSCs in the two other cases. The insertion of the new molecular electrolyte-based layer ZnTPPIm,TFSI between ZnO and C_{70} was also tested for better electron-extraction.

A suspension of ZnO (80 μL) prepared by sol-gel process (see experimental procedure), was spun-cast onto a patterned ITO surface at 2000 rpm for 60 s and the resulting substrate was baked at 180°C for 15 min. The thickness of the ZnO layer was about 28±4 nm as measured by profilometry. In device number 3, the zinc porphyrin derivative ZnTPPIm,TFSI was tested for the first time as buffer layer to facilitate the electron extraction to the ZnO layer. Typically, the ZnTPPIm,TFSI compound (0.5 mg) was dissolved in 1 mL of methanol and the solution was allowed to stir for at least 2 h at 40 °C. Then 40 μL of this solution was spun-cast at 5000 rpm for 60 s, the speed rate and quantity of solution being optimized. As discussed before (section 2.3), the thin layer thickness is about 1 nm. After transferring the different substrates in the vacuum chamber within the glove-box, C_{70} and **DPMA-T-DCV** were successively vacuum deposited using thicknesses of 30 and 25 nm, respectively. Finally 7 nm of MoO_3 as hole transporting layer (HTL) and 100 nm of silver (Ag) as a top electrode were evaporated through a mask defining two disk cells of 28 mm^2 area on each of the nine ITO substrates introduced in the vacuum chamber. The resulting inverted bi-layer OSCs have been characterized (Table 2.8).

Table 2.8. J-V parameters of inverted OSCs based on **DPMA-T-DCV** (25 nm of thickness) with different ETLs.

Str. nb	ETL	J_{sc} [mA cm^{-2}]	V_{oc} [V]	FF [%]	PCE_{max} [%]	PCE_{ave} [%]	R_s [Ω.cm^2]	R_{sh} [Ω.cm^2]	Cell nb
1	C_{70}	0.5	0.05	20	0.002	0.001	-	-	6
2	ZnO/C_{70}	6.47	0.82	52	2.78	2.48±0.18	78.68	893	8
3	ZnO/ZnTPPIm,TFSI/C_{70}	6.74	0.88	47	2.80	2.51±0.19	116	1022	6

Structure number 1 with direct deposition of C_{70} on ITO showed a negligible PV effect. The use of ZnO as ETL, which exhibits high electron mobility (μ_e = 155 cm^2/Vs) and transparency is essential here.[46] The best PCE values measured for devices 2 (ZnO/C_{70}) and devices 3 (ZnO/ZnTPPIm,TFSI/C_{70}) were comparable giving both a value of *ca*. 2.8%. Average values of PCE around 2.4-2.5% are very homogeneous over 6-8 devices for each structure. Contrary to analogues devices with a conventional structure, these PV performance were directly obtained without thermal treatment and no improvement were obtained after subsequent thermal treatment.

The J−V characteristics of structures 2 (ZnO/C_{70}) and 3 (ZnO/ZnTPPIm,TFSI/C_{70}) are represented in Figure 2.19. It can be seen that the addition of the electrolyte ZnTPPIm,TFSI slightly improved the J-V curve in the dark leading to an improved diode-like behaviour.

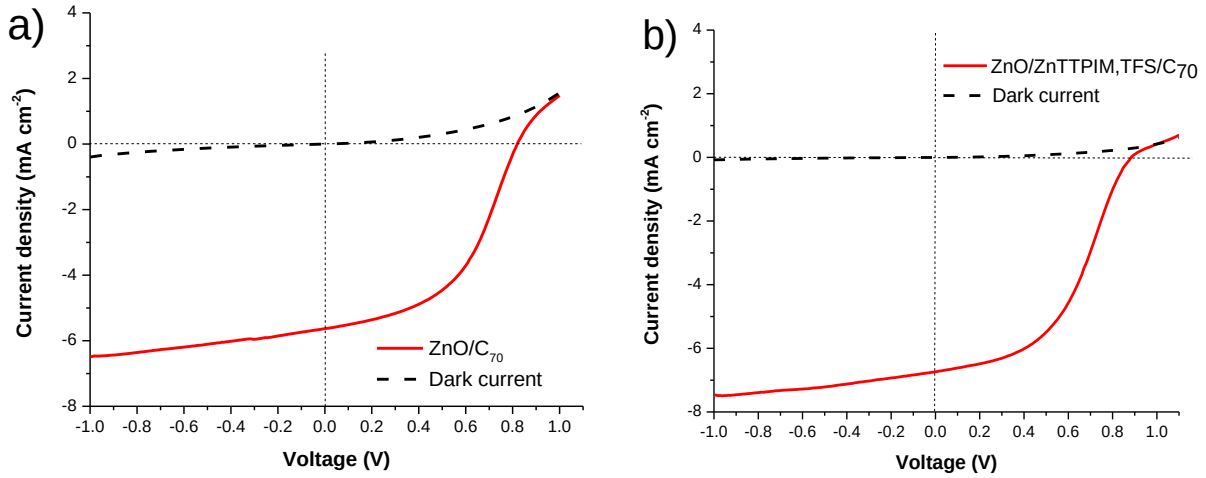

Figure 2.19. J-V characteristics of inverted bi-layer OSCs of structures a) 2 (ZnO/C_{70}) and b) 3 (ZnO/ZnTPPIm,TSFI/C_{70}).

Structures 2 and 3 show a S-shaped J-V curve under illumination which maybe due in part to the difference in hole and electron mobilities of **DPMA-T-DCV** (μ_h = 5 x 10^{-4} cm^2 V^{-1} s^{-1}) [19] and C_{70} (μ_e = 3.4 x 10^{-3} cm^2 V^{-1} s^{-1})[38] respectively. To avoid this S-shape, the thickness of donor has been decreased from 25 to 15 nm in order to compensate its lower charge mobility compared to that of C_{70}. As shown in Figure 2.20 (a and c), the S-shape of the J-V curves completely disappeared hence validating our hypothesis.

Table 2.9 shows the J-V characterics of inverted OSCs with ZnO or ZnO/ZnTPPIm,TFSI as ETL with a donor layer of 15 nm. The as-prepared OSCs gave a maximum PCE of 2.93% and 2.51% for ZnO and ZnO/ZnTPPIm,TFSI as ETL. The stability of the devices was also tested after 9 days of storage in the glove-box. Interestingly, the PCE slightly increased up to 3.11% and 3.12% respectively (Figure 2.20, b and d) mainly due to an increase of V_{oc} whose origin is not clear. One possible explanation could be related to the enhancement of the conductivity of the ZnO layer with time or upon UV-illumination which could improved the Omhic contact with ITO, however an increase of J_{sc} would have been expected.[47] In this regards the use of more conductive of Al^{3+} doped ZnO (AZO) as ETL would have been interesting. Again, it is worth noting that those performance reported in Table 2.9 were obtained without thermal annealing.

Table 2.9. J-V parameters of inverted OSCs based on **DPMA-T-DCV** (15 nm of thickness) with different ETLs.

Str. nb	Time (day) [a]	ETL	J_{sc} [mAcm^{-2}]	V_{oc} [V]	FF [%]	PCE_{max} [%]	PCE_{ave} [%]	R_s [Ω.cm^2]	R_{sh} [Ω.cm^2]	Cell nb
1	1	ZnO	6.73	0.75	58	2.93	2.46±0.26	10.67	1044	6
1	9	ZnO	6.95	0.82	55	3.11	2.91±0.12	43.11	735	6
2	1	ZnO/ZnTPPIm	7.21	0.64	54	2.51	1.57±0.61	10.74	1040	6
2	9	ZnO/ZnTPPIm	7.13	0.78	56	3.12	2.68±0.41	14.71	727	6

[a] *J-V characteristics measurement from the first day and after nine days under inert atmosphere.*

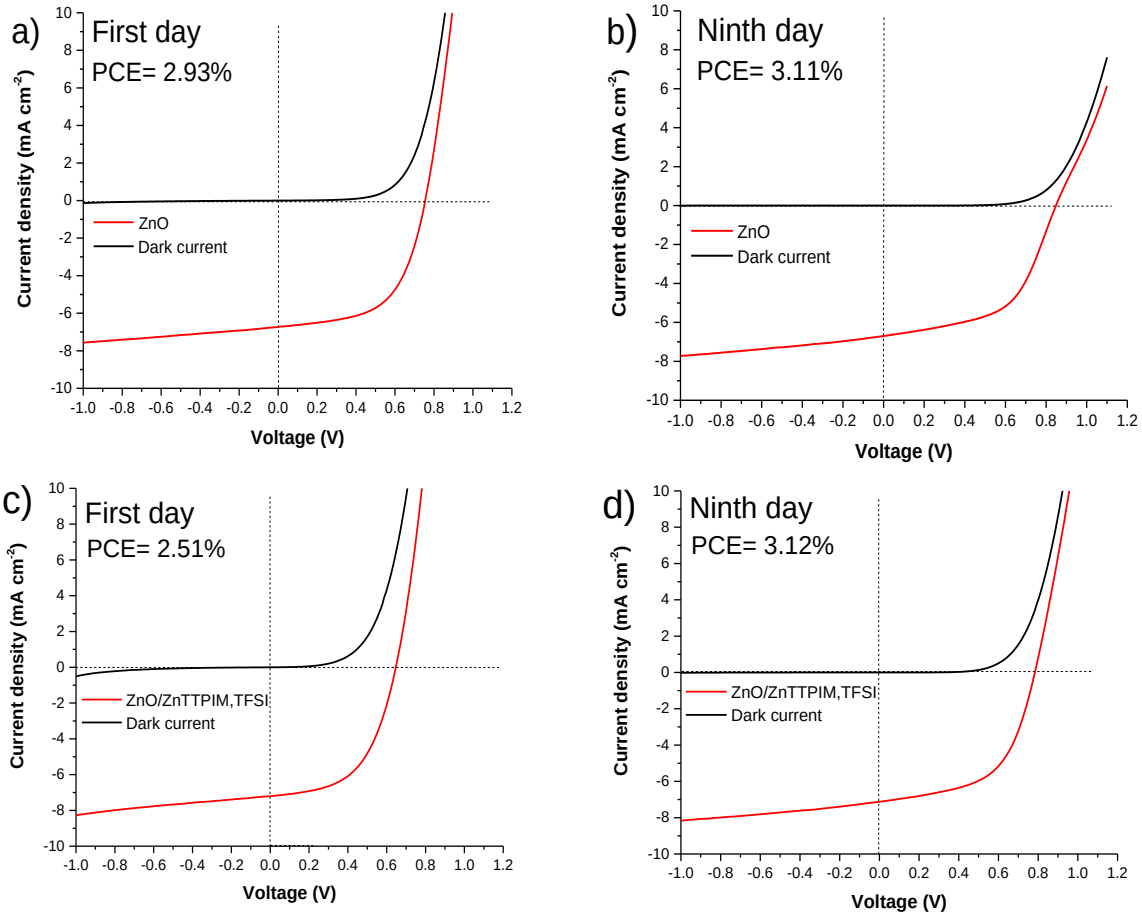

Figure 2.20. J-V characteristics of ITO/ETL/C_{70}/**DPMA-T-DCV** (15 nm)/MoO_3/Ag devices using as ETL: a) ZnO (1st day), b) ZnO (9th day), c) ZnO/TTPIM,TFSI (1st day) and d) ZnO/TTPIM,TFSI (9th day).

It is worth noting that all cells show relatively high FF values (> 50%). The series and shunt resistances, R_s and R_{sh}, were calculated according to the inverse of the slope of the corresponding J–V curves under illumination at J = 0 and V= 0 respectively. Although the PCEs slightly increase with time, the shunt resistances R_{sh} decrease and the series resistances R_{sh} increase.

The external quantum efficiency (EQE) spectra of the best devices (after 9 days) are illustrated in Figure 2.21. The EQE spectra of OSCs with ZnO and ZnO/ZnTPPIM,TFSI are similar and indicate that both C_{70} and **DPMA-T-DCV** contribute to the photocurrent generation.

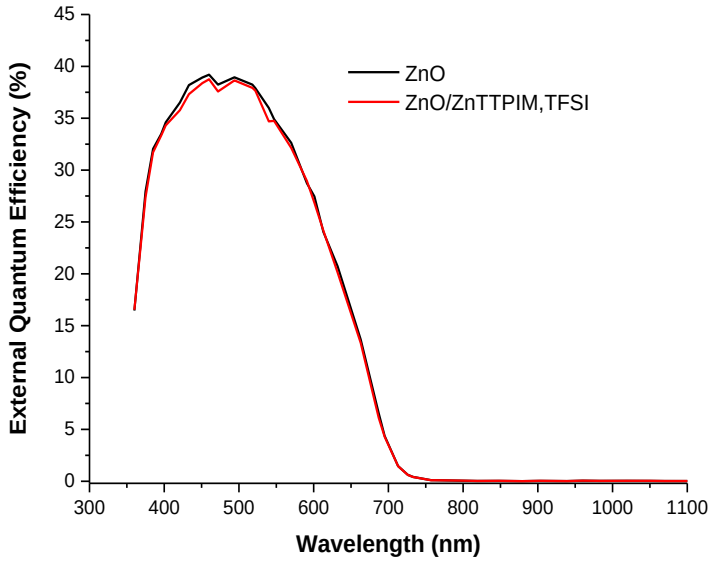

Figure 2.21. External quantum efficiency spectra of inverted bi-layer OSCs ITO/ETL/C_{70}/**DPMA-T-DCV** (15 nm)/MoO_3/Ag after 9 days of storage using ZnO (black line) and ZnO/TPPIM,TFSI (red line) as ETL.

The calculated J_{sc} values obtained by integration of the EQE spectra are about 5.72 mA cm^{-2} and 5.64 mA cm^{-2} for ZnO and ZnO/ZnTPPIM,TFSI respectively, in quite good agreement with the values obtained from the J-V curves, 6.95 mA cm^{-2} and 7.13 mA cm^{-2}.

Our work has shown that inverted bi-layer OSCs of architecture ITO/ETL/C_{70}/**DPMA-T-DCV**/MoO_3/Ag using ZnO or ZnO covered by an ultra thin films of porphyrin-based electrolyte as ETL lead to reproducible diode-like behaviour in the dark. In addition by reducing the thickness of the donor layer from 25 to 15 nm, the initial S-shape J-V curves are suppressed due to a more balanced transport of holes and electrons at the electrodes. Relatively stable OSCs were obtained exhibiting PCEs higher than 3%. On the other hand, the preparation of conventional bi-layer OSCs prepared by solution or vacuum deposition of **DPMA-T-DCV** on PEDOT:PSS, is less reproducible and very often leads to poor J-V curves in the dark probably due to the change in homogeneity of the **DPMA-T-DCV** layer with time or thermal annealing. To circumvent this issue and improve the PV performance, **DPMA-T-DCV** has been also used for the first time in BHJ OSCs.

2.5. Solution-processed bulk heterojunction organic solar cells

Conventional or inverted BHJ OSC architectures with **DPMA-T-DCV** as donor and soluble fullerene derivatives $PC_{61}BM$ and $PC_{71}BM$ as electron acceptors, have been fabricated by solution process and compared to the ones prepared from the reference compound **TPA-T-DCV** in which the methyl group of **DPMA-T-DCV** has been replaced by a phenyl ring. Previous work by our group on conventional BHJ OSCs prepared from **TPA-T-DCV** and $PC_{61}BM$ has been reported.[15] Optimization of BHJ OSCs was investigated by playing with the thickness of the photoactive layer and the weight-to-weight (w/w) ratio of donor and acceptor, the architecture of the devices and the use of a buffer layer.

2.5.1. Conventional BHJ OSCs

The general architecture of the devices corresponds to ITO/PEDOT:PSS/**Push-pull**:PC_xBM/LiF (1 nm)/Al (100 nm). By combining the two donors and two acceptors, four different combinations of BHJ OSCs have been investigated as summarized in Figure 2.22.

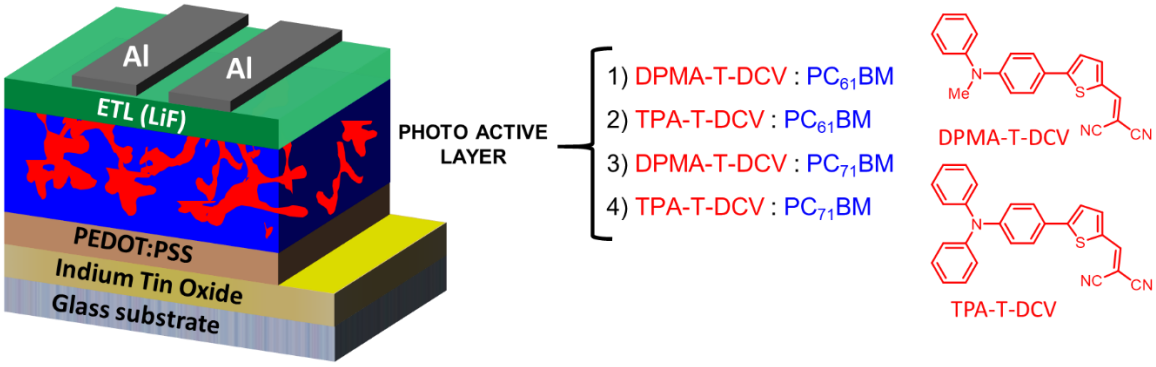

Figure 2.22. Solution-processed BHJ OSCs with four different photoactive blends.

First of all, the PV performance of devices prepared from the couple **DPMA-T-DCV**:$PC_{71}BM$ have been optimized by using different D:A w/w ratio of 1:1, 1:2 and 1:3 in chloroform with a total concentration of 10 mg/mL as follows:

1) **DPMA-T-DCV**:$PC_{71}BM$ (1:1): 5 mg:5 mg/mL in $CHCl_3$.
2) **DPMA-T-DCV**:$PC_{71}BM$ (1:2): 3.33 mg:6.66 mg/mL in $CHCl_3$.
3) **DPMA-T-DCV**:$PC_{71}BM$ (1:3): 2.5 mg:7.5 mg/mL in $CHCl_3$.

After stirring at room temperature for 60 min in a vial, the later was transferred in the glove-box and 80 μL of solution was quickly deposited all at once on a ITO/PEDOT:PSS substrate by spin-coating just after the maximum rotation speed of 1300 rpm was reached to get more repeatable results (5 s of

acceleration ramp to 1300 rpm and further 55 s at this speed rate). Then LiF and Al layers were deposited by vacuum evaporation to reach thicknesses of 1 and 100 nm, respectively.

Table 2.10 gathers the performance of the best devices. The best results were obtained with a 1:2 D:A w/w ratio leading to a maximum PCE of 2.70% associated with a high V_{oc} of 0.94 V, a J_{sc} of 7.66 mA cm^{-2} and a relatively poor FF of 37%. The measurement of the thickness of the phoactive layer by profilometry gave a value of 47±3 nm. The other ratios 1:1 and 1:3 gave slightly lower performance. Contrary to bi-layer OSCs, those PV performance were directly obtained after fabrication of the BHJ OSCs whereas a further thermal annealing was detrimental.

Table 2.10. Optimization of the **DPMA-T-DCV**:$PC_{71}BM$ w/w ratio and J-V parameters of related BHJ OSCs.

D:A (w/w) ratio	Speed rate (rpm)	J_{sc} (mA cm^{-2})	V_{oc} (V)	FF (%)	PCE_{max} (%)	PCE_{ave}[a] (%)
1:1	1300	7.06	0.98	36	**2.50**	2.45±0.05
1:2	1300	7.66	0.94	37	**2.70**	2.59±0.11
1:3	1300	8.35	0.86	32	**2.28**	2.04±0.28

[a] *Average PCEs were obtained from 6 cells.*

Next, the four types of BHJ OSCs combining **DPMA-T-DCV**, **TPA-T-DCV**, $PC_{61}BM$ and $PC_{71}BM$ were prepared using a 1:2 D:A w/w ratio and a fixed speed rate of 1300 rpm for deposition by spin-coating. Table 2.11 summarises all J-V parameters obtained with these different photoactive layers. As described above, the best PV performance have been obtained with the **DPMA-T-DCV**:$PC_{71}BM$ couple (PCE = 2.70%) whereas the replacement of **DPMA-T-DCV** by **TPA-T-DCV** leads to a slight decrease of PCE down to 2.52%.

Table 2.11. J-V parameters of BHJ OSCs with different photoactive layers.

D:A (w/w) ratio	Photoactive layer	Thickness (nm)	J_{sc} (mA cm^{-2})	V_{oc} (V)	FF (%)	PCE (%)	PCE_{ave}[a] (%)
1:2	**DPMA-T-DCV**:$PC_{61}BM$	46±3	5.65	0.92	37	1.96	1.84±0.08
	TPA-T-DCV:$PC_{61}BM$	42±3	4.07	0.96	39	1.51	1.47±0.05
	DPMA-T-DCV:$PC_{71}BM$	47±3	7.66	0.94	37	2.70	2.59±0.11
	TPA-T-DCV:$PC_{71}BM$	45±2	6.88	1.07	34	2.52	2.47±0.04

[a] *Average PCEs were obtained from 6 cells*

BHJ OSCs using $PC_{61}BM$ gave PCEs of 1.96% and 1.51% respectively for **DPMA-T-DCV** and **TPA-T-DCV** (Table 2.11). Thus **DPMA-T-DCV** provided better results due to higher values of J_{sc} in agreement with its higher hole mobility compared to that of **DPMA-T-DCV** (μ_h = 1 x 10^{-5} cm^2/Vs).[16] Also, BHJ OSCs based on $PC_{71}BM$ exhibited significantly better efficiency associated to higher J_{sc} due to the better absorption properties of $PC_{71}BM$. Interestingly, all BHJ OSCs showed very high V_{oc} between 0.92 and 1.07 V, much higher values than the ones measured for bilayer OSCs (0.5-0.6 V).

The J–V characteristics of the four types of BHJ OSCs are displayed in Figure 2.23. Contrary to the bilayer OSCs, the conditions used for our BHJ OSCs gave quite good dark current density curves.

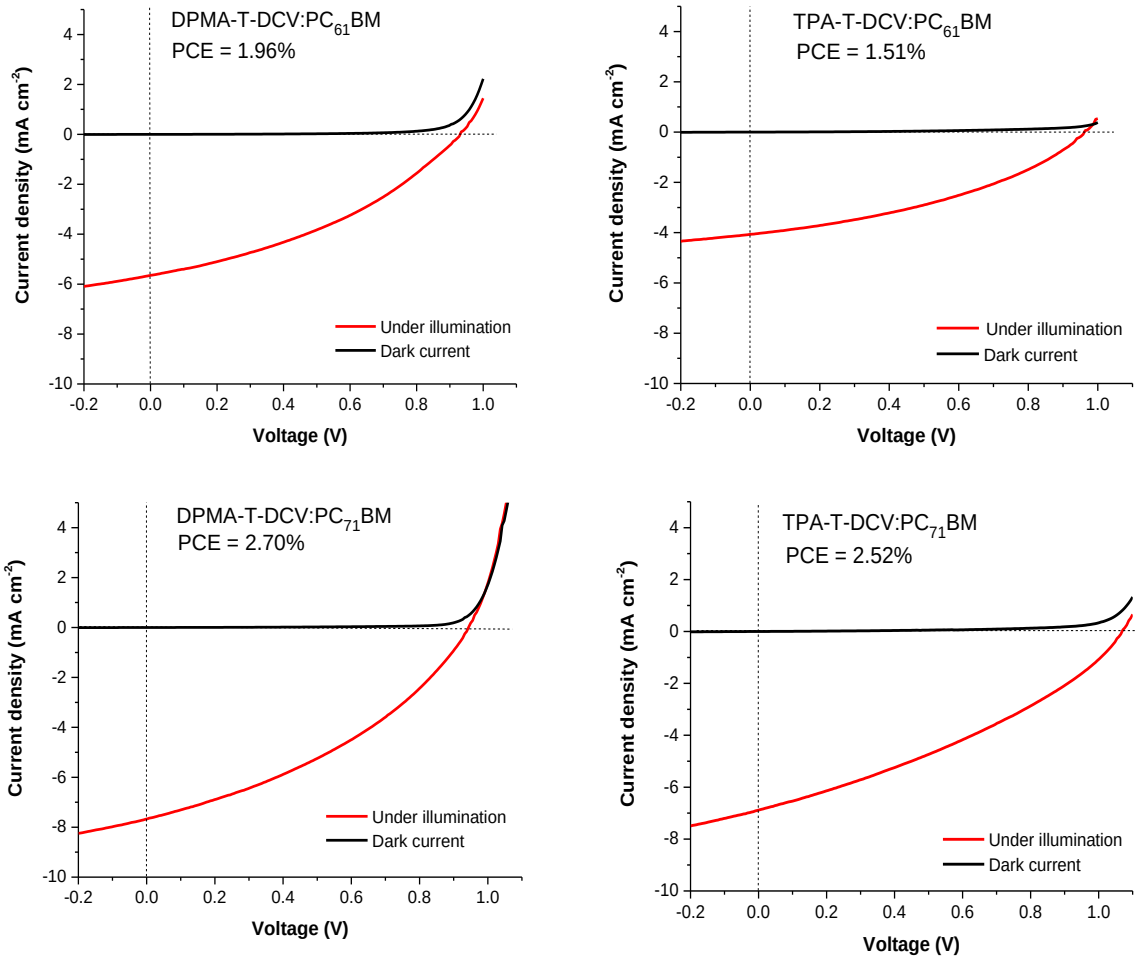

Figure 2.23. J-V curves of the four types of BHJ OSCs under illumination (red line) and dark (black line).

The EQE spectra of the best BHJ devices are illustrated in Figure 2.24 and show for all of them one broad band centered at *ca*. 519 nm corresponding to the contribution to the photocurrent of the push-pull molecule in its π-extended violet form in the solid state. A sharp peak is also observed for all blends at 397 nm which may be assigned to the contribution of PC_XBM. As expected, the BHJ OSCs made of **DPMA-T-DCV** and $PC_{71}BM$ exhibit the more intense EQE spectrum in agreement with the highest J_{sc} value measured in the J-V curve under illumination.

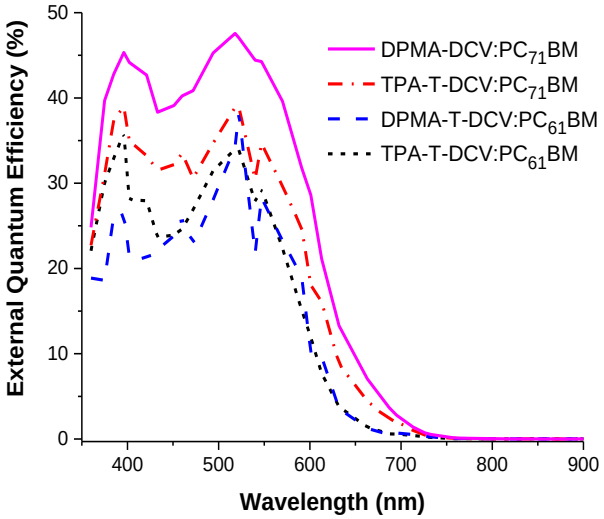

Figure 2.24. EQE spectra of solution-processed BHJ OSCs.

Then, the impact of a buffer layer in the architecture ITO/PEDOT:PSS/**DPMA-T-DCV**:$PC_{71}BM$ (1:2)/Buffer layer/Al, has been investigated (Figure 2.25). LiF has been suppressed or replaced by two different polyelectrolytes, one derived from polythiophene (P3HTPMe$_3$,TFSI) and the other derived from porphyrin (ZnTPPIm,TFSI) as already used above.

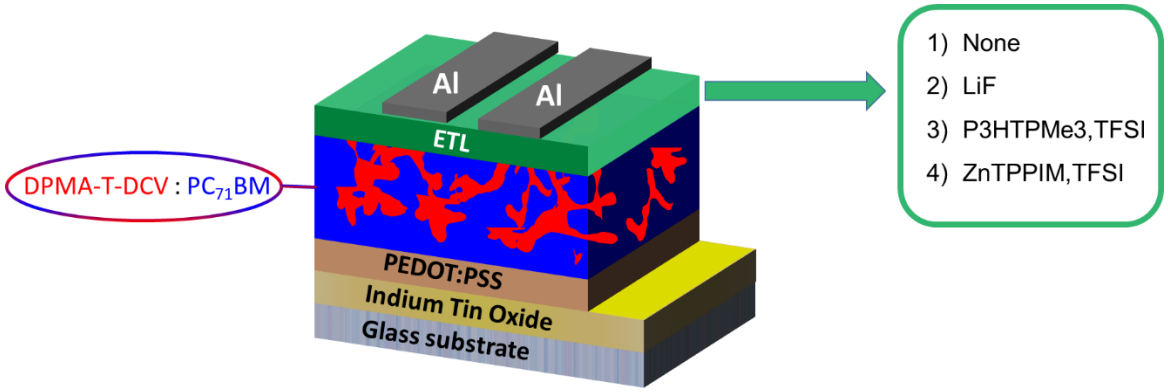

Figure 2.25. Structure of BHJ OSCs using **DPMA-T-DCV**:$PC_{71}BM$ as photoactive layer and various cathode buffer layers: 1) none, 2) LiF, 3) P3HTPMe$_3$,TFSI and 4) ZnTPPIM,TFSI.

It is possible to prepare BHJ OSCs without buffer layer at the cathode, the average value of PCE calculated from 6 cells reachs 2.14% with a maximum value of 2.84%. However the performance are less homogeneous and show relatively low V_{oc} values in comparison with the values obtained in presence of LiF, highlighting the role of the latter in extracting electrons. In addition, the J-V curve of the best cell in the dark does not show the behavior expected for an ideal diode (Table 2.12, Figure 2.26).

Table 2.12. Photovoltaic parameters of BHJ OSCs prepared without ETL with the following structure ITO/PEDOT:PSS/**DPMA-T-DCV**:$PC_{71}BM$ (1:2 w/w ratio, 1300 rpm speed rate)/Al.

Device nb	Speed rate (rpm)	FF (%)	J_{sc} (mA cm^{-2})	V_{oc} (V)	PCE (%)
1	1300	27	11.66	0.59	1.86
		28	11.50	0.64	2.05
2		27	7.86	0.58	1.23
		32	8.11	0.88	2.30
3		*27*	*11.25*	*0.85*	*2.84*
		29	11.31	0.78	2.56

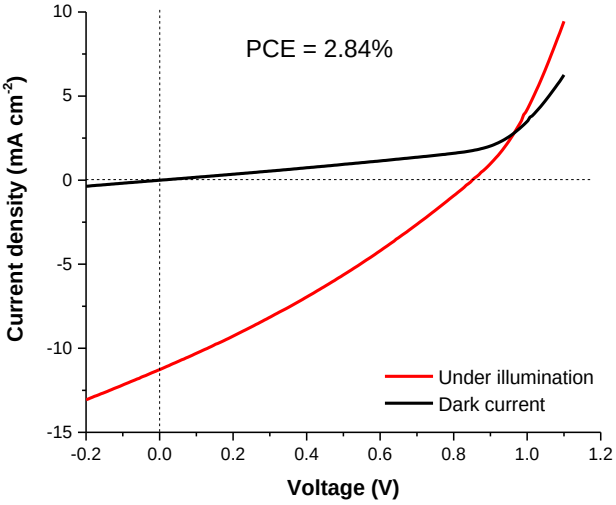

Figure 2.26. J-V curves of the best ITO/PEDOT:PSS/**DPMA-T-DCV**:$PC_{71}BM$ (1:2 w/w ratio, 1300 rpm speed rate)/Al prepared without ETL under illumination and in the dark.

For the preparation of the buffer layers based on P3HTPMe$_3$,TFSI and ZnTPPIm,TFSI, 0.5 mg of each compound was dissolved in 1 mL of methanol of HPLC grade (an orthogonal solvent for the photoactive layer). These solutions were allowed to stir for at least 2 h at 40 °C. Then 40 μL of each solution were spun-cast at high a speed rate of 5000 rpm for 60 s on the top of the photoactive layer before evaporation of aluminium. The speed rate and the quantity of solution have been optimized. As before, the thickness of these buffer layers is estimated to be close to 1 nm. Results for P3HTPMe$_3$,TFSI and ZnTPPIm,TFSI are gathered in Table 2.13. Note that when only MeOH without electrolyte was spin-coated, the performance of the cells were close to zero. More reproducible BHJ OSCs and more homogeneous PCE values have been measured in the presence of a buffer layer. The best cell efficiency reaches 2.91% with a high V_{oc} of 0.90 V, a J_{sc} of 10.40 mA cm^{-2} and a FF of 31% in the presence of P3HTPMe$_3$,TFSI while the use of the zinc porphyrin electrolyte ZnTPPIm,TFSI leads to relatively close performance (PCE = 2.72%, J_{sc} = 8.35 mA cm^{-2}, V_{oc} = 0.87 V and FF = 44%).

Table 2.13. Photovoltaic parameters of BHJ OSCs based on **DPMA-T-DCV**:$PC_{71}BM$ (1:2 w/w ratio) with LiF, $P3HTPMe_3$,TFSI or ZnTPPIm,TFSI as cathode buffer layer.

Buffer Layer (BL)	Speed rate for D/A (rpm)	Speed rate for BL (rpm)	J_{sc} (mA cm^{-2})	V_{oc} (V)	FF (%)	PCE_{max} (%)	PCE_{ave} (%)	Cell nb
LiF	1300	-	7.66	0.94	37	2.70	2.59±0.11	6
P3HTPMe3,TFSI	1300	5000	10.37	0.90	31	2.91	2.52±0.30	8
ZnTPPIM,TFSI	1300	5000	8.35	0.87	37	2.72	2.24±0.25	8

Thus the presence of a buffer layer is beneficial in terms of reproducibility, homogeneity and performance, in particular the V_{oc} value becomes significantly higher. In addition, very good dark current curves were also obtained in the presence of the charged polythiophene and porphyrin (Figure 2.27) as well as LiF.

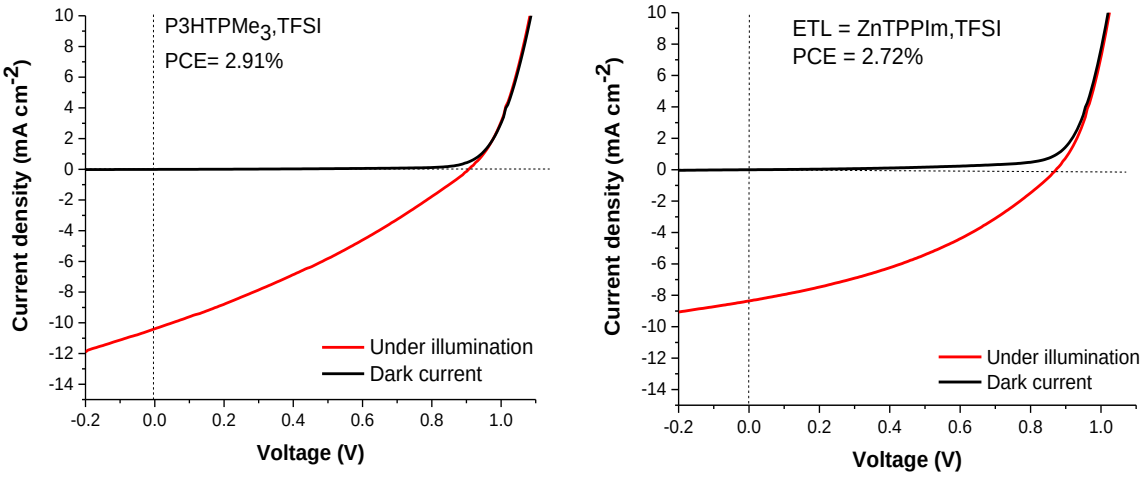

Figure 2.27. J-V characteristics of BHJ OSCs based on **DPMA-T-DCV**:$PC_{71}BM$ (1:2 w/w ratio) using $P3HTPMe_3$,TFSI or ZnTPPIM,TFSI as cathode buffer layer.

The EQE spectra of the best BHJ OSCs with $P3HTPMe_3$,TFSI or ZnTPPIm,TFSI are quite similar and show a broad band centered at *ca*. 518 nm with a maximum of ~ 44% corresponding to the contribution of the push-pull molecule **DPMA-T-DCV** and a sharp peak at *ca*. 390 nm which may be associated to the contribution of $PC_{71}BM$ (Figure 2.28). It is interesting to note that the EQE spectra extend over 700 nm suggesting the co-existence of amorphous and more crystalline domains of **DPMA-T-DCV** within the photoactive blend.

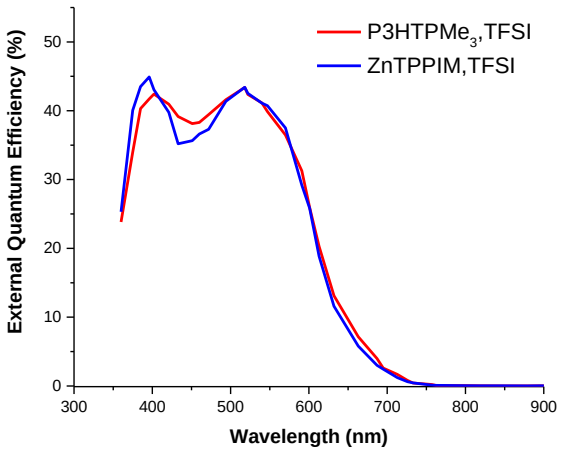

Figure 2.28. EQE spectra of the best **DPMA-T-DCV**-based BHJ OSCs with P3HTPMe$_3$,TFSI or ZnTPPIm,TFSI.

The calculated J_{sc} values obtained by integration of the EQE spectra are about 5.80 mA cm^{-2} (10.37 mA cm^{-2} from J-V curve) and 5.66 mA cm^{-2} (8.35 mA cm^{-2} from J-V curve) for devices with P3HTPMe$_3$,TFSI and ZnTPPIm,TFSI, respectively.

2.5.2. Inverted BHJ OSCs

Inverted BHJ OSCs based on **DPMA-T-DCV**:$PC_{71}BM$ (1:2 w/w) as photoactive layer were also investigated using different architectures as shown in Figure 2.29. ZnO was used as ETL and deposited on ITO substrates by spin-coating as previously described. In addition, a buffer layer of P3HTPMe$_3$,TFSI or ZnTPPIm,TFSI was also coated on top of the ZnO layer. Then, the photoactive layer was deposited by spin coating (1300 rpm) followed by the successive thermal evaporations of MoO_3 (7 nm), as hole transporting layer, and Ag (100 nm) as top electrode. The three types of devices are summarized:

1) ITO/ZnO/ **DPMA-T-DCV**:$PC_{71}BM/MoO_3$/Ag,
2) ITO/ZnO/P3HTPMe$_3$,TFSI/**DPMA-T-DCV**:$PC_{71}BM/MoO_3$/Ag,
3) ITO/ZnO/ZnTPPIm,TFSI / **DPMA-T-DCV**:$PC_{71}BM/MoO_3$/Ag.

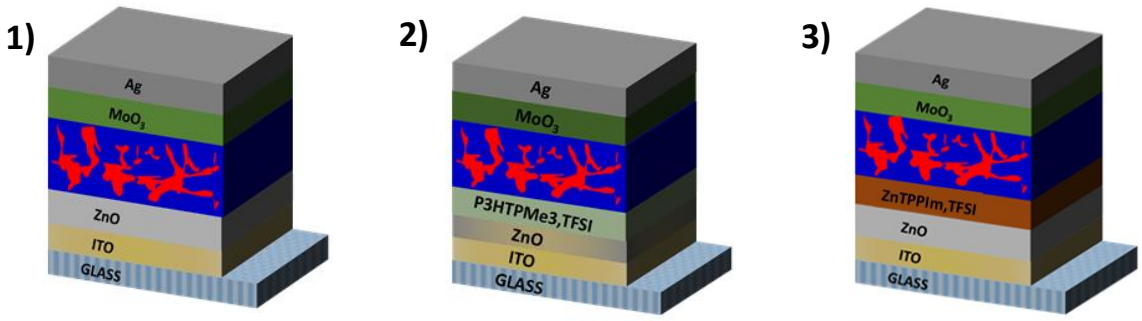

Figure 2.29. Inverted BHJ OSCs based on ZnO only (1) or ZnO coated with a buffer layer (2 and 3).

The J-V curves of the best devices for each architecture are compared in Figure 2.30.

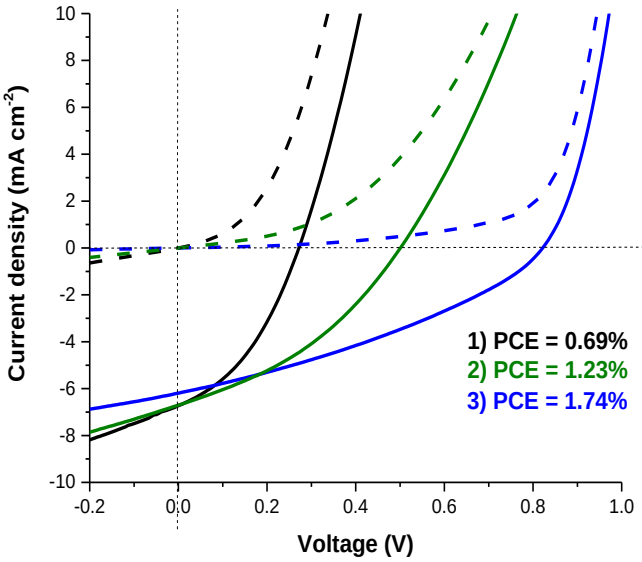

Figure 2.30. J-V characteristics of inverted BHJ OSCs of architecture 1 (black), 2 (dark green) and 3 (blue) under illumination (solid line) and in the dark (dashed line).

The corresponding photovoltaic parameters of these devices (between 4 and 13 devices depending on the configuration) are summarized in Table 2.14.

Table 2.14. J-V parameters of inverted BHJ OSCs based on **DPMA-T-DCV**:$PC_{71}BM$ with different ETLs

Structure	ETL	J_{sc} [mA cm^{-2}]	V_{oc} [V]	FF [%]	PCE_{max} [%]	PCE_{ave} [%]	Cell nb
1	ZnO	6.71	0.27	38	0.69	0.55±0.12	9
2	ZnO/P3HTPMe$_3$,TFSI	6.73	0.50	36	1.23	0.94±0.15	13
3	ZnO/ZnTPPIm,TFSI	6.18	0.82	34	1.74	1.24±0.33	4

Table 2.14 shows that PCE is progressively improving going from structure **1** (ZnO only, PCE = 0.69%), **2** (ZnO/P3HTPMe$_3$,TFSI, PCE = 1.23%) to **3** (ZnO/ZnTPPIm,TFSI, PCE = 1.74%). The FF and J_{sc} values are quite comparable whereas the V_{oc} value depends strongly on the architecture of the devices. The later has been significantly increased from 0.27 V for ZnO only, 0.50 V for ZnO/P3HTPMe$_3$,TFSI to 0.82 V for ZnO/ZnTPPIm,TFSI. The origin of this interfacial effect between ZnO and the buffer layer is not understood for the moment although those buffer layers are expected to favor electron extraction highlighting the interest of the zinc porphyrin interlayer. By comparison with the performance of vacuum-processed inverted bi-layer solar cells (section 2.4.3, PCE = 3.12% using ZnO/ZnTPPIm,TFSI)), solution-processed inverted BHJ OSCs remain less performant.

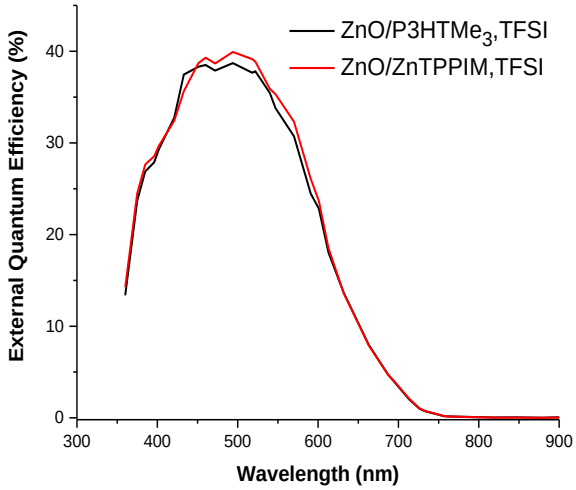

Figure 2.31. EQE spectra of inverted BHJ OSCs based on **DPMA-T-DCV** using different buffer layers.

As expected from the same range of J_{sc} values measured from the J-V characteristics (J_{sc} *ca*. 6.2-6.7 mA cm^{-2}), the EQE spectrum of the best inverted BHJ OSCS using ZnO modified by P3HTPMe$_3$,TFSI or ZnO/ZnTPPIm,TFSI are similar in shape and intensity. They show a broad band centered at *ca*. 518 nm with a maximum of 38%-40% corresponding again to the contribution of the push-pull molecule, leading to calculated J_{sc} values from the integration of the EQE spectra, of about 5.16 mA cm^{-2} and 5.28 mA cm^{-2} respectively (Figure 2.31), values which are comparable but slightly lower than the ones obtained from the J-V characteristics.

2.6. All vacuum-processed BHJ organic solar cells

Finally, we have fabricated photovoltaic devices by depositing all layers by vacuum evaporation. First, it avoids to use PEDOT:PSS which is known to become acidic with time and second, all steps are achieved successively under vacuum. A conventional architecture was chosen allowing to replace PEDOT:PSS by MoO_3 (15 nm) as hole transporting material. The photoactive layer was deposited by co-evaporation of **DPMA-T-DCV** and C_{60} by adjusting the deposit rate at 0.5 Å/s (~119 °C) for the donor and 1 Å/s for the acceptor, thus giving a volume ratio of 1:2. The thickness of the donor-acceptor bulk heterojunction photoactive layer was optimized using 50, 60, 70, 80, 90 and 100 nm as monitored by a quartz crystal microbalance. A thin-layer of bathocuproine (BCP, 8 nm) used as exciton blocking layer onto the photoactive layer, was deposited with a rate of 0.4 Å/s (~ 104 °C). The device was completed by vacuum deposition of a thick layer of aluminum (100 nm) as top electrode (Figure 2.32). The general architecture is as follows: ITO/MoO_3 (15 nm)/**DPMA-T-DCV**:C_{60} (1:2, v/v)/BCP (8 nm)/Al (100 nm). Note that the thickness of MoO_3 and BCP was fixed and chosen according to literature data.[48-50]

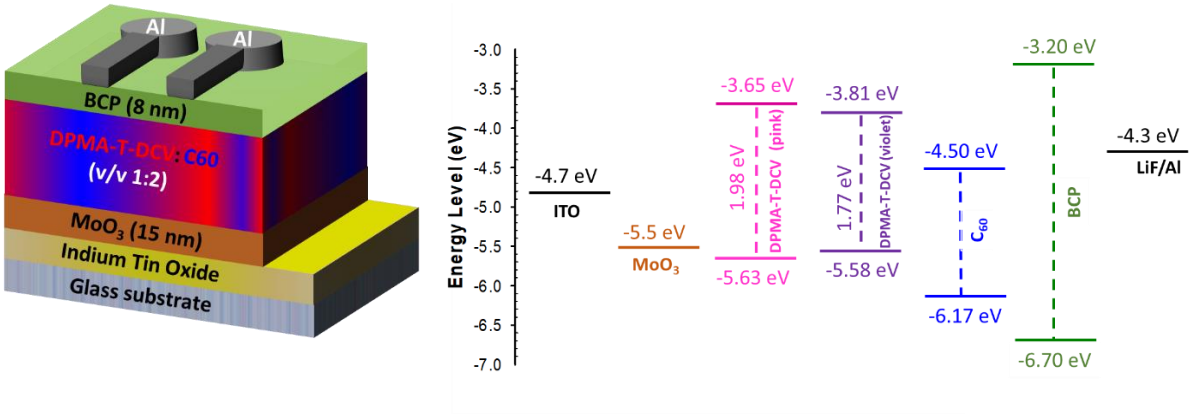

Figure 2.32. All vacuum-processed conventional BHJ OSCs with a co-evaporated blend of **DPMA-T-DCV** and C_{60} and corresponding energy level diagram.

The optimal thickness of the photoactive layer will depend on different parameters such as its absorption as well as exciton diffusion lengths and carrier recombination rates. Experimentally different thicknesses have been tested and corresponding J-V parameters are gathered in Table 2.15.

Table 2.15. Photovoltaic parameters for all vacuum-processed conventional BHJ OSCs with **DPMA-T-DCV**:C_{60} (1:2) as photoactive layer of different thicknesses.

Device nb	Thickness (D:A) [nm]	J_{sc} [mA cm^{-2}]	V_{oc} [V]	FF [%]	PCE_{max} [%]	PCE_{ave} [%]	Cell nb
1	50	6.69	0.78	41	2.18	1.22±0.65	14
2	60	7.47	0.92	49	3.41	3.26±0.13	11
3	70	15.33	0.76	36	4.24	3.69±0.45	5
4	80	10.63	0.91	34	3.33	2.98±0.24	12
5	90	11.13	0.92	34	3.51	3.07±0.28	6
6	100	7.09	0.90	39	2.47	2.21±0.18	11

Table 2.15 shows that the best performance correspond to device number 3 with a photoactive layer thickness of 70 nm. A maximum of PCE of 4.24% was recorded with a V_{oc} of 0.78 V, a very high J_{sc} of 15.33 mA cm^{-2} and a FF of 36%, while the average PCE value over 5 devices remains quite high (PCE_{ave} = 3.69%). This all vacuum-processed BHJ OSC architecture provides the best efficiencies as compared to all other device structures of this work. Interestingly, the PCE of the best cell only decreases down to 3.9% after 11 days of storage in the glovebox indicating a relatively good stability. Figure 2.33 shows J-V curves and EQE spectrum of the best cell with a photoactive layer of 70 nm of thickness.

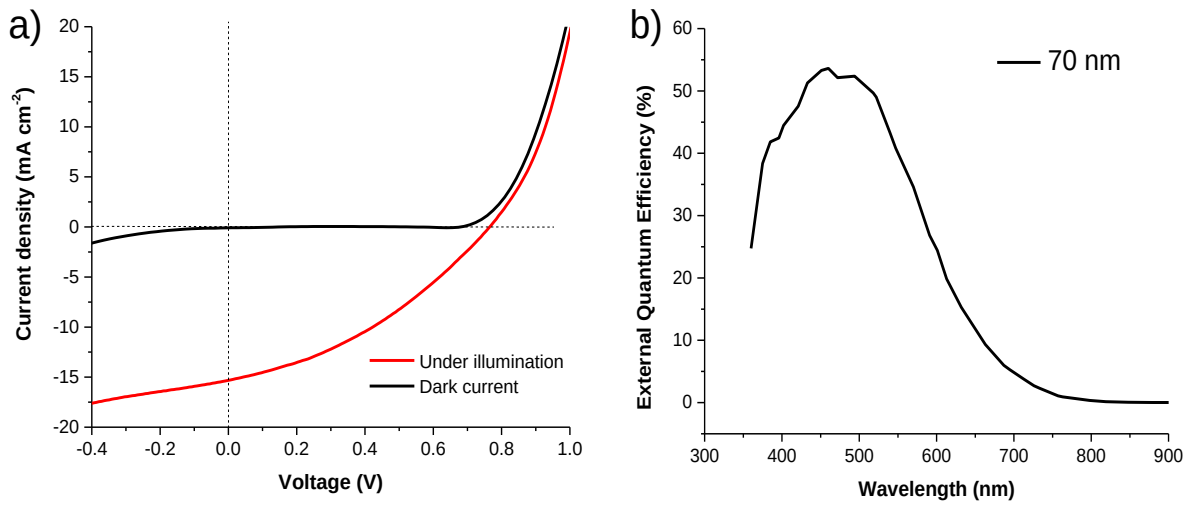

Figure 2.33. a) J−V characteristics of the best all vacuum-processed conventional BHJ OSCs with **DPMA-T-DCV**:C_{60} (1:2, 70 nm) as photoactive layer. b) Corresponding EQE spectrum.

The EQE spectrum shows a broad band centered at *ca*. 518 nm with a maximum of 55% corresponding to the contribution of the push-pull molecule while the integration of the curve leads to a calculated J_{sc} values of *ca*. 14.2 mA cm^{-2} a value in full agreement with the high value of 15.33 mA cm^{-2} recorded in the J-V curve under illumination (Figure 2.33).

Conclusion

In summary, a small push pull molecule **DPMA-T-DCV** has been synthesized in relatively large quantity (0.5 to 1 g) allowing us to evaluate its photovoltaic (PV) potential as donor material in organic solar cells (OSCs) of various architectures and in different conditions. The analysis of its electronic properties in solution and as thin-films by absorption spectroscopy, PYSA and cyclic voltammetry confirmed its donor character compared to fullerene derivatives as acceptors.

First, conventional bi-layer OSCs with the following architecture ITO/PEDOT:PSS/**DPMA-T-DCV**/C_{60} or C_{70}/Al were fabricated using a solution- or a vacuum-process for the deposition of the **DPMA-T-DCV** layer, the thickness of the later being optimized. In each case, thermal annealing of the completed devices at 80 °C improved the PV performance. For solution-processed bi-layer OSCs, the use of C_{70} instead of C_{60} led to current density-voltage (J-V) curves with a better diode-like behaviour in the dark and maximum PCE of 2.40% for a donor layer thickness of 33 nm. When the donor layer is deposited by vacuum evaporation, the J-V curves showed a diode-like behaviour in the dark and a maximum PCE of *ca*. 2.4% whatever the use of C_{60} or C_{70}.

Inverted bi-layer OSCs with the ITO/ZnO/buffer layer/C_{70}/**DPMA-T-DCV**/MoO_3/Ag architecture were also elaborated by using a sol-gel process for the formation of the ZnO layer and a vacuum-process for the deposition of the donor layer. Whatever the presence or not of a buffer layer, a maximum efficiency of *ca*. 2.8% was obtained for OSCs using a layer of **DPMA-T-DCV** with 25 nm of thickness. However the presence of a very thin layer (*ca*. 1 nm) of the new zinc porphyrin electrolyte ZnTPPIm,TFSI as buffer layer, provided a better diode-like behaviour of the J-V curve in the dark. In addition, the J-V curves under illumination showed an S-shape suggesting unbalanced hole and electron transport properties between **DPMA-T-DCV** and C_{70}, respectively. In order to solve this issue, the thickness of the donor layer was decreased down to 15 nm to compensate the difference in charge transport hence undergoing the suppression of the S-shape of the J-V curves under illumination, an increase of the fill factor (FF) beyond 50% and PCE values of 2.9% and 2.5% without or with ZnTPPIm,TFSI, respectively. Interestingly, for both cases, the PCE could reach 3.1% efficiency after nine days of storage in a glovebox. This work on bi-layer OSCs showed that better and more reproducible PV performance were obtained for inverted bi-layer OSCs compared to devices with a conventional architecture.

Then solution-processed bulk heterojunction (BHJ) OSCs were investigated with the conventional architecture ITO/PEDOT:PSS/D:A (*ca*. 50 nm)/LiF/Al using **DPMA-T-DCV** or its triphenylamine analogue **TPA-T-DCV** as donor (D) and $PC_{61}BM$ or $PC_{71}BM$ as acceptor (A). After optimization of the **DPMA-T-DCV**:$PC_{71}BM$ couple, a 1:2 D/A w/w ratio was selected and applied to the four photoactive layer resulting from the combination of the two donors and two acceptors. To summarize, BHJ OSCs exhibited good J-V curves in the dark and the use of **DPMA-T-DCV** *vs* **TPA-T-DCV** gave slightly higher PCEs as well as for $PC_{71}BM$ compared to $PC_{61}BM$. Thus the best BHJ OSCs based on the **DPMA-T-DCV**:$PC_{71}BM$ blend led to a PCE of 2.7%. The cathode buffer layer LiF was also replaced by a polymeric electrolyte derived from polythiophene, namely P3HTPMe$_3$,TFSI, or the previous zinc porphyrin salt ZnTPPIm,TFSI affording comparable performance or even slightly higher in the former case (PCE = 2.9%), showing the interest of these two types of electrolytes as cathode buffer layers.

Solution-processed inverted BHJ OSCs with the structure ITO/ZnO/buffer layer/**DPMA-T-DCV**:$PC_{71}BM$ (1:2)/MoO_3/Ag were tested in the absence of buffer layer and in the presence of P3HTPMe$_3$,TFSI or ZnTPPIm,TFSI, the PCE progressively increasing from 0.69%, to 1.23% and 1.74% as a result of a progressive increase of V_{oc}. The PV performance of the latter BHJ OSCs remained lower than the ones obtained for the corresponding inverted bi-layer OSCs (PCE = 3.1%).

Finally, a careful optimization of the thickness of the photoactive layer of all-vacuum processed BHJ OSCs with the structure ITO/MoO_3/**DPMA-T-DCV**:C_{60} (1:2)/BCP/Al, led to a high PCE value of 4.24% for a photoactive layer of 70 nm thickness. This efficiency was associated with a V_{oc} of 0.78 V, a J_{sc} of 15.33 mA cm^{-2} and FF of 36%. The very high J_{sc} value was in good agreement with the one determined from the external quantum efficiency spectrum of the OSC (14.2 mA cm^{-2}).

To conclude, this work on the evaluation of **DPMA-T-DCV** as donor in organic photovoltaics has revealed that vacuum process represents a deposition technique of choice for this small push-pull molecule. In addition, preparation of bulk hetrojunction by co-evaporation of this compound and C_{60} could lead to OSCs with PCE beyond 4%. Further improvements are expected with C_{70} owing to its better absorption properties in the visible spectrum.

References:

1. J. Roncali, P. Leriche and P. Blanchard, *Advanced Materials*, 2014, **26**, 3821-3838.
2. V. Malytskyi, J.-J. Simon, L. Patrone and J.-M. Raimundo, *RSC Advances*, 2015, **5**, 354-397.
3. P. Blanchard, C. Malacrida, C. Cabanetos, J. Roncali and S. Ludwigs, *Polymer International*, 2019, **68**, 589-606.
4. A. Mishra, C. Wetzel, R. Singhal, P. Bäuerle and G. D. Sharma, *The Journal of Physical Chemistry C*, 2018, **122**, 11262-11269.
5. Y.-H. Chen, L.-Y. Lin, C.-W. Lu, F. Lin, Z.-Y. Huang, H.-W. Lin, P.-H. Wang, Y.-H. Liu, K.-T. Wong and J. Wen, *Journal of the American Chemical Society*, 2012, **134**, 13616-13623.
6. L.-Y. Lin, Y.-H. Chen, Z.-Y. Huang, H.-W. Lin, S.-H. Chou, F. Lin, C.-W. Chen, Y.-H. Liu and K.-T. Wong, *Journal of the American Chemical Society*, 2011, **133**, 15822-15825.
7. O. V. Kozlov, Y. N. Luponosov, A. N. Solodukhin, B. Flament, O. Douhéret, P. Viville, D. Beljonne, R. Lazzaroni, J. Cornil and S. A. Ponomarenko, *Organic Electronics*, 2018, **53**, 185-190.
8. H.-S. Shim, C.-K. Moon, J. Kim, C.-K. Wang, B. Sim, F. Lin, K.-T. Wong, Y. Seo and J.-J. Kim, *ACS applied materials & interfaces*, 2016, **8**, 1214-1219.
9. X. Che, X. Xiao, J. D. Zimmerman, D. Fan and S. R. Forrest, *Advanced Energy Materials*, 2014, **4**, 1400568.
10. X. Che, Y. Li, Y. Qu and S. R. Forrest, *Nature Energy*, 2018, **3**, 422.
11. C. Cabanetos, P. Blanchard and J. Roncali, *The Chemical Record*, 2019, **19**, 1123-1130.
12. S. Roquet, A. Cravino, P. Leriche, O. Alévêque, P. Frere and J. Roncali, *Journal of the American Chemical Society*, 2006, **128**, 3459-3466.
13. A. Leliège, C.-H. Le Régent, M. Allain, P. Blanchard and J. Roncali, *Chemical Communications*, 2012, **48**, 8907-8909.
14. A. Leliège, J. Grolleau, M. Allain, P. Blanchard, D. Demeter, T. Rousseau and J. Roncali, *Chemistry–A European Journal*, 2013, **19**, 9948-9960.
15. A. Labrunie, Y. Jiang, F. Baert, A. Leliege, J. Roncali, C. Cabanetos and P. Blanchard, *RSC Advances*, 2015, **5**, 102550-102554.
16. J. W. Choi, C.-H. Kim, J. Pison, A. Oyedele, D. Tondelier, A. Leliege, E. Kirchner, P. Blanchard, J. Roncali and B. Geffroy, *Rsc Advances*, 2014, **4**, 5236-5242.
17. S. Mohamed, D. Demeter, J.-A. Laffitte, P. Blanchard and J. Roncali, *Scientific reports*, 2015, **5**, 9031.
18. Y. Jiang, C. Cabanetos, S. Jungsuttiwong, D. Alberga, C. Adamo and J. Roncali, *ChemistrySelect*, 2017, **2**, 6296-6303.
19. Y. Jiang, C. Cabanetos, M. Allain, P. Liu and J. Roncali, *Journal of Materials Chemistry C*, 2015, **3**, 5145-5151.
20. S. Haid, A. Mishra, C. Uhrich, M. Pfeiffer and P. Bäuerle, *Chemistry of Materials*, 2011, **23**, 4435-4444.
21. C. M. Cardona, W. Li, A. E. Kaifer, D. Stockdale and G. C. Bazan, *Adv Mater*, 2011, **23**, 2367-2371.
22. H. Sun, S. Ryno, C. Zhong, M. K. Ravva, Z. Sun, T. Korzdorfer and J. L. Bredas, *J Chem Theory Comput*, 2016, **12**, 2906-2916.
23. C. Yi, X. W. Hu, X. Gong and A. Elzatahry, *Materials Today*, 2016, **19**, 169-177.
24. H. L. Yip and A. K. Y. Jen, *Energy & Environmental Science*, 2012, **5**, 5994-6011.
25. B. Walker, H. Choi and J. Y. Kim, *Current Applied Physics*, 2017, **17**, 370-391.
26. L. Lu, T. Zheng, Q. Wu, A. M. Schneider, D. Zhao and L. Yu, *Chem Rev*, 2015, **115**, 12666-12731.
27. L. Groenendaal, F. Jonas, D. Freitag, H. Pielartzik and J. R. Reynolds, *Advanced materials*, 2000, **12**, 481-494.
28. M. Al-Hashimi, B. Kadem, Y. Rahaq, R. G. Kadhim and A. Hassan, *J Mater Sci-Mater El*, 2018, **29**, 13889-13896.

29. Z. Su, L. Wang, Y. Li, G. Zhang, H. Zhao, H. Yang, Y. Ma, B. Chu and W. Li, *ACS Appl Mater Interfaces*, 2013, **5**, 12847-12853.
30. J. Boucle and J. Ackermann, *Polymer International*, 2012, **61**, 355-373.
31. P. S. Mbule, T. H. Kim, B. S. Kim, H. C. Swart and O. M. Ntwaeaborwa, *Solar Energy Materials and Solar Cells*, 2013, **112**, 6-12.
32. C. He, C. M. Zhong, H. B. Wu, R. Q. Yang, W. Yang, F. Huang, G. C. Bazan and Y. Cao, *Journal of Materials Chemistry*, 2010, **20**, 2617-2622.
33. L. Zhang, C. He, J. Chen, P. Yuan, L. Huang, C. Zhang, W. Cai, Z. Liu and Y. Cao, *Macromolecules*, 2010, **43**, 9771-9778.
34. Z. He, C. Zhang, X. Xu, L. Zhang, L. Huang, J. Chen, H. Wu and Y. Cao, *Adv Mater*, 2011, **23**, 3086-3089.
35. M. Chevrier, J. E. Houston, J. Kesters, N. Van den Brande, A. E. Terry, S. Richeter, A. Mehdi, O. Coulembier, P. Dubois and R. Lazzaroni, *Journal of Materials Chemistry A*, 2015, **3**, 23905-23916.
36. J. E. Houston, S. Richeter, S. Clement and R. C. Evans, *Polymer International*, 2017, **66**, 1333-1348.
37. Z. Q. Wang, X. F. Wang, D. Yokoyama, H. Sasabe, J. Kido, Z. Y. Liu, W. J. Tian, O. Kitao, T. Ikeuchi and S. Sasaki, *J Phys Chem C*, 2014, **118**, 14785-14794.
38. S. Pfuetzner, J. Meiss, A. Petrich, M. Riede and K. Leo, *Applied Physics Letters*, 2009, **94**, 145.
39. M. Riede, T. Mueller, W. Tress, R. Schueppel and K. Leo, *Nanotechnology*, 2008, **19**, 424001.
40. C. H. Cui, Y. W. Li and Y. F. Li, *Advanced Energy Materials*, 2017, **7**, 1601251.
41. L. Sims, U. Hormann, R. Hanfland, R. C. I. MacKenzie, F. R. Kogler, R. Steim, W. Brutting and P. Schilinsky, *Organic Electronics*, 2014, **15**, 2862-2867.
42. B. Y. Finck and B. J. Schwartz, *Applied Physics Letters*, 2013, **103**, 143_141.
43. F. Holzmueller, L. Wilde, F. Wölzl, C. Koerner, K. Vandewal and K. Leo, *Organic Electronics*, 2015, **27**, 133-136.
44. C. Koerner, C. Elschner, F. Selzer, K. Leo, M. Riede, N. Miller, R. Fitzner, E. Reinold, P. Bäuerle and M. Toney, *Organic Electronics: physics, materials, applications*, 2012, **13**.
45. M. S. Wrackmeyer, M. Hein, A. Petrich, J. Meiss, M. Hummert, M. K. Riede and K. Leo, *Solar Energy Materials and Solar Cells*, 2011, **95**, 3171-3175.
46. N. A. Jayah, H. Yahaya, M. R. Mahmood, T. Terasako, K. Yasui and A. M. Hashim, *Nanoscale research letters*, 2015, **10**, 7.
47. K. Akaike, K. Kanai, H. Yoshida, J. Tsutsumi, T. Nishi, N. Sato, Y. Ouchi and K. Seki, *Journal of Applied Physics*, 2008, **104**, 023710.
48. C.-H. Chen, H.-C. Ting, Y.-Z. Li, Y.-C. Lo, P.-H. Sher, J.-K. Wang, T.-L. Chiu, C.-F. Lin, I.-S. Hsu and J.-H. Lee, *ACS applied materials & interfaces*, 2019, **11**, 8337-8349.
49. H. W. Lin, C. W. Lu, L. Y. Lin, Y. H. Chen, W. C. Lin, K. T. Wong and F. Lin, *Journal of Materials Chemistry A*, 2013, **1**, 1770-1777.
50. Y. Shibata, T. Kono, N. Komura and Y. Yoshida, *Organic Electronics*, 2013, **14**, 1073-1080.

Chapter 3:
OSCs based on DPMA-T-T-DCV, a π-extended push-pull molecule

3.1. Introduction

As shown previously by our group in the case of push-pull **DPMA-T-DCV** molecule, the introduction of as diphenylmethylamine (DPMA) instead of the triphenylamine (TPA) group represents an interesting strategy to achieve *p*-type organic semiconductors with improved hole transporting properties and hence to produce optimized donor materials for efficient bi-layer organic solar cells (OSCs).[1, 2]

The purpose of chapter 2 was to evaluate more broadly the photovoltaic (PV) potential of **DPMA-T-DCV** by optimizing the conditions of fabrication of the OSCs and developing new architectures.

On these basis, the goal of this chapter deals with the description and the characterization of a π-extended analogue of **DPMA-T-DCV** resulting from the insertion of an additional thiophene ring in the π-spacer. Compared to **DPMA-T-DCV**, this new compound, namely **DPMA-T-T-DCV**, is expected to show different properties in solution and in the solid state and, in particular better absorption in the visible spectrum is expected possibly leading to enhanced PV performance. The impact of the additional thiophene ring will be discussed in terms of electrochemical, optical, thermal and structural properties as well as PV performance.

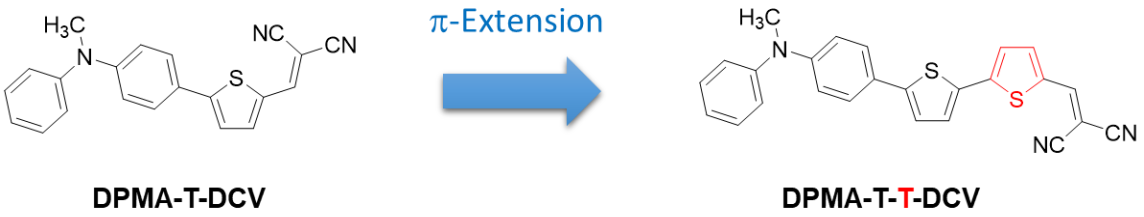

Chart 3.1. π-Extended **DPMA-T-T-DCV** as push-pull molecular donor for OPV.

3.2. Synthesis and characterization of DPMA-T-T-DCV

The push-pull molecule **DPMA-T-T-DCV** has been synthesized according to Scheme 3.1 by Illia Lenko during his Master Internship at MOLTECH-Anjou. The experimental procedures are described in the experimental part as well as analytical data on **DPMA-T-T-DCV** obtained from ^{1}H NMR, infrared spectroscopy and mass spectrometry, confirming its structure.

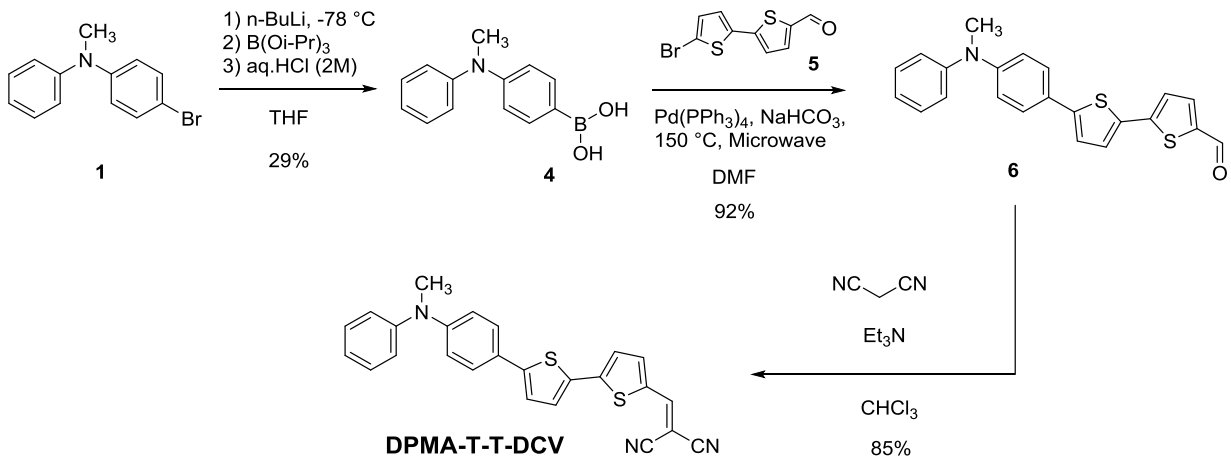

Scheme 3.1. Synthesis of **DPMA-T-T-DCV**

3.2.1. Crystalline structure of DPMA-T-T-DCV

Single crystals were grown by slow evaporation of a solution of **DPMA-T-T-DCV** in a mixture of chloroform and methanol. X-ray diffraction analysis was carried out by Magali Allain, engineer at MOLTECH-Anjou. The molecular structure of **DPMA-T-T-DCV** is represented in Figure 3.1.

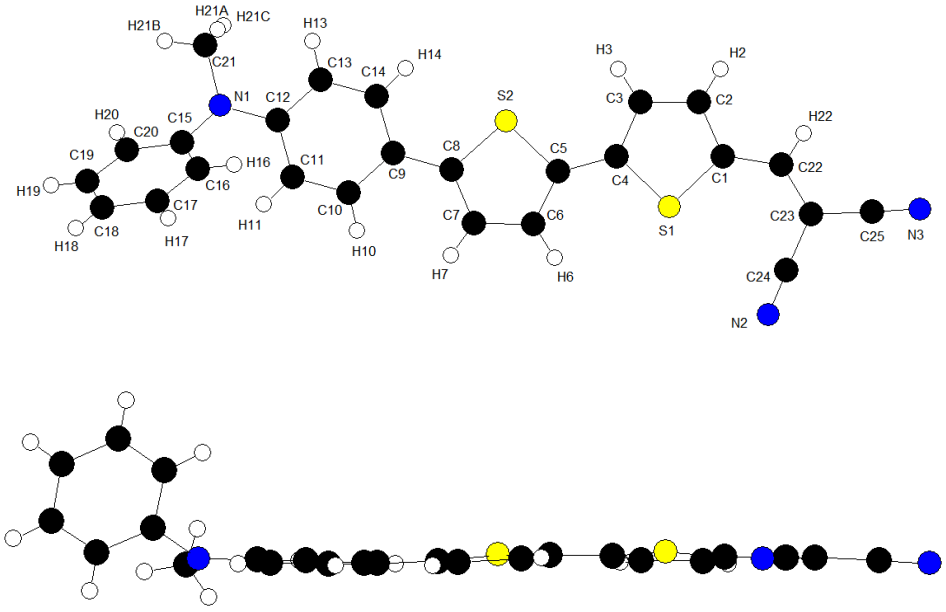

Figure 3.1. Molecular structure of **DPMA-T-T-DCV** obtained from X-ray analysis.

DPMA-T-T-DCV crystallizes in the monoclinic space group $P2_1/c$ with four independent molecules. The π-conjugated push-pull system extending from the *N*-methyl group to the DCV unit through the thiophene-based π-spacer is almost planar with dihedral angles of 1.49° (C14-C9-C8-C7),

3.88° (S2-C5-C4-S2) and 2.42° (S1-C1-C22-C23) between the phenyl and the neighboring thiophene, the two thiophene units and the thiophene and the DCV unit, respectively. On the other hand, the terminal phenyl ring of the DPMA group is out of the main plane of the molecule as demonstrated by a value of 42.96° measured for the C12-N1-C15-C16 dihedral angle. The bithiophene moiety adopts an *anti* conformation while the dicyanovinyl group is in *syn* conformation relative to the sulfur atom of the vicinal thiophene as usually reported in the literature.[3-5]

Figure 3.2 shows the molecular packing of **DPMA-T-T-DCV** and the existence of columns where molecules are regularly stacked with a parallel orientation and a head-to-tail arrangement as very often observed for D-π-A dipolar molecules.[6] Interestingly, this result differs from the co-facial arrangement observed for shorter analogue **DPMA-T-DCV** with only one thiophene unit.[1] Within the stack, short distances d_1 (3.60 Å) and d_2 (3.42 Å) are observed between two consecutive parallel median planes containing one molecule suggesting the existence of π–π stacking.

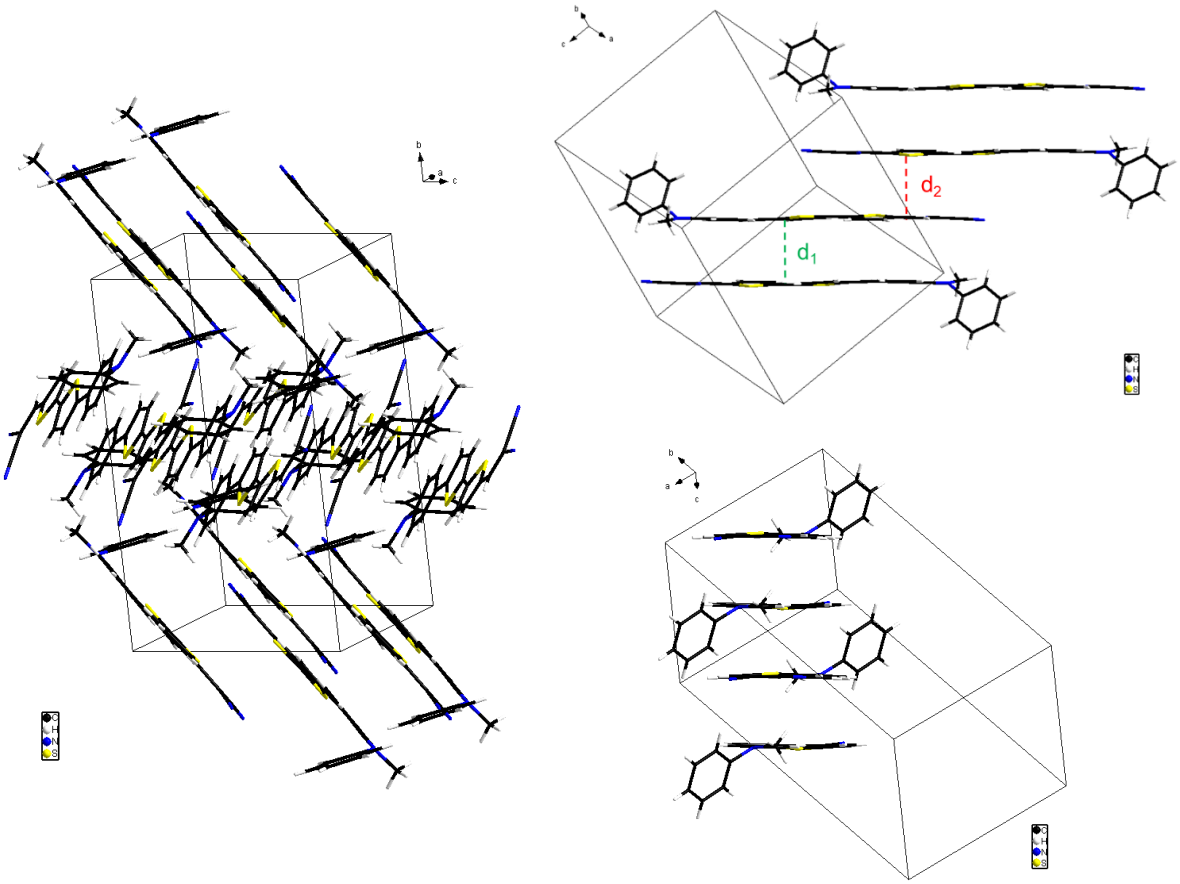

Figure 3.2. Left: Molecular packing of molecules **DPMA-T-T-DCV**. Right: Formation of columns of molecules with short intermolecular distances (only four molecules have been selected for clarity).

3.2.2. Optical properties in solution and as thin films

The UV-Vis spectrum of **DPMA-T-T-DCV** was recorded in diluted dichloromethane solution (*ca*. 10^{-5} M) and as thin films prepared by spin-casting a chloroform solution of **DPMA-T-T-DCV** on

clean glass substrates. The emission spectrum of **DPMA-T-T-DCV** in diluted dichloromethane (10^{-6} M) is also described in Figure 3.3. All optical data are summarized in Table 3.1.

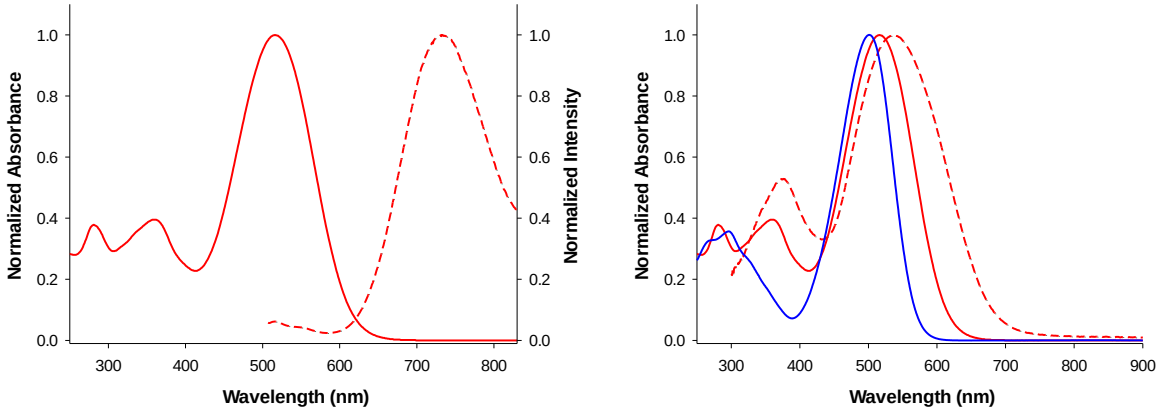

Figure 3.3. Left: Normalized absorption (solid red line) and emission (dashed red line) spectra of **DPMA-T-T-DCV** in CH_2Cl_2. Right: Normalized absorption spectra of **DPMA-T-T-DCV** in CH_2Cl_2 (solid red line) and as thin-film on glass (dashed red line) and reference **DPMA-T-T-DCV** (blue line) in CH_2Cl_2.

The absorption spectrum of **DPMA-T-T-DCV** in solution exhibits a main broad absorption band with a maximum at 516 nm attributed to an internal charge transfer (ICT) band. In solution, this compound shows also a broad emission band with a maximum at 734 nm in the red region, giving rise to a quite large Stokes shift of 0.71 eV (5726 cm^{-1}) in agreement with a significant change in geometry between the ground and excited states. Due to the limitation of the spectrofluorimeter (Shimadzu RF-6000) that does not allow to record data beyond 830 nm, it has not been possible to determine the photoluminescence quantum yield (Φ_f) of **DPMA-T-T-DCV**. However, by integrating the emission signal until 830 nm and using rhodamine B as standard (Φ_f = 50% in ethanol), a minimum value of *ca.* 13% was measured which suggests a slightly higher value compared to the one of **DPMA-T-DCV** (see chapter 2, Φ_f = 7%). The HOMO-LUMO gap (ΔE^{opt}) in solution was estimated to 2.0 eV as calculated from the intercept between absorption and emission spectra at 620 nm.

As expected, the introduction of an additional thiophene unit leads to a bathochromic shift of λ_{max} as compared to **DPMA-T-DCV** (λ_{max} = 498 nm) (Figure 3.3, right). Homogeneous thin-films of **DPMA-T-T-DCV** were deposited by solution process on clean glass substrates. The corresponding absorption spectrum is broader and 20 nm bathochromically shifted compared to its spectrum in solution, suggesting the existence of molecular π-π interactions in the solid-state. The optical bandgap E_g^{opt} of the thin-film was estimated from the onset of absorption at 702 nm, giving a value of 1.76 eV. Importantly, in contrast to **DPMA-T-DCV**, the absorption spectra of thin films of **DPMA-T-T-DCV** do not evolve with time at 25 °C or after few minutes of thermal annealing at 80 °C. This result indicates the absence of reorganization of the materials hence leading to more stable thin films.

Table 3.1. Optical data of **DPMA-T-T-DCV** *vs* **DPMA-T-DCV** in solution and as thin film

Compd	solution				thin film	
	λ_{abs} (nm)	ΔE^{opt} (eV)	λ_{em} (nm)[a]	Φ_f (%)	λ_{abs} (nm)	E_g^{opt} (eV)
DPMA-T-T-DCV	516	2.00	734	> 13	536	1.76
DPMA-T-DCV	498	2.17	628	7	515 (pink) 610 (violet)	1.98 1.77

3.2.3. Electrochemical properties

The electrochemical properties of **DPMA-T-T-DCV** have been analyzed by cyclic voltammetry in dichloromethane in the presence of 0.10 M of tetrabutylammonium hexafluorophosphate (Bu_4NPF_6) as the supporting electrolyte and Pt as a working and counter electrodes. The cyclic voltammogram (CV) is shown in Figure 3.4 and the electrochemical data of **DPMA-T-T-DCV** together with those of **DPMA-T-DCV** for comparison, are summarized in Table 3.2.

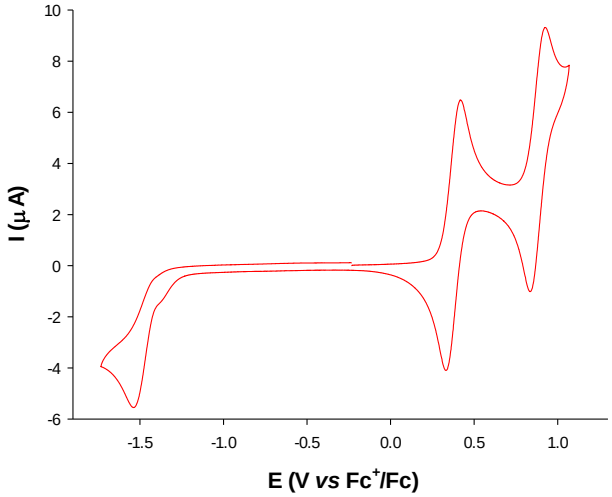

Figure 3.4. Cyclic voltammogram of **DPMA-T-T-DCV** (1 mM) in 0.1 M *n*-Bu_4NPF_6/CH_2Cl_2 using a Pt working electrode (∅ = 1 mm), scan rate 100 mV/s.

The CV of **DPMA-T-T-DCV** shows two successive fully reversible oxidation waves peaking at E_{pa}^1 = 0.42 V and E_{pa}^2 = 0.93 V corresponding to the formation of stable radical cation and dication species, respectively. In the negative potentials, an irreversible reduction wave at E_{pc} = -1.54 V was observed, which is assigned to the reduction of the DCV group.[7] Compared to compound **DPMA-T-DCV** (Chapter 2, section 2.2.3), the addition of a thiophene π-spacer leads to a significant increase of the reversibility of the first oxidation wave associated to a stabilization of the radical cation and a 170 mV negative shift of the related peak potential. HOMO and LUMO energy levels of this compound were calculated from the onset of first oxidation and reduction waves, respectively. As expected for a

more π-extended system, the HOMO level of **DPMA-T-T-DCV** is destabilized whereas its LUMO level is stabilized affording a reduced electrochemical HOMO-LUMO gap (ΔE^{elec} = 1.66 eV) compared to **DPMA-T-DCV** (ΔE^{elec} = 1.92 eV).

Table 3.2. Cyclic voltammetric data of **DPMA-T-T-DCV** and **DPMA-T-DCV**, potential values are given *vs* ferrocene/ferrocenium (Fc^+/Fc).

Compd	E_{pc} [V]	E_{pa}^1 [V]	E_{pa}^2 [V]	$E_{ox,onset}$ [V]	$E_{red,onset}$ [V]	E_{HOMO}[a] [eV]	E_{LUMO}[b] [eV]	ΔE^{elec} [eV]
DPMA-T-T-DCV	-1.54	0.42	0.93	0.29	-1.37	-5.39	-3.73	1.66
DPMA-T-DCV	-1.57	0.59 irr.	-	0.46	-1.46	-5.56	-3.64	1.92

[a] E_{HOMO} *(eV) = - (*$E_{ox,onset}$ *vs* Fc/Fc^+ *+ 5.1),* [b] E_{LUMO} *(eV) = - (*$E_{red,onset}$ *vs* Fc/Fc^+ *+ 5.1).*

3.2.4. Energetic Diagram from PYSA and E_g^{opt}

The ionisation potential (assimilated to the energy the HOMO level) of the push-pull molecule **DPMA-T-T-DCV** in the solid state was determined by using photoemission yield spectroscopy in air (PYSA) measurements on thin-films prepared from chloroform solutions spun-casted on ITO substrates. The PYSA spectrum was recorded from 4.2 eV to 6.2 eV (Figure 3.5.a).

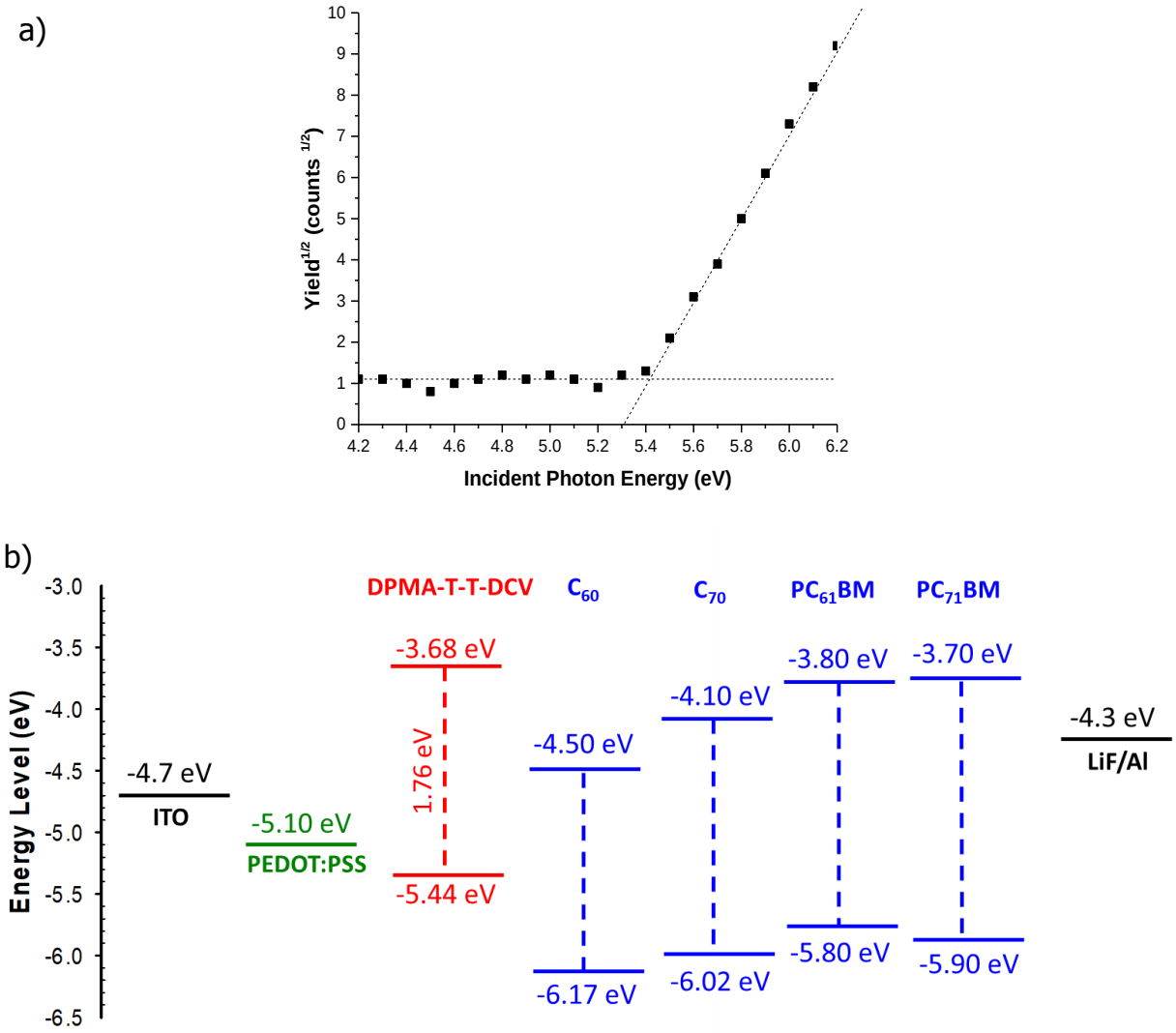

Figure 3.5. **a)** PYSA of **DPMA-T-T-DCV** and **b)** energy level diagram of related OSCs with different fullerene acceptors.

A value of -5.44 eV was obtained for the HOMO level which, combined with the E_g^{opt} value, gave an energy level of -3.68 eV for the LUMO of **DPMA-T-T-DCV**. As illustrated on the energetic diagram (Figure 3.5.b), the shallowest LUMO level of **DPMA-T-T-DCV** matches well with those of fullerene acceptors which can be used as the complementary accepting material in photovoltaic cells. In addition the HOMO level of **DPMA-T-T-DCV** is relatively close to the level of PEDOT-PSS favoring holes extraction.

3.3. Organic photovoltaic cells

The photovoltaic potential of **DPMA-T-T-DCV** has been investigated using different types of device architectures such as conventional bi-layer OSCs with C_{60} or C_{70} as acceptor and solution or vacuum-processed BHJ OSCs using the soluble derivatives $PC_{61}BM$ or $PC_{71}BM$ and C_{60} respectively. These devices have been optimized as described in sections 3.2.1, 3.2.2 and 3.2.3.

3.3.1 Conventional bi-layer organic solar cells

As in Chapter 2, bi-layer OSCs with the following conventional architecture ITO/PEDOT:PSS/**DPMA-T-T-DCV**/C_{60} or C_{70} (30 nm)/Al (100 nm) have been fabricated and optimized by varying the thickness of the **DPMA-T-T-DCV** layer and making thermal annealing treatment of the resulting devices. The ITO substrates coated by a PEDOT:PSS layer were prepared as in Chapter 2 (see also experimental procedure) and put inside the glove box. Then a donor layer was deposited by spin-casting a solution of **DPMA-T-T-DCV** (10 mg/mL in $CHCl_3$) with different speed rates giving rise to different thicknesses. C_{60} or C_{70} was deposited by vacuum evaporation (30 nm of thickness) with an evaporation rate of ~1.5 Å/s. Next, an Al (100 nm) electrode was thermally deposited on the active layer at a vacuum of 10^{-7} mbar and then all devices were characterized inside the glove box under N_2.

In the case of C_{60}, the PV performance were optimized by controlling the thickness of the donor thin-film using speed rates of 2000, 4000 or 6000 rpm. As-prepared OSCs gave very low PCE around ~ 0.2-0.5% and further thermal treatment of the OSCs, typically for *ca*. 20-30 min at 80 °C, significantly increased the performance leading to better efficiencies. Note that for the optimization of the thermal annealing time, J-V measurements of the resulting OSCs were recorded after each 10 min at 80 °C by following the evolution of the power conversion efficiency.

Table 3.3. J-V characteristics of ITO/PEDOT:PSS/**DPMA-T-T-DCV** (*solution processed*)/C_{60}/Al after 20 min of thermal annealing at 80 °C.

Speed rate [rpm]	Photoactive Layer	Thickness of donor [nm]	J_{sc} [mA cm^{-2}]	V_{oc} [V]	FF [%]	PCE_{max} [%]	PCE_{ave} [%]	Cell nb
2000	**DPMA-T-T-DCV**/ C_{60}	48±2	6.27	0.63	41	1.63	1.50±0.04	4
4000		41±2	10.27	0.61	38	2.38	2.13±0.06	6
6000		32±2	7.14	0.59	43	1.85	1.59±0.06	5

The best PV performance were obtained with a speed rate of 4000 rpm and after thermal annealing of 20 min at 80 °C leading to the highest PCE of 2.38% associated to a J_{sc} of 10.27 mA cm^{-2},

a V_{oc} of 0.61 V and a FF of 35% (Table 3.3). By contrast with bi-layer OSCs prepared with **DPMA-T-DCV**, the ones derived from **DPMA-T-T-DCV** present the advantage to exhibit good J-V characteristics in the dark with a diode like behavior (Figure 3.7). This fact is maybe due to the more stable morphology of the donor layer of **DPMA-T-T-DCV** with time and upon thermal annealing which gives also more reproducible results.

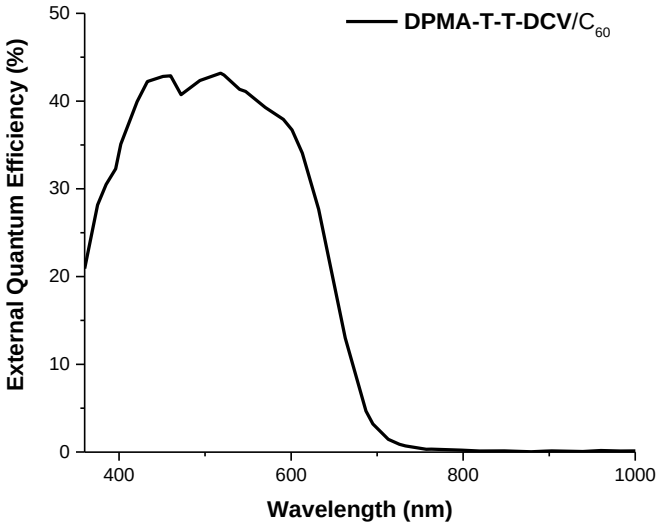

Figure 3.6. External quantum efficiency spectra of **DPMA-T-T-DCV**/C_{60} device (4000 rpm).

The external quantum efficiency (EQE) of the bi-layer OSC shows a broad band centered at *ca*. 518 nm with a maximum of 42% corresponding to the contribution of the push pull molecule to the photocurrent. Another peak is observed at *ca*. 451 nm which may correspond to the contribution of C_{60} as illustrated in Figure 3.6. The integration of the surface area below the EQE curve leads to a value of J_{sc} of 6.57 mA cm^{-2} that remains inferior to 10.27 mA cm^{-2}, value obtained from the J-V curves under illumination. This difference may be partly explained by the fact that the EQE spectrum is recorded beyond 360 nm hence neglecting the photocurrent produced from the UV light of the solar spectrum.

Then bi-layer OSCs of structure ITO/PEDOT:PSS/**DPMA-T-T-DCV**/C_{70} (30 nm)/Al (100 nm), were also prepared knowing that C_{70} absorbs better in the visible spectrum.

Table 3.4. J-V characteristics of ITO/PEDOT:PSS/**DPMA-T-T-DCV** (*solution-processed*)/C_{70}/Al.

Speed rate [rpm]	Photoactive Layer	Thickness of donor [nm]	J_{sc} [mA cm^{-2}]	V_{oc} [V]	FF [%]	PCE_{max} [%]	PCE_{ave} [%]	Cell nb
2000		44±2	5.63	0.48	32	0.91	0.83	6
4000	**DPMA-T-T-DCV**/C_{70}	39±3	7.78	0.49	32	1.24	1.10	6
6000		32±2	9.18	0.55	34	1.73	1.55	5

As shown in Table 3.4, the best PV performance were obtained with a speed rate of 6000 rpm for the deposition of the donor layer and after thermal annealing of 30 min at 80 °C leading to a PCE of 1.73% with a V_{oc} of 0.55 V, J_{sc} of 9.18 mA cm^{-2} and FF of 34%. Again, much better J-V curves in the dark were obtained as compared to **DPMA-T-DCV**. Surprisingly, slightly better PV performance were obtained with C_{60} compared to C_{70} although the latter should give higher J_{sc} (Figure 3.7). The same behaviour has been observed in the case of **DPMA-T-DCV**.

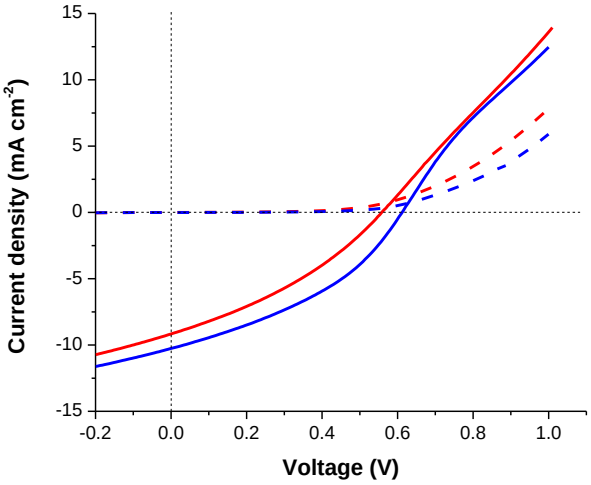

Figure 3.7. J-V curves of the best bi-layer OSCs fabricated from **DPMA-T-T-DCV** and C_{60} (blue) or C_{70} (red) under illumination (solid line) and in the dark (dashed line).

3.3.2. Solution-processed bulk heterojunction organic solar cells

BHJ OSCs using **DPMA-T-T-DCV** and soluble fullerene derivatives $PC_{61}BM$ or $PC_{71}BM$ were fabricated with the following architecture ITO/PEDOT:PSS/**DPMA-T-T-DCV**:PC_xBM (x = 61 or 71)/ LiF (1 nm)/Al (100 nm). For comparison with **DPMA-T-DCV**, a 1:2 D/A weight-to-weight ratio was selected for **DPMA-T-T-DCV**/PCxBM (3.33 mg:6.66 mg /mL of $CHCl_3$) and a speed rate of 1300 rpm for spin-casting. Table 3.5 shows the J-V characteristics of the BHJ OSCs.

Table 3.5. J-V characteristics of BHJ OSCs with **DPMA-T-T-DCV**:PC_XBM (x = 61 or 71).

Photoactive Layer	Speed rate [rpm]	D/A	Thickness [nm]	J_{sc} [mA cm^{-2}]	V_{oc} [V]	FF [%]	PCE_{max} [%]	PCE_{ave} [%]	Cell nb
DPMA-T-T-DCV:$PC_{61}BM$	1300	1:2	39±2	6.04	0.81	36	1.76	1.64±0.06	6
DPMA-T-T-DCV:$PC_{71}BM$			50±3	7.48	0.84	40	2.51	2.43±0.05	4

The best J-V curves are described in Figure 3.8. Contrary to bi-layer OSCs, the best PV performance for BHJ OSCs were obtained with the C_{70} derivative, namely $PC_{71}BM$. Thus a PCE_{max} value of 2.51% was reached for BHJ OSCs using $PC_{71}BM$ whereas $PC_{61}BM$ led to 1.76%. This decrease results mainly from the lower short-circuit current density J_{sc} of 6.04 mA cm^{-2} for $PC_{61}MB$-based devices compared to the ones measured for $PC_{71}BM$ (7.48 mA cm^{-2}). The V_{oc} is not very much affected by the nature of the fullerene whereas the fill factor FF is slightly better in the case of $PC_{71}BM$ (40% *vs* 36%). Compared to BHJ OSCs using **DPMA-T-DCV**/$PC_{71}BM$ (PCE_{max} = 2.70%) or **DPMA-T-DCV**/$PC_{61}BM$ (PCE_{max} = 1.96%) as photoactive layer (see Chapter 2), the introduction of an additional thiophene in **DPMA-T-T-DCV**, which was supposed to improve the absorption properties and hence the J_{sc} values, did not lead to enhanced PV performance. On the other hand, it is interesting to mention that a similar push-pull molecule as **DPMA-T-T-DCV**, with a TPA electron-donating group instead of DPMA has recently been reported in solution-processed BHJ OSCs of architecture ITO/PEDOT:PSS/Donor:$PC_{71}BM$ (1:2)/Ca/Al with a 10.4 mm^2 surface area affording a PCE of 1.8%.[8] This value is lower than the one we obtained with **DPMA-T-T-DCV** (PCE = 2.50%) with a higher surface area of 28 mm^2 showing also the interest of the DPMA electron-donating group in push-pull molecules as donors for OPV.

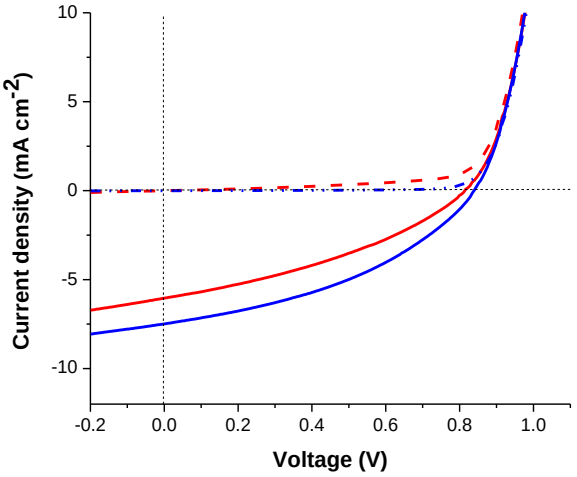

Figure 3.8. J-V curves of the best BHJ OSCs based on **DMPA-T-T-DCV** and $PC_{61}BM$ (red) or $PC_{71}BM$ (blue) under illumination (solid line) and in the dark (dashed line).

The EQE spectra of the best BHJ OSC derived from $PC_{71}BM$ and $PC_{61}BM$ show a broad band centered at *ca*. 540 nm with a maximum of 39% and 32%, respectively, corresponding to the contribution of the push pull molecule to the photocurrent (Figure 3.9). A sharp peak is observed at 396 nm and 421 nm which may correspond to the contribution of $PC_{71}BM$ (black curve) and $PC_{61}BM$ (red curve), respectively. The integration of the surface area below the EQE curves leads to a value of J_{sc} of 6.13 mA cm^{-2} for **DPMA-T-T-DCV**:$PC_{71}BM$ and 4.81 mA cm^{-2} for **DPMA-T-T-DCV**:$PC_{61}BM$ that remain inferior to the values measured from the J-V curves under illumination, respectively 7.48 mA cm^{-2} and 6.04 mA cm^{-2}.

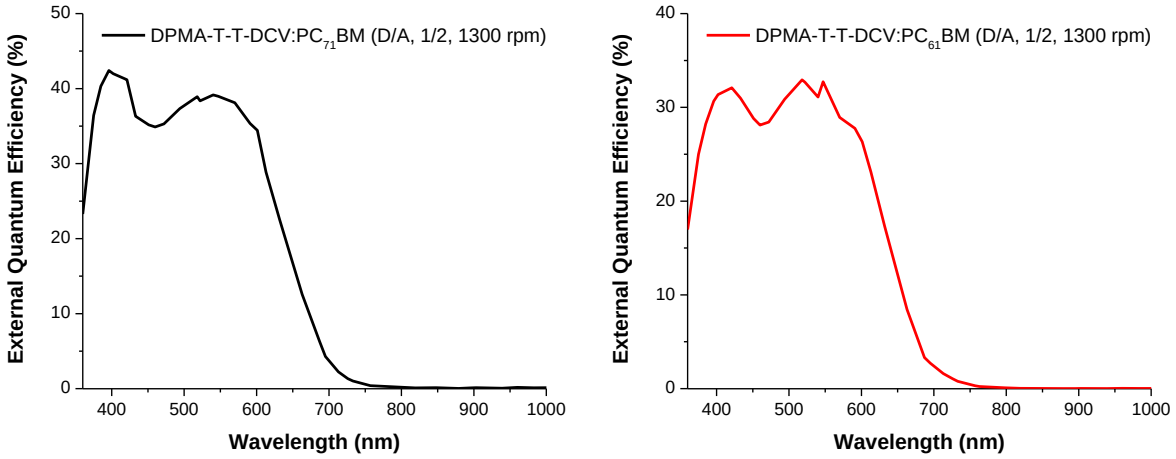

Figure 3.9. External quantum efficiency spectra of BHJ OSCs with **DPMA-T-T-DCV** and $PC_{71}BM$ (left) or $PC_{61}BM$ (right).

3.3.3. Vacuum-processed bulk heterojunction organic solar cells

As in Chapter 2, all vacuum-processed BHJ OSCs were elaborated by co-evaporation of **DPMA-T-T-DCV** and C_{60} with the following architecture: ITO/MoO_3/**DPMA-T-T-DCV**:C_{60} (v/v 1:2 ratio)/BCP/Al (Figure 3.10). The thickness of the photoactive layer was fixed at 70 nm, as in the case of the **DPMA-T-T-DCV**:C_{60} layer reported in Chapter 2 for which PV performance were relatively constant between 60 and 90 nm. The 70 nm thick photoactive layer corresponds to the concomitant deposition of 23 nm of **DPMA-T-T-DCV** and 47 nm of C_{60}.

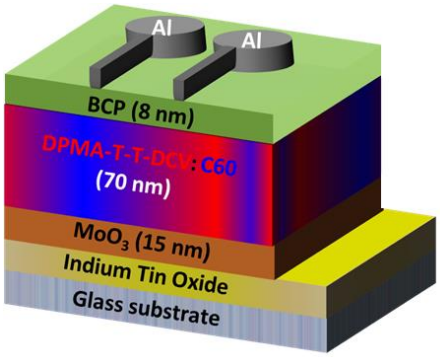

Figure 3.10. Architecture of vacuum-processed BHJ OSCs prepared by co-evaporation of **DPMA-T-T-DCV** and C_{60}.

Before vacuum deposition, the thermal properties of **DPMA-T-T-DCV** have been studied by thermogravimetric analysis (TGA) and differential scanning calorimetry (DSC) under an inert atmosphere of nitrogen (Figure 3.11).

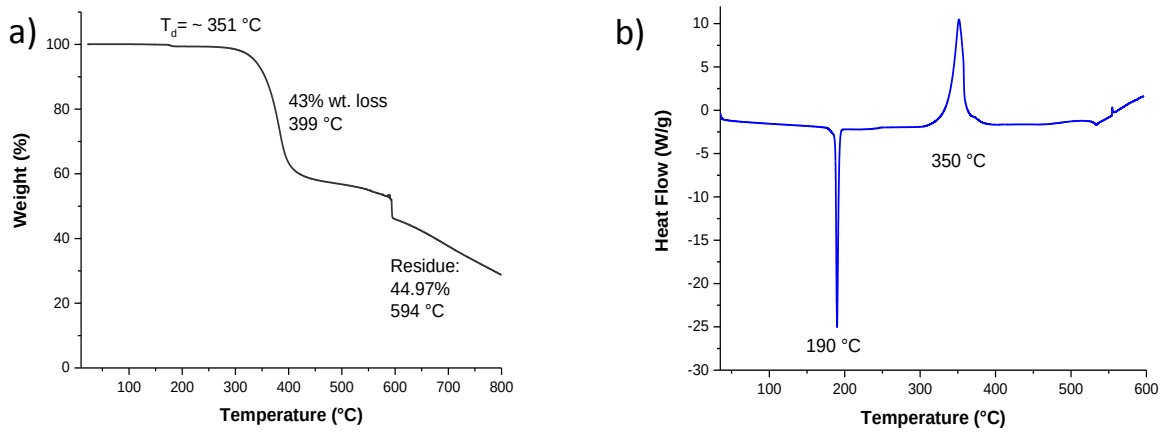

Figure 3.11. a) TGA thermogram and b) DSC curve of **DPMA-T-T-DCV** measured under N_2 (10 °C/min).

The TGA curve allowed us to determine the decomposition temperature T_d (at ~5% weight loss) at 351 °C, this high value indicating the good thermal stability of the push-pull molecule. The DSC analysis shows one sharp endothermic peak corresponding to the melting temperature (T_m) at 190 °C while the push-pull molecule starts to decompose far away from the T_m value above 350 °C as illustrated by the presence of an exothermic peak in the DSC curve. All these results suggest that **DPMA-T-T-DCV** can be deposited as thin films by thermal vacuum processing. Thus, as confirmed by the integrity of the absorption spectrum of the re-dissolved evaporated thin-film, **DPMA-T-T-DCV** was successfully deposited at ~125 °C under the pressure of 10^{-7} mbar within the thermal evaporator using a deposition rate of around 1 Å/s.

For the OSCs fabrication, cleaned ITO substrates were covered by an evaporated MoO_3 layer (15 nm) as hole transporting layer (HTL). **DPMA-T-T-DCV** and C_{60} were subsequently co-evaporated with a 1:2 v/v ratio to reach a 70 nm thickness that was monitored by a quartz crystal microbalance. Finaly BCP (8 nm), used as hole blocking layer, was evaporated and deposited onto the photoactive layer and, a thick contact layer of Al (100 nm) was used as top electrode (Figure 3.10). The photovoltaic parameters of these devices are shown in Table 3.6.

Table 3.6. Photovoltaic parameters of vacuum-processed BHJ OSCs.

Donor	Acceptor	v/v ratio	Thickness [nm]	J_{sc} [mA cm^{-2}]	V_{oc} [V]	FF [%]	PCE_{max} [%]	PCE_{ave} [%]	Cell nb
DPMA-T-T-DCV	C_{60}	1:2	70	8.39	0.69	52	3.01	2.83±0.10	6
DPMA-T-DCV	C_{60}	1:2	70	15.33	0.76	36	4.24	3.69±0.45	5

As for **DPMA-T-DCV**, the performance of the OSCs based on **DPMA-T-T-DCV** have been significantly improved by using co-evaporation. In these conditions, a PCE_{max} value of 3.01% has been measured with a V_{oc} of 0. 69 V, a J_{sc} of 8.39 mA cm^{-2} and a FF of 52% (Figure 3.12). The relatively low

value of V_{oc} compared to that of **DPMA-T-DCV** is in agreement with the smaller difference HOMO (**DPMA-T-T-DCV**) – LUMO (C_{60}). The use of co-evaporation leads to a higher FF value compared to solution process while this value for **DPMA-T-T-DCV** (52%) is higher than the one obtained for **DPMA-T-DCV** (36%). This higher FF may result from better hole transport properties and hence to a better balanced charge mobilities with C_{60}. In addition, the average PCE value of 2.83% calculated from 6 cells shows a quite good homogeneity of the performance.

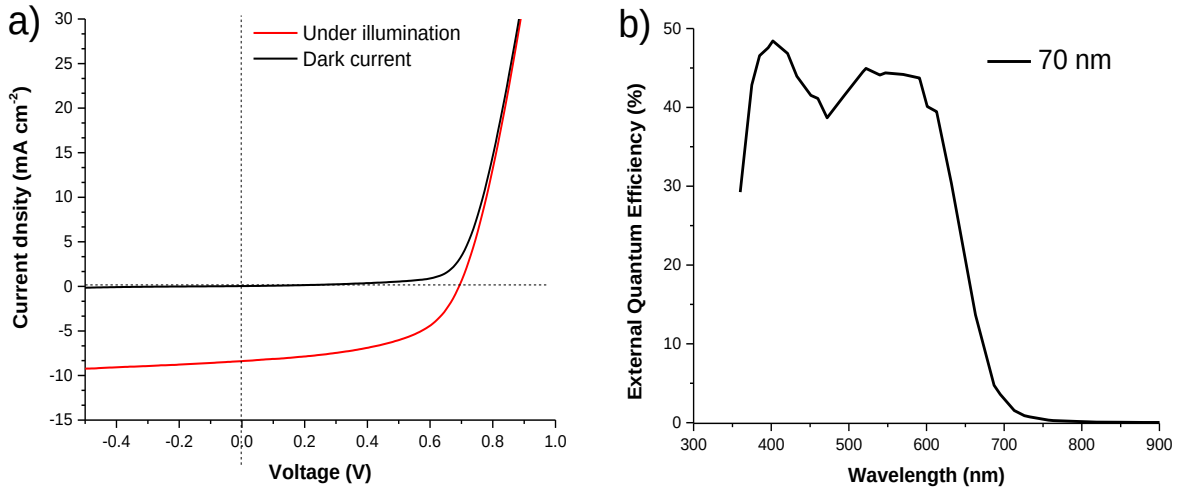

Figure 3.12. a) J-V curves of the best vacuum-processed BHJ OSCs based on a co-evaporated **DMPA-T-T-DCV**:C_{60} (1:2, v/v) photoactive layer under illumination and in the dark. b) Corresponding EQE spectrum.

The EQE spectrum shows a broad band centered at *ca*. 564 nm with a maximum of *ca*. 44% corresponding to the contribution of the push-pull molecule while the integration of the curve leads to a calculated J_{sc} values of *ca*. 7.25 mA cm^{-2} a value which is in full agreement with the value of 8.39 mA cm^{-2} recorded on the J-V curve under illumination (Figure 3.12).

Conclusion

The new π-extended push-pull molecule **DPMA-T-T-DCV** has been investigated as molecular donor in OSCs. This compound has been fully characterized and various device architectures such as bi-layer and solution- or vacuum-processed OSCs, have been optimized.

Compared to **DPMA-T-DCV**, the addition of one more thiophene unit within the π-spacer leads to a bathochromic shift of the absorption and emission bands in solution. The absorption spectrum of a thin-film of **DPMA-T-T-DCV** is slightly red-shifted indicative of intermolecular π-π interactions. Interestingly, the X-ray analysis of single crystals of **DPMA-T-T-DCV** evidences the presence of π-π intermolecular interactions. In strong contrast with **DPMA-T-DCV**, thin films of **DPMA-T-T-DCV** are

not subject to morphological and optical changes with time at 25 °C or upon thermal annealing at 80 °C. Thus these thin-films are more stable allowing for more reproducible results in bilayer-OSCs. The performance of the latter were systematically improved after thermal annealing at 80 °C of the completed devices, presumably due to an interdifusion of the donor and the acceptor layer leading to a BHJ at the donor-acceptor interface, although further analysis are required to confirm this point. Conventional bi-layer OSCs based on **DPMA-T-T-DCV** and C_{60} or C_{70} as acceptors led to PCEs of *ca*. 2.4% and 1.7%, respectively.

Finally, vacuum-processed BHJ OSCs prepared by co-evaporation of **DPMA-T-T-DCV** and C_{60} have led to PCE up to 3% while solution-processed BHJ OSCs gave lower values of *ca*. 2.5% with $PC_{71}BM$ and 1.8% with $PC_{61}BM$. As perspectives of this work, the fabrication of all vacuum-processed BHJ OSCs using C_{70} instead of C_{60} could be of high interest.

References:

1. Y. Jiang, C. Cabanetos, M. Allain, P. Liu and J. Roncali, *Journal of Materials Chemistry C*, 2015, **3**, 5145-5151.
2. D. Alberga, I. Ciofini, G. F. Mangiatordi, A. Pedone, G. Lattanzi, J. Roncali and C. Adamo, *Chemistry of Materials*, 2016, **29**, 673-681.
3. R. Fitzner, E. Reinold, A. Mishra, E. Mena- Osteritz, H. Ziehlke, C. Körner, K. Leo, M. Riede, M. Weil and O. Tsaryova, *Advanced Functional Materials*, 2011, **21**, 897-910.
4. A. Leliège, J. Grolleau, M. Allain, P. Blanchard, D. Demeter, T. Rousseau and J. Roncali, *Chemistry–A European Journal*, 2013, **19**, 9948-9960.
5. F. Baert, C. Cabanetos, A. Leliege, E. Kirchner, O. Segut, O. Alévêque, M. Allain, G. Seo, S. Jung and D. Tondelier, *Journal of Materials Chemistry C*, 2015, **3**, 390-398.
6. H. Bürckstümmer, E. Tulyakova, M. Deppisch, M. Lenze, N. Kronenberg, M. Gsänger, M. Stolte, K. Meerholz and F. Würthner, *Angew. Chem., Int. Ed*, 2011, **50**, 11628-11632.
7. S. Haid, A. Mishra, C. Uhrich, M. Pfeiffer and P. Bäuerle, *Chemistry of Materials*, 2011, **23**, 4435-4444.
8. O. V. Kozlov, X. Liu, Y. N. Luponosov, A. N. Solodukhin, V. Y. Toropynina, J. Min, M. I. Buzin, S. M. Peregudova, C. J. Brabec and S. A. Ponomarenko, *The Journal of Physical Chemistry C*, 2017, **121**, 6424-6435.

Chapter 4:
Carbazole and selenophene analogues of DPMA-T-DCV for OPV

4.1. Introduction

Minimal structural modifications of **DPMA-T-DCV** were investigated in this chapter. As described in Chart 4.1, the **DPMA** electron-donating group was first rigidified by a covalent bridge leading to the formation of a 9-methylcarbazole moiety (**MeCz**), affording the new push-pull molecule **MeCz-T-DCV**. Secondly, the thiophene ring of **DPMA-T-DCV** and **MeCz-T-DCV** was replaced by a selenophene ring. The effect of the rigification and the exchange from Sulphur to Selenium on the electronic and structural properties of the three new molecular donors has been analyzed while their PV potential has been assessed.

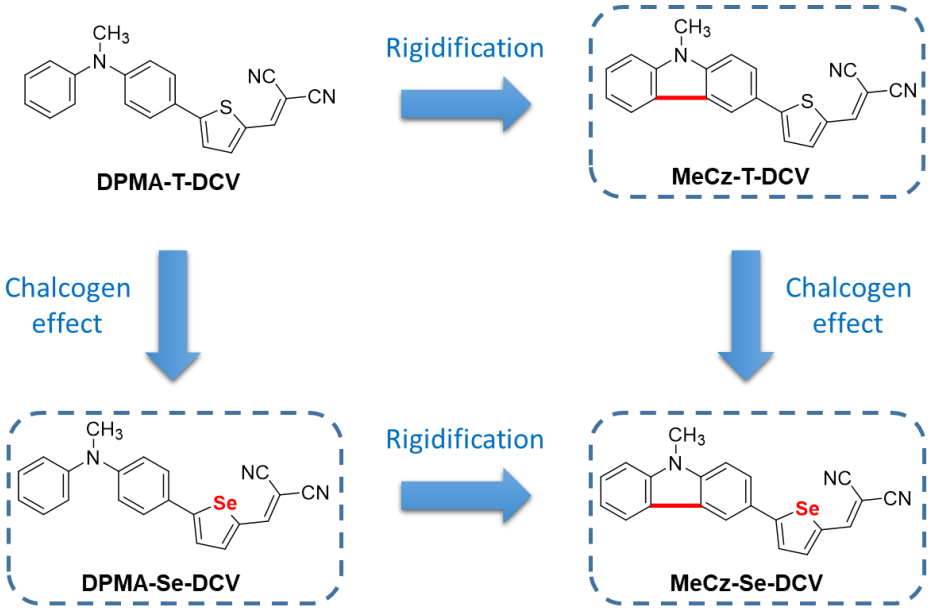

Chart 4.1. Rigidification and variation of the nature of the chalcogenophene ring of **DPMA-T-DCV**.

Carbazole and its derivatives are widely used as hole-transporting materials for DSSCs or hybrid perovskite solar cells [1, 2] or as a source for host materials and emitters.[3, 4] Carbazole is an excellent hole-transporter.[5] In addition, the HOMO level of a carbazole-based donor is in general slightly lower than that of a triphenylamine-based donor,[6, 7] thus a higher open-circuit voltage V_{oc} can be expected for corresponding OSCs.

On the other hand, the replacement of thiophene ring(s) by selenophene ones in π-conjugated oligothiophenes is known to lead to a bathochromic shift of the UV-vis spectrum associated with an increased of absorption coefficient.[8] Selenophene-based π-conjugated systems can also lead to more performant OSCs as compared to their thiophene analogues.[9] More recently, our group has shown that the selenophene analogue of **TPA-T-DCV** (Chapter 2) was efficiently used as donor in BHJ OSCs with $PC_{61}BM$ giving a slightly higher PCE of 3.3% *vs*. 3.0% for the thiophene derivative.[10]

In this context, the three new carbazole and/or selenophene analogues of **DPMA-T-DCV** could represent promising push-push molecular donors for OPV.

4.2. Synthesis of the four targeted push-pull molecules

The three new push-pull derivatives **DPMA-Se-DCV**, **MeCz-T-DCV** and **MeCz-Se-DCV** have been synthesized by Dr. Pierre Josse as described in Schemes 4.1 and 4.2.

4.2.1. Synthesis of DPMA-Se-DCV

DPMA-Se-DCV has been prepared starting from 4-bromo-*N*-methyl-*N*-phenylaniline **1** following the same strategy developed for the thiophene analogue **DPMA-T-DCV** as described in Chapter 2. A Stille cross-coupling of **1** with the commercially available tributyl(selenophen-2-yl)stannane in toluene with tetrakis(triphenylphosphine)palladium(0) as catalyst, gave compound **7** in 50% yield. A Vilsmeier formylation led to the selective formation of carboxaldehyde **8** in 55% yield. The target compound **DPMA-Se-DCV** was finally obtained in 96% yield by Knoevenagel condensation between malononitrile and **8**. Note that during the course of this project, **DPMA-T-DCV** has been re-synthesized through a shorter and cleaner route implying a direct heteroarylation between **1** and thiophene-2-carbaldehyde leading to the intermediate **3** subsequently engaged in a Knoevenagel condensation with malononitrile.

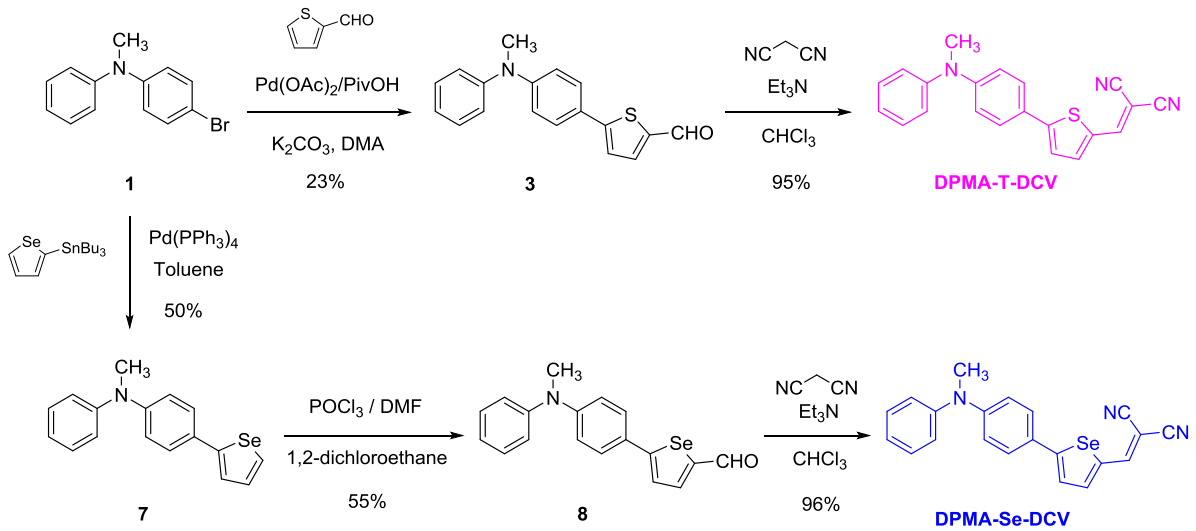

Scheme 4.1. Synthesis of DPMA-based push-pull molecules with thiophene or selenophene π-spacers.

4.2.2. Synthesis of Carbazole derivatives

The synthesis of carbazole derivatives **MeCz-T-DCV** and **MeCz-Se-DCV** has been carried out by starting from 3-bromo-9-methyl-9H-carbazole **9**. After a Stille cross coupling with tributyl(selenophen-2-yl)stannane, compound **11** was obtained in 45% yield and further formylated to give aldehyde **12** which was subjected to a Knoevenagel condensation with malononitrile to give **MeCz-Se-DCV** in 94% yield. On the other hand, **MeCz-T-DCV** was obtained in 60% yield after a Knoevenagel condensation between malononitrile and the intermediate aldehyde **10** which was prepared by direct heteroarylation between the starting material **9** and thiophene-2-carbaldehyde.

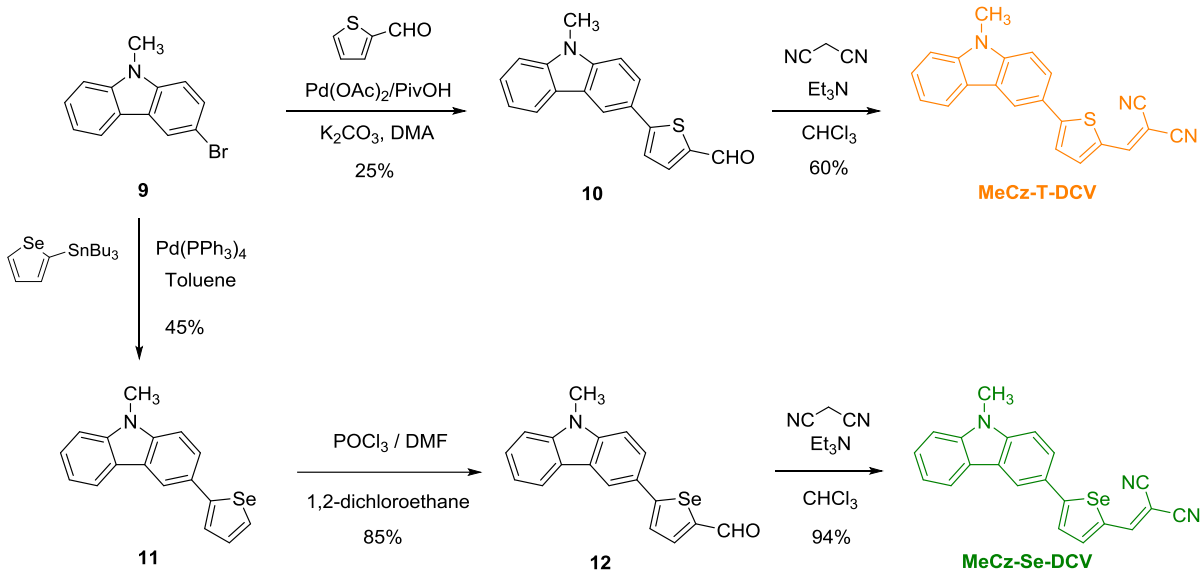

Scheme 4.2. Synthesis of carbazlole-based push-pull molecules with thiophene or selenophene π-spacers.

4.2.3. Crystalline structures of carbazole derivatives

Single crystals were grown by slow evaporation of a solution of **MeCz-T-DCV** or **MeCz-Se-DCV** in toluene and analyzed by X-ray diffraction. The molecular structures of **MeCz-T-DCV** and **MeCz-Se-DCV** are represented in Figure 4.1.

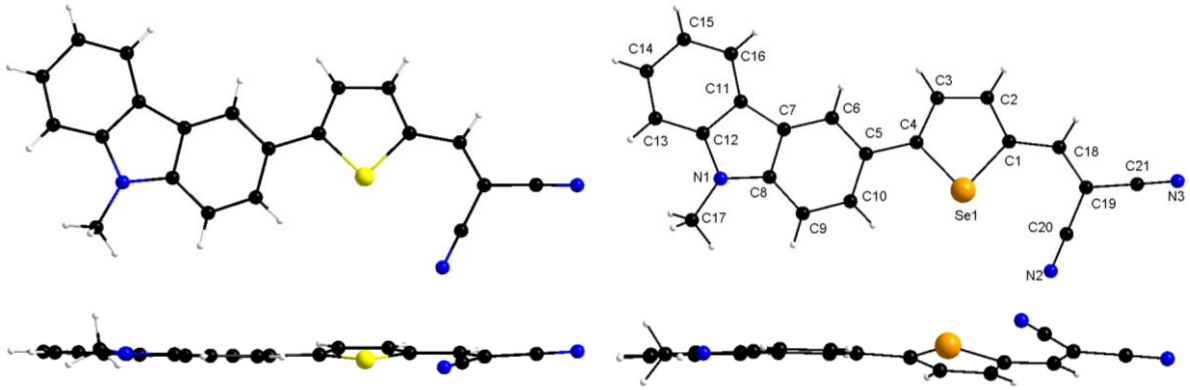

Figure 4.1. Molecular structures of **MeCz-T-DCV** and **MeCz-Se-DCV** obtained from X-ray analysis.

Whereas the thiophenic analogue crystallizes in a monoclinic system within a P 21/c space group with four independent molecules in the unit cell, the crystalline structure of the selenophene derivative belongs to a triclinic system with a P-1 space group and two independent molecules by unit cell. In both cases, the DCV unit exhibits a *syn* conformation relative to the chalcogen atom as in the case of **DPMA-T-DCV**.[11] **MeCz-T-DCV** is almost planar with a slight torsion angle between the two planar MeCz and T-DCV moieties associated to the following dihedral angles C3-C4-C5-C6 = 8.75°, C3-C4-C5-C10 = 9.21° and S-C4-C5-C10 = 5.64°. For comparison, **MeCz-Se-DCV** is less planar with higher dihedral angles C3-C4-C5-C6 = 12.44°, C3-C4-C5-C10 = 14.09° and Se-C4-C5-C10 = 12.50°.

Molecules of **MeCz-Se-DCV** shows a brickwall packing where two neighbouring carbazole moieties adopt a face-to-face arrangement with a shortest intermolecular C-C distance of 3.52 Å (Figure 4.2, right). In the case of **MeCz-T-DCV**, molecules stack in the *c* direction with dipoles oriented in the same direction. Within this stack, neighbouring carbazole units are relatively close with a shortest intermolecular C-C distance of 3.58 Å (Figure 4.2, left) while contacts are possible between two thiophenic carbon atoms of two different stacks, as shown by the existence of a short lateral intermolecular C-C distance of 3.45 Å.

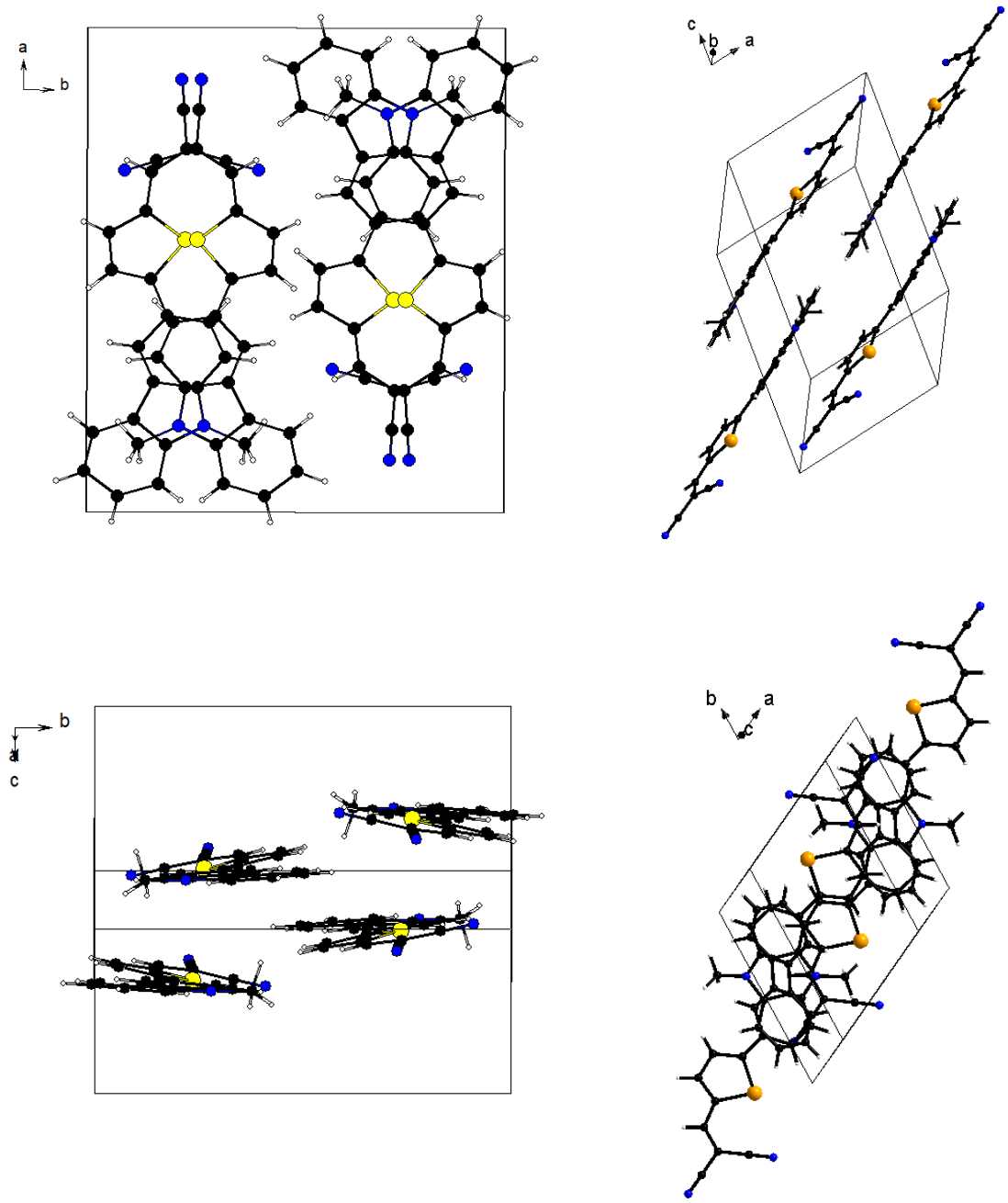

Figure 4.2. Molecular packing of **MeCz-T-DCV** (left) and **MeCz-Se-DCV** (right).

4.3. Optical and electrochemical properties

The optical properties of the targeted molecules were examined by UV-Vis spectroscopy in solution (CH_2Cl_2) and as thin films on glass. The electrochemical properties were investigated in solution by cyclic voltammetry allowing us to determine the frontier molecular orbital (FMO) energies to assess the potential of these materials as donors in OSCs based on fullerene acceptors.

4.3.1. Absorption and emission spectroscopy in solution

The optical properties of the D-π-A push-pull molecules were investigated by UV-Vis and emission spectroscopy in diluted dichloromethane solutions, *ca.* 10^{-5} and 10^{-6} M, respectively (Figure 4.3). All optical data are gathered in Table 4.1.

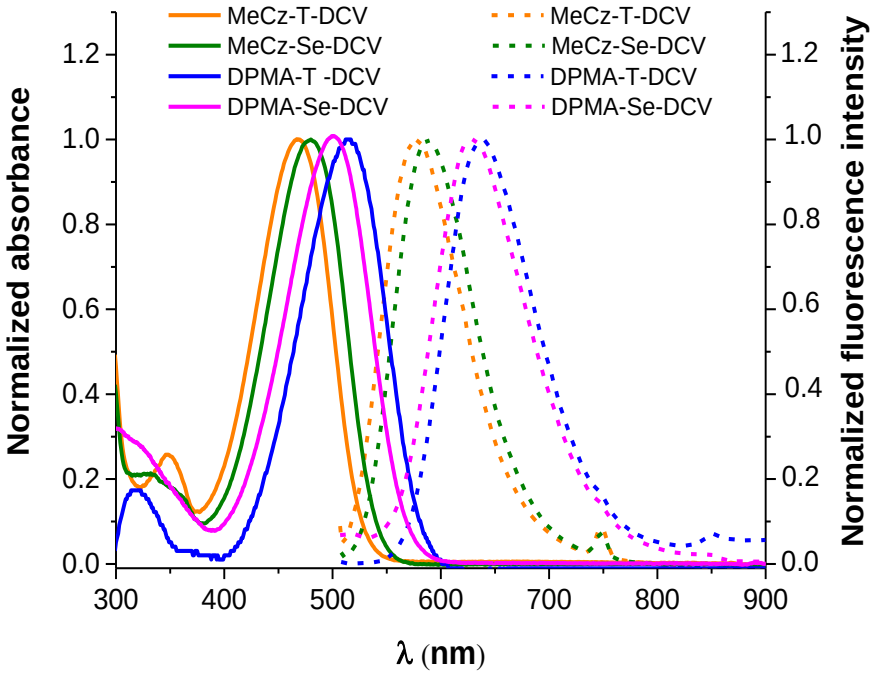

Figure 4.3. Normalized absorption (solid line) and emission (dash line) spectra of **MeCz-T-DCV** (brown), **MeCz-Se-DCV** (green), **DPMA-T-DCV** (pink) and **DPMA-Se-DCV** (blue) in CH_2Cl_2.

The normalized absorption spectra of all compounds show a broad absorption band in the visible spectrum between 400 and 600 nm. As usually observed for D-π-A push-pull molecules,[12] this intense band, with similar molecular extinction coefficients (ε) of *ca.* 40000 M^{-1} cm^{-1} for all compounds, is related to an internal charge transfer (ICT) from the electron-rich D unit to the electron-withdrawing A unit. Replacement of the DPMA by MeCz, while using the thiophene π-spacer for both molecules, leads to a hypsochromic shift of λ_{max} from 498 to 467 nm. This result shows that DPMA is a stronger electron-donating group than the *N*-methylcarbazole one. On the other hand, the replacement of the thiophene spacer by selenophene, while using the same electron-donating group, leads to a higher π-conjugation as evidenced by the bathochromic shifts of 16 nm and 13 nm observed in the DPMA and MeCz series, respectively.

Table 4.1. Optical data of titled compounds in CH_2Cl_2.

Compound[2]	λ_{max} [nm]	λ_{em} [nm][a]	Φ_f (%)[a]	ε [M^{-1} cm^{-1}]	ΔE^{opt} [eV][b]
MeCz-T-DCV	467	576	2	39900	2.37
MeCz-Se-DCV	480	588	2	40100	2.32
DPMA-T-DCV	498	628	7	44100	2.20
DPMA-Se-DCV	514	638	6	40400	2.15

[a] λ_{exc} = *500 nm, Standard : Rhodamine B in Ethanol* (Φ_f = *0.50),* [b] ΔE^{opt} *values were determined at the intercept between absorption and emission spectra.*

All compounds exhibit photoluminescence properties in solution after excitation at 500 nm leading to the presence of a broad emission band with maxima close to *ca*. 580-590 nm and 630-640 nm for the carbazole and DPMA derivatives, respectively. The corresponding fluorescence emission quantum yields (Φ_f) have been measured using Rhodamine B as reference giving values of *ca*. 2% for the carbazole series while a slight increase up to 7% is observed for the DPMA derivatives.

The HOMO-LUMO gap of the titled molecules has been estimated by measuring the wavelength corresponding to the intercept of the absorption and emission spectra which is expected to be close to the $\lambda_{0\text{-}0}$ electronic transition and by using the following equation $\Delta E_{HOMO\text{-}LUMO}$ (eV) ≈ ΔE^{opt} (eV) = 1240 / λ (nm) for the conversion in eV. Combining the stronger electron-donating effect of DPMA and the enhanced π-electronic delocalization associated to selenophene, compound **DPMA-Se-DCV** exhibits the highest λ_{max} value of 514 nm together with the lowest HOMO-LUMO gap estimated to 2.15 eV. Thus, considering the good photovoltaic performance of **DPMA-T-DCV**, **DPMA-Se-DCV** appears as a promising candidate as donor material for OPV.

4.3.2. Characterization of electrochemical properties in solution

The electrochemical properties of the four push-pull molecules have been analyzed by cyclic voltammetry using 1 mM solution of compound dissolved in dichloromethane in the presence of in 0.10 M of tetrabutylammonium hexafluorophosphate (Bu_4NPF_6) as the supporting electrolyte and Pt as a working and counter electrodes. The electrochemical data are summarized in Table 4.2.

Table 4.2. Oxidation and reduction potentials with respect to the ferrocene/ferrocenium couple (Fc/Fc^+).

Compound	E_{pc} [V]	E_{pa} [V]	$E_{ox,onset}$ [V]	$E_{red,onset}$ [V]	E_{HOMO} [eV][a]	E_{LUMO} [eV][b]	ΔE^{elec} [eV]
MeCz-T-DCV	-1.58	0.83	0.70	-1.48	-5.80	-3.62	2.18
MeCz-Se-DCV	-1.55	0.81	0.67	-1.46	-5.77	-3.64	2.13
DPMA-T-DCV	-1.57	0.59	0.46	-1.46	-5.56	-3.64	1.92
DPMA-Se-DCV	-1.52	0.57	0.44	-1.43	-5.54	-3.67	1.87

[a] E_{HOMO} *(eV) = - (*$E_{ox,onset}$ *vs* Fc/Fc^+ *+ 5.1),* [b] E_{LUMO} *(eV) = - (*$E_{red,onset}$ *vs* Fc/Fc^+ *+ 5.1).*

4.3.2.1. Impact of the bridged MeCz group on electrochemical properties

In order to assess the impact of the bridged MeCz electron-donating group *vs* DPMA, Figure 4.4 compares the first cyclic voltammogram (CV) of **DPMA-T-DCV** and **MeCz-T-DCV**, having a thiophene π-linker on one hand, and **DPMA-Se-DCV** and **MeCz-Se-DCV** exhibiting a selenophene ring, on the other hand. The first CV trace of all compounds shows a quasi-reversible one-electron oxidation wave assigned to the formation of a radical cation. In the case of the thiophene series, the corresponding oxidation peak potential (E_{pa}) is observed at 0.59 V and 0.83 V *vs* Fc/Fc^+ for **DPMA-T-DCV** and **MeCz-T-DCV**, respectively. Thus the replacement of DPMA by MeCz leads to a significant positive shift of 240 mV of the oxidation wave in agreement with the lesser electron-donating properties of the MeCz unit concomitantly leading to a decrease of the HOMO level. The same positive shift is observed in the selenophene series for which **DPMA-Se-DCV** and **MeCz-Se-DCV** exhibit E_{pa} values of 0.57 V and 0.81 V, respectively, confirming the stronger electron-donating properties of DPMA.

In the negative potentials region, an irreversible reduction wave is observed with very close reduction peak potentials E_{pc} at – 1.57 V and – 1.58 V *vs* Fc/Fc^+ for **DPMA-T-DCV** and **MeCz-T-DCV** suggesting identical LUMO levels and the absence of effect of the electron-donating effect of the D unit on the LUMO orbital. As expected, **DPMA-Se-DCV** and **MeCz-Se-DCV** exhibit also irreversible reduction waves with close E_{pc} values of – 1.52 V and – 1.55 V, respectively. To summarize, the replacement of DPMA by MeCz mainly affects the HOMO levels of the resulting push-pull molecules.

The HOMO and LUMO levels of the push-pull molecules and the resulting electrochemical HOMO-LUMO gap (ΔE^{elec}) have been estimated by using the oxidation ($E_{ox,onset}$) and reduction ($E_{red,onset}$) onsets (Table 4.2). In agreement with the aforementioned results, whereas the LUMO levels are not or weakly affected, the replacement of DPMA by MeCz induces an increase of the ΔE^{elec} values of 0.26 eV for both thiophene and selenophene series, due to a stabilization of the HOMO levels. Thus lower HOMO-LUMO electrochemical gaps of 1.92 eV and 1.87 eV are measured for **DPMA-T-DCV** and **DPMA-Se-DCV**, respectively, while higher values up to 2.18 eV and 2.13 eV are obtained for **MeCz-T-DCV** and **MeCz-Se-DCV**. Note that although the values of electrochemical HOMO-LUMO gaps

(ΔE^{elec}) are slightly lower, they follow the same trend as the corresponding values (ΔE^{opt}) measured by absorption and emission spectroscopy.

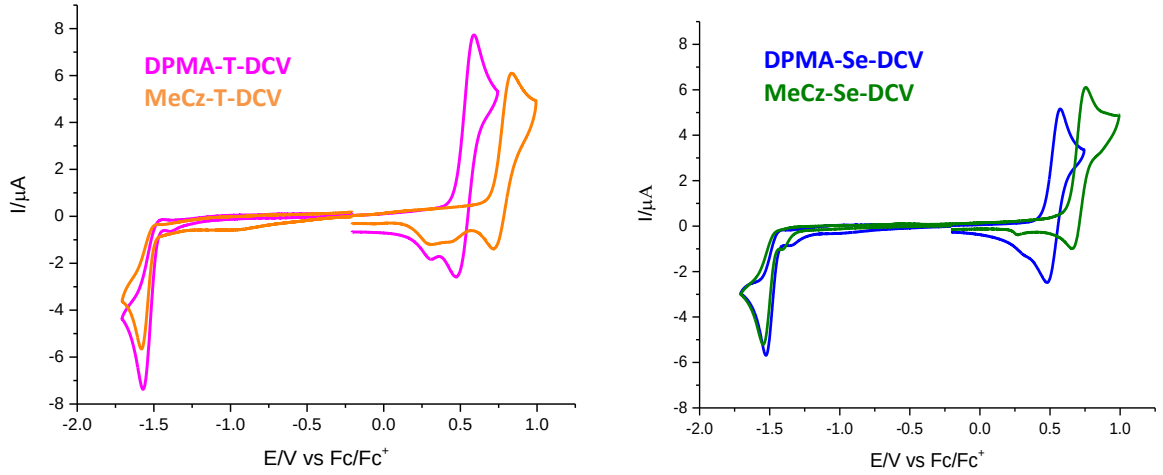

Figure 4.4. CVs of push-pull molecules highlighting the impact of the nature of the electron-donating group: 1 mM in 0.10 M Bu_4NPF_6/CH_2Cl_2, scan rate 100 mV s^{-1}, Pt working electrodes.

4.3.2.2. Impact of the selenophene *vs* thiophene π-spacer on electrochemical properties

Figure 4.5 shows the impact of the chalcogen atom of the five-membered ring on the electrochemical properties of titled push-pull molecules. In short, the use of a selenophene instead of a thiophene ring induces a slight negative shift of the oxidation wave (*ca*. - 20 mV) and a slight positive shift of the reduction wave (*ca*. 30-50 mV) resulting in an overall reduced HOMO-LUMO gap for selenophene-based push-pull molecules.

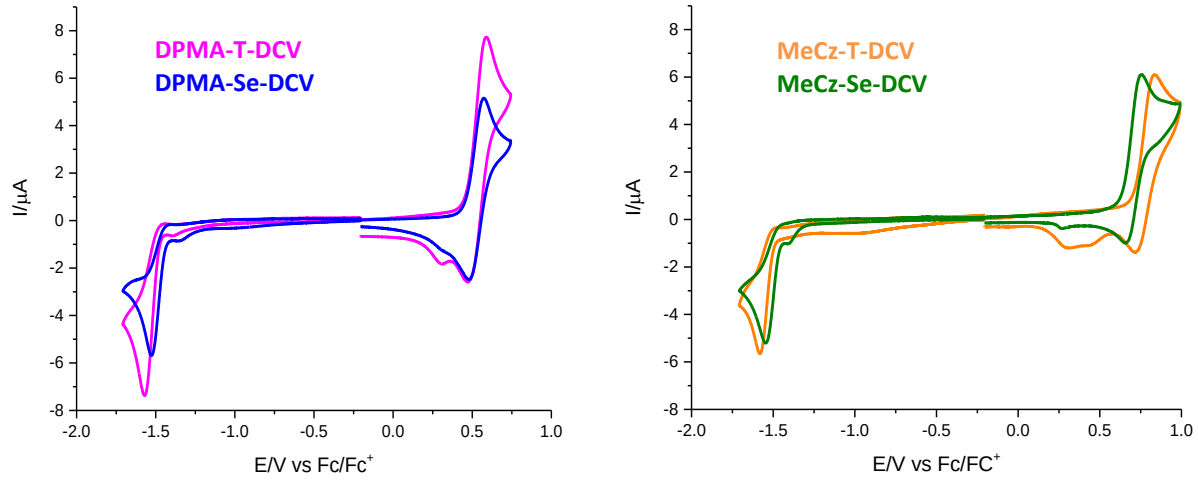

Figure 4.5. CVs of push-pull molecules highlighting the impact of the chalcogen atom: 1 mM in 0.10 M Bu_4NPF_6/CH_2Cl_2, scan rate 100 mV s^{-1}, Pt working electrodes.

Thus **DPMA-Se-DCV** with a selenophene π-spacer and a strong electron-donating group DPMA, shows the highest HOMO level together with the smallest electrochemical HOMO-LUMO gap in agreement with optical data. On the contrary, **MeCz-T-DCV** corresponds to the weakest molecular donor among titled compounds with the largest ΔE^{elec} value. The evolution of the donor strength and the HOMO-LUMO gap of the push-pull molecules is represented in Scheme 4.3.

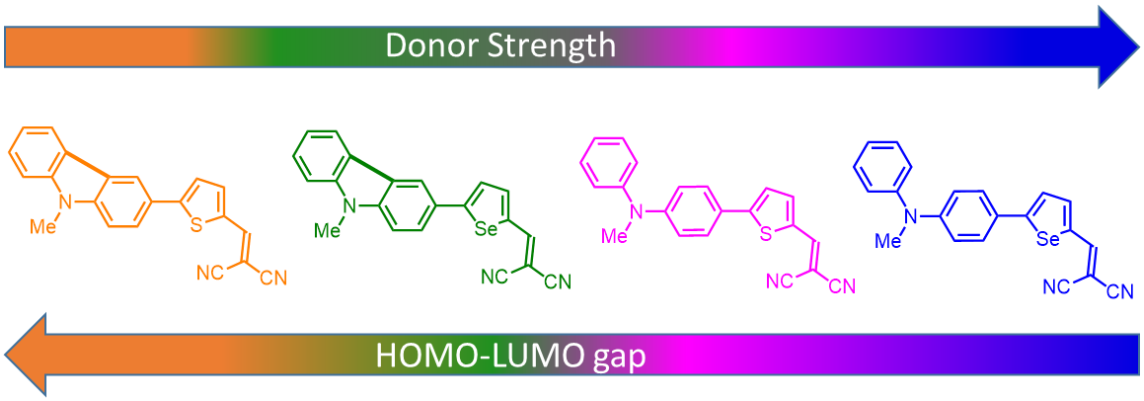

Scheme 4.3. Evolution of the donor ability and HOMO-LUMO gap of titled push-molecules.

4.3.3. Absorption properties of thin films

Homogeneous thin-films were prepared by spin-casting chloroform solutions of push-pull molecules (10 mg/mL, speed rate 1300 rpm during 60 sec.) on clean glass substrates. Figure 4.6 describes the normalized absorption spectra of the corresponding as-cast thin-films which are broader and slightly bathochromically shifted from 7 nm to 19 nm compared to the spectra in solution,

suggesting the existence of molecular π-π interactions in the solid-state. The optical bandgap E_g^{opt} of each thin-film was estimated from the onset of absorption at low energy giving decreasing values from 2.10 eV, 2.05 eV, 1.98 eV and 1.87 eV for **MeCz-T-DCV**, **MeCz-Se-DCV**, **DPMA-T-DCV** and **DPMA-Se-DCV** respectively, hence following the same trend as observed for the evolution of the HOMO-LUMO gap.

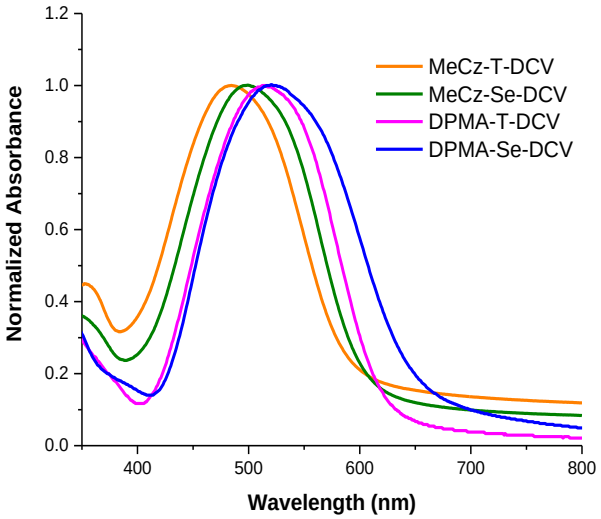

Compound	λ_{max} [nm]	E_g^{opt} [eV]
MeCz-T-DCV	484	2.10
MeCz-Se-DCV	499	2.05
DPMA-T-DCV	515	1.98
DPMA-Se-DCV	525	1.87

Figure 4.6. Normalized absorption spectra of thin-films of push pull molecules on glass substrates and related optical data.

Contrary to their MeCz push-pull analogues which remain unaffected, the optical properties of thin-films of **DPMA-Se-DCV** are subject to substantial changes upon thermal annealing or simply with time at 25 °C, as already reported for it sulfur counterpart **DPMA-T-DCV**.[13] Figure 4.7 shows the evolution with time at 25°C of the optical spectrum of a thin-film of **DPMA-Se-DCV** and that of **DPMA-T-DCV** for comparison.

For both compounds, the broad absorption band of the as-prepared thin-film (dashed pink curve) is progressively subjected to a significant bathochromic shift together with the appearance of a vibrational structure with new bands at 553 and 610 nm for **DPMA-T-DCV** and 567 and 647 nm for **DPMA-Se-DCV** (Table 4.3). This evolution associated with a structural reorganization of the materials, stops after 70 min for **DPMA-T-DCV** and 20 h for **DPMA-Se-DCV**. As displayed in Figure 4.7, these optical changes are accompanied by a color evolution from pink to violet. Interestingly the same result can be obtained more rapidly upon thermal annealing at 80 °C for 3 min for each compounds.

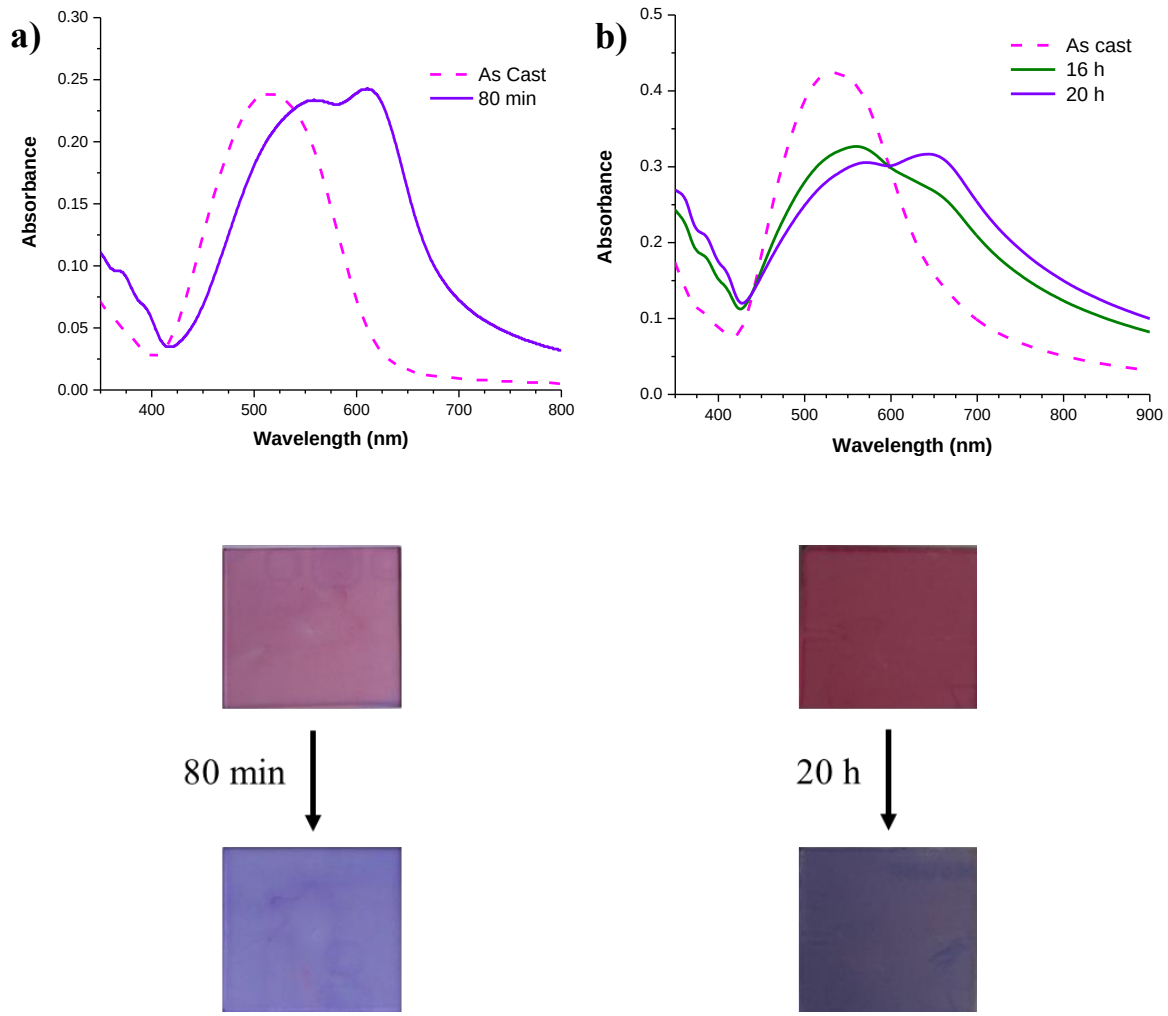

Figure 4.7. UV-Vis spectra of thin films of a) **DPMA-T-DCV** and b) **DPMA-Se-DCV** as prepared (dashed pink line) and after evolution with time at 25 °C under atmospheric conditions and pictures of corresponding glass substrates.

Table 4.3. Optical data of thin films of DPMA-based push-pull molecules prepared in different conditions

Compound	λ_{max} [nm]	E_g^{opt} [eV]
DPMA-T-DCV (Pink)	515	1.98
DPMA-T-DCV (Violet)	553, 610	1.77
DPMA-Se-DCV (Pink)	525	1.87
DPMA-Se-DCV (Violet)	567, 647	1.70

As a consequence, the optical band-gap of **DPMA-T-DCV** and **DPMA-Se-DCV** can vary from 1.98 and 1.87 eV (pink curves) to 1.77 and 1.70 eV (violet curves) respectively, depending on the exposition time in air at room temperature. (Table 4.3). This result is *a priori* of high importance when preparing bi-layer organic solar cells for which the electronic properties of the DPMA derivatives will depend on the fabrication conditions. On the other hand, thin-films of **DPMA-T-DCV** or **DPMA-Se-**

DCV mixed with $PC_{61}BM$ or $PC_{71}BM$ for example, are not subjected to changes with time or thermal annealing allowing for more reproducible bulk heterojunction organic solar cells.

4.4. Energetic Diagram from PYSA and E_g^{opt}

The ionisation potential ("HOMO" level) of the push-pull molecules in their solid state was determined by photoemission yield spectroscopy in air (PYSA) measurements on thin-films prepared from chloroform solutions spun-casted on ITO (Indium tin oxide) substrates (Figure 4.8). The energy levels of the fullerene derivatives as acceptors and the work functions of the electrodes have been found from the literature.[14-18] The HOMO energy level of **MeCz-T-DCV** was found to be -5.83 eV, 0.09 eV lower than that of **MeCz-Se-DCV** (-5.74 eV). Similarly the HOMO energy level of **DPMA-T-DCV** of -5.63 eV, is lower than that of **DPMA-Se-DCV** (-5.60 eV). In agreement with data obtained in solution, the HOMO energy levels in the solid state increase with the donor strength and the insertion of a selenophene ring (Figure 4.8) following the trend: **MeCz-T-DCV < MeCz-Se-DCV < DPMA-T-DCV < DPMA-Se-DCV**. It is interesting to note that thermal annealing or exposure with time in air of thin-films derived from **DPMA-T-DCV** and **DPMA-Se-DCV**, leads to a slight increase of the HOMO energy levels by *ca*. 0.05-0.06 eV giving values of –5.58 eV and – 5.56 eV, respectively. This result highlights the effect of the structural organization of thin-films on their electronic properties. The LUMO energy levels were determined by adding the optical band gap of the thin-films to their HOMO level. The HOMO and LUMO levels and the optical bandgap for each compound and those of C_{60} and $PC_{71}BM$ that will be used as acceptors in organic solar cells, are represented in the energetic diagram of Figure 4.9. Like in the case of **DPMA-T-DCV**, the passage from the "pink" state of **DPMA-Se-DCV** to its "violet" state, is mainly accompanied by a stabilization of the LUMO level.

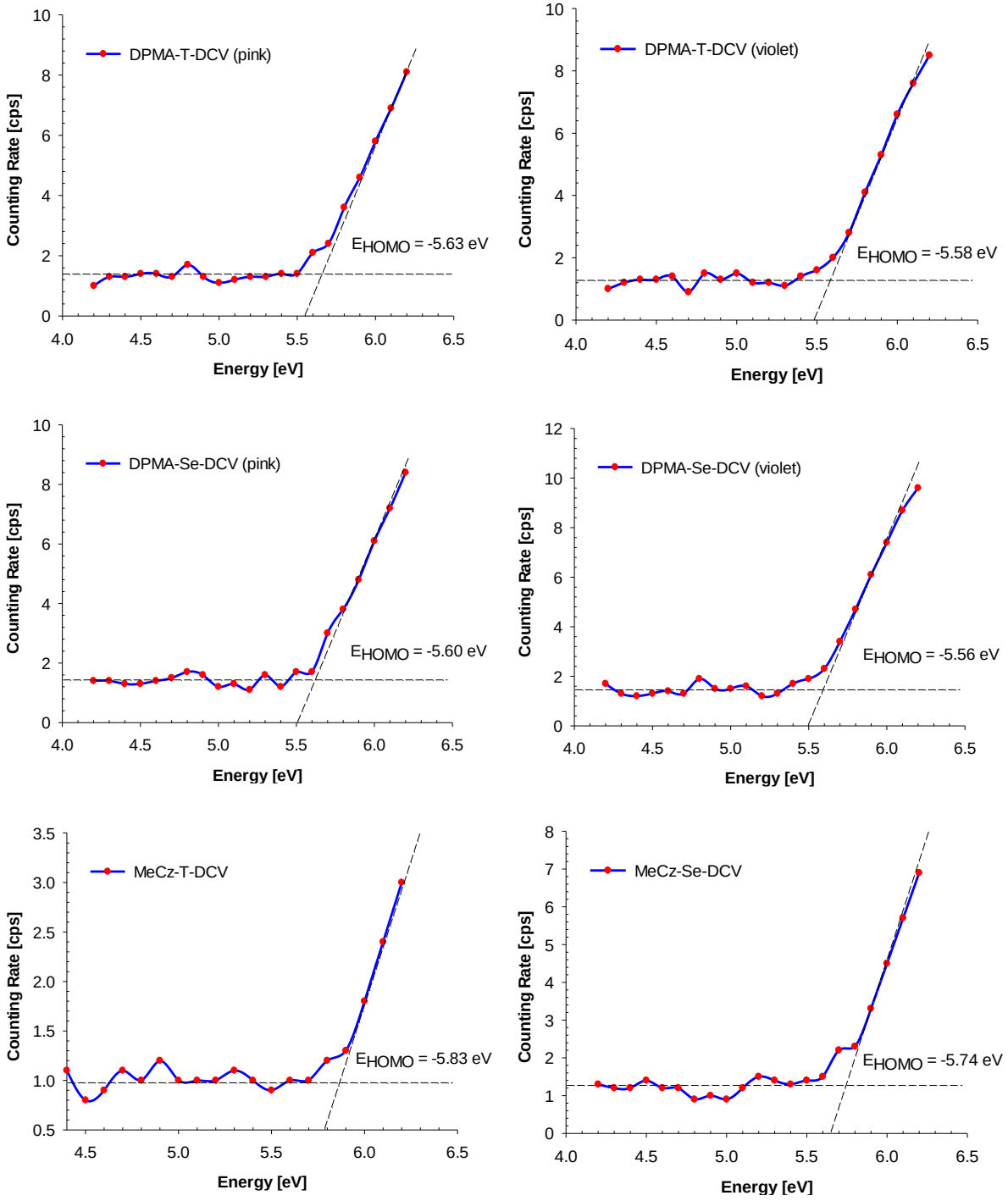

Figure 4.8. Photoemission yield spectroscopy in air of thin-films of push-pull molecules spin-casted on ITO substrates.

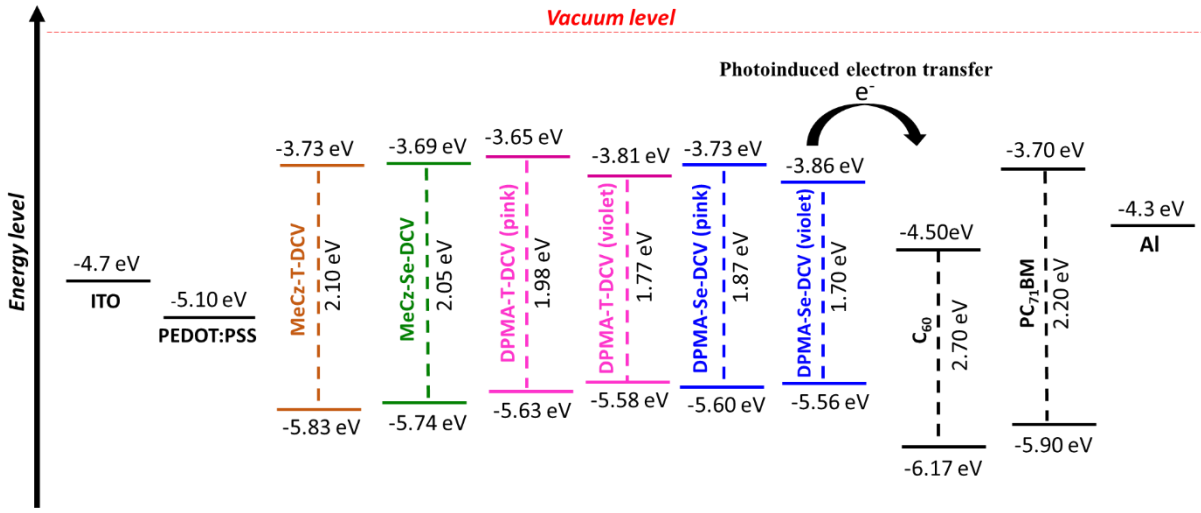

Figure 4.9. Energetic diagram of push-pull molecules, C_{60}, $PC_{71}BM$, buffer layers, and electrodes used in OPV devices.

MeCz-T-DCV exhibits the deepest HOMO energy level (- 5.83 eV) and hence it is supposed to have the largest gap with the LUMO energy level of acceptor materials $PC_{71}BM$ or C_{60}, possibly leading to the highest V_{oc} value. In fact although V_{oc} depends on different parameters, it is known to be proportional to the difference between the HOMO energy level of the donor material and the LUMO level of the acceptor materials such as fullerene derivatives.[19, 20] In addition, the LUMO energy level of all push-pull molecules are positioned above that of the acceptor (*i.e.*, $PC_{71}BM$) by 0.17–0.25 eV ensuring, in principle, an efficient photoinduced electron transfer (PET) from the donor in its excited state to the acceptor [21]. Thus, the driving force for electron transfer from the donor excited state to $PC_{71}BM$ is sufficient and larger in the case of C_{60}.[22]

4.5. Organic photovoltaic cells

The photovoltaic potential of titled push-pull molecules has been first tested in conventional bi-layer with C_{60} as acceptor while in a second step, solution-processed bulk heterojunction organic solar cells using the soluble $PC_{71}BM$ as acceptors have been fabricated and characterized, emphasizing the relationship between molecular structure and properties and device performance.

4.5.1. Conventional bi-layer organic solar cells

Bilayer OSCs of the following configuration have been fabricated: ITO/PEDOT:PSS/push-pull molecules/C_{60}/Al (Scheme 4.4).

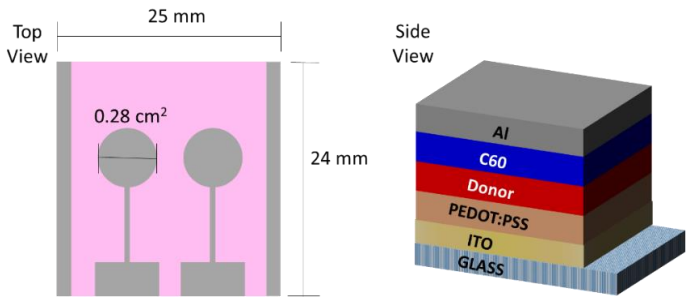

Scheme 4.4. Illustration of top and side views of the ITO/PEDOT:PSS/Donor/C_{60}/Al device

A layer of the conducting polymer PEDOT:PSS was deposited by spin-coating on cleaned commercially transparent conductive ITO substrates at 5000 rpm for 60 s, and subsequently dried at 130 °C for 15 min in air to remove water. Then, solutions of donor molecules in $CHCl_3$ (10 mg/mL) were deposited by spin-coating to give homogeneous films which thickness was optimized using different speed rates (2000, 4000 and 6000 rpm). A 30 nm thick film of C_{60} was subsequently deposited by vacuum evaporation under a pressure of 2×10^{-7} mbar with a deposition rate of *ca*. 1.2 Å/s. The top electrode in aluminum (100 nm) was also deposited by vacuum evaporation using evaporation rates of *ca*. 0.6 Å/s from 0 to 30 nm and then *ca*. 2 Å/s from 30 to 100 nm. Except the elaboration of the PEDOT:PSS film, all devices fabrication steps were carried out inside a glove box under N_2.

4.5.1.1. Bi-layer organic solar cells optimization and characterization

The performance of bi-layer OSCs were optimized concomitantly by playing with two parameters, the first one being the thickness of the donor materials which was adjusted by using different spin rates during the spin-coating process (2000, 4000 and 6000 rpm) and the second parameter being the thermal annealing time of the completed OSCs at 80 °C in the glove box. For the optimization of the latter parameter, J-V measurements of the resulting OSCs were performed after each 10 min of thermal annealing following the evolution of the power conversion efficiency.

As in Chapter 2, the as-prepared OSCs for all donor materials always gave very low PCE around ~ 0.2-0.5% and further thermal treatment of the OSCs, typically for *ca*. 40-50 min, significantly increased the performance leading to higher efficiencies. The best photovoltaic performance, after optimization of thermal annealing times for different thicknesses of donor, are reported in Table 4.4. Except in the case of **MeCz-Se-DCV** for which the best PCE was obtained with a thicker layer, higher speed rates such as 4000 or 6000 rpm for donor deposition gave higher PCEs. Figure 4.10 displays the best J-V curves and the corresponding EQE curves for each push-pull molecules.

Table 4.4. Photovoltaic parameters of ITO/ PEDOT:PSS/Donor/C_{60}/Al devices.

Compound	Speed rate [rpm]	J_{sc} [mA cm^{-2}]^b	J_{sc} [mA cm^{-2}]^c	V_{oc} [V]	FF [%]	PCE_{max} [%]	TA time [min]^d	PCE_{ave} [%]	Cell nb
DPMA-T-DCV	2000	11.50	-	0.56	33	2.17	50	1.99	6
DPMA-T-DCV	**3000**	**13.40**	**6.36**	**0.59**	**35**	**2.78**	**40**	**2.46**	**5**
DPMA-T-DCV	4000	11.43	6.36	0.52	35	1.91	30	1.80	5
DPMA-T-DCV	6000	10.42	-	0.57	38	2.26	20	2.05	8
DPMA-Se-DCV	2000	2.44	1.90	0.68	53	0.87	50	0.64	7
DPMA-Se-DCV	**4000**	**7.41**	**3.70**	**0.65**	**38**	**1.84**	**30**	**1.34**	**8**
DPMA-Se-DCV	6000	4.77	3.67	0.69	50	1.67	30	1.45	8
MeCz-T-DCV	2000	1.95	1.40	0.56	38	0.41	40	0.38	5
MeCz-T-DCV	4000	2.68	1.90	0.65	34	0.59	20	0.55	4
MeCz-T-DCV	**6000**	**3.21**	**2.35**	**0.71**	**37**	**0.84**	**40**	**0.81**	**2**
MeCz-Se-DCV	**2000**	**6.25**	**3.04**	**0.70**	**33**	**1.43**	**50**	**1.05**	**7**
MeCz-Se-DCV	4000	3.87	2.61	0.75	42	1.22	50	0.83	7
MeCz-Se-DCV	6000	4.51	2.10	0.68	35	1.09	20	0.75	2

[a] *Power incident light of 100 mW/cm^2 under AM 1.5 conditions.* [b] *J_{sc} from J-V curve.* [c] *J_{sc} from integration of EQE spectra.* [d] *Overall time of thermal annealing (TA) corresponding to multiple process of 10 min at 80 °C.*

The best photovoltaic performance was obtained for DPMA derivatives in agreement with their enhanced π-electronic delocalization. However, the thiophenic derivative **DPMA-T-DCV** exhibited the highest PCE of 2.78% associated to a J_{sc} of 13.40 mA cm^{-2}, a V_{oc} of 0.59 V and a FF of 35% while **DPMA-Se-DCV** showed a J_{sc} of 7.41 mA cm^{-2}, a V_{oc} of 0.65 V and a FF of 38% resulting in a lower PCE of 1.84%. The difference in PCE is essentially due to the much higher short-circuit current density J_{sc} observed for **DPMA-T-DCV** which cannot be explained by different absorption properties but probably to different morphology of the donor thin-films and/or different hole-transport properties. As discussed in Chapter 2, another explanation could stem from the poor diode-like behavior recorded for bi-layer OSCs derived from **DPMA-T-DCV** in the dark which may, in turn, affect the J-V characteristic under illumination. On the contrary, although the reason remains unclear, the J-V curves in the dark for other analogues show a much better diode-like behaviour (Fig. 4.8). The comparison of the EQE spectra of OSCs derived from **DPMA-T-DCV** and **DPMA-Se-DCV** confirmed the higher photocurrent observed for **DPMA-T-DCV**: although their EQE curve extended similarly from 350 nm to *ca*. 725 nm, the highest maximum of EQE of 45% at 541 nm was found for **DPMA-T-DCV** whereas **DPMA-Se-DCV** revealed a maximum of EQE of 23% at 518 nm, all of them corresponding to the contribution of the push-pull molecules to the photocurrent. In addition, an intense band was also observed at *ca*. 385 nm due to the contribution of C_{60}.

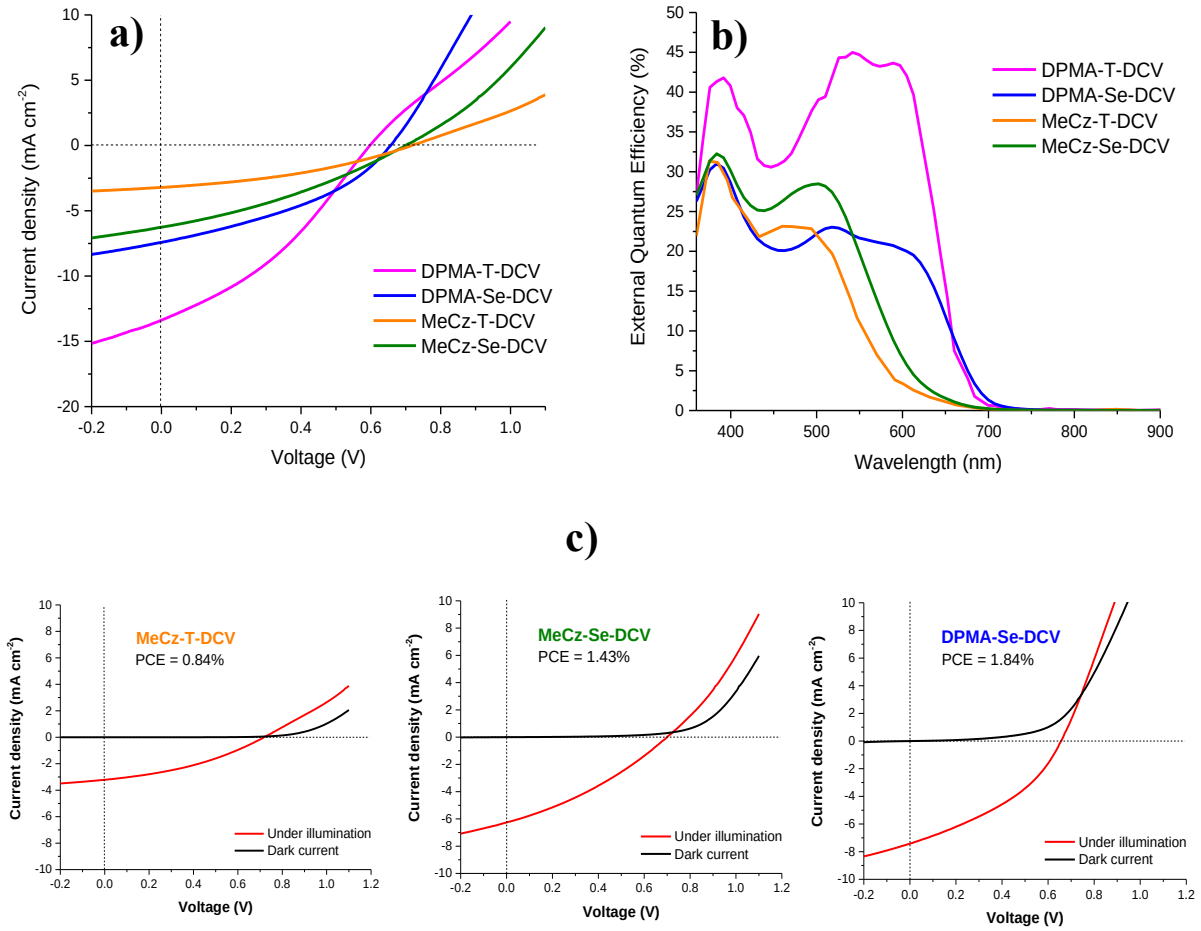

Figure 4.10. a) J-V curves of the bi-layer OSCs for the four push-pull molecules under illumination, b) EQE spectra and c) J-V curves under illumination and in the dark.

The J-V characteristics of **MeCz-T-DCV** and **MeCz-Se-DCV** derivatives showed lower PCEs of 0.84% and 1.43% in agreement with their lower J_{sc} of 3.21 and 6.25 mA cm^{-2}due to their larger optical bandgap E_g^{opt}. As a consequence, their EQE spectra are less intense and significantly shifted toward lower wavelengths. As expected, **MeCz-T-DCV** and **MeCz-Se-DCV** exhibit slightly hiher V_{oc} values in agreement with their higher oxidation potentials.

4.5.1.2. Optical microscope images of push-pull molecules

The morphology of thin-films of push-pull molecules deposited on glass substrates by spin coating (10 mg/mL in $CHCl_3$, 4000 rpm), was studied by optical microscopy before and after thermal annealing at 80 °C for 1 h. Pictures obtained with a camera show apparently homogeneous thin-films for all molecules before thermal annealing (Figure 4.11).

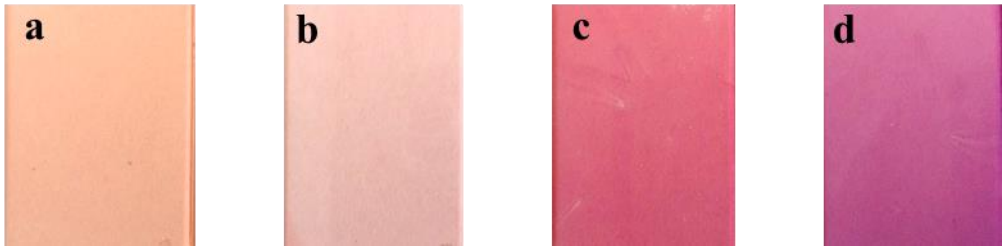

Figure 4.11. Images of thin films of a) **MeCz-T-DCV**, b) **MeCz-Se-DCV**, c) **DPMA-T-DCV** and d) **DPMA-Se-DCV** deposited on glass substrates (25 mm x 24 mm) by spin-coating.

In fact, as illustrated in Figure 4.12, images obtained with an optical microscope show that thin-films of **MeCz-T-DCV** and **MeCz-Se-DCV** are not homogenous (Figures a and b) exhibiting small dots characteristic of nucleation sites on the surface. This observation is more pronounced in the case of **MeCz-Se-DCV** which shows the presence of small crystalline domains as confirmed by the picture obtained under polarized light. On the other hand, thin-films of **DPMA-T-DCV** and **DPMA-Se-DCV** appeared very homogenous (Figure c and d).

After thermal annealing at 80 °C for 1 h, the morphology of all thin-films was affected leading to an enhanced crystallization as demonstrated by the images observed under normal or polarized light. In addition, dewetting or retractation process appeared in the case of **MeCz-T-DCV**, **MeCz-Se-DCV** and **DPMA-Se-DCV** while the surface of the glass remained covered in the case of **DPMA-T-DCV**.

Push pull	Ac-cast	As-cast under polarization light	Thermal annealing (1h @ 80°C)	Thermal annealing (1h @ 80°C) under polarization light
a	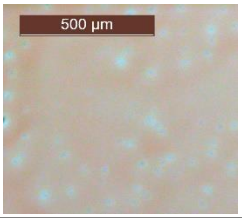		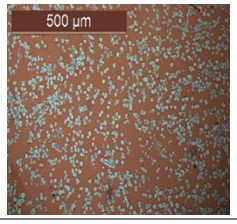	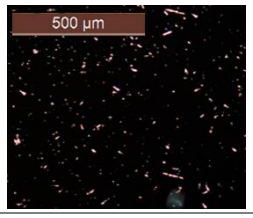
b	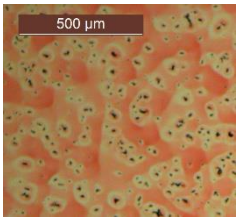	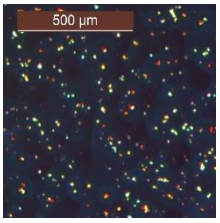	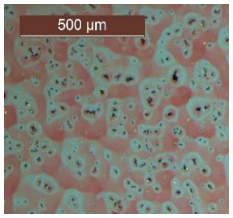	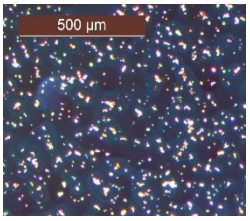
c	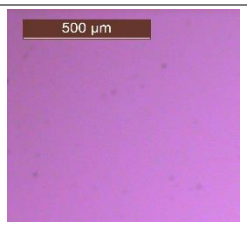		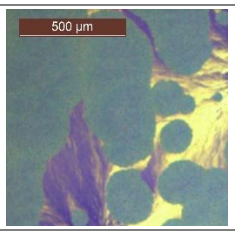	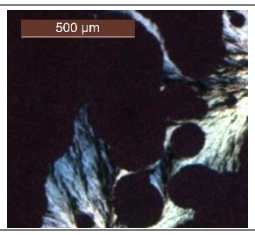
d			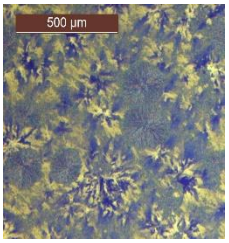	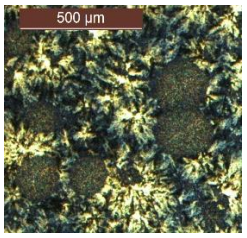

Figure 4.12. Images from optical microscope before and after thermal annealing of thin-films of a) **MeCz-T-DCV**, b) **MeCz-Se-DCV**, c) **DPMA-T-DCV** and d) **DPMA- Se-DCV** on glass.

Since the morphology of layers of the titled push-pull molecules can be affected with time or upon thermal treatment, the realization of performant bi-layer OSCs is not trivial. In this context, solution-processed BHJ have been investigated in the next paragraph.

4.5.2. Bulk heterojunction organic solar cells

BHJ photovoltaic devices were fabricated using a conventional architecture as follows: ITO/PEDOT:PSS/Donor:$PC_{71}BM$/LiF/Al (Schematic 4.5). The photoactive layer was prepared using a solution process by mixing each push-pull molecule with $PC_{71}BM$ in $CHCl_3$. A layer of 1 nm thickness of LiF was deposited by thermal evaporation under a pressure of 10^{-7} mbar at an evaporation rate of *ca*. 0.4 Å/s, this buffer layer facilitating the extraction of electrons at the cathode.

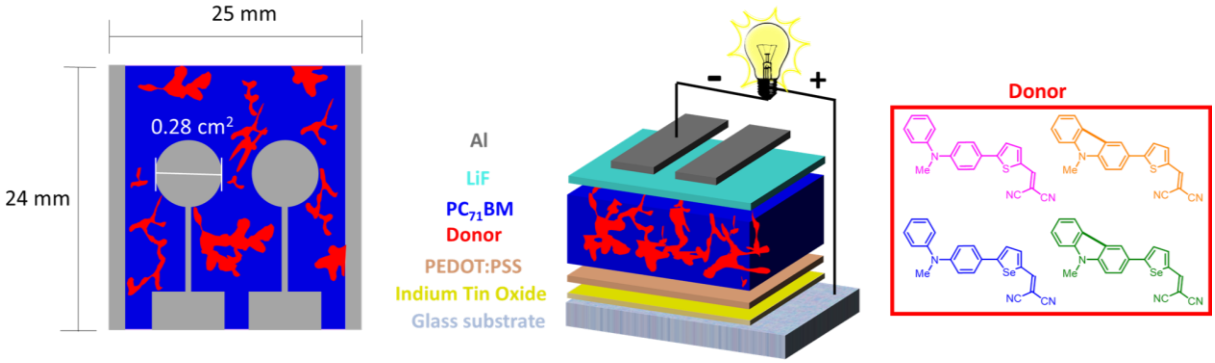

Scheme 4.5. Illustration of the ITO/PEDOT:PSS/Donor:$PC_{71}BM$/LiF/Al devices.

Note that the spin-coater for the deposition of the active layer and the thermal evaporator were located inside a glove box. All the solar cells were tested in the glove box under standardized AM 1.5 (100 mW/cm^2) conditions and the photoactive area of solar cells was 0.28 cm^2.

Based on the optimization of BHJ OSCs derived from **DPMA-T-DCV** and $PC_{71}BM$ described in Chapter 2, a weight-to-weight Donor:Acceptor ratio of 1:2 and a speed rate of 1300 rpm for the deposition of the photoactive layer, were chosen in the following study. Typically, a mixture of one selected push-pull molecule (3.33 mg) and $PC_{71}BM$ (6.66 mg) was dissolved in 1 mL of $CHCl_3$, the resulting solution was stirred for 1 h at 40 °C and then deposited onto ITO substrates pre-coated by PEDOT:PSS under rotation at 1300 rpm. Interestingly, the morphology of all photoactive blend becomes much more stable than that of neat thin-films of donors. The photovoltaic parameters of the BHJ OSCs are summarized in Table 4.5.

Table 4.5. Photovoltaic parameters of ITO/ PEDOT:PSS/Donor:$PC_{71}BM$/ LiF/Al devices.

Weight ratio [w/w]	Photoactive layer	Thickness [nm][a]	J_{sc} [mA cm^{-2}][b]	J_{sc} [mA cm^{-2}][c]	V_{oc} [V]	FF [%]	PCE_{max} [%]	PCE_{ave} [%]	Cell nb
1:2	**MeCz-T-DCV**:$PC_{71}BM$	45±3	2.89	1.41	0.85	30	0.72	0.65±0.02	6
	MeCz-Se-DCV:$PC_{71}BM$	46±2	5.35	3.08	0.73	27	1.05	0.96±0.05	2
	DPMA-T-DCV:$PC_{71}BM$	47±3	7.66	6.15	0.94	37	2.70	2.59±0.11	6
	DPMA-Se-DCV:$PC_{71}BM$	53±3	10.49	6.70	0.89	33	3.08	2.75±0.23	6

[a] *The thickness of the photoactive layer was measured by profilometry.* [b] *J_{sc} determined from J-V curve.* [c] *J_{sc} determined by integration of EQE spectra.*

The highest PCE value of 3.08% was obtained for BHJ OSCs based on **DPMA-Se-DCV** resulting from a very high J_{sc} value of 10.49 mA cm^{-2}, a V_{oc} of 0.89 V and a modest FF of 33%. Although the sulfur analogue **DPMA-T-DCV** exhibits a slightly lower efficiency of 2.70%, Table 4.6 clearly shows that the photoactive layers based on DPMA derivatives lead to more performant BHJ OSCs as

compared with MeCz derivatives, mainly due to their higher J_{sc} values in agreement with their better absorption properties at higher wavelengths. In addition, contrary to what was expected from their higher HOMO levels, DPMA derivatives led also to higher V_{oc} values compared to those of MeCz derivatives showing that the V_{oc} value is not solely dependent on the LUMO (Acceptor)-HOMO (Donor) difference. As in the DPMA series, BHJ OSCs based on the selenophene derivative gave higher efficiency in the MeCz series, namely 1.05% for **MeCz-Se-DCV** *vs* 0.72% for **MeCz-T-DCV**.

Figure 4.13a and b represent the current density-voltage curves and EQE spectra of the best devices for each donor materials. Figure 4.13a clearly evidences the increase of J_{sc} value in the following order: **MeCz-T-DCV** < **MeCz-Se-DCV** < **DPMA-T-DCV** < **DPMA-Se-DCV** leading to the same trend for PCE in agreement with the progressive increase of the π conjugation of the push-pull molecules. This is also reflected in the EQE curves for which the generated photocurrent increases in the same aforementioned order and becomes progressively significant in the 600-700 nm range for **DPMA-T-DCV** and **DPMA-Se-DCV**. For instance, **DPMA-T-DCV** and **DPMA-Se-DCV** show a maximum of EQE of 43% and 48% at 522 nm, respectively, with an onset of EQE up to 750 nm. In the case of the more efficient donor **DPMA-Se-DCV**, the J_{sc} value extracted by integration of the EQE spectrum (6.40 mA cm^{-2}) remains relatively lower than the J_{sc} values directly measured on the J-V curve under illumination.

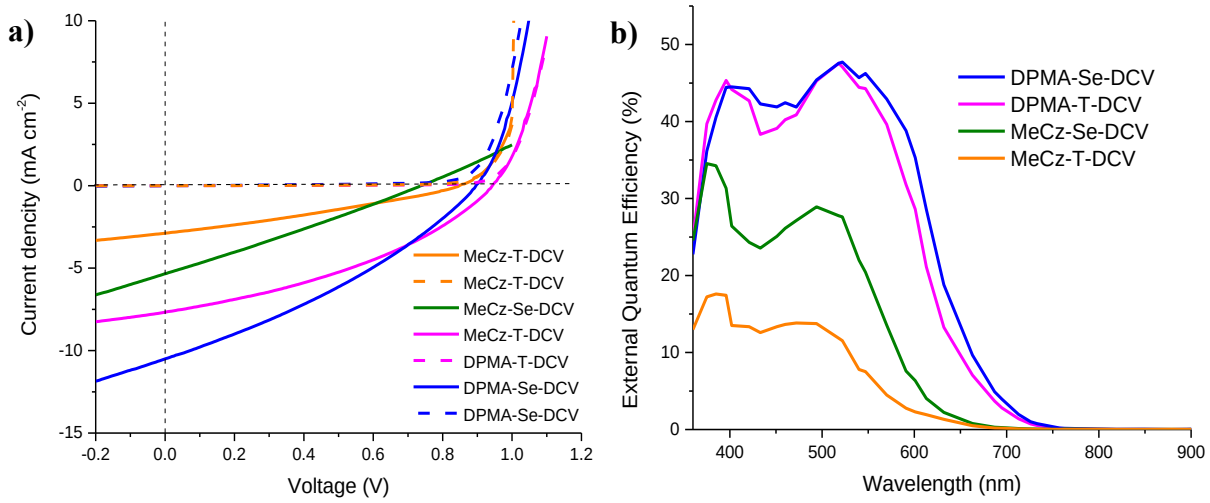

Figure 4.13. a) J-V characteristics in the dark (dash-lines) and under illumination (solid line) and b) EQE spectra of BHJ devices.

The EQE spectra of BHJ OSCs derived from **MeCz-T-DCV** and **MeCz-Se-DCV** show a broad band at *ca*. 472 nm and 494 nm with a maximum of EQE of 14% and 29% corresponding to the contribution of the push-pull molecules in coherence with the UV-Vis spectrum of the blend (Figure 4.14). These EQE spectra extend only up to 675 nm. The sharp band observed in the EQE spectra of all BHJ OSCs at *ca*. 380-400 nm correspond to the contribution of $PC_{71}BM$ to the photocurrent.

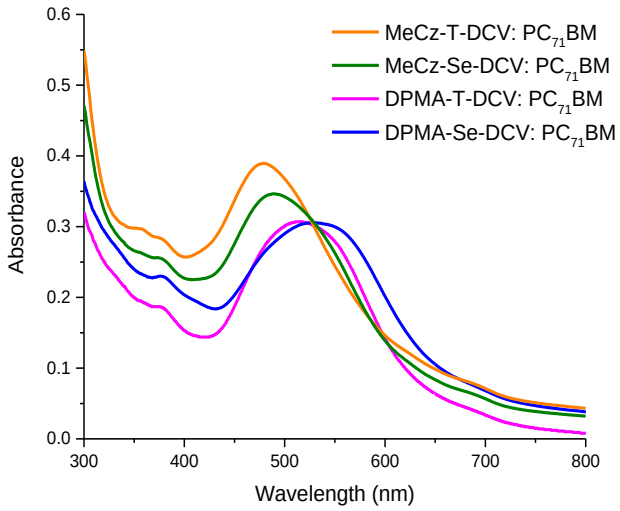

Figure 4.14. UV-Vis spectra of thin-films on glass of 1:2 w/w blends (deposition at 1300 rpm) of push-pull derivatives and $PC_{71}BM$ used for the fabrication of corresponding BHJ OSCs

4.6. Conclusion

Following the work on OSCs derived from the push-pull molecule **DPMA-T-DCV** described in Chapter 2, three new analogues have been designed and synthesized by replacing i) the DPMA electron-donating block by a *N*-methyl carbazol-3-yl group MeCz or ii) the thiophene π-spacer by a selenophene one, while keeping the dicyanovinyl (DCV) group constant. The analysis of the electrochemical properties of the resulting four molecules in solution showed that the DPMA unit is a stronger electron-donating group than the MeCz one whereas the replacement of thiophene by a selenophene further decreased the oxidation potentials. The examination of the absorption spectra of the titled molecules in solution revealed their good absorption properties in the visible spectrum and that the use of DPMA and that of the selenophene ring provided an extension of π-conjugation. As a consequence, the HOMO level increases and the HOMO-LUMO gap decreases successively from **MeCz-T-DCV** going to **MeCz-Se-DCV**, **DMPA-T-DCV** and **DPMA-Se-DCV**. The same trend is also observed in the solid state as confirmed by absorption spectroscopy and photoemission yield spectroscopy in air allowing us to estimate the optical band gap and the ionization potential respectively, of thin-films derived from the push-pull molecules. The energetic diagram of the push-pull molecules confirmed their potential role as donor materials in OSCs in combination with fullerene derivatives as acceptors.

Whereas the performance of bilayer OSCs based on the solution-processed thin-films of push-pull molecules and vacuum-evaporated C_{60} was shown to depend strongly on the morphology and structure of the donor layer, the fabrication of solution-processed BHJ OSCs with $PC_{71}BM$ gave more straightforward results. In particular, it was shown, thanks to absorption spectroscopy of thin-films, J-V measurements and EQE spectra of BHJ OSCs, that the better the π-conjugation of the push-pull molecule, the higher PCE of BHJ

OSCs is. Thus **DPMA-Se-DCV** led to the most efficient BHJ OSCs showing the highest PCE of 3.08% mainly due to a significant short-circuit current density J_{sc} of 10.49 mA cm^{-2} related to the improved absorption of the push-pull molecule at longer wavelengths.

Based on the conclusions of this work and Chapter 2, the fabrication of vacuum-processed BHJ OSCs using **DPMA-Se-DCV** combined with C_{60} or C_{70}, could provide even higher PV performance.

References:

1. A. Michaleviciute, M. Degbia, A. Tomkeviciene, B. Schmaltz, E. Gurskyte, J. V. Grazulevicius, J. Boucle and F. Tran-Van, *Journal of Power Sources*, 2014, **253**, 230-238.
2. R. Nakar, F. J. Ramos, C. Dalinot, P. S. Marques, C. Cabanetos, P. Leriche, L. Sanguinet, M. Kobeissi, P. Blanchard, J. Faure-Vincent, F. Tran-Van, N. Berton, J. Rousset and B. Schmaltz, *J Phys Chem C*, 2019, **123**, 22767-22774.
3. B. Wex and B. R. Kaafarani, *Journal of Materials Chemistry C*, 2017, **5**, 8622-8653.
4. P. Moonsin, N. Prachumrak, R. Rattanawan, T. Keawin, S. Jungsuttiwong, T. Sudyoadsuk and V. Promarak, *Chemical Communications*, 2012, **48**, 3382-3384.
5. T. Nishimoto, T. Yasuda, S. Y. Lee, R. Kondo and C. Adachi, *Materials Horizons*, 2014, **1**, 264-269.
6. N. Koumura and K. Hara, *J Syn Org Chem Jpn*, 2010, **68**, 399-408.
7. Z. S. Wang, N. Koumura, Y. Cui, M. Takahashi, H. Sekiguchi, A. Mori, T. Kubo, A. Furube and K. Hara, *Chemistry of Materials*, 2008, **20**, 3993-4003.
8. S. Haid, A. Mishra, C. Uhrich, M. Pfeiffer and P. Bäuerle, *Chemistry of Materials*, 2011, **23**, 4435-4444.
9. S. Haid, A. Mishra, M. Weil, C. Uhrich, M. Pfeiffer and P. Bäuerle, *Advanced Functional Materials*, 2012, **22**, 4322-4333.
10. A. Labrunie, Y. Jiang, F. Baert, A. Leliege, J. Roncali, C. Cabanetos and P. Blanchard, *RSC Advances*, 2015, **5**, 102550-102554.
11. Y. Jiang, C. Cabanetos, M. Allain, P. Liu and J. Roncali, *Tetrahedron Letters*, 2015, **56**, 2324-2328.
12. A. Leliège, J. Grolleau, M. Allain, P. Blanchard, D. Demeter, T. Rousseau and J. Roncali, *Chemistry–A European Journal*, 2013, **19**, 9948-9960.
13. Y. Jiang, C. Cabanetos, M. Allain, P. Liu and J. Roncali, *Journal of Materials Chemistry C*, 2015, **3**, 5145-5151.
14. C. Z. Li, H. L. Yip and A. K. Y. Jen, *Journal of Materials Chemistry*, 2012, **22**, 4161-4177.
15. Y. He, G. Zhao, B. Peng and Y. Li, *Advanced Functional Materials*, 2010, **20**, 3383-3389.
16. H. Sun, S. Ryno, C. Zhong, M. K. Ravva, Z. Sun, T. Korzdorfer and J. L. Bredas, *J Chem Theory Comput*, 2016, **12**, 2906-2916.
17. K. Akaike, K. Kanai, H. Yoshida, J. Tsutsumi, T. Nishi, N. Sato, Y. Ouchi and K. Seki, *Journal of Applied Physics*, 2008, **104**, 023710.
18. N. Sato, Y. Saito and H. Shinohara, *Chemical physics*, 1992, **162**, 433-438.
19. D. Yeboah and J. Singh, *Electronics*, 2017, **6**, 75.
20. G. Dennler, M. C. Scharber and C. J. Brabec, *Advanced materials*, 2009, **21**, 1323-1338.
21. H. Hoppe and N. S. Sariciftci, *Journal of Materials Research*, 2004, **19**, 1924-1945.
22. N. S. Sariciftci, L. Smilowitz, A. J. Heeger and F. Wudl, *Science*, 1992, **258**, 1474-1476.

Chapter 5: OSCs based on push-pull multimers as donor materials

`

5.1. Introduction

Compared to polymers, molecular systems prepared in few steps without batch-to-batch variations due to their well-defined chemical structures, appeared to be an appealing option for OPV.[1] In this context, our group has synthesized various classes of simple and synthetically accessible arylamine based push–pull materials.[2, 3] For example, the reference compound **TPA-T-DCV** prepared in only two steps at the gram scale, showed promising PCEs either in planar and bulk heterojunction solar cells.[4-6] Few years later, the replacement of one terminal phenyl ring of **TPA-T-DCV** by a methyl group produced improved PV performance mainly due to the higher hole mobility of the resulting **TPMA-T-DCV**.[7]

More recently, our group has synthesized an original push-pull tetramer **T-1** (Chart 5.1) by grafting four triphenylamine (TPA)-based push–pull molecules onto a central cheap and commercially available pentaerythritol core.[8] This efficient strategy allowed us to prepare original materials which can combine the well-defined electronic properties of discrete conjugated systems with the good film-formation properties of polymers. Only few examples of multimers based on non-conjugated (σ) cores have been reported in the literature.[9] In addition, a promising power conversion efficiency of 4.5% was reached in bulk heterojunction (BHJ) OSCs combining **T-1**, as donor, and $PC_{71}BM$.

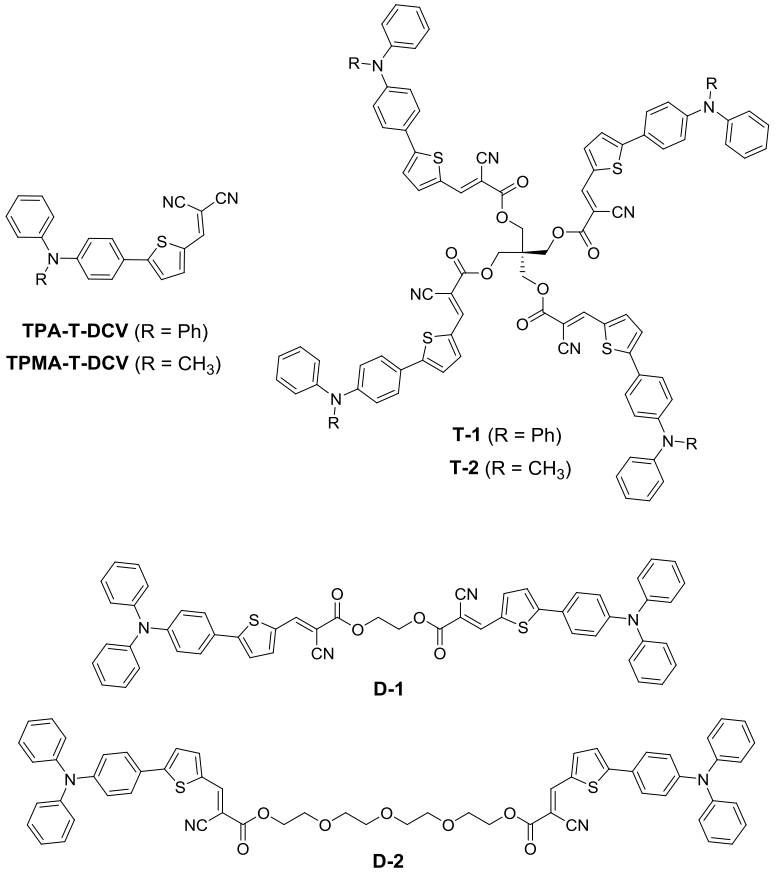

Chart 5.1. Molecular structures of push-pull monomers, dimers and tetramers

In this work, one of our objective has consisted in synthesizing, characterizing and assessing the photovoltaic (PV) potential of the new tetramer **T-2**, the analogue of **T-1** for which each TPA electron-donating group of the four push-pull system has been replaced by a diphenylmethylamine (DPMA). This latter unit is expected to improve PV performance as in the case of **TPMA-T-DCV** compared to **TPA-T-DCV**. To further investigate this "push-pull multimer" approach, new simpler and easily accessible TPA-based push-push dimers **D-1** and **D-2** have also been synthesized and tested in OPV.

5.2. A new push-pull tetramer as donor for OPV

5.2.1. Synthesis of the push-pull tetramer

The new tetramer **T-2** was synthesized in 54% yield by a Knœvenagel polycondensation between an excess of aldehyde **3** and the pentaerythritol derivative **13** containing four activated methylene groups (Scheme 5.1).[10] The aldehyde **3** was synthesized according to the procedure described in Chapter 2 (section 2.2) while compound **13** has already been described.[8]

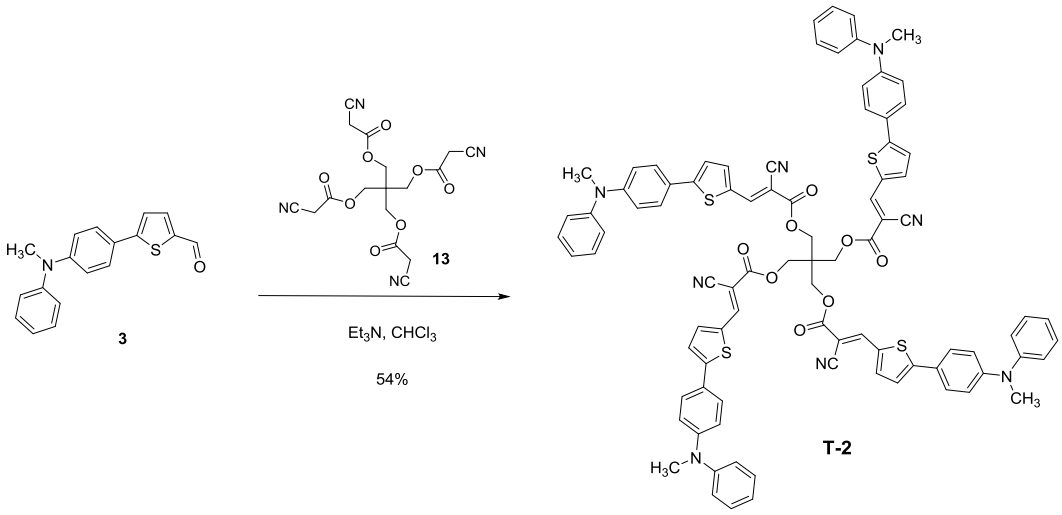

Scheme 5.1. Synthesis of tetramer **T-2**.

The replacement of one external phenyl ring by a methyl group for each push-pull moiety in **T-2** induces a significant decrease of solubility in dichloromethane or chloroform as compared to its derivative **T-1**. However **T-2** was successfully characterized by ^{1}H NMR spectroscopy in deuterated 1,1,2,2-tetrachloroethane, infrared spectroscopy and mass spectrometry (see experimental procedure).

5.2.2. Optical properties in solution and as thin films

The absorption spectrum of **T-2** in CH_2Cl_2 (*ca.* 10^{-5} M) exhibits a main broad absorption band with a maximum at 486 nm attributed to an ICT band associated with the four push-pull moieties. Compared to the reference **DPMA-T-DCV** (λ_{max} = 498 nm, see chapter 2), the hypsochromic shift recorded for **T-2** results from the replacement of the DCV group of each push-pull moiety by the less electron-withdrawing cyanoacrylate ester group. As expected, the molar extinction coefficients ε of **T-2** (138000 L mol^{-1} cm^{-1}) is approximately four times higher than that of **DPMA-T-DCV** (ε = 44100 L mol^{-1} cm^{-1}, see chapter 2). **T-2** exhibits also a broad emission band in solution with a maximum at 620 nm and a photoluminescence quantum yield of 8% measured using rhodamine B as standard (Φ = 50% in ethanol) (Figure 5.1). The optical HOMO-LUMO gap in solution was calculated at the intercept of the absorption and emission spectra in solution giving a value of ΔE^{opt} = 2.23 eV.

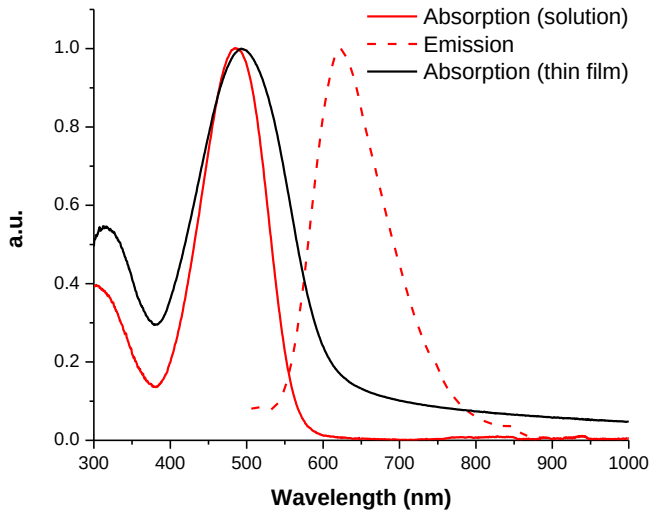

Figure 5.1. Normalized absorption (*ca.* 10^{-5} M) and emission (*ca.* 10^{-6} M, λ_{exc} = 500 nm) spectra of **T-2** in CH_2Cl_2 (red lines) and absorption spectrum of a thin-film on glass (black line).

Thin-films were prepared by spin-casting a solution of **T-2** in a 9:1 mixture of chloroform and 1,1,2,2-tetrachoroethane on glass substrates (Figure 5.1, black line). The use of small amount of this later highly chlorinated (and toxic!) solvent allowed us to form homogenous thin-films for solar cells fabrication. Compared to the solution (Figure 5.1, red line), the ICT band of thin-films is broadened and its absorption maximum is slightly red-shifted to 493 nm in agreement with the existence of π-π intermolecular interactions in the solid state. The optical bandgap of **T-2** was estimated from the onset of absorption at low energy (λ_{onset} = 612 nm) leading to a value E_g^{opt} of 2.02 eV. The optical data are summarized in Table 5.1.

Table 5.1. Thermal and optical data of tetramer **T-2** in solution and as thin film.

			solution					thin film	
Compd	**T_d [a]**	**T_m [b]**	**λ_{abs} (nm)**	**ε_{max} (L.mol^{-1}.cm^{-1})**	**ΔE^{opt} (eV)**	**λ_{em} (nm)[c]**	**Φ_f (%)[c]**	**λ_{abs} (nm)**	**E_g^{opt} (eV)**
T-2	160	204	486	138000	2.23	620	8	493	2.02

[a] Decomposition temperature corresponding to 5% weight loss in N_2 determined by TGA. [b] Melting temperature determined from DSC .[c] λ_{exc} = 500 nm, Standard : Rhodamine B in Ethanol (Φ_f = 0,50).

5.2.3. Energetic Diagram from PYSA and E_g^{opt}

The HOMO level of **T-2** was estimated by PYSA on thin-films prepared from solutions spun-casted on ITO (Figure 5.2a). A relatively high value of – 5.72 eV was obtained for the HOMO level which, combined with the E_g^{opt} value, gave an energy level of – 3.70 eV for the LUMO. As represented on the energetic diagram (Figure 5.2b), the HOMO level of **T-2** is higher than the one of $PC_{71}BM$ which is favorable for a PHT (Channel 2) while their LUMO levels are surprinsingly similar.

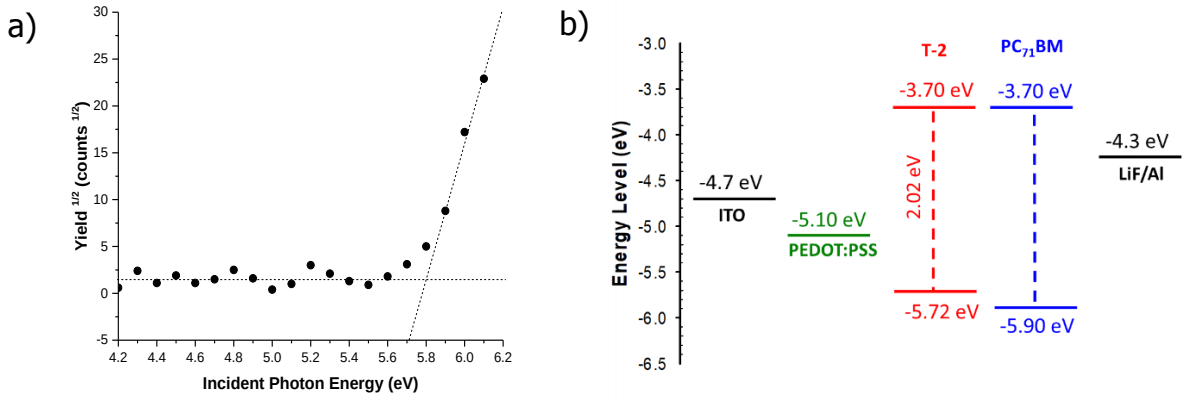

Figure 5.2. a) PYSA of **T-2** and b) energy level diagrams of electrodes, **T-2** and $PC_{71}BM$ used in OSCs.

5.2.4. Thermal properties

The thermal stability of **T-2** has been investigated by thermogravimetric analysis (TGA) and differential scanning calorimetry (DSC) under an inert atmosphere of nitrogen. The first decomposition temperature (T_d, ~5% weight loss) occurs at 160 °C and second decomposition temperature was 338 °C (T_d, ~20% weight loss) as observed by TGA (Figure 5.3a). The relatively low T_d value that may be associated to the cleavage of ester groups, shows that preparation of thin-films of **T-2** by solution process will be preferred.

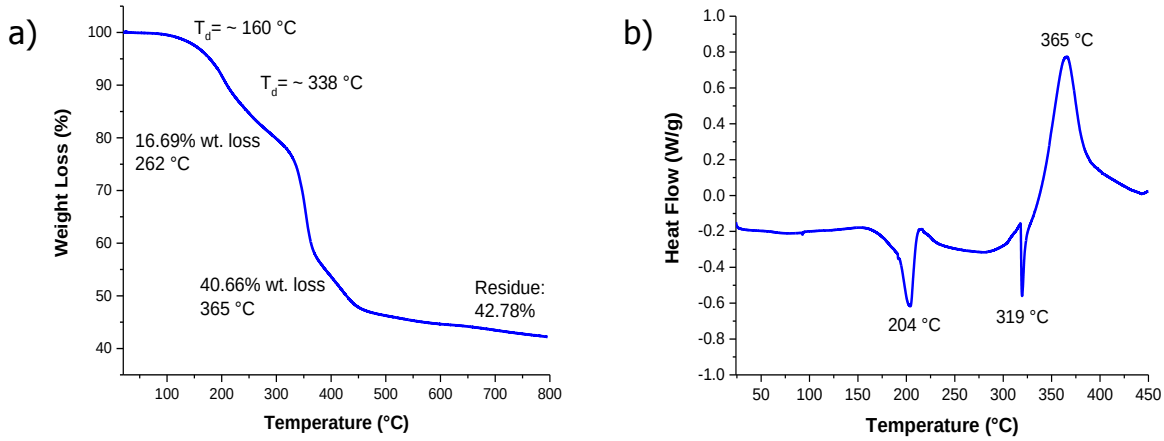

Figure 5.3. a) TGA and b) DSC curves of **T-2** measured under N_2 using a heating rate of 10 °C/min.

The DSC curve exhibits a first endothermic peak probably related to the melting temperature (T_m) at 204 °C while the intense exothermic peak at 365 °C shows decomposition (Figure 5.3b).

5.2.5. Electrochemical properties

The electrochemical properties of **T-2** have been analyzed by cyclic voltammetry. Unlike tetramer **T-1** which exhibits a fully reversible oxidation wave assigned to the concomitant oxidation of the four independent push-pull units to the radical cation state,[8] the first CV trace of **T-2** recorded in 0.1 M *n*-Bu_4NPF_6/CH_2Cl_2 shows an irreversible oxidation wave peaking at E_{pa}^1 = + 0.52 V *vs* Fc/Fc^+. In addition, scanning between *ca*. - 0.2 V and + 0.6 V leads to the efficient and rapid development of two new broad oxidation waves peaking at + 0.33 V and + 0.47 V associated with the electropolymerization of **T-2** on the working platinum electrode (Figure 5.4). The response of poly(**T-2**) in 0.1 M *n*-Bu_4NPF_6/CH_3CN shows an oxidation peak at + 0.36 V *vs* Fc/Fc^+ which is stable upon potential scans between - 0.2 V and + 0.6 V.

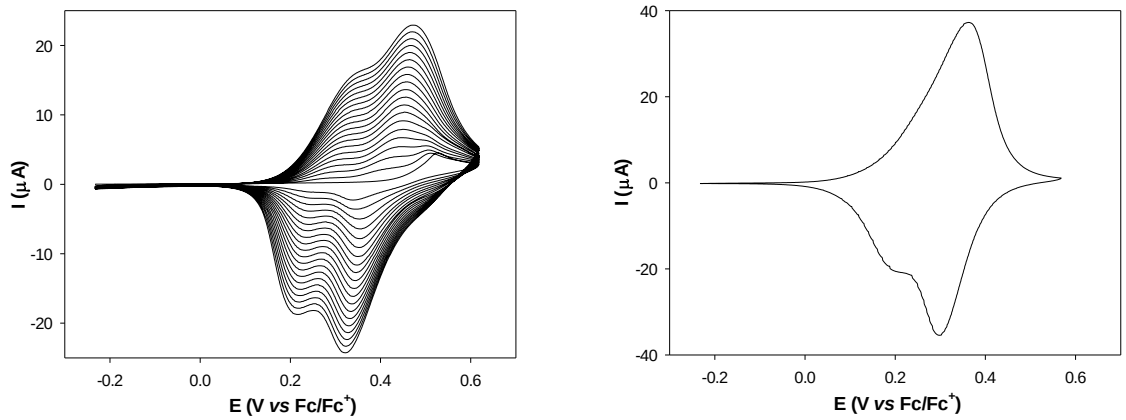

Figure 5.4. Left: Potentiodynamic electropolymerization of **T-2** (0.5 mM) in 0.1 M *n*-Bu_4NPF_6/CH_2Cl_2 using a Pt working electrode (∅ = 1 mm), scan rate 100 mV/s. Right: CV response of poly(**T-2**) in 0.1 M *n*-Bu_4NPF_6/CH_3CN, scan rate 100 mV/s.

T-2 was also electropolymerized in potentiostatic conditions at a potential of + 0.52 V (E_{pa}^{1}) *vs* Fc/Fc^{+} using 50 mC/cm^2 (*ie*. 0.393 mC). The response of poly(**T-2**) in 0.1 M *n*-Bu_4NPF_6/CH_3CN shows an oxidation peak at + 0.36 V, the same value obtained by potentiodynamic electropolymerization. The electrogenerated polymer is also very stable upon potential scans (Figure 5.5).

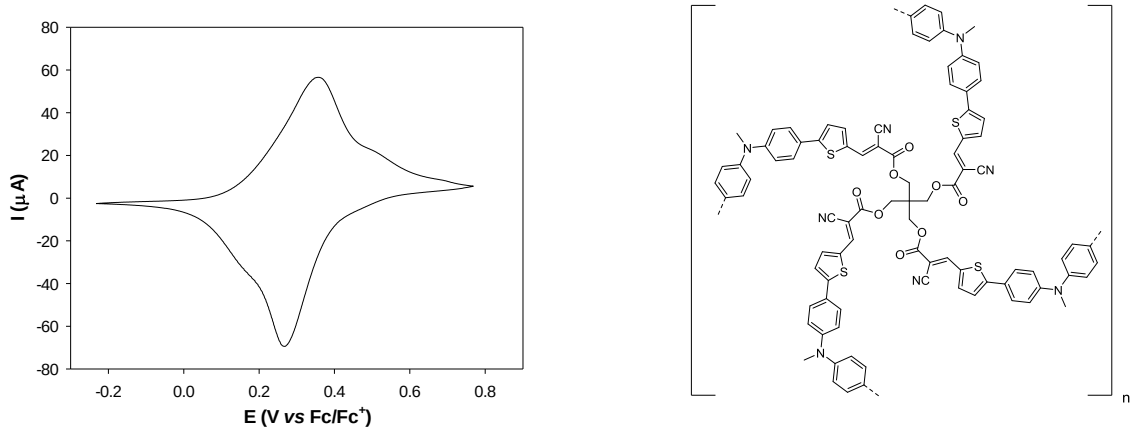

Figure 5.5. Left: CV response of poly(**T-2**) in 0.1 M *n*-Bu_4NPF_6/CH_3CN, scan rate 100 mV/s, grown in potentiostatic conditions using 0.5 mM of **T-2** in 0.1 M *n*-Bu_4NPF_6/CH_2Cl_2 (E = 0.52 V, 50 mC/cm^2). Right: structure of the expected electrogenerated polymer.

The structure of the material deposited on the Pt surface presumably corresponds to a redox polymer as described in Figure 5.5 and stems from multiple radical cation couplings at the *para* position of the external phenyl ring of each push-pull units.

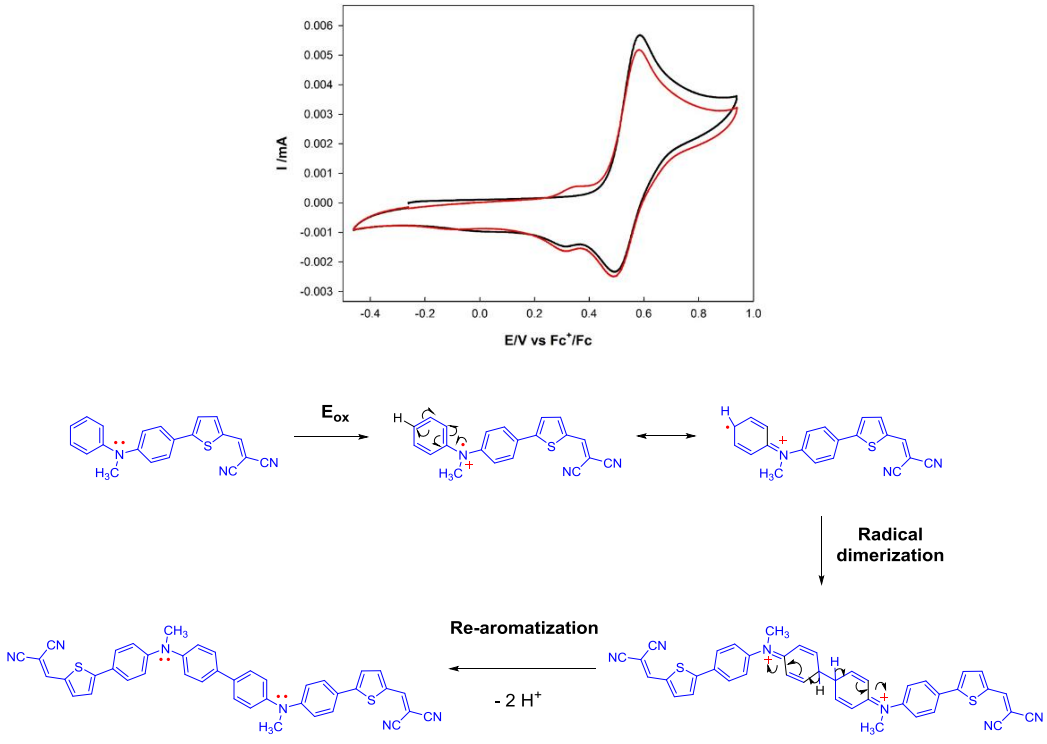

Figure 5.6. CVs of **DPMA-T-DCV**, 0.5 mM in 0.10 M Bu_4NPF_6/CH_2Cl_2, scan rate 100 mV s^{-1}, Pt working electrodes (1st and 2nd traces in black and red, respectively). Mechanism of formation of the benzidine product.

Indeed, this type of coupling also takes place after the electrochemical oxidation of **DPMA-T-DCV** in radical-cation, as demonstrated by the presence of a weakly intense reduction peak at *ca*. + 0.3 V during the reduction back scan of the first CV trace (Figure 5. 6). Then the second CV trace evidences a new oxidation peak corresponding to the formation of an electroactive π-extended benzidine system which is enough soluble to diffuse from the working electrode to the electrolyte solution. The synthesis of benzidine derivatives endowed with a biphenyl bond upon electrooxidation of arylamine is known and the related mechanism formation is represented below.[11-16]

5.2.6. Solution-processed BHJ OSCs based on tetramer T-2

BHJ OSCs were fabricated with **T-2** as donor material with the following configuration ITO/PEDOT:PSS (40 nm)/**T-2**:$PC_{71}BM$/LiF (1 nm)/Al (100 nm). A 1:3 D:A w/w mixture (*ca.* 11 mg/mL of total concentration) of **T-2** (1.25 mg) and $PC_{71}BM$ (3.75 mg) was dissolved in a 9:1 mixture of chloroform and 1,1,2,2-tetrachoroethane (400 µL:40 µL). This solution was then spun cast onto ITO/PEDOT:PSS substrates with an optimized speed rate of 2000 rpm. The use of *ca*. 10% of 1,1,2,2-tetrachloroethane was necessary for a complete solubilisation of **T-2.** Finally, devices were completed by thermal depositions of LiF (1 nm) and aluminium (100 nm) at a pressure of 10^{-7} mbar through a shadow mask defining two discoidal cells of 28 mm^2 for each substrate. Figure 5.7 shows the best J-V characteristic recorded over 8 devices under simulated AM 1.5 solar illumination at 100 mW cm^{-2}. This J-V curve exhibits an open-circuit voltage V_{oc} of 0.86 V, a short-circuit current density J_{sc} of 5.43 mA cm^{-2} and a fill-factor FF of 31% leading to a maximum PCE of 1.44% (Table 5.2).

Table 5.2. J-V parameters for BHJ OSCs derived from **T-2**:$PC_{71}BM$.

Weight ratio (w/w)	Photoactive layer	Speed rate of D:A (rpm)	J_{sc} (mA cm^{-2})	V_{oc} (V)	FF (%)	PCE_{max} (%)	PCE_{ave} (%)	Cell nb
1:3	**T-2**:$PC_{71}BM$	2000	5.43	0.86	33	1.44	1.16±0.28	8

Note that decreasing the speed rate to 1300 rpm for the photoactive layer deposition led to PCE lower than 1% while the use of pure chloroform as solvent afforded less homogenous thin-films and a maximum PCE of 0.4%.

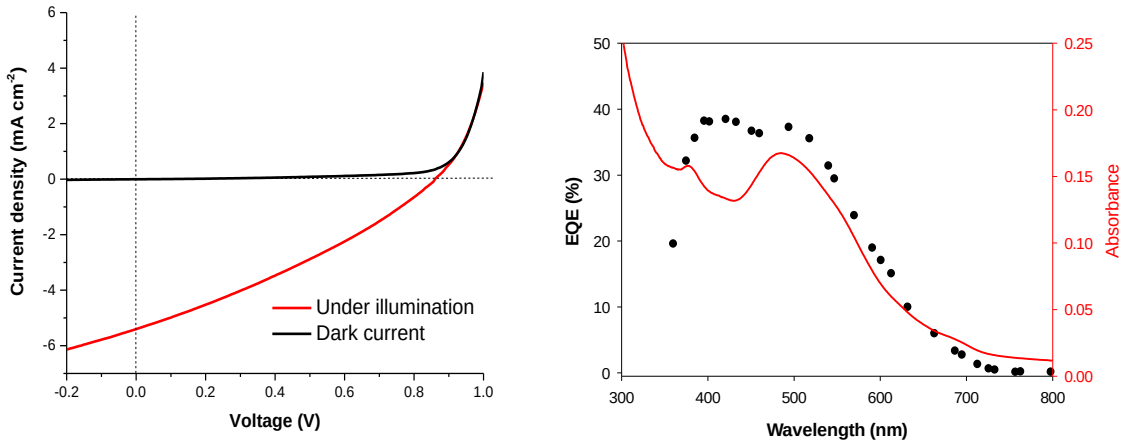

Figure 5.7. a) Best current density-voltage characteristic of the BHJ OSC in the dark and under AM 1.5 solar simulation (100 mW cm^{-2}). b) EQE spectrum of the BHJ OSC and UV-vis spectrum of the blend **T-2**:$PC_{71}BM$ (1:3 w/w) on glass.

The external quantum efficiency (EQE) spectrum of the best BHJ OSC derived from **T-2** shows two maxima at *ca*. 420 nm (39%) and 490 nm (38%), the former may be associated to the contribution of $PC_{71}BM$ to the photocurrent whereas the latter corresponds to that of **T-2** in agreement with the absorption spectrum of the photoactive layer on glass (Figure 5.7).

Compared to tetramer **T-1** which led to BHJ OSCs with PCE as high as 4.5%,[8] the lower PV performance of **T-2** are clearly related to its weaker solubility in chloroform requiring to use of 10% of 1,1,2,2-tetrachoroethane which may affect the morphology of the photoactive layer.

In order to extend the investigation of the push-pull multimers approach for OPV, smaller push-pull dimers were synthesized in the following paragraph. TPA groups instead of DPMA were chosen as electron-donating groups for solubility purpose.

5.3. New push-pull dimers as donors for OPV

5.3.1. Synthesis of push-pull dimers

Two new dimers of push-pull molecules **D-1** and **D-2** have been synthesized by Dr. Pierre Josse and Dr. Antoine Labrunie as described in schemes 5.2 and 5.3, respectively. The synthetic procedures and analytical data are described in the experimental part. Both dimers exhibit two identical push-pull moieties, consisting of a triphenylamine-thienyl-cyanoacrylic ester segment, linked together through an ethylene (**D-1**) or a tetraethyleneglycol (**D-2**) chain. The later one was expected to increase the solubility of the dimer due to its increased length and to induce a different structural organization in the solid-state.

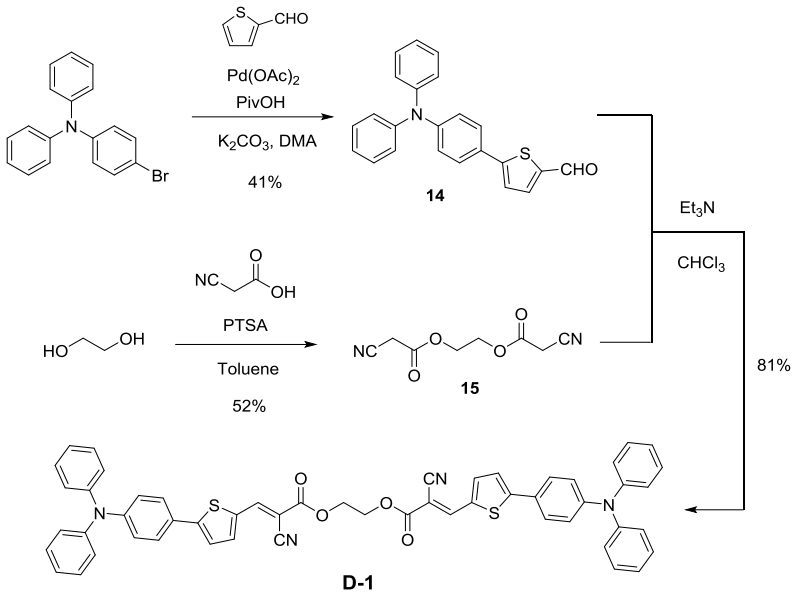

Scheme 5.2. Synthesis of dimer **D-1**.

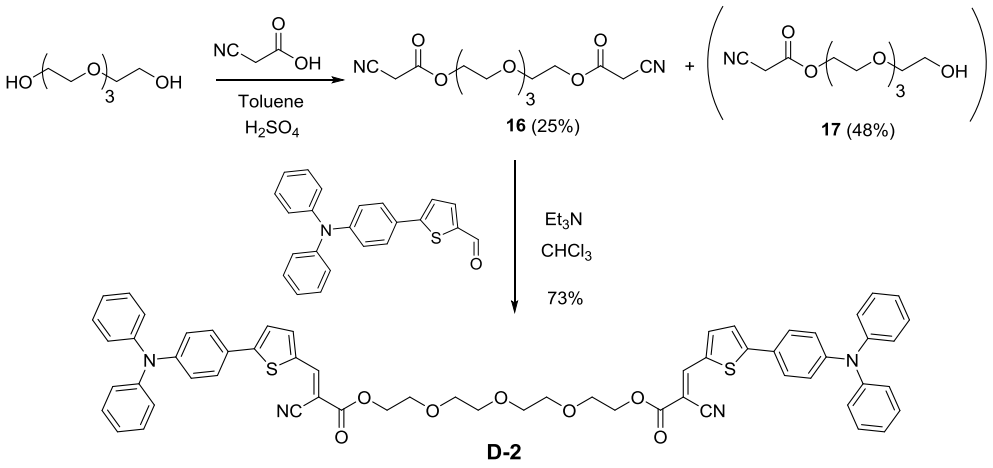

Scheme 5.3. Synthesis of dimer **D-2**.

5.3.2. Optical properties in solution and thin films

The absorption and emission spectra of **D-1** and **D-2** were recorded in diluted dichloromethane solutions, *ca*. 10^{-5} and 10^{-6} M, respectively. Absorption properties of thin-films prepared by spin-casting solutions of these dimers in chloroform solutions on clean glass substrates, have been studied by UV-Vis spectroscopy. Figure 5.8 describes the normalized absorption and emission spectra in solution and as thin films.

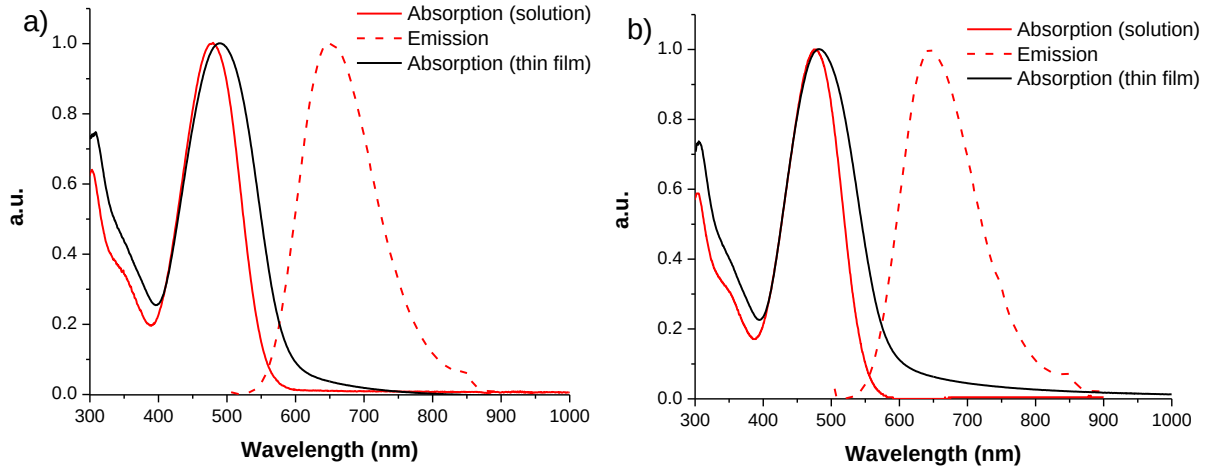

Figure 5.8. UV-Vis and photoluminescence spectra of a) **D-1** (left) and b) **D-2** (right) in solution (red line) and as thin-films (black line).

Both dimers **D-1** and **D-2** display an ICT band peaking at 478 and 476 nm with relatively high extinction coefficients ε of 66500 $L.mol^{-1}.cm^{-1}$ and 69700 $L.mol^{-1}.cm^{-1}$, respectively, due to the presence of two push-pull segments *per* dimer. The dimers **D-1** and **D-2** show also emission bands at 648 nm and 645 nm, respectively, with a relatively high fluorescence quantum efficiency of 22%. The HOMO-LUMO gaps were calculated at the intercept of the absorption and emission spectra in solution giving values of *ca*. 2.20 eV. The absorption spectra in the solid state are broader and slightly bathochromically shifted from 5 nm to 11 nm compared to the spectra in solution, suggesting the formation of molecular π-π interactions. The absorption spectra of **D-1** and **D-2** in the solid state show the same behavior suggesting that the oligo(ethylenoxy) chain has no much effect on the structural organization. The optical bandgap E_g^{opt} of each thin-film was estimated from the onset of absorption at 593 nm and 584 nm, which correspond to optical band gaps of approximately 2.09 eV and 2.12 eV for **D-1** and **D-2**, respectively. The optical data of dimers as well as **TPA-T-DCV** as reference, are summarized in Table 5.3.[17]

Table 5.3. Optical data of dimers in solution and as thin films.

Compd	solution					thin film	
	λ_{abs} (nm)	ε_{max} ($L.mol^{-1}.cm^{-1}$)	ΔE^{opt} (eV)	λ_{em} (nm)[a]	Φ_f (%)	λ_{abs} (nm)	E_g^{opt} (eV)
D-1	478	66500	2.21	648	22	489	2.09
D-2	476	69700	2.23	645	22	481	2.12
TPA-T-DCV	501	33900	2.18	651	22	523	1.98

[a] *λ_{exc} = 500 nm, Standard : Rhodamine B in Ethanol (Φ_f = 0.50).*

Compared to **TPA-T-DCV** (λ_{max} = 501 nm) with a DCV group, the use of a less electron-withdrawing cyanoacrylic ester (see paragraph below) in dimers **D-1** and **D-2** leads to a *ca*. 25 nm blue shift of the absorption maximum. As expected the extinction coefficients ε of the dimers are approximatively twice than that of **TPA-T-DCV**. In addition, the dimers and **TPA-T-DCV** show similar emission properties with a *ca*. 20% fluorescence quantum yield, a significantly higher value than the one observed for DPMA derivatives (see Chapter 4), highlighting the role of TPA.

5.3.3. Electrochemical properties

The electrochemical properties of the dimer molecules have been analyzed by cyclic voltammetry using 1 mM solution of compound dissolved in dichloromethane in the presence of in 0.10 M of tetrabutylammonium hexafluorophosphate (Bu_4NPF_6) as the supporting electrolyte and Pt as a working and counter electrodes.

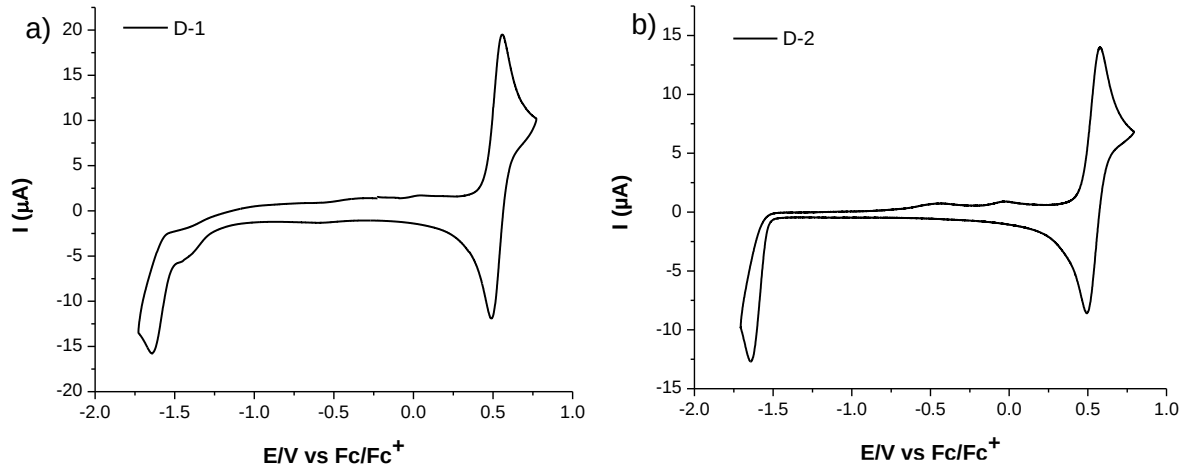

Figure 5.9. CVs of dimers a) **D-1** and b) **D-2**, 1 mM in 0.10 M Bu_4NPF_6/CH_2Cl_2, scan rate 100 mV s^{-1}, Pt working electrodes.

These compounds showed one reversible oxidation wave at 0.55 V for **D-1** and 0.58 V for **D-2**, indicating the formation of stable radical cations (Figure 5.9). In the negative potential, an irreversible reduction wave -1.63 V for **D-1** and -1.65 V for **D-2** was assigned to the reduction of the acceptor group.[18] As compared to **TPA-T-DCV**, the replacement of DCV by the cyanoacrylic ester group has a weak impact on the oxidation peak potentials whereas it leads to a significant negative shift of the reduction peak potentials demonstrating the stronger electron-withdrawing effect of DCV. Cyclic voltammetry was used to calculate the energy levels of the HOMO and LUMO which have been estimated from the onsets of oxidation and reduction waves leading to electrochemical energy gaps of

1.94 eV for **D-1** and 2.02 eV for **D-2** (Table 5.4). These later values are slightly smaller than the ones obtained from absorption and emission spectroscopy in solution.

Table 5.4. Oxidation and reduction potentials of dimers with respect to the ferrocene/ferrocenium (Fc/Fc^+).

Compd	E_{pc} [V]	E_{pa} [V]	$E_{ox,onset}$ [V]	$E_{red,onset}$ [V]	E_{HOMO} [eV][a]	E_{LUMO} [eV][a]	ΔE^{elec} [eV]
D-1	-1.63	0.55	0.45	-1.49	-5.55	-3.61	1.94
D-2	-1.65	0.58	0.47	-1.55	-5.57	-3.55	2.02
TPA-T-DCV	-1.63	0.61	0.50	-1.33	-5.60	-3.77	1.83

[a] E_{HOMO} *(eV)* = - ($E_{ox,onset}$ *vs* Fc/Fc^+ + 5.1), [b] E_{LUMO} *(eV)* = - ($E_{red,onset}$ *vs* Fc/Fc^+ + 5.1).

5.3.4. Energetic Diagram from PYSA and E_g^{opt}

The energy of the HOMO level of molecules **D-1** and **D-2** in their solid state was determined by using photoemission yield spectroscopy in air (PYSA) measurements on thin-films prepared from chloroform solutions spun-casted on ITO substrates. The LUMO energy levels were determined by adding the optical band gap of the thin films to their HOMO level, which leads to the energetic diagram are illustrated in Figure 5.10.

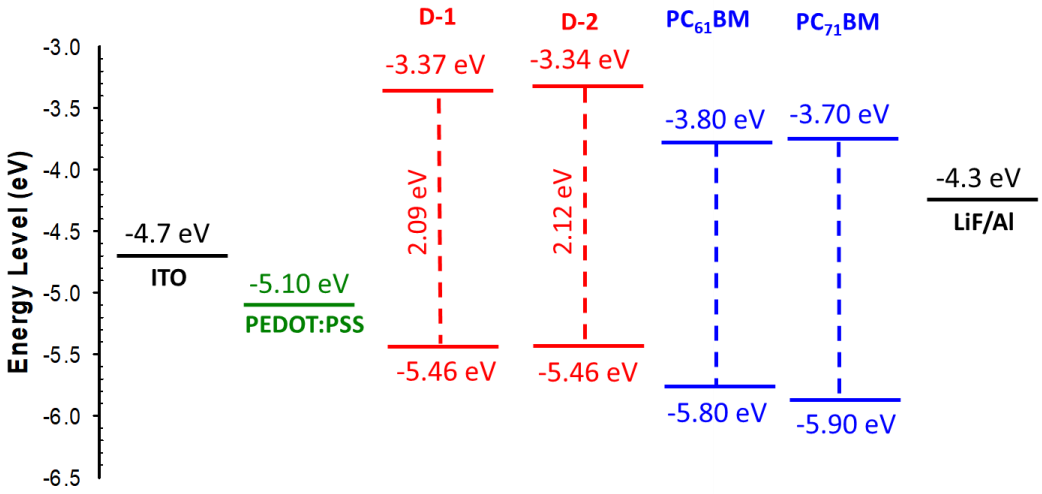

Figure 5.10. Energy level diagrams of electrodes, **D-1**, **D-2** and acceptors used in OSCs devices.

The same value of - 5.46 eV was obtained for the HOMO energy levels of **D-1** and **D-2** hence leading to comparable LUMO energy levels of - 3.35 and - 3.37 eV. Thus the energetic diagram shows that both dimers can be used in BHJ OSCs as donor materials in combination with $PC_{61}BM$ or $PC_{71}BM$.

5.3.5. Solution-processed BHJ OSCs based on dimer D-1

The photovoltaic potential of **D-1** has been tested in BHJ OSCs using the soluble $PC_{71}BM$ as acceptor and with the following device configuration: ITO/PEDOT:PSS/**D-1**:$PC_{71}BM$/LiF/Al (Figure 5.11).

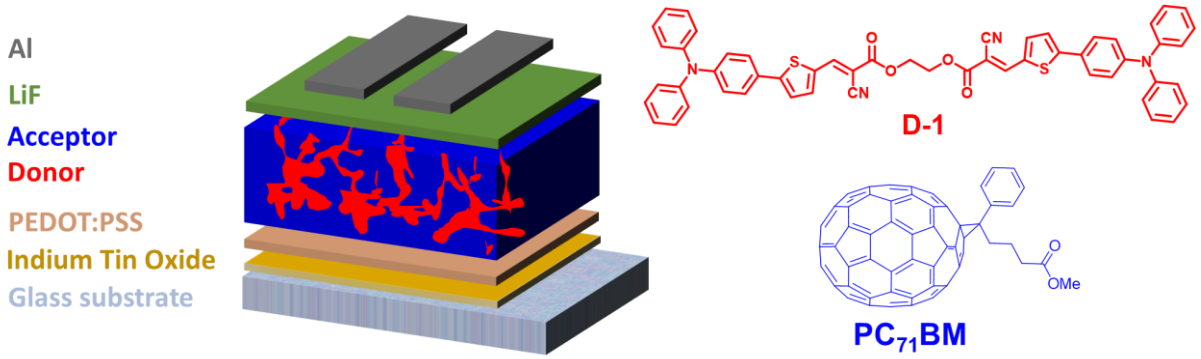

Figure 5.11. General device architecture of BHJ OSCs based on **D-1** push-pull molecule and $PC_{71}BM$.

BHJ OSCs have been optimized by using various w/w ratio of D:A and then different photoactive layer thicknesses from the best w/w D:A ratio. Blends of **D-1**:**$PC_{71}BM$** with w/w ratio of 1:2, 1:3, 1:4 and 1:5 were prepared in $CHCl_3$ with a total concentration of 10 mg/mL. Stirring of the solutions for 1 h at *ca*. 40 °C was required to completely solubilize **D-1** allowing us, after the solution was returned to room temperature, to achieve homogeneously thin films by spin-casting. In fact, the solubility of **D-1** in $CHCl_3$ has been estimated to be close to 3 mg/mL at 20 °C. The solution mixture (80 μL) was deposited on ITO/PEDOT:PSS by spin-coating at once when the maximum rotational speed was reached 1300 rpm. Then, LiF (1 nm) and aluminium (100 nm) were deposited by thermal evaporation. Table 5.5 summarizes the current density-voltage (J-V) parameters of BHJ OSCs measured upon optimization of the D:A weight-to-weight ratio.

Table 5.5. J-V parameters for BHJ OSCs with different **D-1**:$PC_{71}BM$ w/w ratio.

Ratio (w/w)	Photoactive layer	Speed rate (rpm)	J_{sc} (mA cm^{-2})	V_{oc} (V)	FF (%)	PCE_{max} (%)	PCE_{ave} (%)	Cell nb
1:2	**D-1**:$PC_{71}BM$	1300	7.09	0.92	36	2.35	2.29±0.02	6
1:3			7.62	0.99	33	2.54	2.49±0.02	5
1:4			8.09	1.00	35	2.81	2.67±0.05	5
1:5			8.93	0.89	30	2.39	2.28±0.03	5

The optimal **D-1**:$PC_{71}BM$ w/w ratio was found to be 1:4 (2 mg:8 mg/mL in $CHCl_3$) which is consistent with the fact that **D-1** contains two push-pull units. This w/w ratio corresponding to a molar

ratio of 1:3.5 mmol/mL, gave a maximum PCE of 2.81% with a short circuit current density J_{sc} of 8.09 mA cm^{-2}, a high open circuit voltage V_{oc} of 1.00 V and a fill factor FF of 35%. The J-V curve of the best BHJ OSCs device (1:4 w/w ratio) is shown in Figure 5.12.

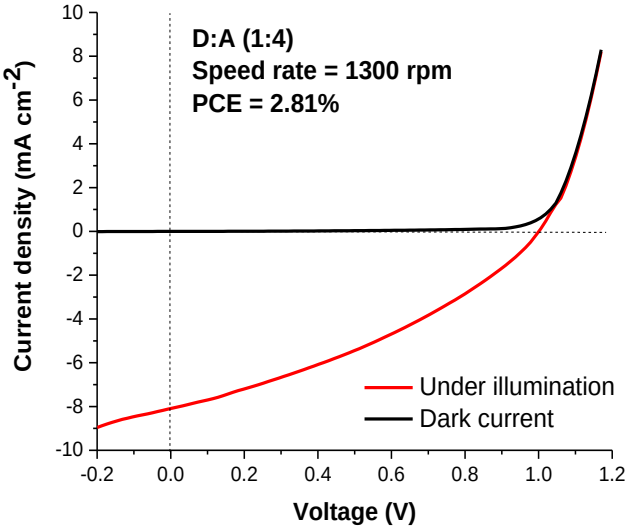

Figure 5.12. J-V characteristics of the best BHJ OSCs with 1:4 **D-1**:$PC_{71}BM$ w/w ratio.

Further optimization was achieved by varying the photoactive layer thickness using different speed rates (800, 1300 and 2000 rpm) for the deposition by spin coating while keeping the best 1:4 D:A w/w ratio. As reported in Table 5.6, the optimal photoactive layer thickness was obtained using 800 rpm which led to a thickness of 68±2 nm, as measured by profilometry.

Table 5.6. J-V parameters for BHJ OSCs with different photoactive layer thicknesses using a 1:4 **D-1**:$PC_{71}BM$ w/w ratio.

Ratio (w/w)	Photoactive layer	Speed rate (rpm)	Thickness of D:A (nm)	J_{sc} (mA cm^{-2})	V_{oc} (V)	FF (%)	PCE_{max} (%)	PCE_{ave} (%)	Cell nb
1:4	**D-1**:$PC_{71}BM$	800	68±2	12.60	0.88	31	3.43	3.18±0.19	3
		1300	54±1	8.09	1.00	35	2.81	2.67±0.05	5
		2000	42±2	5.57	0.74	38	1.58	1.32±0.04	5

Keeping the 1:4 **D-1**:$PC_{71}BM$ w/w ratio constant, the decrease of the speed rate of deposition from 1300 rpm to 800 rpm successfully produced an increase of PCE from 2.81% up to 3.43%, resulting essentially from an increase of J_{sc} up to 12.60 mA cm^{-2} whereas V_{oc} and FF slighltly decreased. This increase of J_{sc} can be correlated to the higher thickness of the photoactive layer inducing better absorption properties. According to Table 5.6, it is important to note that decreasing the thickness of the photoactive layer (from 68 to 42 nm) can lead to a decrease of the J_{sc} from 12.60 to 5.57 mA.cm^{-2}. On

the other hand, it would have been interesting to increase the thickness by decreasing further the speed rate however, much less homogeneous layers have been obtained while increasing the concentration in $CHCl_3$ was not possible due to solubility limitation. Figure 5.13 (left) depicts the current density-voltage characteristics of the best device (1:4 D:A w/w, 800 rpm) under illumination and in the dark showing a good diode behavior.

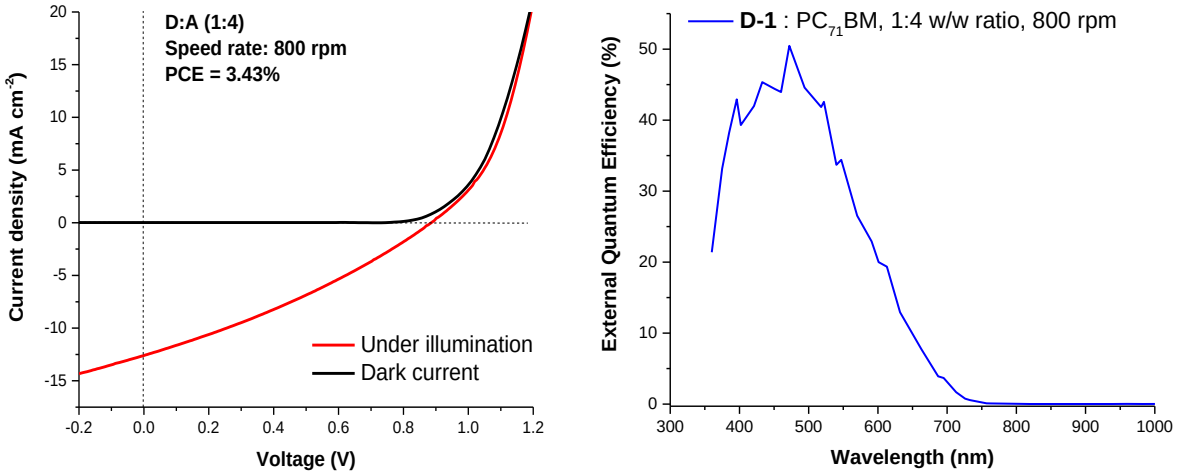

Figure 5.13. J-V characteristics (left) and EQE spectrum (right) of the BHJ OSC using a 1:4 w/w **D-1**:$PC_{71}BM$ ratio and a speed rate of 800 rpm for deposition.

The corresponding EQE curve extended from 350 nm to *ca*. 750 nm and the highest maximum of EQE of 51% was found at 471 nm in agreement with the contribution of **D-1** to the photocurrent (Figure 5.13, right).

In the course of this study, the **D-1** analogue with DPMA electron-donating groups instead of TPA, has been synthesized. However its very low solubility in $CHCl_3$ prevented the formation of homogeneous thin-films with the expected D:A w/w ratio. On the other hand, we improved the solubility of **D-1** by introducing a longer oligoethyleneoxy sigma-spacer between the two push-pull moieties.

5.3.6. Solution-processed OSCs based on dimer D-2

In the case of dimer **D-2**, BHJ OSCs of the following architecture ITO/PEDOT:PSS/**D-2**:PC_XBM (x = 61 or 71)/LiF/Al were fabricated using $PC_{61}BM$ or $PC_{71}BM$ (Figure 5.14). **D-2** presents a higher solubility in chloroform at 20 °C than the one of **D-1** (3 mg/mL). In fact it was possible to prepare a solution of **D-2** with a concentration of at least 40 mg/mL which easily led to homogeneous thin films.

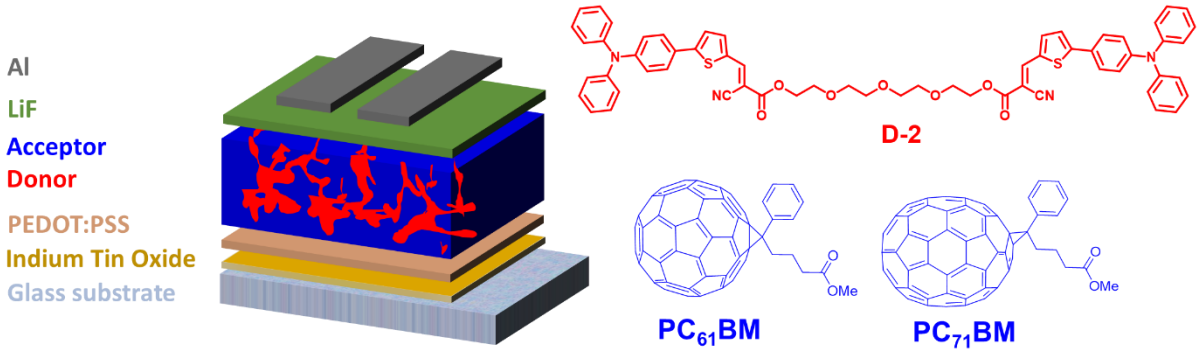

Figure 5.14. Architecture of BHJ OSCs based on dimer **D-2**.

As a first step, a 1:3 w/w **D-2:**PC_xBM (X=61 or 71) ratio was selected and the thickness of the photoactive layer was optimized by using the following speed rates for deposition by spin-coating 800, 1300 and 2000 rpm. The optimal photoactive layer thickness was found to be 2000 rpm for **D-2**:$PC_{61}BM$ and 1300 rpm for **D-2**:$PC_{71}BM$ which correspond to 42±2 nm and 51±2 nm, respectively, as measured by profilometry (Table 5.7). In these conditions, the best PCE values of 2.05% and 2.80% were recorded for **D-2**:$PC_{61}BM$ and **D-2**:$PC_{71}BM$, respectively.

Table 5.7. J-V parameters for BHJ OSCs with different photoactive layer thicknesses using a 1:3 **D-2**:PC_xBM w/w ratio.

Ratio (w/w)	Photoactive layer	Speed rate (rpm)	Thickness of D:A (nm)	J_{sc} (mA cm^{-2})	V_{oc} (V)	FF (%)	PCE_{max} (%)	PCE_{ave} (%)	Cell nb
1:3	**D-2**:$PC_{61}BM$	800	58±2	4.28	0.92	31	1.22	0.89±0.08	5
		1300	49±3	6.43	0.76	28	1.41	1.21±0.05	5
		2000	42±3	6.68	0.89	35	2.05	1.87±0.12	5
1:3	**D-2**:$PC_{71}BM$	800	69±3	7.37	0.90	33	2.21	2.16±0.07	5
		1300	51±2	8.71	0.87	37	2.80	2.66±0.12	5
		2000	44±1	8.02	0.78	31	1.94	1.54±0.33	5

Then blends of **D-2**:$PC_{61}BM$ (1:2, 1:3 and 1:4) and **D-2**:$PC_{71}BM$ (1:1, 1:2, 1:3 and 1:4) with different weight ratios were prepared in chloroform with a total concentration of 10 mg/mL. From these solutions, 80 μL were spin-coated above the PEDOT:PSS layer at 2000 and 1300 rpm for **D-2**:$PC_{61}BM$ and **D-2**:$PC_{71}BM$ respectively. Next, LiF (1 nm) and aluminium (100 nm) were successively deposited by thermal evaporation. The J-V data are presented in Table 5.8.

Table 5.8. J-V parameters for BHJ OSCs with different w/w D:A ratios using a fixed photoactive layer of **D-2**:PC_xBM.

Ratio (w/w)	Photoactive layer	Speed rate (rpm)	Thickness of D:A (nm)	J_{sc} (mA cm^{-2})	V_{oc} (V)	FF (%)	PCE_{max} (%)	PCE_{ave} (%)	Cell nb
1:2	**D-2**:$PC_{61}BM$	2000	44±1	6.04	0.92	34	1.90	1.54±0.23	5
1:3			42±3	6.68	0.89	35	2.05	1.87±0.12	5
1:4			44±1	3.43	0.89	36	1.10	1.04±0.08	5
1:1	**D-2**:$PC_{71}BM$	1300	49±3	5.80	0.97	30	1.58	1.43±0.06	5
1:2			49±3	4.68	0.96	37	1.74	1.63±0.05	5
1:3			51±2	8.71	0.87	37	2.80	2.66±0.12	5
1:4			49±3	3.84	0.88	37	1.25	1.13±0.06	5

The optimal weight ratio for **D-2**:$PC_{61}BM$ was found to be 1:3 (2.5 mg : 7.5 mg/mL in $CHCl_3$) for which a PCE of 2.05% was measured resulting from a J_{sc} of 6.68 mA cm^{-2}, and V_{oc} of 0.89 V and FF of 35%. The optimal weight ratio for **D-2**:$PC_{71}BM$ was also found at 1:3, leading to a higher PCE of 2.80% with a J_{sc} of 8.71 mA cm^{-2}, a V_{oc} of 0.87 V and a FF of 37%. The main difference between these two types of BHJ OSCs is related to the better absorption properties of $PC_{71}BM$ affording a higher J_{sc} value. The corresponding J-V curves are shown in Figure 5.15.

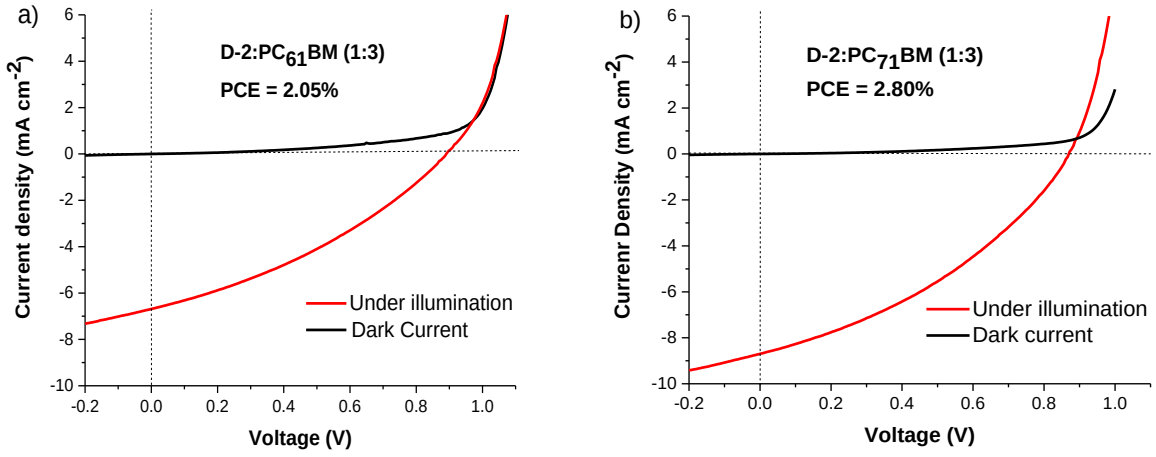

Figure 5.15. J-V characteristics of the best BHJ OSCs using a) **D-2**:$PC_{61}BM$ and b) **D-2**:$PC_{71}BM$ as photoactive layer.

The EQE spectrum of the best BHJ OSC based on **D-2** and $PC_{71}BM$ extends to *ca*. 750 nm with maxima of EQE of 48% at 421 nm and 46% at 492 nm in agreement with the contribution of $PC_{71}BM$ and **D-2** to the photocurrent, respectively (Figure 5.16). The J_{sc} value of 5.77 mA cm^{-2} calculated by integrating the surface area below the curve is lower than the one deduced from the J/V characteristic

under illumination (8.71 mA cm^{-2}) due, in part, to the fact the EQE spectrum did not take into account the UV region below 350 nm.

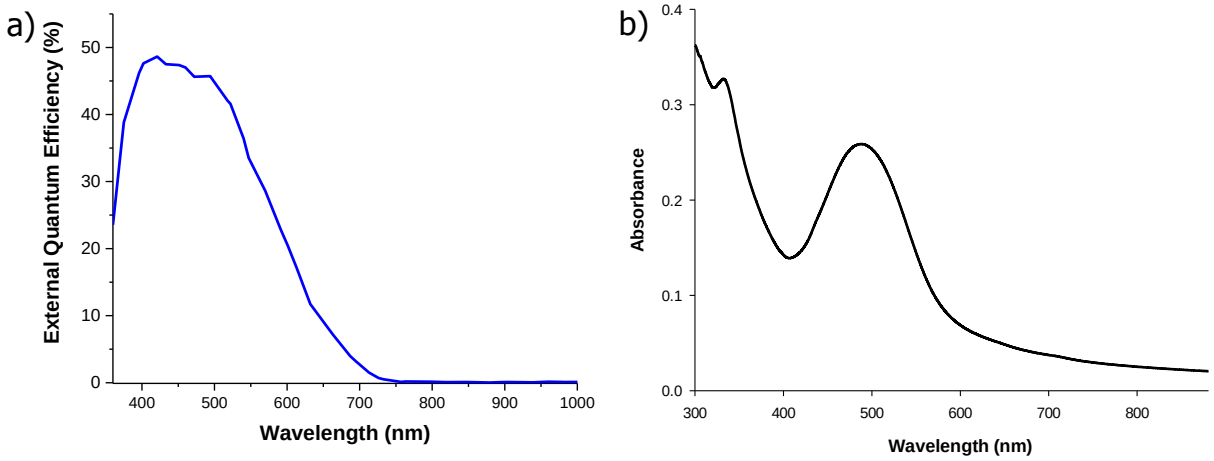

Figure 5.16. a) EQE spectrum of the best BHJ OSCs derived from **D-2**:$PC_{71}BM$ (1:3 w/w, 1300 rpm) and b) UV-Vis spectrum of the photoactive blend.

To summarize, optimizations of BHJ OSCs prepared from the simple dimer of push-pull **D-1** in combination with $PC_{71}BM$ led to a relatively high PCE of 3.4 % while the more soluble **D-2** derivative gave rise to slightly lower performance (PCE = 2.8 %).

Conclusion

In this chapter, we have investigated further the "push-pull multimer" approach recently developed in our group. In particular, we previously showed that tetramer **T-1** was able to produce BHJ OSCs with $PC_{71}BM$ affording PCE up to 4.5%. As a next step and based on the better PV performance of **DPMA-T-DCV** (Chapter 2), the triphenylamine (TPA) units of **T-1** have been herein replaced by DPMA groups affording the new target **T-2** which has been synthesized during this PhD work. However, due to a weaker solubility in chloroform, the processability of **T-2** implied the use of a fraction of 1,1,2,2-tetrachloroethane in chloroform. In these conditions, a maximum PCE of 1.4% was finally reached. These lower performance combined with the use of such highly toxic solvent, pushed us to study simpler and more soluble push-pull dimers.

Meanwhile, by contrast with **T-1**, **T-2** has shown a peculiar electrochemical behaviour upon oxidation. In fact, the high reactivity of the four radical cation species of **T-2** electrogenerated at the same oxidation potential, resulted in the straightforward formation of a redox polymer at the surface of the working electrode, consisting in multiple benzidine-based push-pull electroactive blocks.

Then two smaller push-pull dimers namely **D-1** and **D-2** based on TPA, for a better solubility, were investigated. They differ only by the σ-linker connecting the two push-pull units. Hence, these compounds show similar optical and electrochemical properties leading to the same optical band gap and HOMO-LUMO energy levels. Dimer **D-2** exhibiting a longer and hydrophilic σ-linker shows a much higher solubility in chloroform than **D-1** having a short ethylene σ-linker. However, it has been possible for both dimers to fabricate BHJ OSCs with optimum PV performance after optimization of the D/A weight-to-weight ratio and the thickness of the photoactive layer. While **D-2** in combination with $PC_{71}BM$ gave a PCE of 2.8%, a high value of 3.4% was achieved with the synthetically accessible dimer **D-1**.

References:

1. R. Po and J. Roncali, *Journal of Materials Chemistry C*, 2016, **4**, 3677-3685.
2. P. Blanchard, C. Malacrida, C. Cabanetos, J. Roncali and S. Ludwigs, *Polymer International*, 2019, **68**, 589-606.
3. C. Cabanetos, P. Blanchard and J. Roncali, *The Chemical Record*, 2019, **19**, 1123-1130.
4. A. Leliege, C. H. Le Regent, M. Allain, P. Blanchard and J. Roncali, *Chemical Communications*, 2012, **48**, 8907-8909.
5. J. W. Choi, C. H. Kim, J. Pison, A. Oyedele, D. Tondelier, A. Leliege, E. Kirchner, P. Blanchard, J. Roncali and B. Geffroy, *Rsc Advances*, 2014, **4**, 5236-5242.
6. A. Labrunie, Y. Jiang, F. Baert, A. Leliege, J. Roncali, C. Cabanetos and P. Blanchard, *RSC Advances*, 2015, **5**, 102550-102554.
7. Y. Jiang, C. Cabanetos, M. Allain, P. Liu and J. Roncali, *Journal of Materials Chemistry C*, 2015, **3**, 5145-5151.
8. A. Labrunie, P. Josse, S. Dabos-Seignon, P. Blanchard and C. Cabanetos, *Sustainable Energy & Fuels*, 2017, **1**, 1921-1927.
9. A. Zitzler-Kunkel, M. R. Lenze, K. Meerholz and F. Wurthner, *Chemical Science*, 2013, **4**, 2071-2075.
10. C. Malacrida, A. H. Habibi, S. Gámez- Valenzuela, I. Lenko, P. S. Marqués, A. Labrunie, J. Grolleau, J. T. López Navarrete, M. C. Ruiz Delgado and C. Cabanetos, *ChemElectroChem*, 2019, **6**, 4215-4228.
11. H.-J. Yen and G.-S. Liou, *Polymer Chemistry*, 2018, **9**, 3001-3018.
12. N. Cocherel, P. Leriche, E. Ripaud, N. Gallego-Planas, P. Frère and J. Roncali, *New Journal of Chemistry*, 2009, **33**, 801-806.
13. K. Karon, M. Lapkowski, A. Dabuliene, A. Tomkeviciene, N. Kostiv and J. V. Grazulevicius, *Electrochimica Acta*, 2015, **154**, 119-127.
14. M. Yada, C. Taniguchi, T. Torikai, T. Watari, S. Furuta and H. Katsuki, *Advanced Materials*, 2004, **16**, 1448-1453.
15. S.-H. Hsiao and J.-W. Lin, *Polymer Chemistry*, 2014, **5**, 6770-6778.
16. T.-G. Sun, Z.-J. Li, J.-Y. Shao and Y.-W. Zhong, *Polymers*, 2019, **11**, 73.
17. A. Leliège, J. Grolleau, M. Allain, P. Blanchard, D. Demeter, T. Rousseau and J. Roncali, *Chemistry–A European Journal*, 2013, **19**, 9948-9960.
18. F. o. Baert, C. m. Cabanetos, M. Allain, V. Silvestre, P. Leriche and P. Blanchard, *Organic letters*, 2016, **18**, 1582-1585.

General conclusion and perspectives

In recent years, organic photovoltaic cells have aroused increasing interest as a possible alternative to silicon. They can bring significant development in the research of low-cost photovoltaic modules and great flexibility for the production of household electricity. The optimization of the power conversion efficiency of organic solar cells (OSCs) is based on understanding the performance of the photoactive layer, the optimization of their interfaces and the analysis of the cell parameters and the related photophysical processes. The photoactive layer of OSCs is mostly prepared by combining one electron-donating (D) and one electron acceptor (A) materials. Since more than three decades, the enthusiasm of academics for these materials and the associated devices have made it possible to obtain high-performance solar cells, which efficiencies now close to 17%. However, those performance are usually achieved with organic materials of a growing structural complexity. Thus photovoltaic efficiency should not be the only figure of merit for OSCs. The synthetic accessibility and the simplicity the structure of organic materials need also to be considered at the early stage of their development. In this context, small push-pull π-conjugated molecules have shown a great interest as donor materials for organic photovoltaics (OPV).

The first chapter of this PhD thesis has briefly described the fundamentals of OSCs by introducing the principle of organic semiconductors, the history of the development of organic photovoltaics and the evolution of OSC architectures over time. Among well-known classes of D and A materials presented in this manuscript, a specific attention has been paid to small push-pull π-conjugated molecules for OPV and their molecular engineering. In particular, some strategies to improve hole transport properties of these molecules have been discussed. Owing to its relatively good hole mobility ($\mu_h = 50 \times 10^{-5}$ cm^2 V^{-1} s^{-1}) and absorption properties in the visible spectrum, the **DPMA-T-DCV** push-pull molecule has recently led to efficient bi-layer OSCs. Based on these preliminary and promising results, this PhD work has been devoted to further investigation of the photovoltaic potential of this molecule and other new derivatives.

In chapter 2, it was shown that **DPMA-T-DCV** could be synthesized in few steps and in a large scale (up to 500 mg). This small push-pull molecule could be processed in solution or by vacuum evaporation allowing us to test various OSC architectures. Although conventional solution- or vacuum-processed bi-layer OSCs prepared with C_{60} led to poor diode-like behavior in the dark, better J-V characteristics were obtained with C_{70} affording PCEs of 2.4% after optimization of the thickness of organic layers and thermal annealing of the completed devices. However, this work on bi-layer OSCs showed that better and more reproducible PV performance were obtained for inverted bi-layer OSCs compared to devices with a conventional architecture. After optimization of the donor thickness to avoid the S-shape of J-V curves and introduction of a charged molecular buffer layer based on a zinc porphyrin derivative, namely ZnTPPIm,TFSI, inverted bi-layer OSCs using ZnO as electron-transporting layer, showed PCEs up to 3.1%.

The second part of this chapter was dedicated to solution-processed bulk heterojunction (BHJ) OSCs fabricated in conventional and inverted modes. Using a conventional architecture, the donor (**DPMA-T-DCV**) and acceptor ($PC_{71}BM$) weight-to-weight ratio has been optimized giving best efficiency with a 1:2 ratio. $PC_{61}BM$ was also tested however $PC_{71}BM$ gave better results. Different buffer layers such as LiF or a polythiophene-based P3HTPMe$_3$,TFSI and a molecular ZnTPPIm,TFSI electrolytes, were also introduced close to the aluminium cathode to favour the electron extraction. The presence of these charged buffer layers produced more reproducible and homogenous BHJ OSCs derived from **DPMA-T-DCV** and $PC_{71}BM$, with very good J-V curves in the dark and PCEs of 2.7%, 2.9% and 2.7% under illumination, respectively. The performance of inverted solution-processed BHJ OSCs using ZnO as electron-transporting layer, remained lower.

More importantly, the last part of chapter 2 showed that efficient conventional all vacuum-processed BHJ OSCs were successively prepared by co-evaporation of **DPMA-T-DCV** and C_{60}, replacing PEDOT:PSS by MoO_3, and introducing a hole-blocking layer such as bathocuproine close to the aluminium cathode. After a thorough optimization of the thickness of the photoactive layer, these OSCs led to increased performance with a PCE as high as 4.24%, this result underlining the interest of small push-pull π-conjugated molecules for vacuum-processed BHJ OSCs.

Chapter 3 deals with the description and the characterization of a π-extended analogue of **DPMA-T-DCV**, namely **DPMA-T-T-DCV**, resulting from the insertion of an additional thiophene ring in the π-spacer. As expected, this push-pull molecule showed a better absorption in the visible spectrum and was tested as donor for OPV. Compared to **DPMA-T-DCV**, this new π-extended molecule provided more stable neat thin-films allowing us to easier prepare solution-processed bi-layer OSCs showing good J-V curves in the dark with PCEs of 2.4% and 1.7% under illumination with C_{60} and C_{70}, respectively. Vacuum-processed BHJ OSCs prepared by co-evaporation of **DPMA-T-T-DCV** and C_{60} led to higher PCEs up to 3% while solution-processed BHJ OSCs with $PC_{71}BM$ or $PC_{61}BM$ gave lower values of *ca*. 2.5% or 1.8%, respectively.

In chapter 4, the impact of the replacement of the diphenylmethylamine (DPMA) electron-donating group of **DPMA-T-DCV** by the bridged carbazole MeCz group, and that of the thiophene π-spacer (T) by a selenophene (Se) one, on the electronic properties and PV performance, was investigated. Briefly, as demonstrated by cyclic voltammetry, the MeCz group is less electron-donating than the DPMA one while, as shown by UV-vis and emission spectroscopy, the use of a selenophene ring leads to a bathochromic shift of the absorption and emission spectra relative to the thiophene ring. The energetic diagram of the four titled molecules was built from the HOMO levels determined in the solid state by photoemission yield spectroscopy in air and from the optical bandgap measured from the absorption spectra of related thin-films. These results suggested the use of titled molecules as donors for OPV in combination with fullerene acceptors. The new **DPMA-Se-DCV** push-pull molecule led to the most efficient solution-processed BHJ OSCs with $PC_{71}BM$ with a PCE of 3.08%. As perspectives, provided it can be

evaporated without degradation, it could be interesting to fabricate all-vacuum processed BHJ OSCs by co-evaporation of **DPMA-Se-DCV** and C_{60} or C_{70}.

Finally, chapter 5 was dedicated to the investigation of push-pull multimers as donors for OPV. A tetramer **T-2** with four push-pull moieties with a DPMA electron-donating group has been synthesized. A study of **T-2** by cyclic voltammetry showed that the electrochemical oxidation of each push-pull moieties led to four reactive radical-cation species prone to a coupling hence leading to an electropolymerization process resulting in the deposition of a polymer at the working electrode. Owing to the low solubility of **T-2** in chloroform, addition of a fraction of 1,1,2,2-tetrachloroethane was necessary to prepared solution-processed BHJ OSCs with $PC_{71}BM$ leading to a poor efficiency of 1.4% as compared to an analogue tetramer bearing triphenylamine (TPA) groups instead of DMPA. On the other hand, two smaller push-pull dimers, namely **D-1** and **D-2** based on TPA, were investigated. The dimer **D-2** exhibiting a longer and hydrophilic oligoethyleneoxy σ-linker between the two push-pull moieties, showed a much higher solubility in chloroform than **D-1** having a short ethylene σ-linker. After optimization of the D/A weight-to-weight ratio and the thickness of the photoactive layer, solution-processed BHJ OSCs of each dimers with $PC_{71}BM$ gave a PCE of 3.4% for **D-1** and 2.8% for **D-2**. Taking into account the ease of synthesis of these multimers and the photovoltaic efficiency of **D-1** for example, this approach would deserve further developments.

In conclusion, this work has shown that small push-pull π-conjugated molecules combining absorption in the visible spectrum and good hole transporting properties such as **DPMA-T-DCV**, can be efficiently used as donors for OPV. In this context, evaluation of hole mobility values of the new donors described in this PhD thesis and future materials by the Space Charge Limited Current method would be useful to complete this work. Some of the titled molecules are particularly suitable for the fabrication of performant all vacuum-processed BHJ OSCs with C_{60} or C_{70}. Work in this direction should be pursued. Using molecular or polymeric non-fullerene acceptors with complementary absorption properties could be also another alternative to increase the performance of OSCs derived from push-pull π-conjugated molecules.

Experimental procedures

1. General information

All reagents and chemicals from commercial sources were used without further purification. Solvents were dried and purified using standard techniques. Column chromatography was performed with analytical-grade solvents using Aldrich silica gel (technical grade, pore size 60 Å, 230-400 mesh particle size). Flexible plates ALUGRAM® Xtra SIL G UV254 from MACHEREY-NAGEL were used for TLC. Compounds were detected by UV irradiation (Bioblock Scientific) or staining with iodine, unless otherwise stated.

NMR spectra were recorded on a Bruker AVANCE III 300 (^{1}H, 300 MHz; ^{13}C, 75 MHz) or a Bruker AVANCE DRX500 (^{1}H, 500 MHz; ^{13}C, 125 MHz). Chemical shifts are given in parts per million (ppm) relative to TMS and coupling constants *J* in Hertz (Hz). **Infrared spectra** were recorded on a Bruker spectrometer Vertex 70. **High Resolution Mass Spectrometry (HRMS)** was performed with a JEOL JMS-700 B/E. **UV-visible absorption spectra** were recorded at room temperature on a Perkin Elmer 950 spectrometer or a Shimadzu UV-1800 spectrometer. **Emission spectra** were recorded on a spectrofluorimeter from Shimadzu RF-6000. **DSC and TGA** were performed with TA Instruments Q20 and Q500 respectively.

Electrochemical measurements were performed using a Biologic SP-150 potentiostat with positive feedback compensation. Samples were dissolved in dichloromethane HPLC grade, purchased from Carlo Erba (HPLC grade). Tetrabutylammonium hexafluorophosphate (0.1 M as supporting electrolyte) was purchased from Sigma-Aldrich and recrystallized prior to use. Experiments were carried out under an inert atmosphere (Ar), in a one-compartment cell equipped with platinum working microelectrode (Ø = 1 or 2 mm) and a platinum wire counter electrode. A silver wire immersed in 0.10 M Bu_4NPF_6/CH_2Cl_2 was used as pseudo-reference electrode and checked against ferrocene/ferrocenium couple (Fc/Fc^+) before and after each experiment.

X-Ray Diffraction: Single crystals of the compounds were mounted on glass fibre loops using a viscous hydrocarbon oil to coat the crystal and then transferred directly to cold nitrogen stream for data collection. Data collection were mostly performed at 150 K on an Agilent Supernova with CuKα (λ = 1.54184 Å). The structures were solved by direct methods with the SIR97 program and refined against all F2 values with the SHELXL-97 program using the WinGX graphical user interface.

Atomic force microscopy (AFM) experiments were performed using the Nano-Observer device from CS Instrument. The topographic images were obtained at room temperature in tapping mode. Images were processed with the Gwyddion free SPM data analysis software.

2. Device fabrication techniques

Organic solar cells (OSCs) have been fabricated by using two different techniques for the deposition of thin-films either by spin-coating or by thermal vacuum evaporation.

2.1 Spin-coating

Spin coating is the simple way to prepare thin films of donors or blend of donors and acceptors for OSCs. The thickness of thin films can be controlled by selecting the speed rate of the spin coater while the thickness can be measured by profilometry.

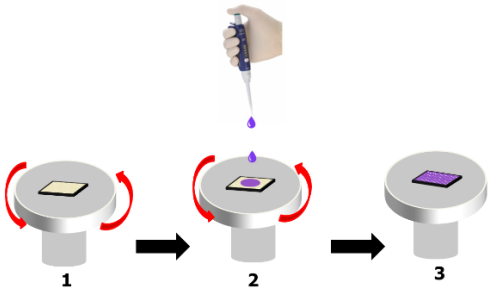

Figure 1: Spin-coating process: 1) acceleration to the maximum speed rate, 2) injection of a precise amount of solution and 3) drying of the thin-film under spinning.

The spin-coating process requires three steps. Initially, the ITO substrate is accelerated to the maximum speed rate, with an acceleration ramp. In the second step, a specified amount of solution is dropped at once on the substrate. The centrifugal force leads to the spreading of the solution to form a film on the surface of the substrate. In the third step, the thin film is dried by acceleration. This process was always used for the deposition of donor materials, blends of donor and acceptor or buffer materials dissolved in a specific solvent. Solution-processed thin-films were prepared in atmospheric conditions (using a spin-coater from Ossila) or within the glovebox (using a spin-coater provided by MBraun).

By contrast, PEDOT:PSS films were prepared in atmospheric conditions (spin coater from Ossila) by depositing four drops of the commercial PEDOT:PSS suspension on the ITO substrate before starting the spinning process.

2.2 Thermal vacuum deposition

Thermal vacuum evaporation was used for deposition of thin films of donors, C_{60} and C_{70}, interlayers (MoO_3, BCP, LiF) and metallic electrodes (Al, Ag). Source boats made of ceramic were used for thermal vacuum evaporation of organic materials whereas deposition of Al, Ag, MoO_3 and LiF was achieved using

boats of molybdenum. The evaporator chamber (MB-ECOVAP from MBraun) which is installed within one of the glovebox of the double glovebox (MBraun), includes shutters and quartz to select the product to be evaporated and exactly control the thickness of each deposited thin-films. The organic/inorganic materials are loaded in the boats and then a high vacuum of *ca*. 10^{-7} mbar is produced within the thermal evaporator chamber. The substrate holder is rotating during evaporation to obtain more homogeneous thicknesses.

Table.1 Compound thermal evaporator deposition rate.

Compound	Evaporation speed rate (Å/S)	Thickness (nm)
LiF	~0.5	1
Ca	~0.5	15
MoO_3	~0.7	7-15
BCP	~0.4 (~104 °C)	8
DPMA-T-DCV	~0.5 (~119 °C)	15-25
DPMA-T-T-DCV	~0.5 (~125 °C)	23
C_{60}/C_{70}	~1.5	30
Al/Ag	First step ~0.8 Second step ~1.5 Third step ~2-2.5	First step 30 Second step 60 Third step 100

3. Device characterization

3.1. J-V characteristics

J-V curves were recorded in the dark and under illumination using a Keithley 236 source-measure unit and a home-made acquisition program. The light source is an AM1.5 Oriel Sol3A^{TM} class AAA solar simulator- Newport equipped with a Xenon lamp, 100 mW.cm^{-2}. The light intensity was measured by a broad-band power meter (13PEM001, Melles Griot). All equipments are installed within the glovebox.

3.2 External Quantum Efficiency measurements (EQE)

EQE spectra were measured under an inert atmosphere with a QUESA–1200 (TFSC Instrument) using monochromatic wavelengths emitted by LEDs.

3.3 Photoemission yield Spectroscopy in Air (PYSA)

PYSA spectra were recorded on thin-film on ITO using a Riken AC-2 photoelectron spectrometer to measure the HOMO level of organic materials.

3.4 Space Charge Limited Current (SCLC) method

The Space Charge Limited Current (SCLC) method has been used for evaluating the mobility of holes and electrons of organic semiconductors. This method is based on the relationship between current density J and voltage V. A space-charge limited current occurs when the metal/semiconductor contact is Ohmic, *i.e.* when the metal resistance is negligible compared to that of the semiconductor. The electrode then behaves as an infinite load reserve and the current is limited only by the volume of the semiconductor. A space charge is formed in the vicinity of the interface which tends to oppose to the flow of the current. With the application of a sufficiently large electric field, this space charge is moved towards the electrode and a saturation current is established.

The mobility μ (in $cm^2\ V^{-1}\ s^{-1}$) can be estimated from the J (in $A\ cm^{-2}$) *vs* V (in V) curve respect to the following equation (Mott-Gurney's law):

$$J_{SCLC} = \frac{9}{8}\frac{\varepsilon_0 \epsilon_r}{L^3}\mu V^2$$

$$\mu = \frac{8}{9}\frac{L^3}{\varepsilon_0 \varepsilon_r}\frac{J_{SCL}}{V^2} \approx 3.35 \times 10^{12}.L^3\frac{J_{SCLC}}{V^2}$$

Where ε_0 is the vacuum permittivity ($8.854187 \times 10^{-14}\ F\ cm^{-1}$), ε_r is the static dielectric constant of the medium (ε_r = 3 ; commonly accepted value for organic materials) and L, the thickness of the active layer (in cm).

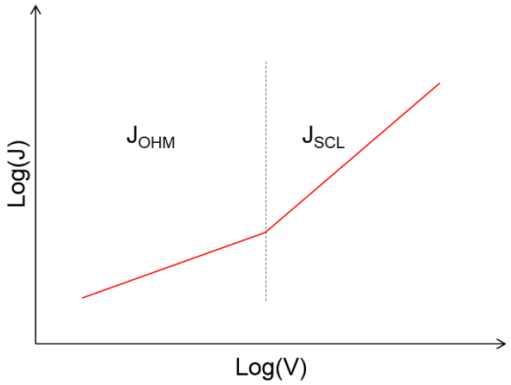

Figure 2: J-V characteristic in logarithmic scale of a unipolar device used to evaluate the mobility of charge carriers by the SCLC method.

3.4.1 Preparation of devices for evaluation of carrier mobility by the SCLC method

ITO substrates are cleaned following the procedure as described in section 4.1 (see below). PEDOT: PSS conducting films were then prepared as in section 4.2 (see below). Then, a solution of the material dissolved in chloroform (20 mg/ mL) is deposited by spin-coating at 800 rpm on an ITO/PEDOT:PSS or ITO substrate only for the determination of the hole-mobility (μ_h) or the electron-mobility (μ_e) value, respectively. Finally, the devices are completed by evaporation of gold (150 nm) using a pressure of 10^{-6} mbar for "hole only " devices, or LiF (1 nm) and then aluminum (150 nm) using a pressure of 10^{-7} mbar for "electron only" devices, through a mask defining four different surface disk areas (28.26 mm², 12.60 mm², 3.10 mm² and 0.78 mm²) as represented in Figure 3.

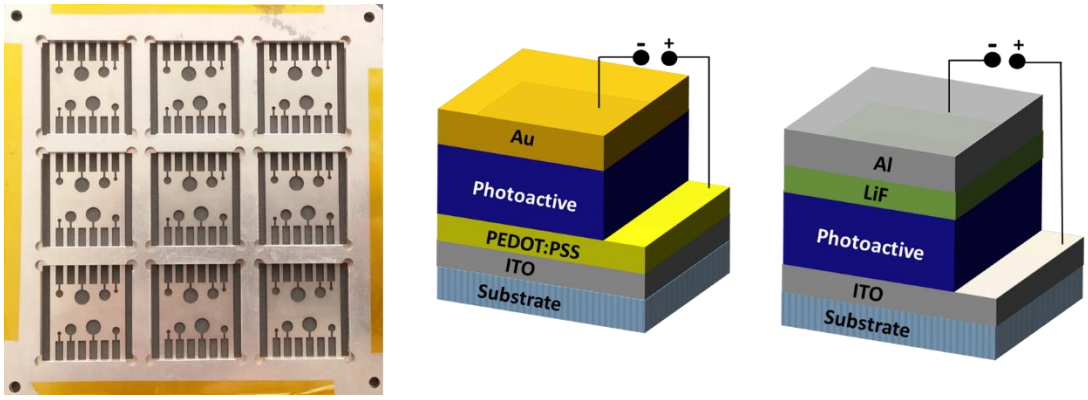

Figure 3: Holder for nine ITO substrates with a mask for each defining four different disk surface areas (left). Architectures of devices for measurement of hole mobility (middle) and electron mobility (right).

These devices are characterized in the glovebox under argon. The J-V curves are recorded by measuring the product current as a function of the voltage that is applied between the terminals using a Keithley 236 unit and an acquisition interface programmed under LabVIEW.

4. Preparation of substrates and deposition conditions

4.1 Preparation of ITO substrates

Pre-patterned *indium-tin oxide* (ITO) coated glass slides of 24 x 25 x 1.1 mm with a sheet resistance of Rs = 7 $\Omega.sq^{-1}$ were purchased from Visiontek Systems. To remove the contaminants from their surface, the ITO substrate were cleaned in ultrasonic baths for at least 15 minutes for each step in the following

order: *deionized water* with *detergent* (Deconex® 12 PA-x solution, 2 drops), then *acetone* and finally *ethanol*. Once dried under a steam of air, a UV-ozone plasma treatment (Ossila UV/Ozone cleaner E511) was performed for 15 minutes ensuring elimination of residual organic contaminants of the ITO substrates which were used rapidly for the next step.

4.2. Deposition of PEDOT:PSS

A filtered aqueous solution of poly(3,4-ethylenedioxy-thiophene):poly(styrenesulfonate) (PEDOT:PSS purchased from Ossila, Al 4083) through a 0.45 μm RC membrane (Minisart® RC 15) was deposited (four to five drops) on the cleaned ITO substrates and then spun-cast at 5000 rpm for 40 s. The edge parts of the conductive polymer film are removed by cotton swabs before being baked at 120 °C for 30 min. All these previous steps have been done outside the glovebox, however the baked PEDOT:PSS films must covered or introduced in the glovebox as soon as possible to avoid any reabsorption of water from the atmosphere. The thickness of PEDOT:PSS thin film was measured by profilometer leading to a value of around 24 nm. The PEDOT:PSS layer has several functions, first it serves as a hole transporter and exciton blocker. Secondly, the deposition of a PEDOT:PSS film on ITO substrates reduces the roughness of the surface. In addition, the PEDOT:PSS film protects the active layer from oxygen diffusion from ITO.

4.3 Deposition of ZnO

Zinc acetate dihydrate (196 mg, 1 equiv.) and ethanol amine (54 μL, 1 equiv.) were added into 6 mL of absolute ethanol. The solution was stirred at 45°C for 2 hours and was used without any further purification. This ZnO solution (80 μL) was then spun-cast onto the patterned ITO surface described above at 2000 rpm for 60 s before being baked at 180°C for 15 min.

4.4. Deposition of electrodes

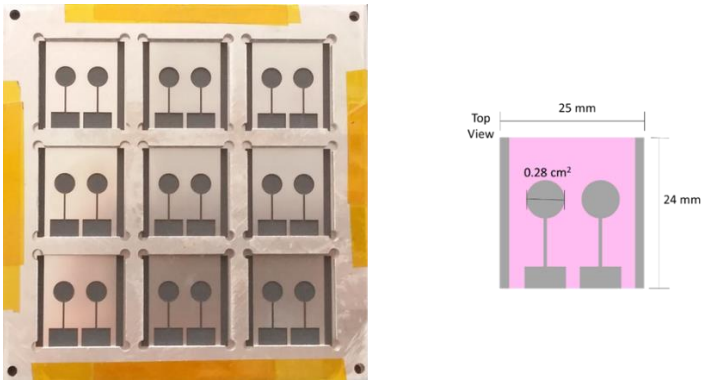

Figure 4: Holder for nine ITO substrates with a mask for each defining two cells with disk surface area of 0.28 cm^2.

The thermal vacuum deposition aluminium or silver electrodes (100 nm of thickness) was performed in the vacuum chamber within the glovebox at a pressure of 10^{-7} mbar, through a mask defining two disk cells per substrate, with an area of 0.28 cm^2 (Figure 4).

5. Synthetic procedures

The synthetic part has involved different contributors:

- I have synthesized compounds **1**, **2**, **3**, **DPMA-T-DCV** and tetramer **T-2**,
- Pierre Josse (PhD) for compounds **7-12**, **DPMA-Se-DCV**, **MeCz-T-DCV**, **MeCz-Se-DCV** and dimer **D-1**,
- Illia Lenko (Master) for compounds **4**, **6** and **DPMA-T-T-DCV**,
- Antoine Labrunie (PhD) for compounds **16**, **17** and dimer **D-2**.

Tributyl(selenophen-2-yl)stannane was prepared according to a reported procedure.[1]

4-Bromo-N-methyl-N-phenylaniline (1): To a suspension of sodium hydride (60% in mineral oil ; 1.93 g ; 48.36 mmol) in anhydrous THF (50 mL) under an argon atmosphere at 0 °C was added a solution of 4-bromo-N-phenylaniline (3 g ; 12.09 mmol) in 30 mL of anhydrous THF. The mixture was stirred at 50 °C for 1 h and iodomethane (10.30 g ; 72.54 mmol) was added dropwise. The reaction mixture was heated overnight at 50 °C before being allowed to cool down to room temperature. Cold water was added slowly and the product was extracted with dichloromethane. Organic layers were washed with water and dried over $MgSO_4$. The solvent was then removed by rotary evaporation and the crude was purified by silica gel column chromatography (petroleum ether:dichloromethane 4:1 v/v) affording the desired product as a white solid (2.99 g ; 95%). Spectroscopic data matched those previously reported.[2]

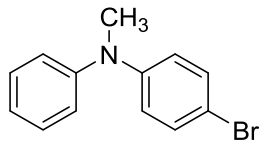

1

N-Methyl-N-phenyl-4-(thiophen-2-yl)aniline (2): Compound **1** (2.9 g ; 11.06 mmol) and tetrakis-(triphenylphosphine)palladium(0) (220 mg ; 5% mol) were degassed under vacuum in a flame dried Schlenk tube equipped with a stir bar for 30 minutes. A solution of 2-(tributylstannyl)thiophene (6.18 g ; 24.28 mmol) in HPLC grade toluene (100 mL ; degassed by argon bubbling for 30 minutes) was added to the powders and the reaction mixture was heated overnight at 90°C under an argon atmosphere. After cooling down to room temperature, dichloromethane was added and the organic layer was washed with water and brine. Solvents were removed *in vacuo* and the crude was purified by silica gel column chromatography (petroleum ether:dichloromethane 8:2 v/v) to afford the product (1.7 g ; 58%). Spectroscopic data matched those previously reported.[2]

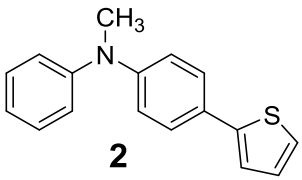

2

5-(4-(Methyl(phenyl)amino)phenyl)thiophene-2-carbaldehyde (3): To a solution of **2** (1 g ; 3.77 mmol) and DMF (390 mg ; 5.34 mmol) in anhydrous 1,2-dichloroethane (50 mL) was added $POCl_3$ (640 mg ; 4.17 mmol) at 0°C. The mixture was then heated overnight at 80°C under an argon atmosphere. After cooling, the mixture was poured into a 1 M aqueous solution of sodium acetate (100 mL) and stirred for 2 h. After separation of the organic phase by decantation, the aqueous phase was extracted with dichloromethane.

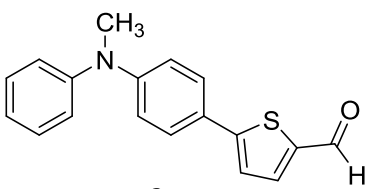

3

Organic layers were gathered and washed with water, dried over $MgSO_4$ and evaporated *in vacuo*. The crude was purified by silica gel column chromatography using dichloromethane as eluent. The product was obtained in a 54% yield (600 mg). Spectroscopic data matched those previously reported.[2] ^{1}H NMR (300 MHz, $CDCl_3$) δ 9.86 (s, 1H), 7.71 (d, J = 3.9 Hz, 1H), 7.56 (d, J = 8.7 Hz, 2H), 7.40, (t, J = 7.7 Hz, 2H), 7.29 (d, J = 3.5 Hz, 1H), 7.22-7.16 (m, 3H), 6.91 (d, J = 8.8 Hz, 2H), 3.39 (s, 3H).

2-((5-(4-(Methyl(phenyl)amino)phenyl)thiophen-2-yl)methylene)malononitrile (DPMA-T-DCV): Compound **3** (500 mg ; 1.70 mmol) and malononitrile (225 mg ; 3.41 mmol) were dissolved in HPLC grade $CHCl_3$ (50 mL). Six drops of triethylamine were added and the reaction mixture was stirred overnight at room temperature. After evaporation of the solvent, the crude was purified two times on silica gel column chromatography using a mixture of petroleum ether and dichloromethane (2:8 v/v) as eluent leading to a blue-green dark powder (502 mg; 88% yield). The green powder was recrystallized from a mixture of CH_2Cl_2 and pentane to give a dark crystalline product (475 mg; 83%). Spectroscopic data matched those previously reported.[2]

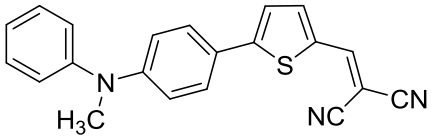

DPMA-T-DCV

(4-(Methyl(phenyl)amino)phenyl)boronic acid (4): Compound **1** (6 g, 22.89 mmol) was dissolved in anhydrous THF (60 mL). Under argon, the mixture was cooled to -78 °C and *n*-Buli (11 mL, 25.18 mmol, 2.5 M in hexanes) was added dropwise. After 1 h at -78 °C, triisopropyl borate (11 mL, 45.78 mmol) was added in one portion and the mixture was allowed to slowly warm up to rt. After 16 h, the mixture was quenched with a 2 M aqueous solution of HCI and the mixture was poured into a large amount of water. After extraction with ethyl acetate, the organic layer was washed with brine dried over $MgSO_4$, and concentrated *in vacuo*. The crude was dissolved in a minimum amount of $CHCl_3$, and pentane was added to precipitate the compound. The resulting precipitate was filtered off and washed thoroughly with pentane affording a white powder (1.5 g ; 29%). Spectroscopic data matched those previously reported.[3] ^{1}H NMR ($CDCl_3$) δ 8.04 (d, J- 8.6 Hz, 2H). 7.43 - 7.32 (m, 2H), 7.24 -7.11 (m, 3H), 6.93 (d, J = 8.7 Hz, 2H), 3.39 (s, 3H).

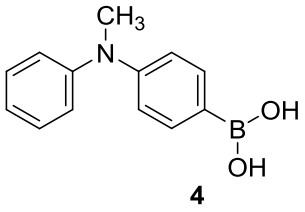

4

5'-(4-(Methyl(phenyl)amino)phenyl)-[2,2'-bithiophene]-5-carbaldehyde (6): $NaHCO_3$ (504 mg, 7.21 mmol), 5'-bromo-[2,2'-bithiophene]-5-carbaldehyde (547 mg, 2 mmol), (4-(methyl(phenyl)amino)phenyl)boronic acid (500 mg, 2.2 mmol,) and $Pd(PPh_3)_4$ (122 mg, 0.1 mmol) was suspended in DMF (16 mL) and H_2O (10 mL). The mixture was irradiated under microwaves (CEM®-Discover) for 20 min at a preselected temperature of 150 °C, using a maximum irradiation power of 150 W. When the solution was cooled down, CH_2Cl_2 (150 mL) was added and the organic layer was washed with brine (30 mL) and water (3 x 30 mL). The crude was purified on silica gel (CH_2Cl_2) to give an orange powder (695 mg, yield: 92%). mp. 149-154 °C. ^{1}H NMR ($CDCl_3$) 9.85 (s, 1H), 7.67 (d, J = 4.0 Hz, 1H), 7.48 (d, J = 8.8 Hz, 2H), 7.39-7.29 (m, 4H), 7.23 (d, J = 4.0 Hz, 1H), 7.19-7.05 (m, 3H), 6.93 (d, J = 8.8 Hz, 2H), 3.36 (s, 3H). ^{13}C NMR ($CDCl_3$) δ 182.41, 149.12, 148.25, 146.85, 141.09, 137.53, 133.50, 129.53, 127.28, 126.68, 124.81, 123.58, 123.40, 123.32, 122.61, 117.76, 40.24. HRMS (EI) calcd for $C_{22}HNOS_2$: [M+]: 375.07225, found: 375.0743.

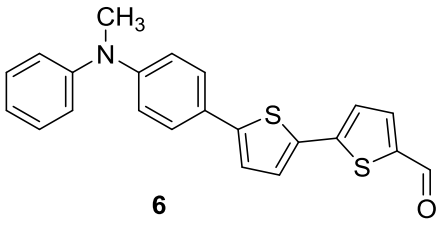

6

2-((5'-(4-(Methyl(phenyl)amino)phenyl)-[2,2'-bithiophenl]-5-yl)methylene)malononitrile (DPMA-T-T-DCV): Three drops of triethylamine were added to a solution of the aldehyde **6** (200 mg) and malononitrile (70 mg) in $CHCl_3$ (50 mL). The mixture was stirred overnight at rt in the dark. Then the solvent was removed by evaporation and the crude was purified by column chromatography on silica gel (eluent: CH_2Cl_2) and precipitation with $CHCl_3$/pentane leading to a green powder (192 mg, 85% yield). mp. 184-187 °C. ^{1}H NMR ($CDCl_3$) δ 7.73 (s, IH), 7.62 (d, J= 4.2 Hz, IH), 7.48 (d, J = 8.8 Hz, 2H), 7.41 7.32 (m, 4H), 7.26 (s, IH), 7.20-7.08 (m, 3H), 6.91 (d. J = 8.8 Hz, 2H), 3.37 (s, 3H). ^{13}C NMR ($CDCl_3$) δ 150.07, 149.96, 149.44, 148.56, 148.07 , 140.34 , 132.90, 132.47, 129.60, 128.59, 126.77, 124.09, 123.90, 123.87, 122.88, 117.16, 113.68, 75.17, 40.24, 30.96. HRMS (EI) calcd for $C_{25}H_{17}N_3S_2$: [M+]: 423.0864, found: 423.0859.

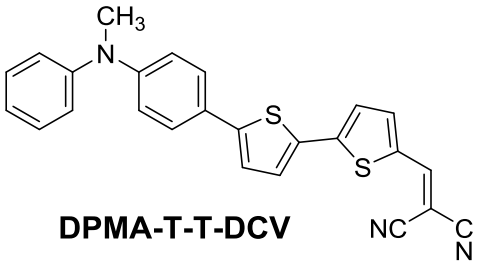

DPMA-T-T-DCV

5-(4-(Methyl(phenyl)amino)phenyl)thiophene-2-carbaldehyde (3): Compound **1** (500 mg ; 1.91 mmol), palladium(II) acetate (21 mg ; 5% mol.), pivalic acid (58 mg ; 30% mol.) and potassium carbonate (395 mg ; 2.86 mmol) were degassed under vacuum in a dry Schlenk tube equipped with a stir bar. Dry and degassed dimethylacetamide (15 mL, argon bubbling for 30 min) and thiophene-2-carbaldehyde (235 mg ; 2.10 mmol) were added to the powders and the reaction mixture was heated overnight at 80 °C under an argon atmosphere. After cooling down to room temperature, dichloromethane was added and the organic layer was washed with water and brine. The solvent was removed by rotary evaporation and the crude was purified by silica gel column chromatography using dichloromethane as eluent. (130 mg ; 23%). Spectroscopic data matched those previously reported.[2]

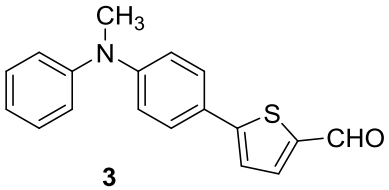

3

N-Methyl-N-phenyl-4-(selenophen-2-yl)aniline (7): Compound **1** (1 g ; 3.81 mmol) and tetrakis(triphenylphosphine) palladium(0) (220 mg ; 5% mol.) were degassed under vacuum in a flame dried Schlenk tube equipped with a stir bar for 30 minutes. A solution of tributyl(selenophen-2-yl)stannane (1.76 mg ; 4.20 mmol) in HPLC grade toluene (40 mL ; degassed by argon bubbling for 30 minutes) was added to the powders and the reaction mixture was heated overnight at 90 °C under an argon atmosphere. After cooling down to room temperature, dichloromethane was added and the organic layer was washed with water and brine. Solvents were removed *in vacuo* and the crude was purified by silica gel column chromatography (petroleum ether:dichloromethane 8:2 v/v) affording compound **7** (600 mg ; 50% yield). ^{1}H NMR (300 MHz, $CDCl_3$) δ 7.85 (dd, *J* = 5.6, 1.1 Hz, 1H), 7.48 – 7.42 (m, 2H), 7.37 – 7.26 (m, 4H), 7.14 – 7.08 (m, 2H), 7.06 – 7.00 (m, 1H), 6.98 – 6.93 (m, 2H), 3.35 (s, 3H). ^{13}C NMR (76 MHz, $CDCl_3$) δ 151.13, 148.69, 148.61, 130.70, 129.48, 128.78, 128.67, 127.31, 123.91, 122.54, 122.16, 119.11, 40.32. HRMS (EI) calculated for $C_{17}H_{15}NSe$ 313.0370, found 313.0364 (Δ = 1.8 ppm).

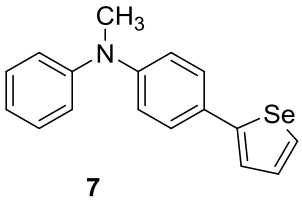

7

5-(4-(Methyl(phenyl)amino)phenyl)selenophene-2-carbaldehyde (8): To a solution of **7** (200 mg ; 640 µmol) and DMF (58 mg ; 800 µmol) in anhydrous 1,2-dichloroethane (10 mL) was added $POCl_3$ (122 mg ; 800 µmol) at 0°C. The mixture was then heated overnight at 80 °C under an argon atmosphere. After cooling, the mixture was poured into a 1 M aqueous solution of sodium acetate (100 mL) and stirred for 2 h. After separation

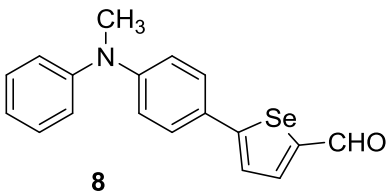

8

of the organic phase by decantation, the aqueous phase was extracted with dichloromethane. Organic layers were gathered and washed with water, dried over $MgSO_4$ and evaporated *in vacuo*. The crude was purified by silica gel column chromatography using dichloromethane as eluent. The product was obtained in a 55% yield (120 mg). ^{1}H NMR (300 MHz, $CDCl_3$) δ 9.71 (s, 1H), 7.93 (d, *J* = 4.2 Hz, 1H), 7.51 – 7.45 (m, 2H), 7.43 (d, *J* = 4.2 Hz, 1H), 7.40 – 7.34 (m, 2H), 7.21 – 7.12 (m, 3H), 6.89 – 6.84 (m, 2H), 3.37 (s, 3H). ^{13}C NMR (76 MHz, $CDCl_3$) δ 183.98, 162.34, 150.29, 147.98, 146.28, 141.29, 129.83, 127.79, 125.97, 124.73, 124.56, 124.20, 116.49, 40.35. HRMS (EI) calculated for $C_{18}H_{15}NOSe$ 341.0319, found 341.0314 (Δ = 1.4 ppm).

2-((5-(4-(Methyl(phenyl)amino)phenyl)selenophen-2-yl)methylene)malononitrile (DPMA-Se-DCV): Compound **8** (120 mg ; 352 µmol) and malononitrile (46 mg ; 705 µmol) were dissolved in HPLC grade $CHCl_3$ (10 mL). One drop of triethylamine was added and the reaction mixture was stirred overnight at room temperature. After evaporation of the solvent, the crude was purified on silica gel column chromatography using dichloromethane as eluent. The collected product was concentrated *in vacuo* and precipitated into freshly distilled pentane (50 mL). The pure product was obtained after filtration and drying under vacuum overnight (132 mg ; 96%). ^{1}H NMR (300 MHz, $CDCl_3$) δ 7.79 (d, *J* = 4.5 Hz, 1H), 7.77 (s, 1H), 7.52 – 7.47 (m, 2H), 7.44 – 7.37 (m, 3H), 7.21 (ddt, *J* = 7.2, 3.1, 1.4 Hz, 3H), 6.84 – 6.79 (m, 2H), 3.38 (s, 3H). ^{13}C NMR (76 MHz, $CDCl_3$) δ 166.20, 153.28, 151.05, 147.49, 145.15, 136.55, 129.99, 128.17, 125.63, 125.43, 124.53, 123.73, 115.59, 114.96, 114.42, 74.07, 40.40. HRMS (EI) calculated for $C_{21}H_{15}N_3Se$ 389.0431, found 389.0430 (Δ = 0.3 ppm).

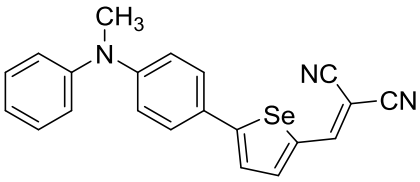

DPMA-Se-DCV

9-Methyl-3-(selenophen-2-yl)-9H-carbazole (9): 3-Bromo-9-methyl-9H-carbazole (300 mg ; 1.15 mmol) and tetrakis(triphenylphosphine) palladium(0) (66 mg ; 5% mol.) were degassed under vacuum in a flame dried Schlenk tube equipped with a stir bar for 30 minutes. A solution of tributyl(selenophen-2-yl)stannane (533 mg ; 1.27 mmol) in HPLC grade toluene (20 mL ; degassed by argon bubbling for 30 minutes) was added to the powders and the reaction mixture was heated overnight at 90 °C under an argon atmosphere. After cooling down to room temperature, dichloromethane was added and the organic layer was washed with water and brine. Solvents were removed *in vacuo* and the crude was purified by silica gel column chromatography (petroleum ether:dichloromethane 7:3 v/v) to afford the product (160 mg ; 45%). ^{1}H NMR (300 MHz, $CDCl_3$) δ 8.28 (d, *J* = 1.8 Hz, 1H), 8.13 (dt, *J* = 7.9, 0.9 Hz, 1H), 7.91 (dd, *J* = 5.6, 1.2 Hz, 1H), 7.71 (dd, *J* = 8.5, 1.9 Hz, 1H), 7.54 – 7.47 (m, 2H), 7.43 – 7.33 (m, 3H), 7.26 (dd, *J* = 14.8, 1.1 Hz, 1H), 3.87 (s, 3H). ^{13}C NMR (76 MHz, $CDCl_3$) δ 152.41, 141.63, 140.76, 130.79, 128.83, 127.92, 126.21, 124.90, 124.22, 123.35, 122.85, 120.62, 119.29, 118.40, 108.85, 108.80, 29.36. HRMS (FAB+) calculated for $C_{17}H_{13}NSe$ 311.0213, found 311.0206 (Δ = 2.3 ppm).

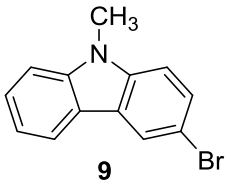

9

5-(9-Methyl-9H-carbazol-3-yl)thiophene-2-carbaldehyde (10): 3-Bromo-9-methyl-9H-carbazole (200 mg ; 768 µmol), palladium(II) acetate (9 mg ; 5% mol.), pivalic acid (23 mg ; 30mol%) and potassium carbonate (159 mg ; 1.15 mmol) were degassed under vacuum in a dry Schlenk tube equipped with a stir bar. Dry and degassed dimethylacetamide (10 mL, argon bubbling for 30 min) and thiophene-2-carbaldehyde (172 mg ; 1.54 mmol) were added to the powders and the reaction mixture was heated overnight at 80 °C under an argon atmosphere. After cooling down to room temperature, the crude was dried by rotary evaporation before being solubilized in a minimum amount of $CHCl_3$ and flashed through a short plug of

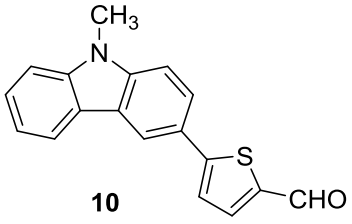

10

silica to remove the catalyst and baseline impurities. Then, to reach a high degree of purity, the resulting product dissolved in $CHCl_3$ was injected in a recycling preparative size-exclusion HPLC. The product was obtained in 25% yield (57 mg). ^{1}H NMR (300 MHz, $CDCl_3$) δ 9.89 (s, 1H), 8.41 (d, *J* = 1.7 Hz, 1H), 8.15 (d, *J* = 7.7 Hz, 1H), 7.81 (dd, *J* = 8.5, 1.9 Hz, 1H), 7.77 (d, *J* = 4.0 Hz, 1H), 7.53 (ddd, *J* = 8.2, 7.1, 1.2 Hz, 1H), 7.48 – 7.42 (m, 3H), 7.33 – 7.27 (m, 1H), 3.90 (s, 3H). ^{13}C NMR (76 MHz, $CDCl_3$) δ 182.79, 156.49, 147.16, 141.73, 141.38, 140.93, 139.81, 138.06, 126.65, 124.61, 123.51, 123.04, 122.69, 120.70, 119.80, 118.64, 113.23, 109.21, 109.02, 29.45. HRMS (CI+) calculated for $C_{18}H_{13}NOS$ 291.0718, found 292.0798 (Δ = 0.6 ppm).

2-((5-(9-Methyl-9H-carbazol-3-yl)thiophen-2-yl)methylene)malononitrile (MeCz-T-DCV):

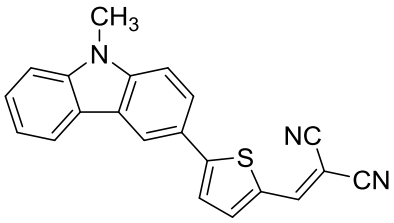

MeCz-T-DCV

Compound **10** (57 mg ; 195 µmol) and malononitrile (26 mg ; 391 µmol) were dissolved in HPLC grade $CHCl_3$ (10 mL). One drop of trimethylamine was added and the reaction mixture was stirred overnight at room temperature. After evaporation of the solvent, the crude was solubilized in a minimum amount of $CHCl_3$ and flashed through a short plug of silica to remove the catalyst and baseline impurities. Then, to reach a high degree of purity, the resulting product dissolved in $CHCl_3$ was injected in a recycling preparative size-exclusion HPLC. The product was obtained in 60% yield (41 mg). ^{1}H NMR (300 MHz, $CDCl_3$) δ 8.43 (d, *J* = 1.8 Hz, 1H), 8.17 (dt, *J* = 7.7, 1.0 Hz, 1H), 7.83 (dd, *J* = 8.6, 1.9 Hz, 1H), 7.79 (s, 1H), 7.73 (d, *J* = 4.1 Hz, 1H), 7.55 (ddd, *J* = 8.3, 7.1, 1.2 Hz, 1H), 7.51 (d, *J* = 4.2 Hz, 1H), 7.45 (d, *J* = 8.4 Hz, 2H), 7.32 (ddd, *J* = 8.0, 7.1, 1.1 Hz, 1H), 3.90 (s, 3H). ^{13}C NMR (126 MHz, $CDCl_3$) δ 159.19, 150.65, 142.22, 141.80, 140.88, 133.24, 126.93, 124.79, 123.73, 123.53, 122.64, 120.87, 120.15, 119.09, 114.82, 113.98, 109.43, 109.17, 74.89, 29.52. HRMS (EI) calculated for $C_{21}H_{13}N_3S$ 339.0830, found 339.0832 (Δ = 0.5 ppm).

9-Methyl-3-(selenophen-2-yl)-9H-carbazole (11): 3-Bromo-9-methyl-9H-carbazole (300 mg ; 1.15 mmol) and tetrakis(triphenylphosphine) palladium(0) (66 mg ; 5% mol.) were degassed under vacuum in a flame dried Schlenk tube equipped with a stir bar for 30 min. A solution of tributyl(selenophen-2-yl)stannane (533 mg ; 1.27 mmol) in HPLC grade toluene (20 mL ; degassed by argon bubbling for 30 minutes) was added to the powders and the reaction mixture was heated overnight at 90 °C under an argon atmosphere. After cooling down to room temperature, dichloromethane was added and the organic layer was washed with water and brine. Solvents were removed *in vacuo* and the crude was purified by silica gel column chromatography (petroleum ether:dichloromethane 7:3 v/v) affording compound **11** (160 mg ; 45%). ^{1}H NMR (300 MHz, $CDCl_3$) δ 8.28 (d, J = 1.8 Hz, 1H), 8.13 (dt, J = 7.9, 0.9 Hz, 1H), 7.91 (dd, J = 5.6, 1.2 Hz, 1H), 7.71 (dd, J = 8.5, 1.9 Hz, 1H), 7.54 – 7.47 (m, 2H), 7.43 – 7.33 (m, 3H), 7.26 (dd, J = 14.8, 1.1 Hz, 1H), 3.87 (s, 3H). ^{13}C NMR (76 MHz, $CDCl_3$) δ 152.41, 141.63, 140.76, 130.79, 128.83, 127.92, 126.21, 124.90, 124.22, 123.35, 122.85, 120.62, 119.29, 118.40, 108.85, 108.80, 29.36. HRMS (FAB+) calculated for $C_{17}H_{13}NSe$ 311.0213, found 311.0206 (Δ = 2.3 ppm).

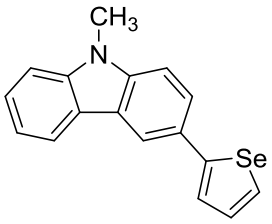

11

5-(9-Methyl-9H-carbazol-3-yl)selenophene-2-carbaldehyde (12): To a solution of **11** (160 mg ; 515 µmol) and DMF (47 mg ; 644 µmol) in anhydrous 1,2-dichloroethane (10 mL) was added $POCl_3$ (99 mg ; 644 µmol) at 0 °C. The mixture was then heated overnight at 80 °C under an argon atmosphere. After cooling, the mixture was poured into a 1 M aqueous solution of sodium acetate (100 mL) and stirred for 2 h. After separation of the organic phase by decantation, the aqueous phase was extracted with dichloromethane. Organic layers were gathered and washed with water, dried over $MgSO_4$ and evaporated *in vacuo*. The crude was purified by silica gel column chromatography using dichloromethane as eluent. The product was obtained in 85% yield (150 mg). ^{1}H NMR (300 MHz, $CDCl_3$) δ 9.76 (s, 1H), 8.33 (d, *J* = 1.9 Hz, 1H), 8.14 (d, *J* = 7.7 Hz, 1H), 8.00 (d, *J* = 4.2 Hz, 1H), 7.74 (dd, *J* = 8.5, 1.8 Hz, 1H), 7.62 (d, *J* = 4.1 Hz, 1H), 7.56 – 7.49 (m, 1H), 7.41 (t, *J* = 8.2 Hz, 2H), 7.29 (ddd, *J* = 8.1, 7.1, 1.1 Hz, 1H), 3.87 (s, 3H). ^{13}C NMR (76 MHz, $CDCl_3$) δ 184.08, 163.44, 146.90, 141.77, 141.74, 141.29, 126.66, 124.98, 123.53, 122.69, 120.72, 119.82, 118.87, 109.17, 109.04, 29.44. HRMS (CI+) calculated for $C_{18}H_{13}NOSe$ 339.0162, found 340.0238 (Δ = 0.8 ppm).

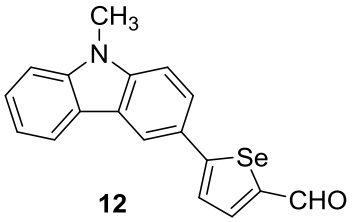

12

2-((5-(9-Methyl-9H-carbazol-3-yl)selenophen-2-yl)methylene)malononitrile (MeCz-Se-DCV): Compound **12** (150 mg ; 443 µmol) and malononitrile (58 mg ; 886 µmol) were dissolved in HPLC grade $CHCl_3$ (10 mL). One drop of trimethylamine was added and the reaction mixture was stirred overnight at room temperature. After evaporation of the solvent, the crude was purified on silica gel column chromatography using dichloromethane as eluent. The collected product was concentrated *in vacuo* and precipitated into freshly distilled pentane (50 mL). The pure product was obtained after filtration and drying under vacuum overnight (162 mg ; 94%). ^{1}H NMR (300 MHz, $CDCl_3$) δ 8.37 (d, *J* = 1.9 Hz, 1H), 8.15 (d, *J* = 7.8 Hz, 1H), 7.86 (d, *J* = 4.4 Hz, 1H), 7.82 (s, 1H), 7.78 (dd, *J* = 8.6, 1.9 Hz, 1H), 7.63 (d, *J* = 4.3 Hz, 1H), 7.55 (ddd, *J* = 8.2, 7.1, 1.2 Hz, 1H), 7.43 (dd, *J* = 8.4, 6.1 Hz, 2H), 7.32 (t, *J* = 7.4 Hz, 1H), 3.89 (s, 3H). ^{13}C NMR (76 MHz, $CDCl_3$) δ 167.15, 153.48, 145.05, 142.31, 141.82, 137.31, 126.96, 125.80, 125.00, 124.62, 123.81, 122.64, 120.82, 120.21, 119.32, 114.79, 114.34, 109.46, 109.21, 74.79, 29.52. HRMS (CI+) calculated for $C_{21}H_{13}N_3Se$ 387.0275, found 387.0273 (Δ = 0.4 ppm).

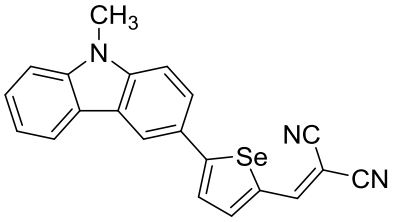

MeCz-Se-DCV

(2E,2'E)-2,2-Bis((((E)-2-cyano-3-(5-(4-(methyl(phenyl)amino)phenyl)thiophen-2-yl)acryloyl)oxy)methyl)propane-1,3-diyl-bis(2-cyano-3-(5-(4-(methyl(phenyl)amino)phenyl)thiophen-2-yl)acrylate) (T-2):[3] Trimethylamine (5 drops) was added to a mixture of aldehyde **3** (250 mg, 0.85 mmol), 2,2-bis((2-cyanoacetoxy)methyl)propane-1,3-diyl bis(2-cyanoacetate) (**13**)[4] (86.14 mg, 0.21 mmol) in $CHCl_3$ (120 mL). This reaction mixture was refluxed for 3 days. After purification by chromatography on silica gel (CH_2Cl_2 to CH_2Cl_2/EtOAc 9.5/0.5 as eluent), the resulting solid was dissolved in $CHCl_3$/ and precipitated with pentane to give **T-2** as red solid (172 mg, 54% yield). mp. 210-212 °C. ^{1}H NMR ($C_2D_2Cl_4$) δ 8.16 (s, 4H), 7.63 (d, J = 4.2 Hz, 4H), 7.42 (d, J = 8.7 Hz, 8H), 7.31 (dd, J = 8.5, 7.1 Hz, 8H), 7.16 (d, J = 4.1 Hz, 4H), 7.15 – 7.06 (m, 12H), 6.75 (d, J = 8.7 Hz, 8H), 4.48 (s, 8H), 3.28 (s, 12H). MS (MALDI) m/z = 1504.4. [M+]. HRMS (FAB) calcd for $C_{89}H_{68}N_8O_8S_4$ [M+]: 1504.4043, found: 1504.4034. IR (neat): $\tilde{\nu}$ = 2218 cm^{-1} (C≡N), $\tilde{\nu}$ = 1703 cm^{-1} (C=O).

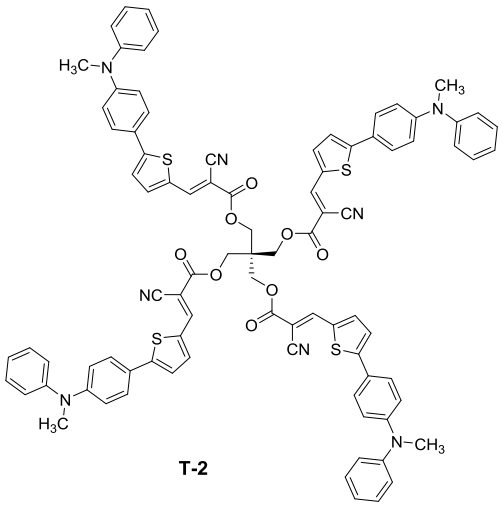

T-2

Ethane-1,2-diyl (2E,2'E)-bis(2-cyano-3-(5-(4-(diphenylamino)phenyl)thiophen-2-yl)acrylate) (D-1):

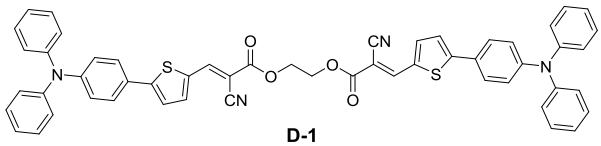

D-1

5-(4-(Diphenylamino)phenyl)thiophene-2-carbaldehyde (**14**)[5-7] (1.20 g ; 3.36 mmol, 2.2 eq.) and ethane-1,2-diyl bis(2-cyanoacetate) (**15**) (300 mg ; 1.53 mmol) were placed in a 250 mL round bottom flask and dissolved into 100 mL of HPLC grade $CHCl_3$. Two drops of Et_3N were added and the reaction mixture was stirred overnight at room temperature. The solvent was then removed by rotary evaporation and the crude was directly subjected to silica gel chromatography (eluent: CH_2Cl_2/PE (8:2), CH_2Cl_2 and then CH_2Cl_2/EtOAc (98:2)) to afford **D-1** (1.08 g ; 81 %) as a red powder. ^{1}H NMR (300 MHz, $CDCl_3$) δ 8.30 (s, 1H), 7.75 (d, *J* = 4.2 Hz, 1H), 7.58 – 7.50 (m, 2H), 7.35 – 7.27 (m, 5H), 7.18 – 7.09 (m, 6H), 7.05 (m, 2H), 4.60 (s, 2H). ^{13}C NMR (76 MHz, $CDCl_3$) δ 163.20, 155.80, 149.58, 147.28, 147.01, 140.17, 133.99, 129.67, 127.58, 125.84, 125.45, 124.19, 123.39, 122.29, 116.15, 96.23, 63.49. HRMS (EI) calculated for $C_{54}H_{38}N_4O_4S_2$ 870.2334, found 870.2338 (Δ = 0.4 ppm).

((Oxybis(ethane-2,1-diyl))bis(oxy))bis(ethane-2,1-diyl) bis(2-cyanoacetate) (16) and 2-(2-(2-(2-hydroxyethoxy)ethoxy)ethoxy)ethyl 2-cyanoacetate (17):

A stirred solution of cyanoacetic acid (3.28 g, 38.61 mmol) and 2,2'-((oxybis(ethane-2,1-diyl))bis(oxy))bis(ethan-1-ol) (5 g, 25.74 mmol) in anhydrous toluene (40 mL) in the presence of 10 drops of conc. H_2SO_4 was heated under reflux for 4 h under argon atmosphere. Then the reaction mixture was cooled to room temperature and quenched with a saturated aqueous solution of $NaHCO_3$ and extracted with AcOEt. The organic layer was washed twice with water and brine, dried over $MgSO_4$ and concentrated *in vacuo*. The residue is purified by column chromatography on silica gel (eluent: AcOEt/petroleum ether 50/50 v/v to 100/0 v/v); TLC stained by $KMNO_4$) to afford compound **17** (3.2 g, 12.25 mmol, 47.6 %) and **16** (2.14 g, 6.52 mmol, 25.3 %) as pale yellow oils.

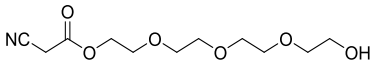

^{1}H NMR (300 MHz, $CDCl_3$): δ 4.38 – 4.32 (m, 2H), 3.75 – 3.68 (m, 4H), 3.65 (bs, 8H), 3.62 – 3.56 (m, 2H), 3.54 (s, 2H). ^{13}C NMR (76 MHz, $CDCl_3$): δ 163.30, 113.23, 77.58, 77.16, 76.74, 72.58, 70.69, 70.56, 70.34, 68.60, 65.79, 61.76, 24.81. HRMS (CI+): calculated for $C_{11}H_{19}NO_6$ 261.12, found 261.1288 (m/z + 1)

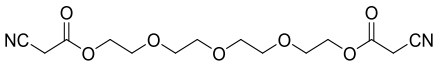

^{1}H NMR (300 MHz, $CDCl_3$): δ 4.40 – 4.31 (m, 4H), 3.76 – 3.69 (m, 4H), 3.66 – 3.61 (m, 8H), 3.52 (s, 4H). ^{13}C NMR (76 MHz, $CDCl_3$): δ 163.21, 113.19, 70.76, 70.66, 68.61, 65.87, 24.83. HRMS (CI+): calculated for $C_{14}H_{20}N_2O_7$ 328.13, found 329.1352 (m/z + 1)

((Oxybis(ethane-2,1-diyl))bis(oxy))bis(ethane-2,1-diyl) (2E,2'E)-bis(2-cyano-3-(5-(4-(diphenylamino)phenyl)thiophen-2-yl)acrylate) (**D-2**): To a stirred solution of **TPA-T-CHO (14)** (170 mg, 0.478 mmol) and **16** (78 mg, 0.239 mmol) in $CHCl_3$ (25 mL) were added 4 drops of Et_3N. The reaction mixture was refluxed under argon atmosphere for 72 h. Then the solvent was removed *in vacuo* and the residue was purified by column chromatography on silica gel (eluent: DCM to DCM/AcOEt 8/2 v/v). The resulting oily solid was further purified by re-precipitation in DCM with pentane to yield **D-2** (175 mg, 0.175 mmol, 73 %) as a flashy red solid. ^{1}H NMR (300 MHz, CD_2Cl_2): δ 8.28 (s, 2H), 7.73 (d, *J* = 4.1 Hz, 2H), 7.55 (d, *J* = 8.7 Hz, 4H), 7.36 – 7.26 (m, 10H), 7.17 – 7.06 (m, 12H), 7.03 (d, *J* = 8.7 Hz, 4H), 4.45 – 4.37 (m, 4H), 3.81 – 3.75 (m, 4H), 3.71 – 3.60 (m, 8H). ^{13}C NMR (76 MHz, CD_2Cl_2): δ 163.47, 155.46, 149.85, 147.37, 146.92, 140.23, 134.34, 129.93, 127.77, 126.13, 125.79, 124.48, 123.71, 122.44, 116.55, 97.21, 71.23, 71.05, 69.28, 65.87. HRMS (FAB): Calculated for $C_{60}H_{50}N_4O_7S_2$ 1002.3121, found 1002.3115.

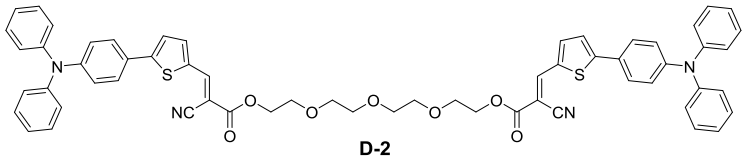

2-((5'-(4-(Methyl(phenyl)amino)phenyl)-[2,2'-bithiophen]-5-yl)methylene)malononitrile

(DPMA-T-T-DCV)

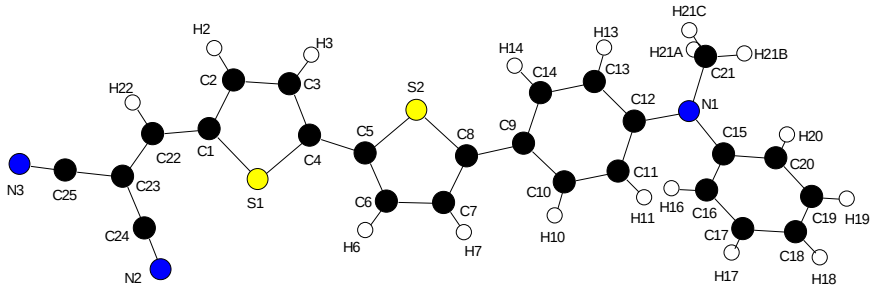

Empirical formula	$C_{25}H_{17}N_3S_2$
Formula weight	423.53
Temperature	150.0(1) K
Wavelength	1.54184 A
Crystal system, space group	Monoclinic, P 21/c
Unit cell dimensions	a = 10.4637(3) A alpha = 90 deg.
	b = 17.4651(5) A beta = 98.417(3) deg.
	c = 11.3889(4) A gamma = 90 deg.
Volume	2058.90(11) A^3
Z, Calculated density	4, 1.366 Mg/m^3
Absorption coefficient	2.471 mm^-1
F(000)	880
Crystal size	0.283 x 0.273 x 0.088 mm
Theta range for data collection	4.271 to 76.555 deg.
Limiting indices	-12<=h<=10, -21<=k<=21, -11<=l<=14
Reflections collected / unique	8339 / 4151 [R(int) = 0.0936]
Completeness to theta = 76.000	98.2 %
Absorption correction	Semi-empirical from equivalents
Max. and min. transmission	1.00000 and 0.73009
Refinement method	Full-matrix least-squares on F^2
Data / restraints / parameters	4151 / 0 / 272
Goodness-of-fit on F^2	1.061
Final R indices [I>2sigma(I)]	R1 = 0.0757, wR2 = 0.1868 [3816 Fo]
R indices (all data)	R1 = 0.0809, wR2 = 0.1964
Largest diff. peak and hole	0.583 and -0.745 e.A^-3

2-((5-(9-Methyl-9H-carbazol-3-yl)thiophen-2-yl)methylene)malononitrile (MeCz-T-DCV)

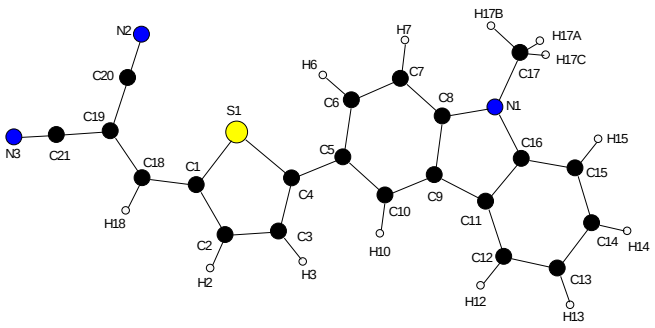

Empirical formula	$C_{21}H_{13}N_3S$
Formula weight	339.40
Temperature	150.0(1) K
Wavelength	1.54184 A
Crystal system, space group	Monoclinic, P 21/c
Unit cell dimensions	a = 15.5633(14) A alpha = 90 deg.
	b = 13.3855(19) A beta = 93.486(10) deg.
	c = 7.8112(11) A gamma = 90 deg.
Volume	1624.2(4) A^3
Z, Calculated density	4, 1.388 Mg/m^3
Absorption coefficient	1.819 mm^-1
F(000)	704
Crystal size	0.111 x 0.041 x 0.023 mm
Theta range for data collection	2.845 to 75.395 deg.
Limiting indices	-18<=h<=18, -15<=k<=15, -8<=l<=9
Reflections collected / unique	4553 / 4553 [R(int) = ?]
Completeness to theta = 76.000	90.6 %
Absorption correction	Semi-empirical from equivalents
Max. and min. transmission	1.00000 and 0.80887
Refinement method	Full-matrix least-squares on F^2
Data / restraints / parameters	4553 / 0 / 228
Goodness-of-fit on F^2	0.793
Final R indices [I>2sigma(I)]	R1 = 0.0580, wR2 = 0.1042 [1779 Fo]
R indices (all data)	R1 = 0.1567, wR2 = 0.1235
Largest diff. peak and hole	0.359 and -0.472 e.A^-3

2-((5-(9-Methyl-9H-carbazol-3-yl)selenophen-2-yl)methylene)malononitrile (MeCz-Se-DCV)

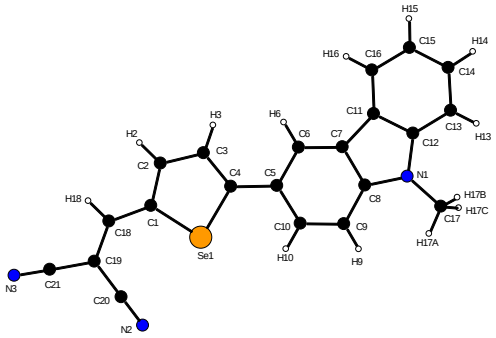

Empirical formula	$C_{21}H_{13}N_3Se$
Formula weight	386.30
Temperature	150.0(1) K
Wavelength	1.54184 A
Crystal system, space group	Triclinic, P -1
Unit cell dimensions	a = 8.5988(3) A alpha = 67.083(4) deg. b = 9.5021A beta = 78.813(3) deg. c = 12.1734(5) A gamma = 64.937(4) deg.
Volume	829.38(7) A^3
Z, Calculated density	2, 1.574 Mg/m^3
Absorption coefficient	3.114 mm^-1
F(000)	388
Crystal size	0.136 x 0.097 x 0.035 mm
Theta range for data collection	3.945 to 76.191 deg.
Limiting indices	-10<=h<=10, -11<=k<=11, -10<=l<=14
Reflections collected / unique	6466 / 3309 [R(int) = 0.0132]
Completeness to theta = 76.000	98.1 %
Absorption correction	Semi-empirical from equivalents
Max. and min. transmission	1.00000 and 0.87653
Refinement method	Full-matrix least-squares on F^2
Data / restraints / parameters	3309 / 0 / 227
Goodness-of-fit on F^2	1.043
Final R indices [I>2sigma(I)]	R1 = 0.0225, wR2 = 0.0586 [3266 Fo]
R indices (all data)	R1 = R1 = 0.0227, wR2 = 0.0588
Largest diff. peak and hole	0.386 and -0.319 e.A^-3

References:

1. B. Kim, H. R. Yeom, M. H. Yun, J. Y. Kim and C. Yang, *Macromolecules*, 2012, **45**, 8658-8664.
2. Y. Jiang, C. Cabanetos, M. Allain, P. Liu and J. Roncali, *J. Mater. Chem. C*, 2015, **3**, 5145-5151.
3. C. Malacrida, A. Hossein, S. Gámez-Valenzuela, I. Lenk, P. Simon, A. Labrunie, J. Grolleau, J. T. López Navarrete, M. C. Ruiz Delgado and C. Cabanetos, *ChemElectroChem*.
4. A. Labrunie, P. Josse, S. Dabos-Seignon, P. Blanchard and C. Cabanetos, *Sustainable Energy & Fuels*, 2017, **1**, 1921-1927.
5. A. Leliège, C.-H. Le Régent, M. Allain, P. Blanchard and J. Roncali, *Chemical Communications*, 2012, **48**, 8907-8909.
6. T. Rousseau and J. Roncali.
7. A. Leliège, J. Grolleau, M. Allain, P. Blanchard, D. Demeter, T. Rousseau and J. Roncali, *Chemistry–A European Journal*, 2013, **19**, 9948-9960.

Matériaux donneurs dérivés de petites molécules conjuguées de type push-pull pour le photovoltaïque organique : caractérisation et optimisation de cellules solaires

Mots clés : Photovoltaïque organique, Cellules solaires organiques, Cellules bicouche, Cellules à réseaux interpénétrés, Systèmes pi-conjugués, Push-pull, Multimères, Fullerènes

Résumé : Les cellules solaires organiques sont en général constituées de deux types de semi-conducteurs organiques, un donneur et un accepteur d'électrons. Ce travail porte sur l'évaluation de matériaux donneurs d'électron dérivés de molécules pi-conjuguées push-pull combinés à des dérivés du fullerène comme matériau accepteur.

Cette thèse décrit d'abord la fabrication et l'optimisation des cellules photovoltaïques (PV) réalisées à partir du DPMA-T-DCV. Cette petite molécule conjuguée push-pull facilement accessible, présente de bonnes propriétés de transport de trous à l'état solide et est constituée d'un groupe électro-donneur diphénylméthylamine (DPMA), une unité thiophène (T) comme espaceur pi-conjugué et un groupe terminal électro-attracteur dicyanovinyle (DCV). Différents dispositifs ont été fabriqués (cellules bicouche ou à réseaux interpénétrés de structure conventionnelle ou inverse) puis optimisés en jouant sur l'épaisseur des couches, le ratio massique entre la molécule push-pull et le dérivé du fullerène sélectionné ainsi que sur le procédé de fabrication en solution ou sous vide. Des cellules à réseaux interpénétrés de structure conventionnelle avec des rendements de conversion PV supérieurs à 4% ont pu être élaborées par co-évaporation du DPMA-T-DCV et de fullerène C_{60}.

De nouvelles molécules dérivées de DPMA-T-DCV, présentant un espaceur conjugué plus étendu ou un noyau sélénophène à la place de l'unité T et/ou un analogue carbazole plus rigide que le groupe DPMA, ont été évaluées en PV. Enfin, des multimères de push-pull ont également été testés dans des cellules à réseaux interpénétrés en présence de $PC_{61}BM$ ou $PC_{71}BM$ pour conduire à des rendements de photo-conversion de 3.4%.

Small Conjugated Push-Pull Molecular Donors for Organic Photovoltaics: Characterization and Devices Optimization

Keywords: Organic photovoltaics, Organic solar cells, Bi-layer solar cells, pi-Conjugated systems, Push-pull, Multimers, Fullerenes

Abstract: Organic solar cells (OSCs) generally consist of two types of organic semiconductors, one electron acceptor and one electron donor. This PhD work deals with the evaluation of electron donor materials derived from pi-conjugated push-pull molecules combined with fullerene derivatives as acceptor materials.

This thesis firstly describes the fabrication and optimization of photovoltaic (PV) cells made from the small DPMA-T-DCV push-pull conjugated molecule known for its good solid-state hole transport properties and constituted by a diphenylmethylamine (DPMA) electron-donating group, a thiophene (T) unit as pi-conjugated spacer and a terminal dicyanovinyl (DCV) electron-withdrawing group. Different devices have been manufactured such as bi-layer or bulk heterojunction (BHJ) OSCs with a conventional or inverted structure, and then optimized by adjusting the thickness of the layers, the weight ratio between the push-pull molecule and the selected fullerene derivative, and by using a solution or a vacuum deposition process as well. Conventional BHJ OSCs with PV conversion efficiencies greater than 4% could be achieved by co-evaporation of DPMA-T-DCV and fullerene C_{60}.

Then, new DPMA-T-DCV derivatives resulting from an extension of the pi-conjugated spacer or by replacing the T unit with a selenophene ring and/or the DPMA unit with its more rigid carbazole analogue, were assessed for PV. Finally, push-pull multimers were also tested in BHJ OSCs in the presence of $PC_{61}BM$ or $PC_{71}BM$ yielding photo-conversion efficiencies up to 3.4%.